Design, Manufacture, and Applications of High Mass Resolution Orbital Trapping for Secondary Ion Mass Spectrometry

James Christopher Hood

School of Engineering

Newcastle University

A thesis submitted for the degree of

Doctor of Philosophy

January 2020

Abstract

Secondary Ion Mass Spectrometry (SIMS) is a widely used analytical technique for characterizing surface chemistry in numerous technical applications, including medical implant surfaces, fault-finding in semi-conductors, proteomics, pharmaceutical development, and in the field of astrobiology and the search for extra-terrestrial life.

The mass resolving power of modern time-of-flight SIMS (ToF-SIMS) instruments does not exceed 12,000. This means that for some mass spectral peaks, a single molecular formula cannot be definitively specified. This is particularly important for high mass molecules, where there can be many possible peak attributions for a given nominal mass.

Orbital ion traps have been shown to achieve mass resolution in excess of 100,000, without the need for the large and expensive superconducting magnets required in Fourier-transform ion cyclotron resonance (FT-ICR) instruments. Therefore, an orbital ion trapping mass analyser has been designed, fabricated, and coupled to the Ionoptika J105 SIMS. Computational modelling has been developed to evaluate proposed designs and examine the effects of manufacturing imperfections on the performance of the orbital ion trap.

A method of exciting a precise mass range of trapped ions has also been developed, using a Stored Waveform Inverse Fourier Transform (SWIFT) technique. This allows fast, high mass resolution analysis after a low-resolution spectrum has been gathered using the time-of-flight analyser.

This thesis will cover the function and capabilities of the Ionoptika J105 SIMS, the need for high mass resolution in SIMS, the mathematical background of electrostatic harmonic ion traps, and the simulation, design, manufacture, and operation of the orbital trapping mass analyser. This research allows mass spectra to be gathered with both high mass and spatial resolution, an advancement with numerous potential applications, including label-free biological imaging and the unambiguous identification of biosignatures in astrobiology.

Acknowledgements

I would like to express my most sincere thanks to the very many people who have helped me over the past four years.

I would like to thank my academic supervisors Dr Jinju Chen, and Professor Peter Cumpson, who have offered generous guidance and motivation, alongside plentiful wit and wisdom.

To my colleagues and friends who have been part of NEXUS; Professor Ian Fletcher, Dr Jose Portoles, Dr Billy Murdoch, Dr Anders Barlow, Dr Naoko Sano, Dr Sabrina Tardio, Dr Sadia Sheraz, Dr Graham Purvis, Ms Lisa Li, Mr Grant Saunby, and Mr Jake Sheriff. Your companionship and expertise have made my time studying a pleasure and a true privilege.

I would like to give my sincere appreciation to Mr Michael Foster for his invaluable assistance throughout my PhD research, including sage advice on wide ranging topics, from the manufacturing of quadro-logarithmic electrode profiles, to the far more complicated matter of becoming a father for the first time.

I would like to gratefully thank Dr Steve Thompson, who kindly visited on multiple occasions to offer uniquely useful insight and many suggestions on ion optics and vacuum technology, alongside motivational words when the vagaries of experimental physics had potential to become overwhelming.

I would like to thank all of the good people of Ionoptika Ltd. for their continued expert technical support for Newcastle University's J105 SIMS, particularly that of Mr Paul Blenkinsopp, Mr Gavyn Trowbridge, Dr Allen Bellew and Mr Ariel Zochowski.

Many other members of staff in the School of Engineering have kindly offered their time and support to this project, including; Mr Richard Burnett on electrical and electronics matters, as well as advice for new parents; Mr Stuart Baker, Mr Jamie Hodgson, Mr Robert Davidson and Mr Peter Chapman, for advice and assistance with manufacturing; Mr Paul Harrison and Dr Zhongxu Hu for electrical support; Dr Barry Gallacher and Dr Harriet Grigg for insightful discussions on the mechanics of ion motion; Mr John Richardson, Mr Derek Simm, and Mr Callum Squires for IT problem solving of many kinds, and Dr Stephen Moore, Dr John Hedley, Dr Kheng-Lim Goh,

and Dr John Appleby for their support across different aspects of life as a research student.

I owe so much to my parents and family, you have given me immeasurable love and support without which I would have not been able to grasp the opportunity to undertake this research. To my Grandad, Dr Peter Rowland, a phone call with you before accepting the PhD studentship opportunity helped me to make the right decision, thank you.

A wide group of friends have also supported me outside of university life, I am deeply grateful to you all for your tolerance and camaraderie over the years. Gratitude is also due to Middlesbrough football club, whose toil over the past four years, punctuated by a few notable successes, happens to accurately reflect the rhythms of a research degree.

To my darling daughter Emily, a smile and a cuddle from you will always reassure me that all things are possible. You joined us part way through this journey, and I now cannot imagine what life was like without you as part of it. I'm very much looking forward to having more time to spend with you.

And finally, to my soulmate Katie, your love and encouragement have spurred me on and sustained me throughout this PhD. Without your ardent support and endless patience none of this would have been possible. You make me feel like my mind is free, and my dreams are reachable, that's why I know you are the one.

List of Publications

1. **Hood, JC** and Cumpson, PJ (2016) 'Design and Manufacture of a High Resolution Orbital-Trapping Mass-Analyser for Secondary Ion Mass Spectrometry', International Journal of Modern Engineering Research, 6(10), pp. 76–83.

2. Nilsson KD, Palm M, **Hood J,** Sheriff J, Farewell A, Fletcher JS. (2019) 'Chemical changes on, and through, the bacterial envelope in E. coli mutants exhibiting impaired plasmid transfer identified using time-of-flight secondary ion mass spectrometry', Analytical Chemistry, 91(17), pp 11355–11361. doi: 10.1021/acs.analchem.9b02533.

3. Purvis G, Sano N, van der Land C, Barlow A, Lopez-Capel E, Cumpson, P, **Hood J**, Sheriff, J, and Gray N (2019) 'Combining Thermal Hydrolysis and Methylation-Gas Chromatography/Mass Spectrometry with X-ray Photoelectron Spectroscopy to Characterise Complex Organic Assemblages in Geological Material', MethodsX, (Accepted)

List of Conference Presentations & Awards

2019

SIMS XXII – *Kyoto, Japan – October 2019*
Abstract accepted for oral presentation on orbital ion trapping SIMS, *"Orbital Trapping Mass Analyser for SIMS"*
Also contributing to poster presentation abstract accepted for Dr Naoko Sano' "*Detection of surface-stabilised trace level biosignatures in fossilised fly using cluster ion beam"*

ASB8 – The 8th Annual Conference of the Astrobiology Society of Britain – *Newcastle University, UK – April 2019*
Award: 2nd place for student presentation.
Oral presentation; "*Nano-imaging + Nano-chemistry = Unambiguous Biomarkers*"

NEPIC (North East Process Industry Cluster) Technology Symposium – *Teesside University, UK – February 2019*
Oral presentation on chemical surface analytical techniques & orbital ion trapping.

2018

Pacsurf – *Hawaii, USA – December 2018*
Oral presentation, including my research on orbital ion trapping, given by Prof. Peter Cumpson.

SIMS Europe – *Münster, Germany – September 2018*
Oral presentation; *"40keV Water Source & Orbital Ion Trap for SIMS"*

VASSCAA-9 - The 9th Vacuum and Surface Science Conference of Asia and Australia – *Sydney, Australia – August 2018*
Poster presentation given on my behalf by Prof. Peter Cumpson, focussing on the design and manufacturing of an orbital ion trap for SIMS

Mechanical Engineering PGR Conference – *Newcastle University, UK – May 2018*
Poster Presentation

2017

SIMS XXI – *Kraków, Poland – September 2017*
Award: Rowland Hill Award for PhD Student presenters
Oral presentation; *"Optimal Stored Waveform Inverse Fourier Transform (SWIFT) Excitation in a SIMS Orbital Trapping Mass Analyser"*

Mechanical Engineering PGR Conference – *Newcastle University, UK – May 2017*
Oral Presentation, 1st Prize

2016

Mechanical Engineering PGR Conference – *Newcastle University, UK – May 2016*
Oral Presentation, 1st Prize

Acknowledgements

1. *Sheraz (née Rabbani), S. et al. Enhanced Ion Yields Using High Energy Water Cluster Beams for Secondary Ion Mass Spectrometry Analysis and Imaging. Anal. Chem. acs.analchem.9b01390 (2019). doi:10.1021/acs.analchem.9b01390*

Mentioned in the Acknowledgements for assistance with the water cluster source for SIMS.

Table of Contents

List of Figures

List of Tables

Nomenclature

Symbols

A_{ln}	Dimensionless proportion of logarithmic-Cassinian potential in distribution
A_{quad}	Dimensionless proportion of quadrupolar potential in distribution
E_k	Ion kinetic energy
E_z	Axial component of electric field
E_ϕ	Ion energy in the rotational direction
F_z	Axial component of force
I_m	Secondary ion current of species m
I_p	Primary ion flux
L_{eff}	Effective length travelled by ions during injection
R_1	Internal electrode radius of orbital ion trap
R_2	External electrode radius of orbital ion trap
R^2	Coefficient of determination
R_m	Characteristic radius of orbital ion trap
R_o	Ion orbital radius
U_{Cassini}	Voltage between internal and external electrodes of Cassinian ion trap
U_{int}	Internal electrode voltage of orbital ion trap
U_{static}	DC voltage component in parametric excitation
U_{RF}	Radio-frequency voltage for parametric excitation
Y_m	Sputter yield
a_i	Cassinian ion trap internal electrode radius
a_o	Cassinian ion trap external electrode radius
a_u	Dimensionless trapping parameter in Mathieu equation
d_m	Particle diameter
f_{res}	Maximum possible frequency resolution for a given recorded frequency
f_s	Sampling frequency at which a signal is recorded
k_p	Time varying field curvature
m_{input}	Specified input mass for orbital ion trapping simulation
m_{output}	Calculated output mass from orbital ion trapping simulation
$m_{\mathrm{reference}}$	Reference output mass corresponding to a given input mass, if no misalignment is present in orbital ion trapping simulation
q_u	Dimensionless trapping parameter in Mathieu equation

$\bar{t}$	Slow time scale in perturbation analysis
$\hat{t}$	Fast time scale in perturbation analysis
t_{inj}	Time-of-flight during injection in orbital ion trapping
t_{max}	Duration of a recorded transient acquisition
u_o	DC potential
v_{crit}	Critical voltage at which parametric excitation is possible.
${\alpha_m}^{+/-}$	Ionisation probability of positive or negative ions
η_m	Transmission factor of the analytical instrument for species m
θ_m	Fractional mass concentration of m in the surface layer
ω_n	Natural frequency of ion oscillation
μ	Ratio of excitation and DC voltages in parametric excitation
Δm_{FWHM}	Mass resolution at full-width half-maximum
Δt	Simulation time step
$\Delta\phi$	Phase shift induced due to ion injection, gradient of electric potential field
Λ	Difference in frequency between excitation frequency and natural oscillation frequency
Ω	Parametric excitation frequency
A	Coefficient of logarithmic portion of potential distribution
B	Magnetic field strength, or a coefficient in a potential field distribution
C	Constant term in potential distribution
E	Electric field strength
F	Force
L	Length of the flight tube in a time-of-flight mass spectrometer
N	Number of ions trapped before coalescence occurs in FT-ICR, or number of data points acquired in a recorded transient
P	Excitation voltage amplitude for parametric excitation
R	Mass resolution
T	Temperature
U	Electric potential distribution
V	Accelerating voltage in a time-of-flight mass spectrometer
b	Radial distance from the centre of the Cassinian trap to the centre of the internal electrodes.
d	Constant term related to voltage offset in Cassinian ion trap potential, or distance travelled by an ion in a single simulation time step
f	Frequency
k	Field curvature, or Boltzmann constant
m	Ion mass

m/z	Mass-to-charge ratio
n	Order of Cassinian trap, equivalent to the number of electrodes
p	Pressure
q	Ion charge
r	Radial co-ordinate
t	Time
v	Ion velocity
z	Axial co-ordinate
Δf	Smallest difference in frequency which can be detected
α	Polar angular co-ordinate
ε	Small perturbation parameter
ζ	Dimensionless parameter in Mathieu equation, damping ratio
κ	Curvature of a mathematical function
λ	Mean free path of a particle
ν	Voltage ratio between AC and DC components of excitation voltage. or adjusted damping ratio
ω	Angular frequency
ϕ	Electric potential field

Acronyms

AES	Auger Electron Spectroscopy
AFM	Atomic Force Microscopy
BNC	Bayonet Neill–Concelman (Connector)
CAD	Computer Aided Design
CID	Collision Induced Dissociation
CNC	Computer Numerically Controlled
CSV	Comma Separated Values
DSUB	D-subminiature
ESA	Electrostatic Assembly
ESI	Electrospray Ionisation
FDM	Finite Difference Method
FFT	Fast Fourier Transform
FTICR	Fourier Transform Ion Cyclotron Resonance
FTMS	Fourier Transform Mass Spectrometry
FWHM	Full-Width Half-Maximum

GCIB	Gas Cluster Ion Beam
GEM	Geometry File
GUI	Graphical User Interface
HIM	Helium Ion Microscope
HPLC	High Performance Liquid Chromatography
ICR	Ion Cyclotron Resonance
ISO	International Organization for Standardization
LIGO	Laser Interferometer Gravitational-Wave Observatory
LIST	Luxembourg Institute of Science and Technology
LMIG	Liquid Metal Ion Gun
MALDI	Matrix-Assisted Laser Desorption/Ionization
NEXUS	National ESCA and XPS Users' Service
NPL	National Physical Laboratory
OCULAR	Operation at Constant Ultrahigh Resolution
PDMS	Polydimethylsiloxane
PEEK	Polyether ether ketone
PID	Proportional-Integral-Derivative
PXI	Proportional-Integral-Derivative
QKC	Quasi-Kinematic Coupling
RAM	Random Access Memory
SAC	Sample Analysis Chamber
SARC	Surface Analysis Research Centre
SEAL	Surface Engineering and Analysis Laboratory
SHV	Safe High-Voltage
SIMS	Secondary Ion Mass Spectrometry
SIS	Scientific Instrument Services
SNMS	Sputtered Neutral Mass Spectrometry
STL	Stereolithography
SWIFT	Store Waveform Inverse Fourier Transform
TBO	Tertiary Beam Optics
TOF	Time-of-Flight
UMIST	University of Manchester Institute of Science and Technology
XPS	X-ray Photoelectron Spectroscopy

Chapter 1. Introduction

1.1 Introduction

This research project was primarily concerned with the production of an ion trap mass analyser, to be coupled with a state of the art Time-of-Flight Secondary Ion Mass Spectrometer (ToF-SIMS) instrument, the J105 SIMS manufactured by Ionoptika (Ionoptika, 2015). Newcastle University's Surface Engineering and Analysis Laboratory (SEAL) took delivery of only the fourth J105 ever produced in 2016. Figure 1.1 shows a schematic of the J105 with key components labelled.

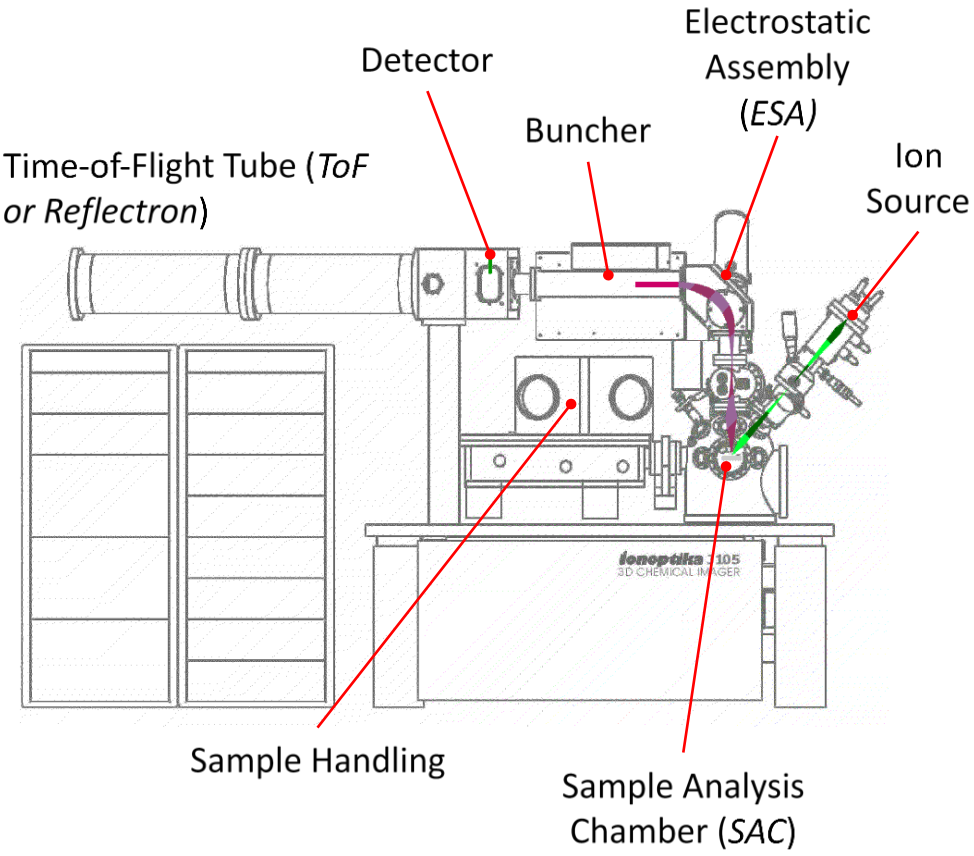

Figure 1.1 - Ionoptika J105 SIMS Schematic Diagram adapted from (SARC Manchester, 2016)

The J105 SIMS has been widely described in the literature, one of the most comprehensive descriptions can be found in a joint paper between John Vickerman's group at the University of Manchester, Ionoptika, and Scientific Analysis Instruments (Fletcher *et al.*, 2008). The basic operation of the J105 is as follows:

1. Primary ions are generated in one of two ion cluster sources, either a 40keV C_{60}^+ fullerene source or 40keV Ar_n^+ (n = 500, 1000, 2000, 4000) gas cluster ion

beam (GCIB). In 2017, the GCIB column was modified with the addition of an in-vacuum heater assembly, allowing the generation of large cluster ions from a liquid source, such as high performance liquid chromatography (HPLC) grade water.

2. The primary ion beam is focussed onto the sample in the sample analysis chamber (SAC) through a series of electrostatic lenses and deflectors.
3. The sample surface is bombarded with a continuous beam of primary ions, causing the emission of secondary particles from the uppermost few nanometres, a proportion of these produce secondary ions which can be analysed in a mass spectrometer.
4. Ions are drawn into a radio-frequency only quadrupole cell using a large extraction voltage. The quadrupole is filled with a bath gas such as nitrogen, which serves to reduce the energy of the secondary ions through collisions.
5. The electrostatic assembly (ESA) then deflects ions through 90° into the buncher, whilst also ensuring that all ions retain a narrow spread of kinetic energies of no greater than ±1eV.
6. Ions are then bunched together into packets with a narrow distribution in space and time, in the aptly named buncher. This is achieved by the rapid application of a varying accelerating voltage across the length of an ion packet, so that heavier ions at the rear of the packet experience greater acceleration than lighter ions, resulting in a time focus of ions at the entrance to the mass analyser section of the J105.
7. Ions are then accelerated into the Time-of-Flight (ToF) reflectron mass analyser. When ions reach the end of the ToF they are reflected by a harmonic electric potential which directs the beam back to the detector, whilst compensating for any remaining small differences in ion energy for ions of equivalent mass.
8. As ions are of equal energy, the heavier mass ions travel slower and have longer flight times, with the converse being true for lower mass ions, thus a mass spectrum of ion species present in the sample can be acquired.

The J105 is capable of mass resolution in excess of 10,000, where mass resolution, the ability to discriminate between ions of different mass, is measured as the target mass divided by the difference in mass at the full-width half-maximum (FWHM) of a mass spectral peak, as defined in equation (1.1).

$$\text{Mass resolution, m}/\Delta\text{m} = \frac{m}{\Delta \text{m}_{\text{FWHM}}} \qquad (1.1)$$

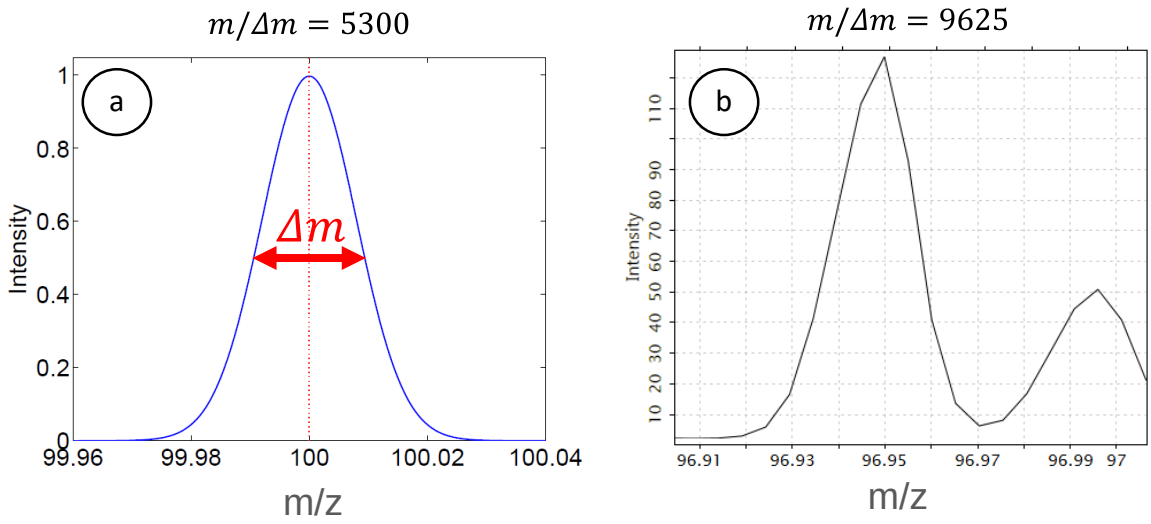

Figure 1.2 - Diagram illustrating how mass resolution is defined in mass spectra, with examples of a) Idealised data plotted in MATLAB, and b) Real mass spectral data from J105.

Figure 1.2 shows the definition of full-width half-maximum on idealised and real mass spectral data.

The J105 differs from conventional time-of-flight SIMS instruments, such as the IONTOF TOF-SIMS V (IONTOF GmbH, 2017), in its use of continuous (DC) primary ion sources. This is possible due to the buncher – ToF configuration employed by the J105, with an accelerating electric field creating a time-focus as ions exit the buncher, which is the datum from which ion flight times are measured. In conventional ToF-SIMS instruments, a nanosecond-scale pulsed primary ion beam is used, and ion flight time is measured as the time between interaction with the sample surface and arrival at the detector. Use of a DC ion beam allows much faster analysis times, for example a 100µm x 100µm analysis with 10pA of primary beam current would take ~9hrs using a 50ns pulsed ion source running at 10kHz, whereas on the J105 this is reduced to less than 16s, assuming in both cases that the primary ion beam dose is set to be equal to the static SIMS limit of 1 x 10^{13} ions cm^{-2} (Fletcher *et al.*, 2008).

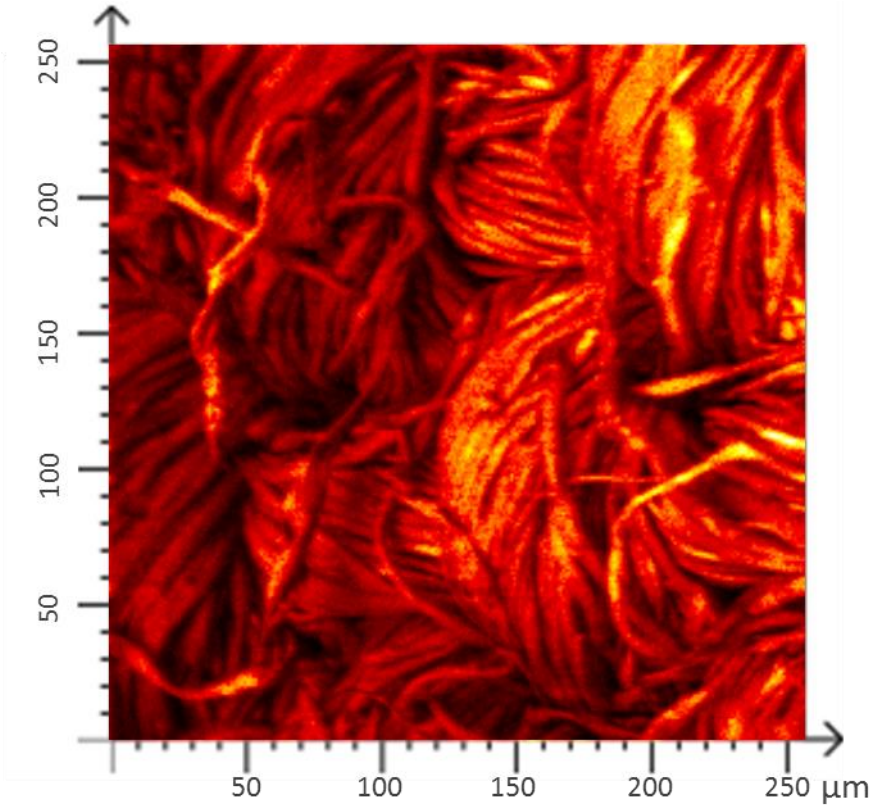

Figure 1.3 - Total ion image of woven fabric sample, imaged with C_{60}^+ primary ion beam on an Ionoptika J105 SIMS, over an area of 256µm x 256µm.

Another advantage of decoupling the sputtering event from time-of-flight measurements, is the possibility of high mass resolution which is independent of sample topography. A demonstration of this can be seen in Figure 1.3, showing the total ion image generated from a rough fabric sample which was analysed on the J105 using the C_{60} cluster beam. The signal present from the lower woven fibres highlights the depth of field of the C_{60} beam, with mass resolution ~10,000 observed from these points as well as the topmost fibres.

1.2 Orbital Ion Trap

The main focus of this project is a high resolution mass analyser which has been designed to be housed on top of the ESA of the J105, with ions travelling vertically upwards instead of being deflected into the time-of-flight analyser. This will allow complementary high mass resolution point analysis to be carried out without the need to remove the sample from the J105. An additional ISO-K63 vacuum flange was requested during the manufacture of the J105 to afford a mounting point for the new device. The ion trap comprises three component electrodes; an internal electrode

around which ions orbit, and two external electrodes, separated by a 100µm gap, between which ions oscillate axially. The electrodes are described by a revolved quadro-logarithmic profile, around which the ions orbit, hence the designation as an orbital ion trap.

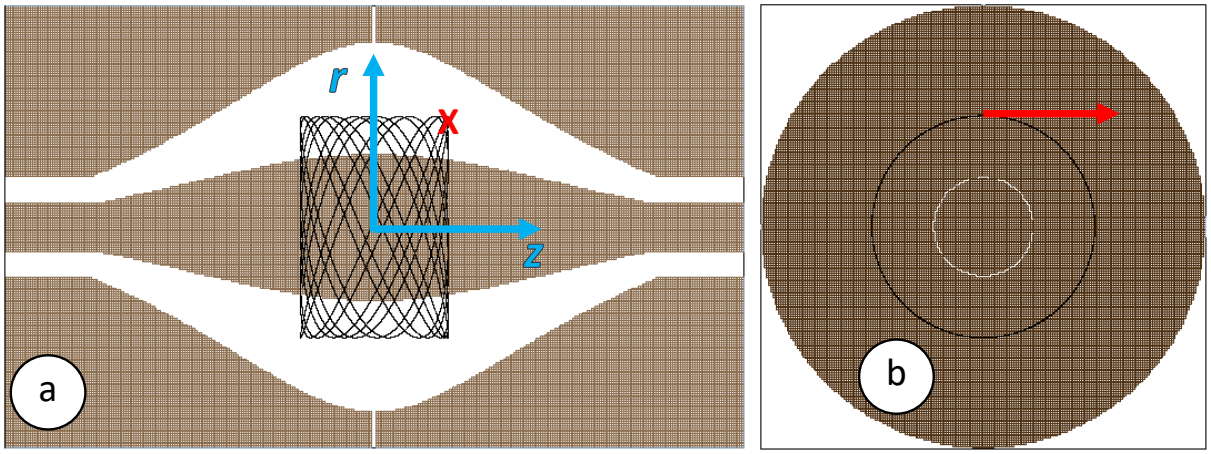

Figure 1.4 - Orbital ion trap geometry, and simulated ion trajectories, calculated in SIMION. Showing a) Axial ion trajectories, harmonic in the z-direction, and b) Orbital ion trajectories around the internal electrode.

Figure 1.4 shows screenshots taken from SIMION, (SIS, 2015), an ion trajectory simulation software package, which was used extensively to model behaviour of ions trapped within the orbital ion trap, and also to optimise transmission of ions from the J105 SIMS into the orbital ion trap. Ions are injected into the orbital ion trap to begin their orbits at the point denoted X, corresponding to a position of z = 6mm, r = 9mm, the initial ion velocity is normal to both r and z axes, as shown in Figure 1.4b.

The motion of ions in the radial plane can be thought of as rotating elliptical orbits, in the ideal case these orbits will be almost circular, in order to reduce the effect of field imperfections on axial motion. For, it is the axial motion of ions which is critical to the function of the device, as the frequency of axial oscillation is independent of ion energy and position, and can be directly related to the mass of an ion by equation (1.2):

$$\omega = \sqrt{\frac{q}{m}k} \qquad (1.2)$$

The main advantage to be gained from successful coupling of the J105 and orbital ion trap would be the increased mass resolution attainable, commercial quadro-logarithmic mass analysers achieve mass resolution in excess of 100,000 (Zubarev and Makarov, 2013), an order of magnitude higher than the mass resolution of 10,000 which can currently be achieved with the time-of-flight analyser of the J105.

High resolution mass spectrometry has a plethora of applications, from biomedical research fields such as drug discovery and proteomics, through to environmental research such as identifying the prevalence of contaminants in drinking water. One specific case in which increased mass resolution would be beneficial is the separation of hydrides from elemental mass peaks at masses above ~90u, which requires mass resolving power in excess of the 10,000 achievable with a conventional ToF-SIMS, as shown in Figure 1.5, adapted from (Stephan, 2001).

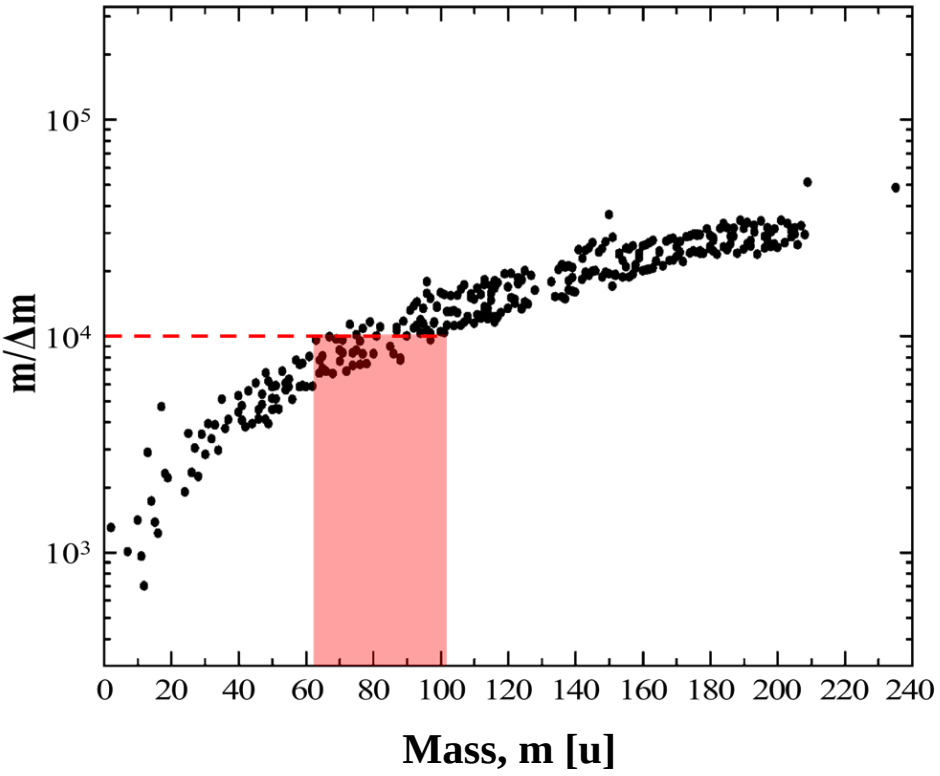

Figure 1.5 - Plot of mass resolution against mass, showing the mass resolution required to separate metal hydrides from their nearest elemental peaks, adapted from (Stephan, 2001).

An example of the extra depth of information gained from increased mass resolution, particularly when multiple species are present, is shown in Figure 1.6, adapted from (Marshall and Hendrickson, 2008). It can be seen that the low resolution data, gathered at mass resolution of approximately 4,000 gives a single spectral peak from 178.04u to 178.10. If this is taken to indicate a peak centred at 178.07u, with a width of 0.02u at half its maximum intensity, then there are 25 possible combinations just using carbon (C), hydrogen (H), nitrogen (N) and oxygen (O) which could give a molecule with a mass in that range. However, when the higher mass resolution data is considered, four distinct peaks become evident, with each peak only having up to three combinations of C, H, N and O able to give a molecular mass within 0.001u, the approximate peak width at half-maximum, of the measured mass.

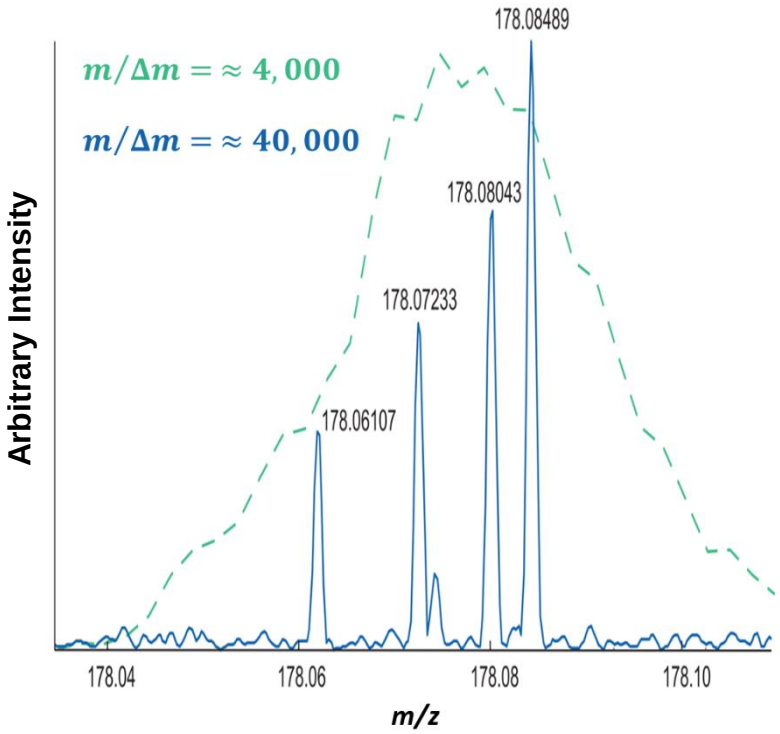

Figure 1.6 - Example of information gained from higher mass resolution. It should be noted that the Ionoptika J105 can achieve mass resolution of up to 10,000 for the mass range shown.

The possibility of combining analysis using the J105, enhanced with an orbital ion trap, and the exceptional spatial resolution of Newcastle University's Helium Ion Microscope (HIM), which can achieve spatial resolution as low as 0.3nm (Carl Zeiss Microscopy GmbH, 2012) would offer world leading surface analysis capabilities. In the past year, the installation of a magnetic sector SIMS analyser on the Helium Ion Microscope has added mass spectrometry capability to the instrument (Wirtz *et al.*, 2016). This makes Newcastle University's HIM the highest spatial resolution SIMS instrument in the UK. The ability to overlay such high spatial resolution chemical images with high mass resolution analysis from the J105, and even higher mass resolution analysis from an orbital ion trap equipped J105 would be truly unique.

The well-defined characteristics of secondary ions generated by the J105 make adding a further mass analyser feasible, as ions enter the ESA they have a narrow kinetic energy spread, making their behaviour more predictable and easier to design for.

One focus of the project has been the design, manufacture and assembly of the orbital ion trap, with particular attention given to accurate machining of the quadro-logarithmic electrode profiles. Simulations have been carried out contemporaneously in SIMION

to inform the manufacturing process. Three prototype orbital ion traps have been manufactured, and an ion transfer assembly has been constructed and mounted to the J105 to transfer ions from the J105 to the orbital ion trap.

Once a functioning device has been realised, the project focus shifted onto optimisation of the orbital ion trap, with particular regard to data analysis and the improvement of fast-Fourier-transform (FFT) analysis, as well as further refining the electronic control of the orbital ion trap to maximise ion retention within the trapping volume.

One of the developments made in this research project is the confirmation via simulation of an alternate method to excite ion motion within the orbital ion trap. This technique, named parametric excitation, is the process of applying a radio frequency (RF) voltage to the internal electrode at twice the resonant frequency of ion oscillation. This allows the injection of ions at the centre of the orbital ion trap, i.e. z = 0mm, with ions then excited to oscillate axially using parametric excitation. One advantage of this is that ion axial oscillations can be more easily kept in phase, as axial oscillations are induced simultaneously, rather than as a function of injection time. A fuller explanation of the mechanism and development of parametric excitation will be given later in this thesis.

1.3 Combining Mass Resolution with Spatial Resolution

The combination of orbital ion trapping with SIMS fills a niche in the capability of mass spectrometry instrumentation, as shown in Figure 1.7. Currently, ToF-SIMS instruments are able to achieve spatial resolution as low as 200nm, but they have not demonstrated mass resolution greater than 20,000 for this level of imaging resolution. In contrast, orbital ion trap mass analysers on MALDI instruments can routinely achieve mass resolution in excess of 100,000, but only at lower spatial resolutions, typically greater than 30µm. The combination of SIMS with an orbital ion trap will allow access to mass resolution far in excess of 10,000, whilst maintaining the excellent spatial resolution of SIMS.

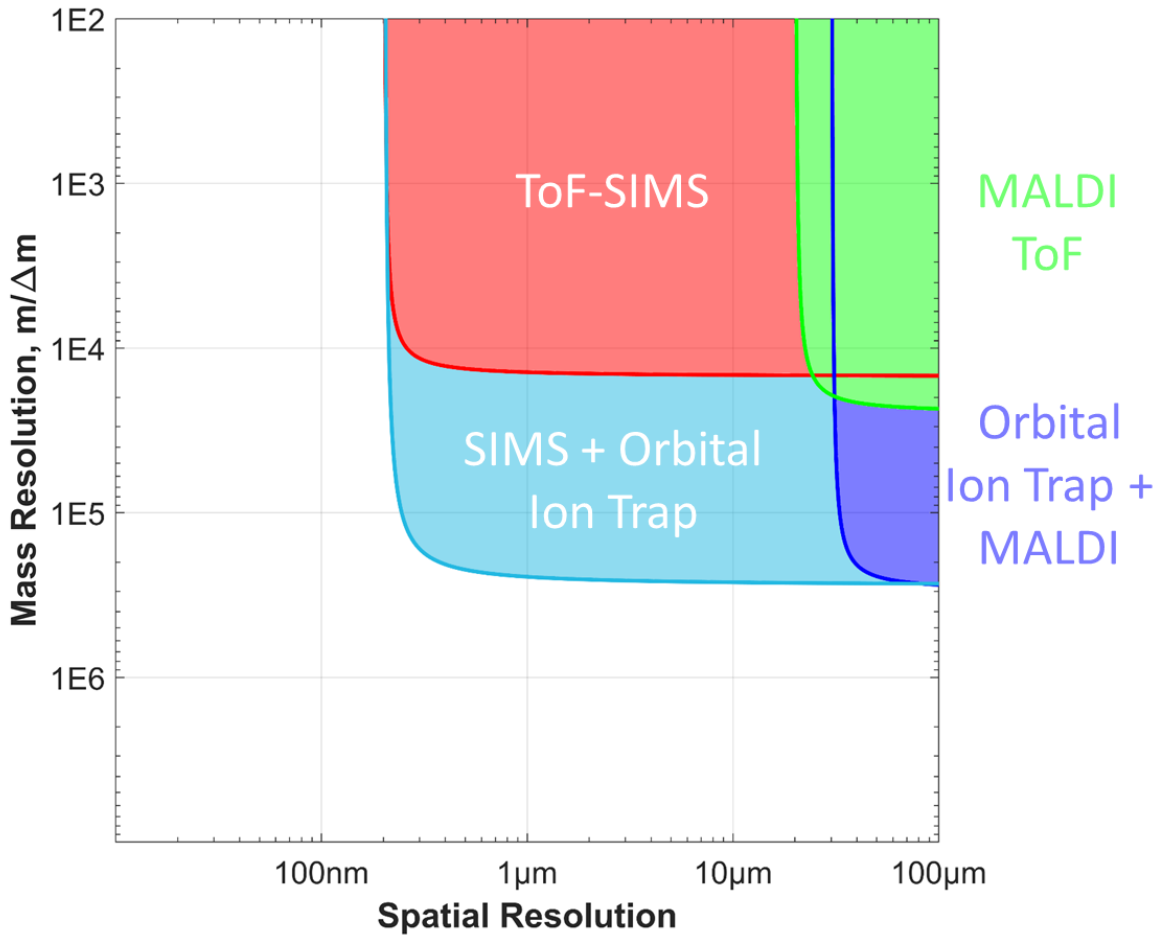

Figure 1.7 - Mass and spatial resolution capabilities of mass spectrometry imaging techniques, highlighting the new performance domain which can be accessed by combining SIMS instrumentation with an orbital ion trap mass analyser.

This combination of high mass resolution with high spatial resolution will allow the unambiguous identification of surface chemistry, and open up new avenues of research.

Chapter 2. Literature Review

This literature survey will cover two main aspects; first an overview of the history of mass spectrometry in general, and SIMS in particular, to give the analytical context in which the Ionoptika J105 fits, followed by a discussion of quadro-logarithmic ion traps, the main avenue of research of this thesis.

2.1 A Brief History of Mass Spectrometry

The basic principle of mass spectrometry is as follows; ions are generated from a sample using one of many ionisation methods, these ions are then separated based on their mass-to-charge ratio (m/z), the abundance of different mass-to-charge ratios is then measured quantitatively. Separation of ions can be achieved through the use of static or dynamic magnetic or electric fields, and combinations thereof (Gross, 2011). Mass spectrometry is widely used in many different scientific fields, ranging from the development of new pharmaceuticals, as in (Fisher *et al.*, 2009), to the pursuit of understanding the origins of life on Earth, and indeed furthering the search for extra-terrestrial life, (Selliez *et al.*, 2019). As such, there are myriad different mass spectrometry instruments now available to suit these many diverse applications, however all instruments can still be described by the same basic structure, consisting of an *ion source*, a *mass analyser*, and a *detector*.

2.1.1 Origins of Mass Spectrometry

The field of mass spectrometry can be followed back to the work of J. J. Thomson, who won the Nobel Prize for Physics in 1906 for the discovery of the electron with experiments to deflect cathode rays using an electrostatic field (Thomson, 1897). It was this discovery which led to the development of Thomson's first 'mass spectrograph', an instrument which was able to measure the mass-to-charge ratio of positive ions by their deflection in a combined electric and magnetic field. Ions generated in a discharge tube were passed through a region of both electric and magnetic fields. Ions were detected along two-dimensional parabolas when they struck a photographic plate, where their deflection from the neutral axis could be measured to determine their mass-to-charge ratio. Parabolic traces arose from the fact that multiple ions of the same mass but different velocities were striking the photographic plate. It was this instrument which generated a famous spectrum showing two distinct parabolas for ^{20}Ne and ^{22}Ne, confirming the existence of stable isotopes of elements,

(Thomson, 1913). The results generated from this instrument were difficult to interpret and could not provide quantitative determination of isotopic abundance.

Significant instrumental developments were made by Francis W. Aston, a researcher invited to Thomson's Cavendish Laboratory in 1909. Mass resolving power and mass accuracy were improved by separating the regions of electric and magnetic field, and orienting both deflections in the same plane. This allowed ions to be focussed in terms of their velocity upon detection, resulting in much clearer spectra as the dependence on ion energy which hindered Thomson's instrument had been removed. This allowed the identification of many more naturally occurring isotopes, resulting in Aston being awarded the Nobel Prize for Chemistry in 1922 (Aston, 1919), (Aston, 1920).

A further important contribution to mass spectrometry along this theme was the development of the double-focussing mass spectrometer by Mattauch and Herzog, which offered velocity and directional focussing of ions. A curved electrostatic deflector provided energy focussing of a wide mass range of ions, before a magnetic sector curved in the opposite direction separated ions by mass-to-charge ratio upon their detection on a single plane (Mattauch and Herzog, 1934).

2.1.2 Mass Spectrometry in the Second World War

During the Second World War, mass spectrometry was engaged in the war effort in the field of nuclear physics, particularly of use to the Manhattan Project set up by the United States of America, with the aim of developing functional atomic weapons. Alfred O. Nier's group at the University of Minnesota built the only mass spectrometer at the time which was capable of measuring the abundance ratios of uranium isotopes, as required to assess the performance of uranium enrichment (Nier, 2009). This was after previously having used magnetic sector mass spectrometry to demonstrate the first successful separation of the naturally occurring ^{235}U fissile isotope, work encouraged by correspondence from Enrico Fermi (Nier, 1939).

After the war, Nier further developed the concept of a double-focussing spectrometer, with the help of a graduate student, Edgar Johnson, leading to the development of the so-called Nier-Johnson geometry, consisting of a 90° electric sector, and a 60° magnetic sector with curvature in the same direction (Johnson and Nier, 1953). Such instruments allowed superior angular focussing of ions and achieved order of magnitude increases in mass accuracy and resolution (Nier, 1991). This was however

at significant expense, which prompted the simultaneous development of alternative instrumentation such as the time-of-flight (ToF) and quadrupole mass analysers.

2.1.3 Time-of-flight Analysers

In the proceedings of the American Physical Society in 1946, William Stephens proposed a 'pulsed mass spectrometer with time dispersion', in which microsecond pulses of ions were allowed to travel down a vacuum tube, with ions of different m/z travelling at different velocities and thus spreading out in space. The ions were collected in a Faraday cage, with the recorded current pulses producing a mass spectrum, with the lowest mass-to-charge ratio ions travelling fastest and thus arriving first. This was the initial concept of a time-of-flight mass analyser (Stephens, 1946). Time-of-flight analysers have some significant advantages compared to other analysers; they are fast and are able to collect a complete mass spectrum every few microseconds, they can also function over a wide mass range, meaning relative intensity patterns can be accurately measured, a wide mass range also allows time-of-flight analysers to be used to detect even large intact bio-molecules, providing they can be ionised without fragmentation. The parallel detection of a broad mass range of ions is the key advantage of time-of-flight analysers.

The recorded times of flight for ions are transformed into a mass spectrum by equation (2.3), which relates the mass-to-charge ratio to the accelerating voltage, V, the length of the flight tube, L, and the flight time, t, assuming all ions are of equal kinetic energy, (Fearn, 2015). Equation (2.3) can be found by combining the two definitions of kinetic energy shown in equation (2.1), with the simple relationship between velocity, distance and time in (2.2).

$$E_k = qV = \frac{1}{2}mv^2 \tag{2.1}$$

$$v = \frac{L}{t} \tag{2.2}$$

$$\frac{m}{q} = \frac{2Vt^2}{L^2} \tag{2.3}$$

Initially, time-of-flight mass spectrometry suffered from poor mass resolution, inferior even to simple magnetic sector instrumentation, with resolution dependent on the initial

spatial and kinetic energy distributions of ions. In this vein, an improved ion source was developed, as reported by W. C Wiley and I. H. McLaren in 1951. This source achieved tighter focussing of ions in terms of space and energy by employing dual accelerating regions, allowing independent tuning of the ionisation process and subsequent ion acceleration (Wiley and McLaren, 1955).

A step change in the utility of time-of-flight analysers was achieved with the invention of the time-of-flight mass reflectron by Boris A. Mamyrin in 1973 (Mamyrin *et al.*, 1973). In a time-of-flight reflectron, ions are slowed at one end of the time-of-flight tube by a retarding electric field, ions penetrate into the reflector to the point of having zero kinetic energy, at which point they are then expelled back into the field-free drift region in the opposite direction, towards the detector (Gross, 2011). The advantage of the reflectron analyser design is that it accounts for the spread in kinetic energy, and thus velocity, of the analyte ions, as ions with greater kinetic energy will penetrate further into the reflector region before being reflected back, achieving a kinetic energy focus at the detector. Separately to this, the reflection also serves to increase the length of the ions flight, achieving superior spatial separation of masses, and thus further improving mass resolution. These advances allowed time-of-flight analysers to equal the capabilities of more complex double-focussing mass spectrometers at a much lower cost.

Alternative analyser designs based on the time-of-flight principle have also been developed, including so-called “orthogonal acceleration” time-of-flight, oa-ToF instruments, first proposed by J. H. J. Dawson in 1989 (Dawson and Guilhaus, 1989). Orthogonal acceleration instruments rapidly accelerate ions to a kinetic energy approximately two orders of magnitude greater than their initial kinetic energy, which reduces the time dispersion of ions and serves to minimise the “turn-around effect”, which refers to the error introduced into the ion flight time by the acceleration of rearward moving ions in the reflection region of the analyser (Dennis *et al.*, 2016). This serves to increase mass resolution for heavier ions, at the expense of reducing resolution for lighter ions (Chen *et al.*, 1999) (Radionaova *et al.*, 2016).

As resolution in time-of-flight analysers is dependent on the temporal separation of ions when they impact the detector, one way to improve resolution is to increase the flight length over which ion trajectories are timed. One approach which can achieve this without dramatically increasing the footprint of the instrument is to employ multiple

reflections in the ion flight path. Many developments in this area have been made by Wolfgang Plaß and colleagues (Plaß *et al.*, 2013). Multi-reflection time-of-flight analysers have demonstrated mass resolving power in excess of 100,000, an order of magnitude higher than is typically achieved by single reflectron type instruments, albeit at the expense of longer acquisition times, due to the increased path length (Piechaczek *et al.*, 2008). Even higher mass resolution, of approximately 200,000 has been shown in multi-reflection time-of-flight instrumentation installed on the ISOLDE beamline at CERN (Wolf *et al.*, 2012). Again, in this case the high mass resolving performance is due to multiple reflections permitting extended flight times, in this case up to 30ms. This is as opposed to flight times of much shorter than 100µs, which are required for the 10kHz repetition rate of reflectron analysers in modern ToF-SIMS instruments.

More recently, mass resolving power has been pushed higher still in multi-reflection time-of-flight analysers with reported figures of full-width half-maximum resolving power of greater than 300,000 (Yavor *et al.*, 2015), 600,000 (Dickel *et al.*, 2015), and indeed as high as 1,000,000 (Verenchikov *et al.*, 2017) found reported in the literature in the past four years. Despite these impressive figures, work is still required to improve the transmission, and thus sensitivity, of multiple reflection time-of-flight systems. If achieved, improved transmission could broaden application of such instruments from their current niches, such as the mass determination of short-lived nuclides at CERN. When combined with the compact footprint of multiple reflection instruments, there are many environments where the ultra-high mass resolving power could be of benefit, such as *in situ* analysis in medical applications, or even on board space exploration missions, where reducing the size and mass of instrumentation is of critical importance (Plaß *et al.*, 2013).

2.1.4 Fourier Transform Ion Cyclotron Resonance Mass Spectrometry

At the same time as the development of the reflectron mass analyser, other mass spectrometry techniques were also being advanced, including Fourier transform ion cyclotron resonance mass spectrometry (FT-ICR MS), invented by Melvin B. Comisarow and Alan G. Marshall in 1974, (Comisarow and Marshall, 1974). FT-ICR MS relies on the Lorentz force induced circular motion of ions in a spatially uniform magnetic field, in which the frequency of ion rotation is dependent only on the mass-

to-charge ratio, and is independent of ion energy, as described by the canonical cyclotron frequency relationship, equation (2.4), (Comisarow and Marshall, 1976).

$$\omega = \frac{qB}{m} \tag{2.4}$$

By itself, this ion cyclotron motion is not inherently useful, as a result FT-ICR MS techniques are based on the excitation of trapped ions by the application of an oscillating electrical field at the cyclotron frequency of a particular mass-to-charge ratio, or indeed across a range of frequencies to simultaneously excite a wide mass range. It is this characteristic frequency that is detected through differential image charge detection in FT-ICR MS, giving a time-domain signal of ion motion, which can be converted into the frequency domain using a Fourier transform, and then readily translated into a mass spectrum. The cyclotron excitation voltage can be used for multiple purposes; to accelerate ions to larger orbital radii thus permitting detection, to promote collisions between ions for tandem mass spectrometry or ion cooling, or to eject ions from the instrument so they are no longer present for detection (Marshall *et al.*, 1998).

Modern developments in FT-ICR have involved efforts to increase the magnetic field strength, and thus increase ion cyclotron frequencies, or to lengthen the period of time for which ion motion is stable and coherent whilst trapped. Mass resolution is linearly dependent on both magnetic field strength and the length of the transient time domain signal acquired, (Marshall *et al.*, 1998).

Over the past decade, there have been significant advances in increasing both the transient length and the magnetic field strength in FT-ICR. Alternative designs for the trapping cell are one avenue which has been successfully pursued to increase the stable trapping time, with transient lengths of up to 3 minutes reported for a novel trap design in 2011, which achieved mass resolution in excess of 24,000,000 at m/z 609, with a 7T magnetic field, (Nikolaev *et al.*, 2011). The trap described by Nikolaev et al. subdivides the surface of the cylindrical FT-ICR cell into eight curved segments, creating a ‘dynamically harmonised’ hyperbolic field inside the cell, as proposed in (Boldin and Nikolaev, 2011). This permits stable cyclotron orbits at larger radii by reducing space charge effects, and consequently increasing the time taken for ion motion to de-phase, therefore permitting longer transients, giving spectra with higher

mass resolution than a typical cylindrical FT-ICR cell with only four compensation segments. Since the initial proposition, mass resolution with harmonised FT-ICR cells has been further improved, with mass resolution of almost 40,000,000 demonstrated at m/z 609, acquired with a 5 minute transient detection and a 7T magnetic field (N. Nikolaev *et al.*, 2013).

2.1.4.1 Increasing Magnetic Field Strength

Throughout its history, further increases in magnetic field strength have also been sought to push the mass resolving power of FT-ICR MS even further ahead of other mass spectrometry techniques. The first 9.4T FT-ICR was reported in 1996, which was able to achieve mass resolution of 250,000 at m/z 1,556 from a single scan, although the transient duration of acquisition was not noted (Senko *et al.*, 1996). There have since been further increases in magnetic field strength, indeed a 20T field instrument was also described in 1996, but due to the poor homogeneity of the magnetic field, mass resolving power was limited to only around 20,000, (Hendrickson *et al.*, 1996). Initial results from an instrument utilising an 11.5T field were reported in 1998, with 450,000 mass resolution demonstrated at m/z 1,500, although this was the result of summing 25 transient acquisitions (Gorshkov *et al.*, 1998). A year later, a 25T FT-ICR was reported, this time with improved homogeneity of the field, however the base pressure achieved in this instrument restricted the maximum possible mass resolution to around 130,000 at m/z 1,182, with the pressure in the ICR cell greater than 1×10^{-8} mbar when acquisitions took place (Shi *et al.*, 1999). In 2008, a 14.5T FT-ICR cell was described, with mass resolving power reaching 800,000 at m/z 400 for a 3s time-domain transient duration, (Schaub *et al.*, 2008). In 2011, Kaiser et al. presented a custom built 9.4T FT-ICR MS instrument, with improvements outside of increasing the magnetic field strength, particularly in terms of detection sensitivity. This instrument was able to accommodate longer transient durations without loss of coherence of the trapped ions, and as such was able to demonstrate mass resolution in excess of 800,000 at m/z 471, gathered with an acquisition duration of 5.6s, (Kaiser *et al.*, 2011).

A recent paper published a useful list of the mass resolving powers demonstrated in the literature for FT-ICR with magnetic field strengths up to 15T, the sample being analysed was also noted in each case, alongside the transient duration used for the acquisition, and number of data points gathered, if these figures were reported in the original research, (Cho *et al.*, 2017). Mass resolving powers in excess of 1,000,000

are reported multiple times, including three times for instruments with magnetic field strengths as low as 9.4T. Although as would be expected, these corresponded to long time domain transient acquisitions, with transient lengths of 5.9s and 6.8s given for two of the 9.4T studies reporting mass resolution above 10^6, both studies reported their mass resolution for m/z ≈500, (McKenna *et al.*, 2013), (Chen *et al.*, 2016). In the remaining 9.4T study, by Carvalho et al., mass resolution of 1,300,000 is shown at m/z 324 although neither the required time domain transient, nor the number of summed scans is given, (Carvalho *et al.*, 2016). It can be assumed that a long time domain transient was also used in this case.

Magnetic field strength has been pushed even higher still, with many members of the group at Florida State University which presented a modified 9.4T FT-ICR in 2011 involved in the introduction of a 21T FT-ICR MS instrument in 2015. This instrument has achieved mass resolution in excess of 2,000,000 at m/z 1385 for a 12s transient detection (Hendrickson *et al.*, 2015). Mass resolution in excess of 2,700,00 at m/z 400 has also been demonstrated, which when combined with mass accuracy of 80ppb has allowed for the unambiguous assignment of thousands more molecular formulae in petroleum distillates than would be possible with a 9.4T instrument, with 49,040 assigned for 21T versus 29,012 for 9T (Smith *et al.*, 2018). Increasing the magnetic field strength is the ultimate method of improving mass resolution in FT-ICR MS, as it also benefits mass accuracy, analysis speed, and the dynamic range of the technique, (Cho *et al.*, 2014). Here dynamic range refers to the ratio of the highest and lowest intensity signals which can be detected simultaneously.

As well as tabulating FT-ICR performance across different magnetic field strengths, Cho et al. also describe the advantage of using so-called 2ω or quadrupolar detection in FT-ICR, (Cho *et al.*, 2017). This method of detection using multiple electrodes to detect higher harmonics of oscillation frequencies was first proposed by Pan in 1988, (Pan *et al.*, 1988). Briefly, quadrupolar detection in FT-ICR is the use of four detection electrodes to detect the second harmonic of ion cyclotron frequencies whilst trapped, in contrast to the typical arrangement using only two opposing electrodes, referred to as dipolar detection. By adding a second pair of detection electrodes, each ion is detected twice by each electrode pair during a single cyclotron revolution, leading to a doubling of both the frequency and mass resolving power for a given magnetic field strength, (Schweikhard *et al.*, 1990). Cho et al. demonstrate this dramatic increase in

mass resolving power, showing that quadrupolar detection has allowed a 7T FT-ICR cell to achieve mass resolution of 1,500,000, at m/z 400, from only a 4s duration transient analysis of a crude oil sample, (Cho *et al.*, 2017). Such performance would be expected to require magnetic field strength of around 12T if using standard dipolar detection.

2.1.4.2 Theoretical FT-ICR Mass Resolution

The theoretical maximum mass resolution which can be attained with FT-ICR for given magnetic field strengths and transient detection times was initially laid out in 1979, and with units updated to reflect the preferred modern unit choices of tesla and seconds for these quantities respectively, gives equation (2.5), where q is the elementary charge, B is the magnetic field strength in tesla, t is the transient recording time in seconds, and m is mass in daltons, for an FT-ICR operating at low pressure in magnitude mode (Comisarow and Marshall, 1976). This highlights the linear dependence of mass resolving power on magnetic field strength and transient detection time. Increasing magnetic field strength is technologically challenging and financially expensive, with the cost of the magnet increasing as a high power of magnetic field strength, as evidenced by the fact that there are currently only two FT-ICR instruments in existence which operate above 15T (Hendrickson *et al.*, 2015), (Shaw *et al.*, 2016). Alternatively, increasing the analysis time would obviously be expensive in terms of experiment duration, reducing the throughput efficiency of the instruments, as such neither avenue offers a straight-forward path to further increases in mass resolution.

$$\frac{m}{\Delta m_{FWHM}} = \frac{1.273 \times 10^7 qBt}{m} \qquad (2.5)$$

Absorption mode is another technique which can be used to generate FT-ICR spectra, rather than the typically used magnitude mode. Absorption mode further increases the accessible mass resolving power of the instrument, without increasing the magnetic field strength or transient detection duration. Briefly, absorption mode experiments are run in exactly the same manner as for magnitude mode, but rather than simply plotting the magnitude information gained after transforming the time domain transient into the complex frequency domain using a Fourier transform, the phase information is also used to calculate and plot the real component of the complex spectrum. This is only possible if the phase of the trapped ions is known, in the ideal case this would be due to all ions beginning the time domain recording with equal phase angle of zero, but

practically this is not the case, with ions of different m/z possessing different phase angles due to the necessary delay between the initiation of ion excitation and the recording start time. As a result, a correction function is required to account for the accumulated phase angle of ions across the mass range being investigated, multiple different methods have been proposed to find a suitable method to address this issue.

One such method is a computational approach to find a quadratic curve fit for the accumulated phase of ions excited at different times during the application of the excitation frequency sweep, (Xian *et al.*, 2010), (Qi *et al.*, 2011). Qi et al. demonstrated an increase in mass resolution of at least 50% for spectra acquired with a 12T instrument, (Qi *et al.*, 2011). This computational method is inexpensive and can be applied retroactively to existing spectra.

There have been other attempts to generate absorption spectra by exciting ions simultaneously with their detection, in which case Fourier deconvolution can be used to recover the idealised response that would be expected for ions with no phase changes induced by excitation, in effect giving broadband phase correction of the spectra (Beu *et al.*, 2004). This method demonstrated an increase in mass resolution by a factor of 1.8 for spectra acquired with a 9.4T FT ICR instrument. However, application of this phase correction method is restricted by the need for the detected time domain transient to include the excitation signal, which in practice is difficult due to the excitation signal causing saturation of the in-vacuum pre-amplifier. Simultaneous excitation and detection has been demonstrated, by cancelling out the capacitive coupling between excitation and detection electrodes using a variable capacitor, (Beu *et al.*, 2004). It is due to such requirements that this phase correction method is not suitable for retroactive application to existing data.

Theoretically, the use of absorption mode can result in an increase in mass resolution of a factor of between $\sqrt{3}$ and 2 compared to magnitude mode spectra, (Comisarow and Marshall, 1974) (Kilgour *et al.*, 2015).

At this point, it is worth considering the ultimate value of mass resolving power that is actually required in an experimental setting. It has been shown that for arbitrarily complex elemental compositions of the form $C_cH_hN_nO_oS_s$, or indeed almost any five elements, up to a mass of 500 u, a mass separation of $\approx 1 \times 10^{-4}$ u is sufficient for unique identification, (Kim *et al.*, 2006). This corresponds to mass resolution, $m/\Delta m \approx$

5×10^6, which is within the achievable range of only the very highest magnetic field strength FT-ICR instruments which are currently operating (Kim *et al.*, 2006), (Smith *et al.*, 2018). Using equation (2.5), a 21T FT-ICR cell would theoretically be able to achieve mass resolution in excess of 5×10^6 at m/z 500 for a transient detection time of 10s, longer detection times have been reported for larger molecules, meaning such performance should be feasible with modern instruments (Hendrickson *et al.*, 2015).

Very recently, a novel experimental and data pre-processing method has been described for FT-ICR, which reports almost constant ultra-high mass resolution across a broad mass range, with mass resolution typically in excess of 3×10^6 presented across a wide mass-to-charge range of m/z 260 to m/z 1500 (Palacio Lozano *et al.*, 2019). This method, referred to as operation at constant ultra-high resolution, or OCULAR, consists of briefly; increasing the time domain transient length as m/z increases, using the phase of ion packets to produce absorption mode spectral segments, and then using an algorithm to decide the best place at which to overlap and stitch these segments together. In the OCULAR method, a quadrupole is used to isolate the m/z range of interest for each scan to be performed with a different length transient. This also serves to reduce the number of ions present in each experiment, thus reducing space-charge effects, which allows the possibility of longer transient acquisition times whilst also increasing the sensitivity of detection, aiding in the identification of lower abundance species.

The compromise made by the OCULAR method compared to traditional broadband spectral acquisition is the increased instrument time required to achieve constant high mass resolution across a wide mass range, the fundamental dependence of mass resolution for a given mass-to-charge ratio on magnetic field strength and acquisition time cannot be overcome. Palacio Lozano et al. reported experimental durations up to 48 hours for the most challenging samples such as a non-distillable petroleum fraction, for which 65 different spectral segments were recorded, with the highest m/z segment requiring a transient acquisition time of greater than 30s per scan, and each segment repeated 100 times before summing for the final spectral dataset, (Palacio Lozano *et al.*, 2019). Using a dynamically harmonised FT-ICR cell would be an alternative route to achieving high mass resolution across a broad mass range without access to higher magnetic fields, however such a device would be restricted in its dynamic range due to ion cloud interactions, (N. Nikolaev *et al.*, 2013). As such, the ability to run

experiments on FT-ICR instruments with higher magnetic field strengths is still desirable, in order to achieve the maximal mass resolution in the shortest possible time.

FT-ICR MS remains a popular mass spectrometry technique, primarily due to its superior broadband mass resolving power compared to other mass analysers, with mass resolution in excess of 1,000,000 now possible across a wide mass range. There are however some drawbacks to the technique, not least the expense of the instruments, due to the required superconducting magnets and the supply of liquid helium needed to cool them.

2.1.5 Quadrupole Mass Analysers

In addition to the time-of-flight, magnetic sector, and FT-ICR mass analysers discussed, there have been numerous other mass analyser designs, including the quadrupole mass analysers used in early SIMS instruments, which suffered from issues of poor transmission and mass range. Quadrupoles are still widely used as components in mass spectrometry instruments, due to their low cost ability to select a mass window of interest for further analysis in tandem mass spectrometry experiments. The modern mass analyser on which this thesis is focussed, the orbital ion trap, will be discussed in greater detail later in this chapter.

The first quadrupole mass spectrometer was proposed as “a new mass spectrometer without a magnetic field” by Wolfgang Paul in 1953, (Paul and Steinwedel, 1953). The discovery of the efficacy of quadrupole electric fields for mass analysis and ion trapping earned Paul the Nobel Prize for Physics in 1989, (Paul, 1989). The quadrupole mass analyser relies on only an electric field to manipulate ions, with four ideally hyperbolic rods mounted in a square configuration, where opposing pairs of rods are given the same electric potential, with both DC and AC components. This time varying field creates a trapping potential which confines ions in both x and y axes. Advantages of modern quadrupoles include that they now allow for high transmission, require only low acceleration voltages, are physically compact, and can achieve high scan speeds as scanning requires only electric potentials to be modulated, (Gross, 2011).

Ion motion in a linear quadrupole is dictated by the voltage ratio between the pairs of rods, with a given voltage ratio only permitting the successful transmission of ions within certain bounds of mass-to-charge ratio. Ions outside of this range exhibit

unstable trajectories and will collide with one of the component rod electrodes. The stability of ion trajectories in a quadrupole field can be understood through the Mathieu equations, which are also applicable to orbital ion traps, as will be further discussed later in Chapter 3. It is this instability which gives rise to the mass analysis function of linear quadrupoles, whereby the amplitude of the AC component of the trapping voltage is linearly increased, which causes unstable ions to be ejected from the trap and impact upon detectors. The m/z value of the ejected unstable ions is linearly dependent on the AC voltage amplitude for a given DC voltage, meaning a mass spectrum of ejected ions can be derived from a plot of the detected signal against time.

The resolving power of quadrupole analysers is typically limited to approximately unit mass resolution, meaning adjacent peaks at nominal unit masses are able to be distinguished from one another, but finer differences in mass-to-charge ratio cannot be discerned. Any distortions in the quadrupole field caused by misalignments or interference from external fields can sharply reduce the transmission and mass resolution of the device. There have been some developments in high-performance quadrupole mass analysers, with increases up to a factor of 10 in mass resolution, with $\Delta m \approx$0.1u observed for masses up to m/z 520, corresponding to mass resolution in excess of 5,000. This was achieved through improving the machining accuracy of the hyperbolic quadrupole rods, (Yang *et al.*, 2002) (Schwartz *et al.*, 2002).

2.1.6 Tandem Mass Spectrometry

As mass spectrometry instrumentation has developed, so too has the ability to analyse more complex samples, with experimental techniques rising to this challenge. One such technique is tandem mass spectrometry, in which ions are selected by their mass before being further fragmented and subject to a second step of mass spectrometry analysis. This technique was first developed in the 1960s, with Shannon and McLafferty reporting that dissociation of analyte ions could be used to determine the isomeric structure of the ion in question, (Shannon and McLafferty, 1966).

Tandem mass spectrometry is used to discern the structure of ionised species, by breaking them into their constituent components, which is particularly useful for more complex and massive molecules, such as large biological species, for which precise identification requires very high mass resolving power instrumentation, (McLafferty,

2011). In tandem mass spectrometry the initial analyte ions are referred to as precursor or ‘parent’ ions with their resulting fragments referred to as product or ‘daughter’ ions.

In general tandem mass spectrometry refers to any method which involves at least two stages of mass analysis, alongside a dissociation or reaction step, typically found in between the two mass analysers. In fact, the ion fragmentation step can take place prior to the first stage of mass analysis. For example, if the fragmentation occurs in a field-free region the resultant combinations of intact ions and their fragments will remain travelling at equal velocity, allowing later separation based only on the mass of the original un-fragmented ions. Tandem mass spectrometry is also referred to as mass spectrometry/mass spectrometry, or abbreviated to MS/MS or MS^2 (Hoffmann and Stroobant, 2007).

Different experimental platforms exist for tandem mass spectrometry, which can be separated based on the combination of mass analysers being used. Essentially, these methods can be split into two broad categories; tandem mass spectrometry in space, or tandem mass spectrometry in time. In the first case, tandem spectrometry in space, two mass analysers are employed which are physically separate from one another, as per the early triple quadrupole instruments, hence the designation of in space. Further mass analysers can be coupled together to produce higher order mass spectrometry, such as MS^3 or even MS^4, although the limitations imposed by low ion transmission make such instruments difficult in practice, and preclude the use of an even greater number of mass analysers.

In the case of tandem mass spectrometry in time, MS/MS is achieved with a single analyser coupled to an ion storage device, which can be used to create an appropriate sequence of steps to analyse fragmented ions, (Gross, 2011). Tandem mass spectrometry in-time instruments can more easily achieve higher order mass spectrometry, represented by MS^n, in which product ions are fragmented a greater number of times. In theory, the exponent *n* is limited only by the number of successive collision steps which can be endured whilst maintaining a detectable number of product ions.

In 1981, McLafferty presented a paper detailing the early state of the art of tandem mass spectrometry, including descriptions of two instruments. The first being a triple quadrupole system, developed at LaTrobe University, in which two quadrupoles were

used for mass analysis, with the middle quadrupole used to allow fragmentation by collision with a gas, this is also referred to as a QqQ formation. This tandem quadrupole setup is able to achieve only in the region unit mass resolution in both MS^1 and MS^2, however it does have the advantage of being compact and relatively straightforward to maintain. The second instrument was a combined magnetic and electric sector mass spectrometer, consisting of two electrostatic sectors and two magnetic sectors, with a collision induced dissociation cell (CID), in an E-B-CID-E-B configuration. This instrument was able to provide higher resolution spectra for both MS^1 and MS^2, due energy and spatial focussing of both combined E-B sector mass spectrometers, although at the expense of a larger physical footprint, and a cost approaching twice that of the early triple quadrupole instruments (Mclafferty, 1981).

In terms of SIMS experiments, tandem mass spectrometry typically refers to the mass-selective dissociation of analyte ions. A second stage of mass analysis is used to determine the mass-to-charge ratios of the produced fragments. In recent years, SIMS instruments have been developed with this capability, with one such example being the Ionoptika J105, which will be described in more detail later in this chapter.

Since the introduction of the Ionoptika J105 in 2008, (Fletcher *et al.*, 2008), (Hill *et al.*, 2011), Physical Electronics of the USA have also introduced a SIMS instrument capable of tandem mass spectrometry, the Phi nanoTOF II, (Fisher *et al.*, 2016). The nanoTOF II design achieves simultaneous MS^1 and MS^2 spectral acquisition by deflecting only a portion of the secondary ion beam into a CID cell for fragmentation, at the point when the beam has undergone time-of-flight separation. This allows a tightly mass-resolved ion packet to be selected for fragmentation, before bunching and acceleration into a second time-of-flight analyser. Ion packets of as narrow a distribution as 1 Da at m/z 500 can be achieved. The advantage of this arrangement is that no produced secondary ions are discarded when running a tandem mass spectrometry experiment, and no external calibration of the MS^2 spectrum is required due to the synchronous nature of both MS^1 and MS^2 spectral acquisition. The MS^2 spectrum is however acquired at lower mass resolution than the MS^1 data, due to the shorter linear time-of-flight analyser used for MS^2. Although, the high mass resolution with which the precursor ion can be selected reduces the importance of this performance characteristic, as there should not be many species present in the

precursor ion, meaning interpretation of the resultant fragmentation spectra is simplified.

2.2 Secondary Ion Mass Spectrometry (SIMS) – An Overview

Secondary ion mass spectrometry (SIMS) is a nanoscale chemical surface analysis technique which dates back to the first prototype instruments of the 1940s and 1950s (Herzog and Viehböck, 1949), (Honig, 1958). However, the acronym SIMS was not coined until the early 1970s by Alfred Benninghoven, after his work on the sputtering process and energy distribution of emitted secondary ions.

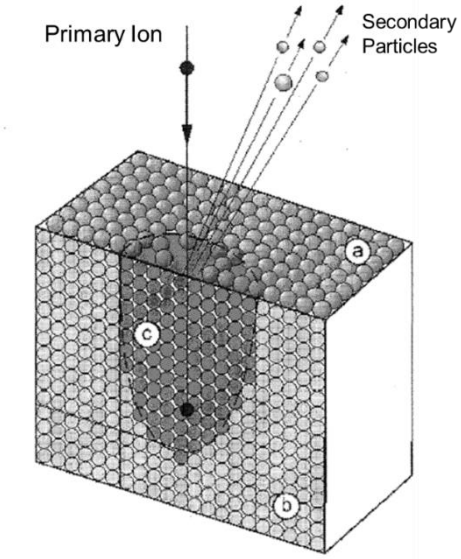

Figure 2.1 – Primary ion collision with a sample surface, adapted from (Vickerman & Briggs, 2001). a) Surface monolayer. b) Bulk sample. c) Collision cascade.

When reduced to a basic explanation, SIMS is the bombardment of a sample with a primary ion beam, energy transfer to the sample surface causes a complex collision cascade resulting in the sputtering of particles from the sample, a proportion of which are ionised. It is worth noting that the intricacies of the ionisation mechanism are not yet fully understood, particularly for organic molecules (Smentkowski, 2014). The emission is not restricted only to secondary ions, there are also low energy secondary electrons, photons, neutral particles and Auger electrons emitted, however it is only the secondary ions which are of interest for mass analysis (Vickerman and Briggs, 2001). Figure 2.1 shows a graphic representation of the primary ion collision with a sample.

2.2.1 The SIMS Equation

The different factors which affect the emission yield of secondary ions can be simply modelled with the basic SIMS equation (2.6), (Vickerman and Briggs, 2001).

$$\boldsymbol{I_m = I_p Y_m \alpha_m{}^{+/-} \theta_m \eta_m} \quad (2.6)$$

$\boldsymbol{I_m}$	Secondary ion current of species m
$\boldsymbol{I_p}$	Primary ion flux
$\boldsymbol{Y_m}$	Sputter yield
$\boldsymbol{\alpha_m{}^{+/-}}$	Ionisation probability of positive or negative ions
$\boldsymbol{\theta_m}$	Fractional mass concentration of m in the surface layer
$\boldsymbol{\eta_m}$	Transmission factor of the analytical instrument for species m

SIMS is a qualitative, and semi-quantitative, surface analytical technique, where quantification is made difficult due to terms in the SIMS equation which vary depending on the sample being analysed, meaning it is difficult to reliably convert a measured secondary ion intensity into a concentration.

Ionisation probability, $\alpha_m{}^{+/-}$, varies depending on numerous experimental factors, including; the analyte ion, the matrix in which it is embedded, the primary ion beam energy, and the angle of incidence of the primary ion beam (McPhail, 2006). Therefore to perform a fully quantitative analysis it would be required to measure the useful ion yield for each combination of analyte and substrate of interest, requiring known concentration standards to be analysed under identical conditions as the unknown. Both Y_m and $\alpha_m{}^{+/-}$ parameters can vary by orders of magnitude across different species (Popczun *et al.*, 2017), meaning two species present in a sample surface at the equal concentrations can produce variable signal intensities in detected SIMS spectra, highlighting the need for rigorous concentration standards when attempting to quantify SIMS data.

The transmission parameter, η_m, is typically a constraint of the instrument being used, which cannot easily be altered without modifying its design. In time-of-flight SIMS instruments, there is little scope remaining to improve the transmission of secondary ions to the detector after ionisation, as transmission of ions across the full mass range can already approach 100% (Vickerman and Briggs, 2001). In terms of this thesis, maintaining a good transmission of ions from the J105 to the orbital ion trap mass analyser is particularly important to take advantage of the sensitivity of orbital ion trapping, as will be discussed later.

2.2.2 Static & Dynamic SIMS

Historically, the analysis of organic, polymeric, and biological samples has been conducted by what is known as static SIMS, where operating conditions cannot exceed what is known as the 'static limit', in which less than 1% of a sample surface is bombarded with a primary ion, meaning each new impact is statistically likely to be from an undamaged area. This is achieved by restricting the primary ion dose per unit area to prevent excessive damage to the sample surface. This allows the uppermost monolayer of the sample surface to be analysed, as the sputtering time for this layer is much greater than the length of the analysis. This static limit is typically stated as between 1×10^{12} and $1 \times 10^{13}\ \mathrm{ion} \cdot \mathrm{cm}^{-2}$, based on the findings of A. Benninghoven in 1970, (Benninghoven, 1970). The top monolayer of a sample was found to have a lifetime on a time scale in excess of $4 \times 10^{4}\ \mathrm{s}$ under irradiation by a $1 \times 10^{-9}\ \mathrm{A} \cdot \mathrm{cm}^{-2}$ primary ion current density. Assuming primary ions are singly charged, with $1.602 \times 10^{-19}\ \mathrm{C}$ per ion, this corresponds to an ion dose of $2.5 \times 10^{12}\ \mathrm{ion} \cdot \mathrm{cm}^{-2}$ to impact less than 1% of the sample surface.

Dynamic SIMS is the name given to analysis conducted with ion doses above the static limit, where an entire layer of the sample can be removed by ion beam sputtering, allowing multiple layers of the sample to be analysed to build-up a three-dimensional description of the sample chemistry, termed as a depth profiling experiment (Vickerman and Winograd, 2015). In this case, the damage done to the sub-surface region by the primary ion beam is of critical importance, if excessive damage is done, then the depth profile will not be representative of the original sample, it will simply show the effect of the damage caused by the ion bombardment and implantation.

The advent of polyatomic cluster ion beams which cause substantially less damage to the sub-surface region has enabled the realisation of molecular depth profiling of 'soft' samples, such as organic or biological samples (Mahoney, 2013). With cluster ion beams, an equilibrium state can be achieved whereby the near-surface damaged caused by the incident cluster beam is efficiently removed and is therefore unable to accumulate. The modern polyatomic cluster ion sources which enable analysis in this steady state regime will be described in more detail later.

2.2.3 Matrix Effect

In static SIMS, the matrix in which an analyte element is embedded can significantly alter its ionisation probability, as briefly discussed in 2.2.1, with problematic implications for the interpretation of spectra (Deline *et al.*, 1978). It has been shown that for a single molecule of interest, homogeneously distributed across a sample, the ionisation probability can vary by orders of magnitude from one region of a sample to another, based only on the chemical composition of these areas, with the presence of different species in a sample serving to enhance or suppress the ionisation of a particular sputtered atom, resulting in substantial differences in the measured intensity (Jones *et al.*, 2007).

The matrix effect is one of the primary reasons that SIMS is not strictly a quantitative technique, as a higher intensity secondary ion yield does not necessarily mean that a particular m/z is more abundant in the sample being analysed. The increased intensity could instead be caused by an increased ionisation probability due to the particular substrate being used acting as a source of protons. The opposite effect, of ionisation suppression, can be a significant impediment to the detection sensitivity of SIMS, which is particularly detrimental to certain biological analyses, where multiple chemical environments can be present across a single substrate, and the key molecule of interest may be of very low concentration to begin with. One such biological example where reducing matrix effects is advantageous, is the characterisation of the distribution of a drug molecule within brain tissue, work to this effect has been carried out by the Winograd group at Penn State, with modification of the primary ion beam by the addition of HCl proving to be effective in moderating matrix effects, particularly if a source of water is present at the sample surface (Tian, Wucher, *et al.*, 2016).

The matrix effect can also be reduced by post-ionisation of sputtered neutral particles, as the ionisation then takes place away from the sample surface, where the chemical environment of the sample has less influence, this technique is termed sputtered neutral mass spectrometry (SNMS) (Wucher, 2013), (Kucher *et al.*, 2014), (Breuer *et al.*, 2017). Laser post-ionisation is the most popular method, but success has been mixed due to increased photo-fragmentation of secondary ions, meaning molecular signals are not necessarily enhanced. Much research is still being pursued in this area due to the potential increases in useful yield which can be accessed by ionising a greater portion of the sputtered material, alongside improved quantification due to the

reduced matrix effects (Wucher, 2013). As such, laser post-ionisation remains an expensive and complex technique, not yet well-suited to widespread deployment in routine analytical SIMS (Vickerman and Winograd, 2015).

In depth profile experiments under dynamic SIMS conditions, matrix effects can cause additional problems, for example preferential sputtering can occur, in which different components of a complex sample sputter with different efficiencies, leading to an effective increase in concentration of the components with lower sputter rates at the sample surface. This makes recreating accurate three-dimensional representations of the sample difficult, as each layer of the gathered depth profile does not necessarily represent the same sputtered depth for heterogeneous samples, meaning correction factors are required. Some corrections can be performed based on measuring the topography of the sample, for example with AFM, both before and after SIMS analysis (Wucher *et al.*, 2007) (Mahoney, 2013).

2.2.4 Mass Analysers in SIMS

The produced secondary ions are guided into a mass spectrometer, typically one of the following three mass analysers can be found in a SIMS instrument; magnetic sector, quadrupole and time-of-flight (ToF) (Vickerman and Winograd, 2015). The different styles of mass analyser vary in their performance in terms of ion transmission, mass resolution, analysis time, and sensitivity. Time-of-flight mass analysers allow parallel detection across a wide mass range, whilst offering good transmission and better sensitivity than quadrupole or magnetic sector analysers. As such, they are the most common analyser found in modern commercial SIMS instruments, such as the Ionoptika J105, in which a reflectron time-of-flight analyser is used. In the case of the J105, ions enter the reflectron in a tightly bunched packet, with a narrow distribution in terms of both time and kinetic energies, as shown in Figure 2.2. The time-of-flight of an ion is measured as the time taken between leaving the time focus, and impacting on the detector. The distance travelled and time taken are both known, therefore ion velocity can be calculated. The mass of ions can then be calculated using both the known kinetic energy, and the calculated velocity.

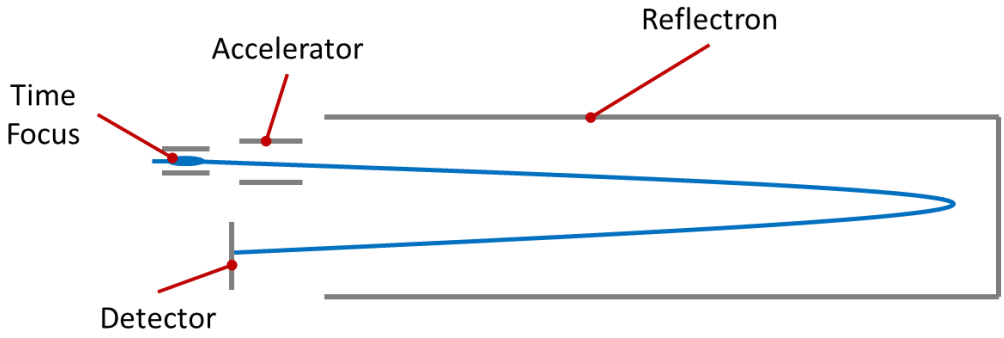

Figure 2.2 - Schematic of modern reflectron operation

SIMS is an extremely useful chemical analysis technique, with parts per million sensitivity and the ability to detect all elements, including hydrogen, which can't be detected by X-ray photoelectron spectroscopy (XPS) due to its lack of core electrons (Stojilovic, 2012). SIMS can be applied to many different types of sample, providing the sample is compatible with ultra-high vacuum. If so, there is typically relatively little sample preparation required beyond mounting the sample to a stub and transferring it into the instrument for analysis. In fact, any further sample preparation is discouraged as it may interfere with the surface of interest.

Traditionally SIMS has been carried out in what is known as the static regime, in which only the top monolayer of the sample surface is analysed, representing less than 1nm in depth. This is achieved by ensuring the sputtering time for the first monolayer is much longer than the analysis time required so that no area receives more than one primary ion impact when generating a spectrum. This can be achieved by maintaining a primary ion current density of less than 1nA/cm^2, (Benninghoven, 1970), corresponding to a primary ion dose below 10^{13} ions/cm^2, resulting in much less than 1% of the surface being impact, meaning the probability of impacting the same area twice is negligible.

In contrast, many modern SIMS experiments are carried out in the dynamic regime, with much greater primary ion doses used in order to sputter a larger volume of material and allow depth profiles to be acquired, to characterise the chemistry of a sample in three dimensions (Shen *et al.*, 2015). Such analyses have only become viable with the advent of quasi-continuous primary ion cluster beams, such as those found on the Ionoptika J105, which allow much faster acquisition of depth profiles than pulsed ion sources developed for static SIMS.

Typically in time-of-flight SIMS instruments, a primary ion source with short pulses is required, with a pulse width of the order of nanoseconds. Short pulses are required as the flight time for an ion is measured starting from its impact with the sample surface. A long pulse would reduce the accuracy of this measurement as not all species would be sputtered simultaneously, leading to a reduction in mass resolution as ions of different masses could arrive at the detector at the same time. It is difficult to produce a tightly pulsed ion source with a beam of large ion clusters, as there will be a distribution of different cluster masses within the primary ion beam itself, meaning the beam will spread out in space during its flight to the sample. Iontof mitigate this with a 90° pulsing system, which separates the component masses of the primary cluster beam by their momentum using a pulsed electronic deflection. This results in a lateral spread of masses, akin to that described in magnetic sector analysers, from which only a selected mass window can pass through a mass selection aperture to form the analysis beam (Kayser *et al.*, 2013), (Mahoney, 2013).

2.2.5 J105 Buncher-ToF Configuration

The Ionoptika J105 SIMS employs a novel buncher-ToF configuration, in which a pulsed ion buncher provides temporally and spatially focussed packets of ions for acceleration into the harmonic reflectron time-of-flight analyser (Fletcher *et al.*, 2008). The buncher decouples the mass spectrometry from the interaction of the primary ion beam and the sample surface, meaning that a quasi-continuous primary ion source can be used. The linear buncher on the J105 operates by allowing the buncher to fill with a packet of ions of equal kinetic energy ~0.3m in length, with the lightest masses at the front of the packet due to mass separation, at this point an accelerating field is rapidly applied across the multiple plates that comprise the buncher, reducing from 7kV at the entry to the buncher to 1kV at the exit. This has the effect of giving greater acceleration to the heavier ions at the start of the buncher, and lesser acceleration to the lighter ions, giving an ion energy spread of 6keV whilst creating a time focus at the entrance to the reflectron. The energy spread of ions at the time focus prior to acceleration into the reflectron is accounted for by the harmonic nature of the reflectron time-of-flight analyser, whereby more energetic ions penetrate deeper into the reflectron field so that they arrive at the detector at the same time as their counterparts with lower energy but equal mass-to-charge ratio, as discussed earlier in this chapter.

The buncher-ToF configuration has multiple advantages, including;

- Faster mass spectrometry imaging and depth profiling.
- The ability to utilise large cluster primary ion beams.
- High mass resolving power independent of sample topography.

Firstly, faster analysis is possible due to the use of continuous primary ion beams, which mean a larger ion dose can be delivered to the sample in a much shorter period of time, as the analysis delay caused by the low duty cycle of a pulsed primary ion source is no longer a factor. One example is that a static SIMS analysis with a primary ion dose of $1 \times 10^{13}\ \mathrm{ion\ cm^{-2}}$ of a 100µm x 100µm area with 10pA of primary beam current would take approximately 16s with the J105, compared to over 9 hours for a pulsed primary ion beam using 50ns primary ion pulses running at 10kHz (Fletcher *et al.*, 2008).

Secondly, large cluster primary ion beams can be utilised as a nanosecond pulsed primary ion beam is no longer required, so a DC beam of larger cluster ions with a distribution of masses is permissible.

Thirdly, mass resolving power in the resultant spectrum is not dependent on the time at which ions leave the sample surface, as the time-focus for acceleration in the reflectron is achieved independently of sputtering the sample. The mass resolution is thus dependent on the quality of the time focus achieved by the buncher, rather than the formation of secondary ions at the sample surface.

Another advantage of the buncher-ToF configuration of the J105 is that it permits tandem mass spectrometry experiments, due to the addition of a gas collision cell located immediately after the buncher, prior to the time-of-flight reflectron. The process of tandem mass spectrometry experiments in the J105 is as follows; after exiting the buncher, ions enter a collision induced dissociation (CID) cell containing a collision gas, typically Ar. Fragmentation of the secondary ions occurs in the CID cell at energies between 1 and 7 keV, with the collision energy determined by the position of the ions in the buncher when the bunching voltage is applied. Fragmentation occurs in a field-free region, meaning both a secondary ion and its associated fragments, referred to as parent and daughter, or precursor and product ions, will continue to travel with the same velocity. A small time-of-flight region follows this, with a timed ion gate used to select which parent and daughter ions are permitted to enter the time-of-flight reflectron

for high resolution mass analysis, to complete the ToF-ToF tandem mass spectrometry (Fletcher *et al.*, 2008).

The interaction between the primary ion source and the sample is critical, as this determines the quantity of secondary ions produced, referred to as the ion yield, whilst also affecting whether large molecules are removed from the surface intact, or are fragmented into their constituent parts. There is much research into the mechanisms of ionisation in SIMS, with a view to improving secondary ion yields through novel primary ion beams, new instrumentation, and post-ionisation techniques such as laser post-ionisation which can provide access to chemical information from the neutral particles sputtered from the sample surface (Popczun *et al.*, 2017).

2.2.6 Primary Ion Sources

The configuration of the primary ion source greatly influences the secondary ions produced; through its chemical composition, mass, and energy. Historically, SIMS instruments have operated with monatomic or small-cluster primary ion sources. The development of liquid metal ion guns (LMIGs) in the 1970s offered ion beams with very high current which were able to be focussed to very small spot sizes, of better than 50nm achievable at the sample surface with the initial Ga LMIG sources proposed (Krohn and Ringo, 1975). Such sources were further developed, by the mid-1980s a pulsed version had been pursued specifically for high resolution imaging SIMS, alongside a 10kV Cs surface ionisation source which offered enhanced negative secondary ion yields (Waugh *et al.*, 1986).

It was found however, that Ga produced a primary ion beam which was ineffective for molecular desorption, with low ion yields for molecular ions due to excessive fragmentation, leading to poor quality SIMS images, particularly in biological analyses carried out below the static SIMS limit (Todd *et al.*, 2001) (Vickerman and Winograd, 2015). It had also been known for some time that cluster sources could provide a large enhancement in ion yield, (Benguerba *et al.*, 1991).

Small cluster ion sources were not widely exploited in SIMS until the turn of the 21st century, with the development of alternative metals being utilised to form small cluster LMIG sources, with a gold cluster LMIG primary ion source described in 2003, (Davies *et al.*, 2003), shortly followed by a bismuth cluster LMIG being developed in 2005 by ION-TOF in Münster, (Touboul *et al.*, 2005).

The Au_n^+ LMIG showed a significantly improved secondary ion yield for organic molecular ions when compared to Ga^+. A non-linear increase in ion yield was demonstrated, with secondary ion yields in the range m/z 400 to 1000 showing much greater yield increase than that observed for lower mass ions (Davies *et al.*, 2003). This increase in secondary ion yield was however at the expense of spatial resolution relative to Ga^+, (Walker and Winograd, 2003). The Bi_n^+ LMIG developed by ION-TOF achieved higher primary ion currents than Au_n^+, allowing faster analysis, whilst also permitting better spatial resolution, down to less than 400nm. This performance was attained with a similar enhancement in secondary ion yields as observed for Au_n^+ sources, in the regime of 100 – 10,000 times higher than those found for Ga^+ projectiles (Touboul *et al.*, 2005). To this day, LMIGs remain unparalleled in terms of their spatial resolution for SIMS imaging, with very few instruments able to surpass them in terms of lateral resolution in SIMS. Once such instrument is the SIMS add-on developed by LIST for Zeiss' Helium Ion Microscope which can achieve spot sizes below 10nm whilst also producing secondary ion mass spectra, albeit at the expense of mass resolution and sensitivity, (Wirtz *et al.*, 2016). Other instruments, such as the Cameca NanoSIMS, utilise Cs^+ thermal ionisation sources to achieve spot sizes of 50-100nm, (Mahoney, 2013). Both HIM-SIMS and NanoSIMS use magnetic sector mass analysers with a number of discrete detectors, as such they are unable to achieve parallel detection of a wide mass range, as can be realised with ToF-SIMS.

Despite the increased secondary ion yield, the weakness of liquid metal ion sources is still the damage done to the sample at the surface, and in the sub-surface region, with further development still required to improve the useful yield of high mass ions. There is also the trade-off between spatial resolution and sensitivity, with regards to the static SIMS limit, whereby there are very few molecules per pixel available for a small spot size primary ion beam, so improved ionisation of these molecules is particularly important. Indeed, a seminal 1988 paper had described how sub-micron molecular imaging would be difficult to achieve with SIMS in the static regime due to limitations imposed by secondary ion yields (Briggs and Hearn, 1988).

2.2.7 Polyatomic Cluster Sources

This has led to the proliferation in the 21st century of ion sources utilising larger polyatomic clusters, such as SF_5^+, C_{60}, or Ar_n, which cause less chemical damage to the sample surface, and thus can desorb larger molecules intact (Mahoney, 2013).

Heavier primary ions were pursued with the goal of increasing secondary ion yields of intact molecules, and larger fragments, with interest beginning as early as the late 1980s when better sensitivity and higher sputter yields were demonstrated with SF^6 clusters (Appelhans and Delmore, 1989). By the turn of the millennium, the advantage of moving from monatomic Ar to polyatomic SF_5^+ cluster sources was evident, with secondary ion yields shown to have been enhanced by up to a factor of 1,000, (Kotter and Benninghoven, 1998). This enhancement in secondary ion yield, particularly for organic samples, was reported to be due to an increased sputter yield, rather than an increased ionisation probability, (Gillen and Roberson, 1998).

However, the issue of accumulating sample damage persisted with SF_5^+ cluster beams, restricting depth profiles to relatively thin films. There are two reasons that damage accumulation still occurs with SF_5^+ projectiles; the first due to the small size of the cluster, relative to modern polyatomic cluster beams, meaning there is a much higher impact energy per atom for SF_5^+ clusters. The second reason for accumulating sample damage is that smaller clusters operate with a quite different sputtering mechanism compared to other projectiles, whereby the detrimental collision cascade characteristics of monatomic ion bombardment, and the thermal spike regime of larger cluster sources are both present, causing increased damage accumulation in organic samples, (Mahoney, 2013). Sample damage with SF_5^+ ion beams has been shown to be mitigated when the sample is held at low temperatures, between -100°C and -150°C, allowing for depth profile experiments of thin films to be undertaken, although some characteristic ion signals of interest did diminish quite rapidly during the depth profiling, likely due to damage accumulation (Mahoney *et al.*, 2006) (Mahoney *et al.*, 2008).

Initial developments of larger polyatomic cluster beams were focussed on the C_{60} projectile, with a 2003 collaboration between UMIST and Ionoptika describing an ion beam capable of achieving a 1µm spot size with up to 1nA of beam current. Secondary ion yield enhancements of the order of 10^3 were found compared to monatomic primary beams, with particular improvement noted for high mass molecular ions, (Weibel *et al.*, 2003) (Wong *et al.*, 2003).

The C_{60} ion source generates primary ions via electron impact ionisation of C_{60} powder, which is heated in a reservoir to temperatures in excess of 475°C, causing evaporation, before ionisation under electron bombardment, (Weibel *et al.*, 2003). Modern C_{60}

sources operate at lower temperatures, ~400°C, prolonging the source lifetime, whilst also being capable of achieving improved spatial resolution down to ~300nm (Tian *et al.*, 2017).

The key advantage of the C_{60} source is the low amount of residual chemical damage done to the sample, with most damage effectively sputtered away, preventing accumulation. This introduced the possibility for efficient three-dimensional molecular depth profiling in SIMS, with analysis beyond the static limit possible, with a steady-state of molecular ion signal observed for ion doses (Vickerman and Winograd, 2015). A study investigating the distribution of pharmaceutical molecules in a coronary stent coating found that the C_{60}^+ beam preserved the characteristic ion signal of interest to a much greater depth than when sputtering with SF_5^+, with C_{60}^+ also permitting of the analysis at room temperature, whereas SF_5^+ required sample temperatures of -100°C (Fisher *et al.*, 2009).

Further improvements in cluster beams have been rapidly advancing over the past decade, with lower damage accumulation and improved ionisation performance sought. The move towards gas cluster ion beams (GCIBs) started with the work of the Matsuo group in Kyoto, when they reported the high sputter yields and shallow ion implantation of the first GCIBs modified for use with SIMS (Yamada *et al.*, 2001). Commercially available Ar_n GCIBs have since been developed by Ionoptika, with large argon clusters showing reduced damage accumulation compared to C_{60} (Rabbani *et al.*, 2011). It has also been shown that Ar_{2000}^+ clusters can increase the secondary ion yield in analysis of complex biological samples, such as the increased yield of intact phospholipids by a factor of two compared to C_{60}^+ (Fletcher *et al.*, 2013).

Argon gas cluster ion beams have proved to be difficult to focus to as fine a spot size as C_{60} beams, initially spatial resolution was limited to around 20µm at best with 20keV Ar_n GCIBs operating with cluster sizes in the range 1,000 to 2,000, (Fletcher *et al.*, 2013). More recently, minimum spot sizes of ~4µm have been achieved for 40keV Ar-GCIBs (Angerer *et al.*, 2016).

GCIB spatial resolution can be further improved by operating at even higher beam energies, there has also been work to seek alternative projectiles including CO_2 which improves imaging resolution by a factor of two versus Ar_n (Tian, Maciazek, *et al.*, 2016), alongside efforts to develop H_2O cluster ion sources (Sheraz née Rabbani *et al.*, 2013),

which will be discussed in greater detail later. Very recently, a GCIB has been developed with a maximum acceleration potential of 70keV, which can achieve spatial resolution as low as 1µm when running with CO_2 gas, (Tian *et al.*, 2019), (Sheraz née Rabbani *et al.*, 2019).

It has been shown that cluster beams can also alleviate charging of samples in SIMS analysis, which can often be a significant impediment to analysing insulating samples. Indeed, it has been found that no charge compensation is required for certain cluster ion beam systems, even in dynamic SIMS operation, due to the increase in secondary ion yield offsetting the charge imbalance caused by additional charge entering the sample due to the primary ion beam (Cheng and Winograd, 2005).

There are circumstances however when cluster sources are not advantageous, such as for the analysis of thin organic layers on dense inorganic substrates, indeed some molecular dynamic simulations have suggested that in this instance C_{60} performs no better than a Ga monatomic projectile (Czerwiński *et al.*, 2006). This has been verified experimentally, with C_{60} shown to cause fragmentation of secondary ions desorbed from sub-monolayer thin films of PDMS on inorganic substrates (Wells *et al.*, 2009). Of course, this is still at the expense of quite substantial sub-surface damage, which would be of concern in thicker samples, or indeed when depth profiling. Some of this fragmentation can be mitigated by employing the larger clusters which are made possible by high energy GCIB systems, where the energy per atom of the primary ion clusters is lower than that of C_{60}, reducing the chance of sputter induced fragmentation of secondary ions, (Sheraz née Rabbani *et al.*, 2019).

Modern SIMS instruments tend towards polyatomic cluster beam primary ion sources, such as C_{60} or Ar_n. These sources utilise clustered atoms to bombard the sample and remove higher mass fragments unbroken, through improved ionisation yields and lower damage accumulation compared to monatomic primary ion beams (Rabbani *et al.*, 2011). The development of such cluster ion beams has allowed 3D dynamic SIMS imaging to be realised, in which layers of the sample can be etched through without compromising the chemical information retrieved. Cluster beams exhibit only a small penetration depth into the sample, whilst achieving a large sputtered volume. This is only possible due to the combination of lower damage cross-section, defined as the surface area affected by a single ion impact, and reduced damage accumulation, allowing the use of ion doses above the static limit, meaning large molecular fragments

can be removed intact from the sample whilst also depth profiling through the sample (Sheraz née Rabbani *et al.*, 2015). It is 3D imaging of this kind for which the Ionoptika J105 SIMS was primarily designed, (Fletcher *et al.*, 2008).

2.2.8 Water Cluster Source

In 2013, a novel water cluster primary ion source for SIMS was described in (Sheraz née Rabbani *et al.*, 2013). The advantage of using water clusters as the primary ion beam can be seen in enhanced secondary ion yields for organic molecular ions. The increase in ion yields is thought to be due to an increase in proton mediated reactions, brought about by the increased number of protons present at the water cluster impact region.

The water cluster source is based on a similar design to Ionoptika's GCIB, which has been operated with various gas supplies to produce primary ions, typically argon, carbon dioxide, or some mixture of the two, (Rabbani *et al.*, 2011), (Tian, Maciazek, *et al.*, 2016). The GCIB consists of two independently pumped main chambers to produce the cluster beam; an expansion chamber, and an ionisation chamber. High pressure gas is introduced into the expansion chamber, where it expands adiabatically into vacuum through a supersonic de Laval style expansion nozzle, forming clusters many thousands of atoms in size. The shape of this nozzle is critical for the formation of large polyatomic clusters, with a divergent exit section critical to allow clusters to form and grow, due to the increased number of collisions between particles in the constrained expansion zone, not present in purely converging nozzles (Pauly, 2000), (Mahoney, 2013). Collimation of the beam is achieved using a conical skimmer with a small exit aperture also permitting differential pumping of the expansion and ionisation chambers. Clusters are ionised via electron bombardment and subsequently filtered by mass using a Wien filter tuned to the desired cluster size. This is followed by an ion optical column to accelerate and focus the beam, whilst also being able to raster it over the analysis area for SIMS imaging. The composition of the cluster beam can be probed by measuring its time-of-flight down the column, from the point of ionisation to impacting a Faraday cup on the sample. A distribution of cluster sizes will be present, where the centre and width of the distribution can be tuned by adjusting the nozzle position, Wien filter, and other ionisation parameters.

The water primary ion source only differs from the design of the original GCIB in terms of the expansion chamber, and the inlet system for the fluid to be expanded, which can

be liquid or gas in this case. If a gas is to be expanded to form the ion cluster beam, the operation is identical to that of the standard GCIB. Alternatively, to produce an ion beam from a liquid, the water source allows for the injection of a small volume of the chosen liquid into the expansion chamber, typically high-performance liquid chromatography (HPLC) grade water. The water is then heated inside an *in vacuo* boiler to prevent condensation at the expansion nozzle. The water vapour produced is then expanded and ionised by the same means as gases in the GCIB, as described above (Sheraz née Rabbani *et al.*, 2015).

Initially, a prototype 10keV water cluster beam was described which achieved secondary ion yield increases of a factor of 10 to 20 for $(H_2O)_{1000}^+$ clusters versus an Ar_{1000}^+ cluster beam, (Sheraz née Rabbani *et al.*, 2013). As would be expected for proton related ionization, further yield increases were found for larger water clusters, up to $(H_2O)_{5000}^+$, when compared to C_{60}^+, in (Sheraz née Rabbani *et al.*, 2014). In 2015, a comparison of 20keV water and argon cluster beams was carried out, which reported yield increases in excess of a factor of 50 for $(H_2O)_{7000}^+$ clusters against Ar_{2000}^+ (Sheraz née Rabbani *et al.*, 2015). It was also found that increases in ion yield are dependent not only on cluster size, but on the energy per nucleon (E/n) in the primary ion projectile, with a maximum increase in the molecular ion yield found at approximately E/n ~0.2eV/nucleon for water clusters. This study confirmed that doubling the ion energy, and doubling the cluster size, thus maintaining a constant energy per nucleon, resulted in a doubling of the ion yield. It was this finding that led to the development and installation of the first 40keV water cluster source in the world on Newcastle University's J105 in 2017, in the hope of further increasing ion yields compared to 20keV beam energy.

In 2019, a study was published which compared results from the 40keV water cluster source at Newcastle University (UK), with results gathered at 70keV from Penn State University (USA), where Newcastle's water ionisation source was on loan from August 2018, (Sheraz née Rabbani *et al.*, 2019). This study reported secondary ion yield increases of 10 to 100 for water cluster beams in an energy per nucleon regime of <0.2eV/n, with a maximum found around 0.16eV/n, whilst also demonstrating better than 1µm spatial resolution when imaging with the 70keV water cluster beam. A further interesting finding from this study is that both positive and negative secondary ion yields were increased by using a high energy water cluster beam, which seems to

support the idea that an activated aqueous environment is formed at the impact region, allowing large analyte molecules to gain or lose protons. It can be anticipated that further increases in primary ion beam energy, which would permit access to larger cluster sizes, would further increase the useful secondary ion yield for large bio-organic molecular ions.

It has also recently been reported that water-containing primary ion sources serve to reduce the matrix effects observed in SIMS data, with the sample matrix found to have no significant effect on ion yields for $(H_2O)_{4000}$ clusters (Alnajeebi *et al.*, 2018). It is thought that the use of a reactive projectile, in this case water, reduces ionisation suppression by providing hydrogen at the impact zone, increasing protonation yields. The mitigation of matrix effects has potentially significant implications for improving quantitative analysis with SIMS, as signal intensity can be more readily converted to a value for concentration in the sample itself.

The development of large cluster ion beams, which increase the secondary ion yields of high mass organic molecules, means that higher mass resolution is even more desirable in SIMS to aid the unambiguous identification of such molecules.

2.2.9 Improving Mass Resolution in SIMS

With the advent of modern cluster beams, which can ionise ever larger bio-molecules, higher mass resolution in SIMS has become a more pressing concern. For large molecules, unambiguous identification of their molecular formula requires an increase in mass resolution, as highlighted by Figure 2.3 which shows the mass resolving power required to separate metal hydrides from their nearest elemental mass peaks (Stephan, 2001). It can be seen that for masses above 100u, mass resolution in excess of 10,000 is required, meaning alternatives to the reflectron time-of-flight mass analysers found in modern SIMS instruments are desirable.

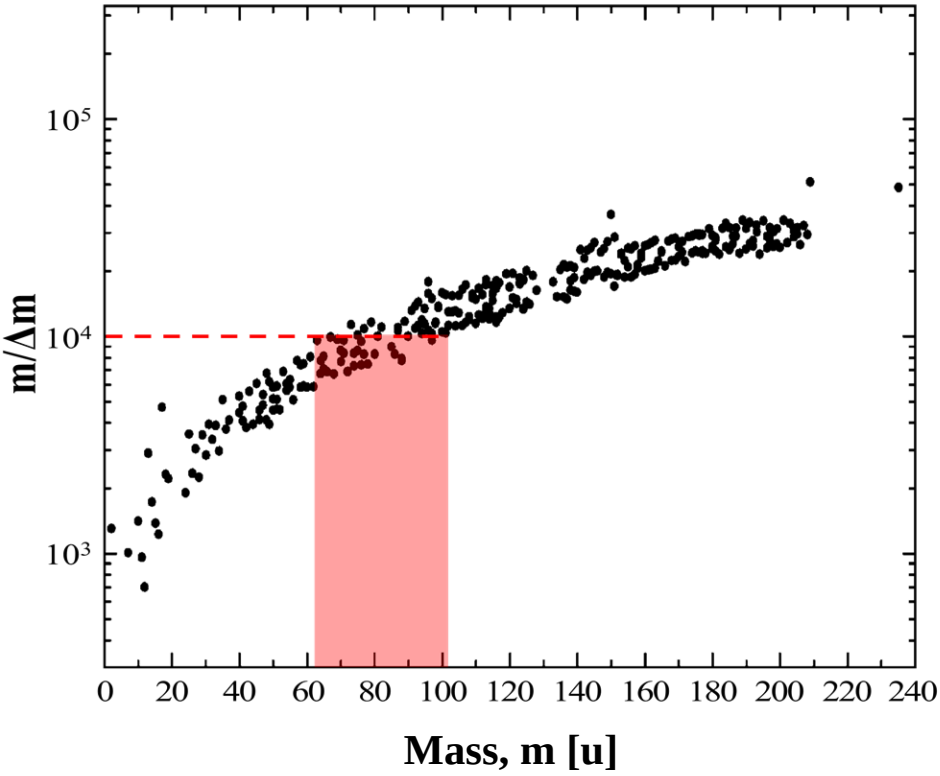

Figure 2.3 - Plot of mass resolution against mass, showing the mass resolution required to separate metal hydride peaks from their nearest elemental mass peaks, adapted from (Stephan, 2001).

Essentially, higher mass resolution, when combined with mass accuracy, allows mass spectral peaks to be unambiguously identified. An accurate mass measurement can only be trusted if it has been measured with suitably high mass resolution. The utility of this becomes particularly pronounced when considering higher mass peaks, above 100 u.

Achievable mass resolution can drastically affect the number of possible peak attributions, even when considering only a small number of elements to make up the

composition. Mass resolution, combined with mass accuracy, effectively sets a confidence interval within which the true mass will lie. For example, the pesticide Pirimicarb has an accurate mass of $[M+H]^+ = 239.15025\ m/z$. When considering only C, H, N, and O elements there are 22 mathematically possible combinations within a ±0.012 m/z range, as would be offered by the mass resolving power of a time-of-flight analyser, $m/\Delta m = 10{,}000$, if it is assumed that at least one atom of each element is present. These possibilities can be further narrowed down by discounting species which are not chemically likely, this can be easily done using software such as SIRIUS, developed for aiding the interpretation of mass spectra (Böcker *et al.*, 2009). SIRIUS reduces the possible peak attributions to 19 viable candidates, for 10,000 resolution. Increasing mass resolution to 100,000 gives a narrower uncertainty range of ±0.0012 m/z, with two composition possibilities. SIRIUS suggests that only one of these is chemically likely, reducing this to a single unique attribution of $C_{11}H_{19}O_2N_4$. An example similar to this was detailed for mass resolutions of 15,000 and 80,000 in (Scigelova *et al.*, 2011).

There are some key characteristics that a mass analyser for useful molecular imaging in SIMS would ideally possess, such a mass analyser should be able to:

- Achieve mass resolution higher than that of existing reflectron time-of-flight SIMS analysers, that is to say $m/\Delta m \gg 1 \times 10^4$, ideally $m/\Delta m > 1 \times 10^5$
- Accept a wide mass range of ions, with a high upper limit of $m/z > 2{,}000$ u
- Allow simultaneous detection across this wide mass range
- Detect a wide dynamic range of signal intensities
- Achieve high mass accuracy, approaching single digit ppm
- Perform high sensitivity analysis, approaching single ion sensitivity, to maximise detection of generated secondary ions
- Allow fast analysis, with repetition rates comparable to the 10kHz of a reflectron time-of-flight analyser

As detailed earlier, there are many different types of mass analyser which could be candidates for use with SIMS, however, few are able to meet the above criteria, and it can be argued that no single analyser can achieve all of them simultaneously. This is particularly the case with regard to speed of acquisition and mass resolution, as there is often a trade-off required between the two attributes.

Potential mass analysers include, but are not limited to:

- FT-ICR cells
- Magnetic sector analysers
- Multi-reflectron time-of-flight analysers
- Ion traps of various geometries;
    - Orbital ion traps, including multiple electrode variants (Sonalikar *et al.*, 2015), (Sonalikar and Mohanty, 2017)
    - Other harmonic ion traps, such as Cassinian ion traps, (Köster, 2009)

There have been attempts to couple an FT-ICR mass analyser to a SIMS primary ion source, as will be discussed in more detail in the next sub-section. In terms of meeting the stated requirements, FT-ICR cells are certainly capable of high mass resolution, comfortably in excess of $m/\Delta m = 1 \times 10^5$, or even $m/\Delta m > 1 \times 10^6$ for slower acquisition on instruments with the strongest magnetic trapping fields, (Hendrickson *et al.*, 2015). However, such performance does come with significant cost and complexity.

Magnetic sector analysers have been covered earlier in this chapter, and whilst they offer a constant mass resolution across their mass range, they are unable to provide parallel detection across the entire mass range, due to the need for discrete detectors. The implementation of array detectors on the focal plane improves the mass range that can be detected simultaneously, but it will still not extend to the entire mass range parallel detection of the time-of-flight analyser. Magnetic sectors are also required to be physically large, which is a disadvantage when coupling to an existing instrument where available space is at a premium.

Multi-reflectron time-of-flight analysers are another candidate which would be capable of high mass resolving power, although there are still significant disadvantages in terms of ion transmission and acquisition times, with transient recording times of the order of 100s of ms required. There is also the difficulty of analysing large numbers of ions, as packets of more than 1,000 ions can cause adverse effects in the spectra due to space charge capacity (Radionaova *et al.*, 2016).

Employing an orbital ion trap mass analyser would satisfy the need for a compact addition to a SIMS instrument, whilst also offering access to mass resolution $m/\Delta m \gg 1 \times 10^5$, although there is still the drawback of much slower analysis than time-of-flight analysers, as will be discussed in the next section on quadro-logarithmic ion traps.

Alternative non-orbital harmonic ion trap designs, such as the Cassinian trap, (Köster, 2009), would also represent a small footprint, potentially high mass resolution mass analyser. However, there is as yet not a great deal of literature on such devices, meaning a lot of research is required to fully characterise the space charge capacity, sensitivity, and mass resolving power across a wide mass range. The reason for the lack of literature could be due to the complexity of manufacturing such devices, as will be discussed in the next section of this chapter. A Cassinian ion trap would suffer from the same slow acquisition rate as orbital ion traps, due to the need to record a sufficiently long time-domain transient of harmonic ion motion to achieve high mass resolution once a fast Fourier transform is applied to convert the data into a mass spectrum.

Table 2.1 details some of the properties of the discussed mass analysers for initial comparison. It should be noted that the values given in the table are only indicative and do not hold for all analytical conditions. Indeed such characteristics can vary significantly between instruments and between experiments, depending on; the primary ion source, the sample being analysed, and even the age and maintenance history of the instrument being used.

Table 2.1 - Properties of different mass analysers

Mass Analyser	Maximum $m/\Delta m$	Upper mass limit†	Dynamic Range	Parallel Detection	Mass Accuracy	Detection Sensitivity	Repetition Rate*
FT-ICR	> 10^6	>10^6 u	> 10^3	Yes	< 0.2 ppm	10^2 – 10^3 ions	< 10 Hz
Magnetic sector	≈ 10^4	> 10^4 u	> 10^6	No	< 5 ppm	< 10 ions	< 5 Hz
Multi-reflectron	> 10^6	> 10^4 u	> 10^3	Yes	< 0.5 ppm	< 10 ions	< 10 Hz
Orbital ion trap	> 2×10^5	> 10^4 u	≈ 10^4	Yes	< 1 ppm	< 5 ions	< 10 Hz
Cassinian trap	> 10^5	> 10^4 u	Limited evidence	Yes	< 1 ppm	Limited evidence	< 20 Hz

† Upper mass limit is restricted only by ion flight time, or length of detected transient, for all techniques except magnetic sector analysers. In principle, higher masses could be detected, provided they are ionised intact after desorption from the sample.

* Repetition rate is dependent on desired mass resolution, or mass range, for all techniques except magnetic sector analysers.

Note. Data for FT-ICR from (Marshall *et al.*, 1998), (Marshall *et al.*, 2013), (Smith *et al.*, 2018), (Hendrickson *et al.*, 2015), for Magnetic sector analysers from (Bristow and Webb, 2003), (Gilmore and Vickerman, 2009), for Multi-reflectron analysers from (Plaß *et al.*, 2013), (Yavor *et al.*, 2015), (Radionaova *et al.*, 2016), (Dickel *et al.*, 2019), for orbital ion traps from (Makarov, Denisov, Lange, *et al.*, 2006), (Rose *et al.*, 2012), (Zubarev and Makarov, 2013), for Cassinian trap from (Köster, 2009), (Köster, 2015).

2.2.10 High mass resolution by coupling FT-ICR to SIMS

There is evidence in the literature of other work to couple alternative mass analysers to SIMS instruments, including the combination of a C_{60} primary ion beam with an FT-ICR MS, (Smith, Robinson, Tolmachev, Heeren and Pasa-Tolic, 2011), (Smith *et al.*, 2013), (Pasa-Tolic *et al.*, 2013), as well as an earlier effort with a Ga^+ primary ion source (Maharrey *et al.*, 2004). Ultra-high mass resolution SIMS was demonstrated, with $m/\Delta m$ in excess of 100,000 shown across a wide mass range, and $m/\Delta m$ up to 3,000,000 demonstrated for a much narrower mass range of interest, centred at m/z 245. There are however trade-offs associated with achieving such high resolution; one drawback of this work is the long accumulation time required per pixel for high-quality spectra to be obtained. Dwell times of up to 15s per pixel were used, which would mean a single small image of 64 x 64 pixels would take over 17 hours to acquire. Acquisition times this long would make high mass resolution SIMS imaging impractical, precluding its use for all but the most demanding samples.

There is also a question over the spatial resolution which is possible, as mass spectral images generated by FT-ICR SIMS which demonstrate the maximal spatial resolution of the C_{60} primary ion source, which should be less than 500nm, have not been presented in the literature at the time of writing. This can be assumed to be due to a combination of low instrument transmission, or poor secondary ion yields. The detection limit of FT-ICR cells is of the order of 10^2 to 10^3 ions for a given m/z, meaning that a high secondary ion yield would be required to permit high spatial resolution SIMS analysis (Marshall *et al.*, 1998). The minimum spatial resolution shown for FT-ICR SIMS is approximately 20µm with a C_{60} primary ion source, (Smith *et al.*, 2013).

There is also an upper limit on the number of charges which can be simultaneously trapped in FT-ICR without a detrimental effect on performance, this limit is referred to as the point at which coalescence occurs, which is when two close mass peaks merge

due to space charge effects caused by the size of the trapped ion population (Paša-Tolić *et al.*, 1995), (Boldin and Nikolaev, 2009).

Computer simulations of ion motion in FT-ICR cells offer a method by which to estimate the number of ions which can be trapped before coalescence occurs, by simulating large ion populations at varying magnetic field strengths and cyclotron radii (Vladimirov *et al.*, 2012). These simulations propose a quadratic relationship between the threshold number of trapped ions for coalescence, and the magnetic field strength, where the coefficient of the quadratic term varies depending on the masses of the trapped ion clouds which are candidates for coalescence. This gives the relationships laid out in equation (2.7), with a reduced space charge capacity for two ion clouds which are closer in mass, as would be expected (Vladimirov *et al.*, 2012) (Nikolaev *et al.*, 2014).

$$\begin{aligned} N &\approx 10{,}000 \cdot B^2 \ (m/z = 500 \text{ u}, \Delta\text{m} = 0.3\text{u}) \\ N &\approx 3{,}000 \cdot B^2 \ (m/z = 500 \text{ u}, \Delta\text{m} = 0.1\text{u}) \end{aligned} \tag{2.7}$$

From these relationships, an estimate for the space charge capacity of different magnetic field strength FT-ICR traps can be found, as shown in Figure 2.4. It can be seen that a 7T FT-ICR cell could accommodate approximately 500,000 ions before coalescence occurs between two ion clouds with a mass difference of 0.3u at m/z 500, yet fewer than 150,000 ions if the mass difference was as low as 0.1u between ion clouds. In the case of 12T magnetic field, the maximum space charge capacity increases to approximately 1.44×10^6 for a mass difference of 0.3u, and 430,000 for a mass difference of 0.1u.

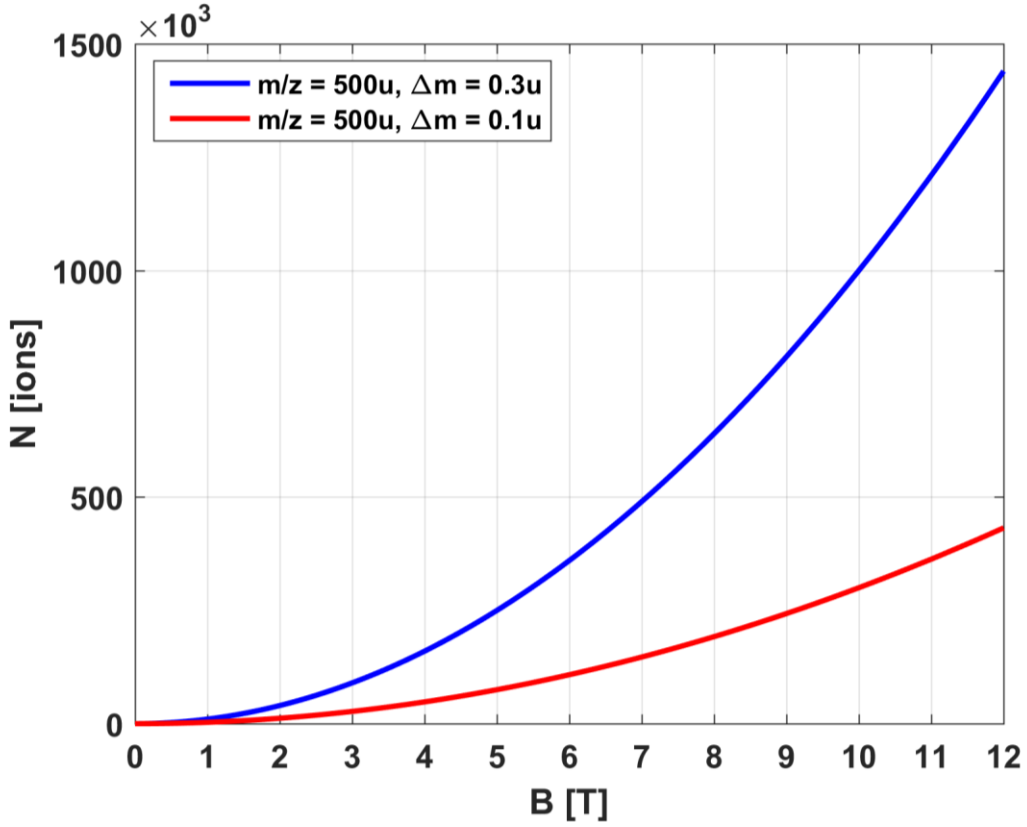

Figure 2.4 - Plot of the number of ions which can be trapped before coalescence occurs for different FT-ICR cell magnetic field strengths

Such large upper limits for the ion populations able to be trapped should not be much of a concern for experiments carried out under the static SIMS limit, but potentially could come into play for dynamic SIMS experiments with large secondary ion yields and high instrumental transmission.

Another disadvantage of FT-ICR MS is the cost of the instrument itself, with a 12T FT-ICR system costing several million dollars, due to the integral superconducting magnets. On top of this, the liquid helium required to cool the magnets would be a substantial operational expense.

2.3 Quadro-Logarithmic Ion Traps

The seminal publication for work on quadro-logarithmic ion traps of the style of the orbital ion trap is (Makarov, 2000), the heritage of which can be traced back to work done by (Knight, 1983), who laid out the general form for electrostatic quadrupole ion traps, through to the origin of orbital ion trapping in (Kingdon, 1923), in which an outer cylindrical anode was used to manipulate positive ion trajectories around a wire cathode. Kingdon's initial design consisted of a thin cathodic filament running axially through a coaxial cylindrical anode, as shown in Figure 2.5. Positive ions with sufficient

tangential velocity can then orbit the filament given appropriate initial conditions, due to the radial logarithmic field produced.

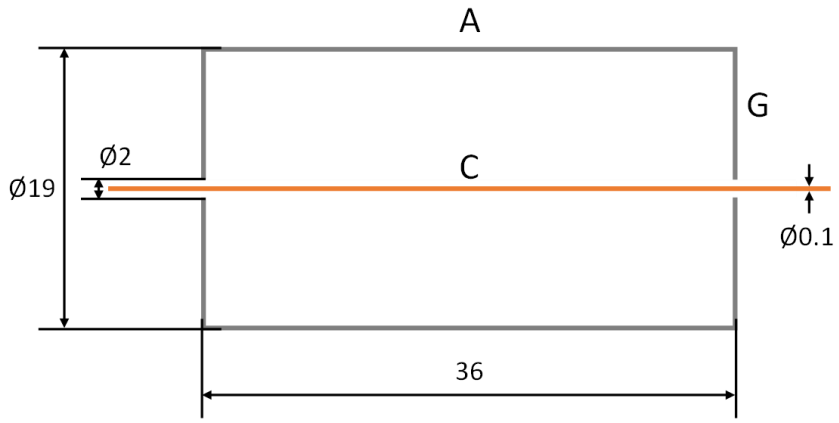

Figure 2.5 - Diagram of Kingdon's original ion trap, where A denotes the anode, C denotes the cathode, and G denotes the guards. All dimensions in mm.

The potential field produced within a Kingdon's ion trap is simply of the logarithmic form described by equation (2.8).

$$U(r) = A\ln(r) + B \tag{2.8}$$

The key development made by Knight in 1981 was to modify the geometry of the external electrode to include a quadrupole term, to give a harmonic axial potential, as described by equation (2.9) , (Knight, 1981). Knight employed two methods of ion detection; an electron multiplier located to determine axial losses, and a collector plate used to detect ions ejected at the mid-plane if a pulsed voltage was applied to the internal electrode.

$$U(r,z) = A\left(z^2 - \frac{r^2}{2} + B\ln(r)\right) \tag{2.9}$$

The potential field promotes the harmonic oscillation of ions within the trap, which in turn allows the identification of the mass-to-charge ratio of trapped ions. One particular advantage gained with Knight's work was the ability to store a large number of ions for a long period of time, in excess of 100ms, after a rapid initial decay due to space-charge effects. This extended trapping ability paved the way for the development of ion traps as viable mass analysers.

Knight split the external electrode in two, to allow an RF voltage to be applied across it. When the frequency of the RF voltage was tuned to match that of an ion's motion, a resonant signal was observed in both detectors. However, the detected resonance was weak due to the distortions to the harmonic field introduced by the internal wire electrode. On top of this, the simplifications made by Knight in the geometry of the external electrodes further limited the prospects of the Knight trap as a mass spectrometer, by introducing further imperfections to the harmonic potential.

In 2000, Makarov further developed the idea of orbital ion trapping mass spectrometry by proposing an ion trap in the ideal form of the Knight trap, without the simplification of a thin wire internal electrode. Instead, a potential field of the form described in (2.10) was achieved by machining both internal and external electrodes of the idealised geometry, as shown in Figure 2.6. This field can be understood as the sum of a quadrupole and logarithmic field, hence it is referred to in the literature as a quadro-logarithmic field. The R_m term refers to the characteristic radius, which is the limiting radius beyond which ions cannot be trapped in stable orbit around the internal electrode, this parameter should be minimised and be as close as possible to $\sqrt{2}$ times larger than the external electrode radius, (Makarov *et al.*, 2009). Further interrogation of the physics of ion trapping can be found in Chapter 3.

$$U(r,z) = \frac{k}{2}\left(z^2 - \frac{r^2}{2}\right) + \frac{k}{2}(R_m)^2 \ln\left[\frac{r}{R_m}\right] + C \qquad (2.10)$$

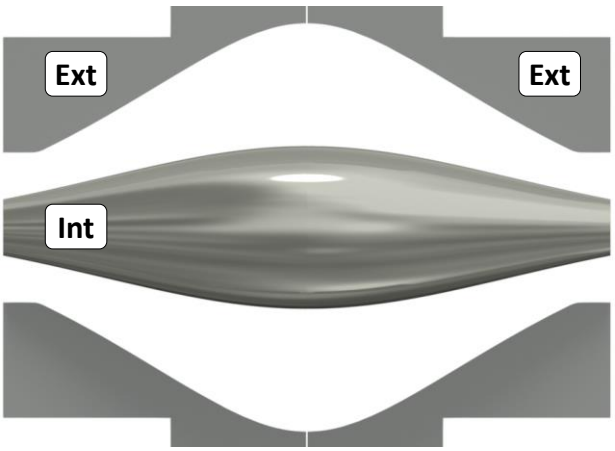

Figure 2.6 - CAD rendering of a simplified orbital ion trap, with internal and external electrodes labelled

Ions are captured in a quadro-logarithmic ion trap by a harmonic potential well induced between the component electrodes through the application of a voltage to the internal electrode, which must occur when ions are within the trapping volume, i.e. after they have entered the ion trap. The resultant ion motion is approximately circular in orbit around the internal electrode, whilst ions demonstrate simple harmonic motion in the axial direction, with the frequency of axial oscillation governed by equation (2.11), (Makarov, 2000). The dependence of frequency on the square-root of the reciprocal of mass-to-charge ratio is one advantage of the orbital ion trap over other mass analysers, such as FT-ICR cells, as will be discussed in greater detail later in this chapter.

$$\omega = \sqrt{\frac{q \cdot k}{m}} \qquad (2.11)$$

As per the Knight trap, the external electrode is split into two, in this case to allow the detection of image charge generated by ion oscillations. As the frequency of ion oscillation in the axial direction is independent of ion energy and spatial distribution of ions, and dependent only on the ions' mass-to-charge ratio, this image charge detection allows the orbital ion trap to function as a mass spectrometer. The detected image charge produces a time-domain signal of the combined oscillations of all trapped ions, which can be converted into the frequency domain using a fast-Fourier transform, before then using the relationship between ion frequency and mass to translate this into a mass spectrum. When a large voltage, up to ±5kV, is applied to the internal electrode of the trap, ions oscillate at frequencies of the order of 100kHz to 1MHz, which permits very high mass resolution, in excess of 100,000, to be attained in a short acquisition times of less than one second. This is still many orders of magnitude slower than other mass analysers, such as time-of-flight reflectrons which can generate spectra at frequencies in excess of 10kHz. This highlights the utility of an instrument combining both techniques, where the ultra-high mass resolving power of an orbital ion trap can be employed only when required.

The most recent developments in quadro-logarithmic ion trapping have been refinements to Makarov's initial design, such as the development of a so-called high-field trap (Makarov *et al.*, 2009), in which the inner electrode radius is increased, from 6mm to 9mm, to provide a higher field strength for a given voltage. An ultra-high-field variant has also been developed in which the radius of the external electrode is

decreased, to reduce the ratio in radii between external to internal electrodes from 2.5 to 2, which when combined with an increased internal electrode voltage increases the frequency of oscillations by a factor of ~1.8 compared to the standard orbital ion trap geometry, leading to higher mass resolution for the same measurement duration (Michalski *et al.*, 2012).

Table 2.2 contains the electrode dimensions of different variants of orbital ion traps from the literature, alongside an example oscillation frequency for an ion with m/z 500. This highlights the almost continual progression towards higher frequency oscillation, thus permitting higher resolution analysis, or faster data acquisition. There is a drop in oscillation frequency seen between the third pre-production device, as used in some ion excitation studies in the literature, and the first standard commercial orbital ion trap, this is likely due to the increased complexity in manufacturing smaller electrodes, which Thermo Fisher perhaps did not want to pursue for the first commercial devices. It should be noted that the frequencies shown assume that the same internal electrode voltage of 3,500 V is used across all ion trap geometries, in reality, the high-field and ultra-high-field variants permit higher internal electrode voltages, which would give further increases in oscillation frequency.

Another example of recent developments would be those made in the control of aberrations and space-charge effects within such devices by (Grinfeld *et al.*, 2015).

Table 2.2 - Electrode dimensions of different commercial orbital ion traps.

Example oscillation frequencies were calculated for an ion with mass-to-charge ratio m/z 500, with an internal electrode voltage of 3,500 V, assuming an ideal characteristic radius, $R_m \approx \sqrt{2}\, R_2$. All frequencies were calculated using an in-house written MATLAB script, *mass2freq,* available via a public GitHub repository (Hood, 2019).

Nominal Geometry	**Internal Electrode Radius [mm]**	**External Electrode Radius [mm]**	**Electrode Radius Ratio**	**Example Oscillation Frequency of m/z 500 [kHz]**	**Reference**
Pre-production I	7	20	2.86	223	(Makarov, 2000)
Pre-production II	7.39	19.97	2.70	235	(Hardman and Makarov, 2003)
Pre-production III	4	10	2.50	492	(Hu *et al.*, 2005)
Standard	6	15	2.50	328	(Makarov *et al.*, 2009)
High-field	9	15	1.67	465	(Makarov *et al.*, 2009)
Ultra-high-field	5	10	2.00	582	(Scheltema *et al.*, 2014)

One significant issue which arises in reducing the ratio of external to internal electrode radii is that the required machining accuracy increases, as ions will be travelling closer to the electrodes whilst trapped, so even small manufacturing imperfections can affect their trajectories to the detriment of mass resolution. This means that the accurate decomposition of the ideal parametric profile into machine-readable code becomes even more important for high and ultra-high-field variants of the orbital ion trap.

2.3.1 Mass Resolution using Orbital Ion Traps

The mass resolution reported in the literature for orbital ion traps has been improved since the first description of the device in 2000. Initially, in (Makarov, 2000), a frequency peak was presented for the measurement of Fe^+, at m/z 56, with a peak width of 2.39Hz at a frequency of 711kHz, corresponding to a frequency resolution of nearly 300,000, and a mass resolution of half this value, approximately 150,000. It should be noted that this value is not constant across the operational mass range of the device, and would in fact drop significantly as mass increases. This decrease in resolution with higher mass comes about due to the relationship between ion mass and oscillation frequency, where frequency is proportional to $m^{-1/2}$. The consequence of this is that a frequency spectrum obtained with a constant frequency resolution will transform into a mass spectrum with decreasing mass resolution for high masses, as mass resolution is dependent on the number of oscillations detected during the chosen recording length (Zubarev and Makarov, 2013).

In orbital ion trapping mass spectrometry, increases in mass resolution can be pursued by increasing the number of oscillations in a given recording time, this can be achieved by increasing the field curvature of the potential within the trapping volume. There are numerous ways to achieve this which have been pursued in the literature, including; increasing the radius of the internal electrode (Makarov *et al.*, 2009), or reducing the dimensions of the trap to further increase the diameter of the internal electrode relative to the external electrodes (Michalski *et al.*, 2012).

Although FT-ICR cells are capable of achieving higher mass resolution than an orbital ion trap, this does not necessarily hold across the entire mass range of interest in an experiment. This is because the mass resolving power in FT-ICR varies in proportion to the reciprocal of m/z whereas in orbital ion trapping, mass resolving power diminishes more slowly as mass-to-charge ratio increases, in proportion to the square-root of the reciprocal of m/z, (Zubarev and Makarov, 2013). As a result, there is a cross-over value of m/z at which a given orbital ion trap geometry will be able to provide higher mass resolution in a set transient time as compared to an FT-ICR with a specified magnetic field strength. According to the 2013 report by Zubarev and Makarov, for all masses above $m/z \approx 300$, a high-field orbital ion trap can offer higher mass resolution than a 15T FT-ICR cell, if both acquire spectra over a 0.76s transient detection time. This is assuming that the FT-ICR is operating in magnitude mode as is

typically the case, which results in approximately a factor of 2 reduction in mass resolving power compared to absorption mode, (Marshall *et al.*, 1998). The mass-to-charge ratio of cross-over is higher for a standard geometry orbital ion trap, at around $m/z \approx$ 4,000, again for a 0.76s detection period. These relationships between theoretical mass resolving power and m/z can be found from the relationships governing the frequency of motion in FT-ICR and orbital ion trapping discussed earlier in this chapter, producing the plot shown in Figure 2.7, which is similar to that of Zubarev and Makarov, (Zubarev and Makarov, 2013).

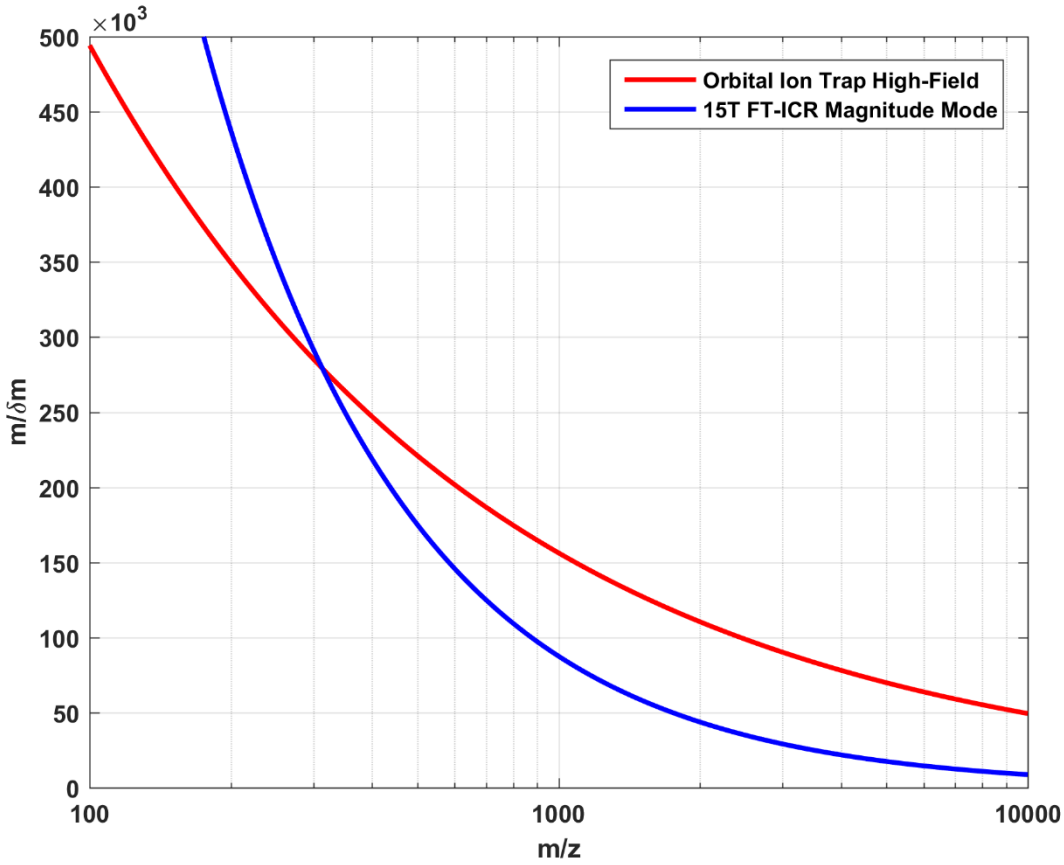

Figure 2.7 – Curves showing the dependence of mass resolution on m/z for a high-field orbital ion trap, assuming a 3.5kV internal electrode voltage, against a 15T FT-ICR cell operating in magnitude mode, both with transient detection lengths of 0.76s.

From this curve, the advantage of an orbital ion trap for higher masses is evident, however transient detection times of as long as 0.76s are not feasible for high throughput mass spectral imaging, as is possible with a reflectron time-of-flight analyser, which would also be capable of attaining roughly constant mass resolution across its entire mass range.

It should be noted that there have been some efforts to achieve high mass resolution across a broad mass range in the field of FT-ICR MS, with some success found very recently through advanced data processing methods, such as the OCULAR method of segmenting the mass range into multiple segments, as discussed earlier (Palacio Lozano *et al.*, 2019). The trade-off that this method makes is that the analysis takes much longer, due to the increased time-domain transients which are required for the spectral segments encompassing the high end of the mass range. A similar approach to the OCULAR method could be applied to orbital ion traps, or indeed any Fourier transform mass spectrometry technique, by segmenting the chosen mass range into separate experiments and calculating the required increase in acquisition time to achieve the desired mass resolution for each segment. In orbital ion trapping, however, the increased transient times required would likely be prohibitive, due to collisional damping of the recorded transient, unless the base pressure in the chamber were able to be reduced below 10^{-10} mbar.

Similar experiments utilising a so-called spectral stitching approach have been trialled in orbital ion trap mass analysers. A more basic method than OCULAR was used, whereby ion packets of only a narrow mass range, approximately 30u, are permitted to enter the orbital ion trap, so that the analyte ions are present in greater abundance and thus only a few repeat scans per 30u mass window are required, as opposed to a much greater number of scans if a broad mass range is injected, (Vetere and Schrader, 2017). Effectively, this is improving the sensitivity of the resultant spectra, rather than increasing the mass resolving power, as is achieved in OCULAR method by increasing transient durations with the m/z of each spectral segment. Vetere and Schrader demonstrated that their spectral stitching method did not increase analysis time compared to analysis using the entire mass range, but with many more repeat scans. A mass range of 200u to 1200u was used, this required 250 repeat scans averaged to produce the ‘full scan’ dataset. For the spectral stitching variant, mass windows of 30u, overlapping by 5u were used, with each window requiring between 5 and 10 repeats, meaning the total number of scans was 250 for both analyses, with all other experimental parameters being equal, meaning analysis time was unchanged.

Spectral stitching in this manner saw a significant improvement in the sensitivity of the orbital ion trap, resulting in an order of magnitude increase in the number of assigned elemental compositions for a 3.04s transient when comparing the stitched spectra to

the ‘full scan’ dataset, with over 70,000 assignments made for the stitched spectra, as opposed to fewer than 7,000 for the broadband ‘full scan’ spectra (Vetere and Schrader, 2017).

However, the maximum observed mass resolution in such experiments, conducted with orbital ion traps, still remains lower than would be possible with high magnetic field strength FT-ICR MS. This is particularly the case if operating the FT-ICR in absorption mode and also using longer duration transients, which would not be possible without further reducing the pressure in an orbital ion trap. As such, FT-ICR would likely still be the preferred tool for analysing complex mixtures such as crude oil. It is also worth mentioning that increasing the transient duration as dramatically, as is required in OCULAR experiments, would be detrimental to any efforts to use the orbital ion trap as an imaging mass spectrometer.

Additional detection electrodes have also been employed in FT-ICR with the aim of improving mass resolution by detecting higher harmonics of the cyclotron frequencies, as already described in the form of quadrupolar detection, (Pan *et al.*, 1988), (Schweikhard *et al.*, 1990), (Cho *et al.*, 2017). This approach would not be suitable for an orbital ion trap, as the characteristic oscillations being detected do not exhibit circular motion, but rather they are simply axially harmonic in one dimension along the z-axis of the trap.

Combined with high mass resolution, orbital ion traps also offer the possibility of extremely sensitive detection of analyte ions, down to single ion levels, if certain experimental conditions can be met. Requisite conditions include; low levels of input noise on the image current detection electronics, which can be achieved by cooling the electronics to cryogenic temperatures, in addition, a sufficiently large number of transients need to be acquired, these can then be summed to reduce the signal-to-noise ratio of the detected single ion signal, (Rose *et al.*, 2012).

2.3.2 Ion Injection

When transferring ions into an orbital ion trap, it is desirable to produce a packet of ions with narrow distributions in both space and time, ideally less than ~2 mm in length, arriving in less than 200 ns temporally, (Perry *et al.*, 2008). This allows the entire ion packet to be trapped when the voltage on the internal electrode is ramped up once the ions are within the trapping volume. Ions are injected tangentially to the internal

electrode, with the rapidly applied voltage on the internal electrode trapping the ions in orbit (Makarov, 2000).

The mass range of ions which can be trapped simultaneously is limited by the dispersion in time and space which will occur during the flight-time of an ion packet to the orbital ion trap, with heavier ions arriving later. To combat this, the voltage on the internal electrode is increased monotonically during a longer injection period of 20 – 100μs. This has the effect of reducing the radii of ion orbits, bringing them closer to the internal electrode and preventing collision with the external electrodes. The voltage ramp also serves to permit the later arriving ions, typically of higher mass, to be successfully trapped and avoid colliding with either external or internal electrodes. This process is termed electrodynamic squeezing, and it finishes when there is no longer a risk of ion collisions with the component electrodes (Makarov, 2000), (Perry *et al.*, 2008). Electrodynamic squeezing does affect the radial and axial amplitudes of ion motion, with later arriving ions having larger final axial amplitudes, and larger orbital radii, with the effect tending to be larger induced image current for higher m/z,

Electrodynamic squeezing may not be necessary if an accurate spatial and temporal focus of a broad range of m/z were able to be realised at the entrance to the orbital ion trap, as is achieved on the Ionoptika J105 at the entrance to the time-of-flight reflectron using its ion buncher.

For successful injection of ions into the orbital ion trap, meaning that they do not collide with either the internal or external electrodes and result in stable trajectories, it is necessary to match the kinetic energy of the ions being injected to the radial component of the electric trapping potential,(Hu *et al.*, 2005). The reason for this is clear if the radial trapping field of the orbital ion trap is thought of as an electrostatic analyser of sorts, in which the radius of orbit is governed by (2.13), derived from balancing the centripetal force with the electrostatic force, as shown in equation (2.12) (Hoffmann and Stroobant, 2007).

$$qE = \frac{mv^2}{r} \tag{2.12}$$

$$r = \frac{2E_k}{qE},$$
$$\text{where}, E_k = \frac{1}{2}mv^2 \tag{2.13}$$

This relationship shows that the ion orbital radius is independent of mass, and dependent only on kinetic energy in an electrostatic field, as is present upon injection into an orbital ion trap. In this case, ion trajectories are separated by their kinetic energy, meaning only those of a kinetic energy well matched to the electrostatic field of the orbital ion trap will 'pass', and result in stable trapped motion. For example, for an orbital radius of 10mm, which is approximately typical in an orbital ion trap, and an internal electrode voltage of 3500V, the electric field strength at this radius will be 350kV/m, and ions will need an initial kinetic energy of 1750eV to achieve a stable circular orbit, as per the calculation shown in (2.14). The effect on trajectory stable of a poor match between ion kinetic energy and the electric potential will be investigated more thoroughly in the Ion Trajectory Simulations chapter.

$$E_k = \frac{r \cdot q \cdot E}{2} = \frac{(10 \times 10^{-3}\ \text{m}) \times 1\text{e} \times (350 \times 10^3\ \text{V/m})}{2} = 1750\text{eV} \tag{2.14}$$

2.3.3 Ion Excitation

There is significant discussion in the literature of different methods of ion excitation within quadro-logarithmic ion traps, with the commercially used technique of excitation by injection commonplace, (Makarov, 2000), (Hu *et al.*, 2005). This involves injection of ions offset from the mid-plane of the orbital ion trap (z=0), it is this offset which gives ions a component of acceleration in the axial direction, promoting harmonic axial oscillations, from which image currents can then be detected (Makarov, 2000).

An alternative method of excitation, once ions are already trapped, can be achieved by applying an RF voltage to either internal or external electrodes, this was discussed in (Makarov, 2000) only with regard to operating the device in a 'mass-selective instability' mode. Mass-selective instability operation in this case involves the excitation of ions of a particular mass by application of an RF voltage to the internal electrode at the resonant frequency of ion axial oscillation, thus promoting increasing oscillation

amplitude until ions are ejected from the trap, to impact with a secondary electron multiplier located outside of the trapping volume. Figure 2.8 shows an example of this mode of operation, modelled in SIMION, in which the extent of the electrode profiles have been shortened in the z-direction to allow ions to be more easily ejected axially to the detector.

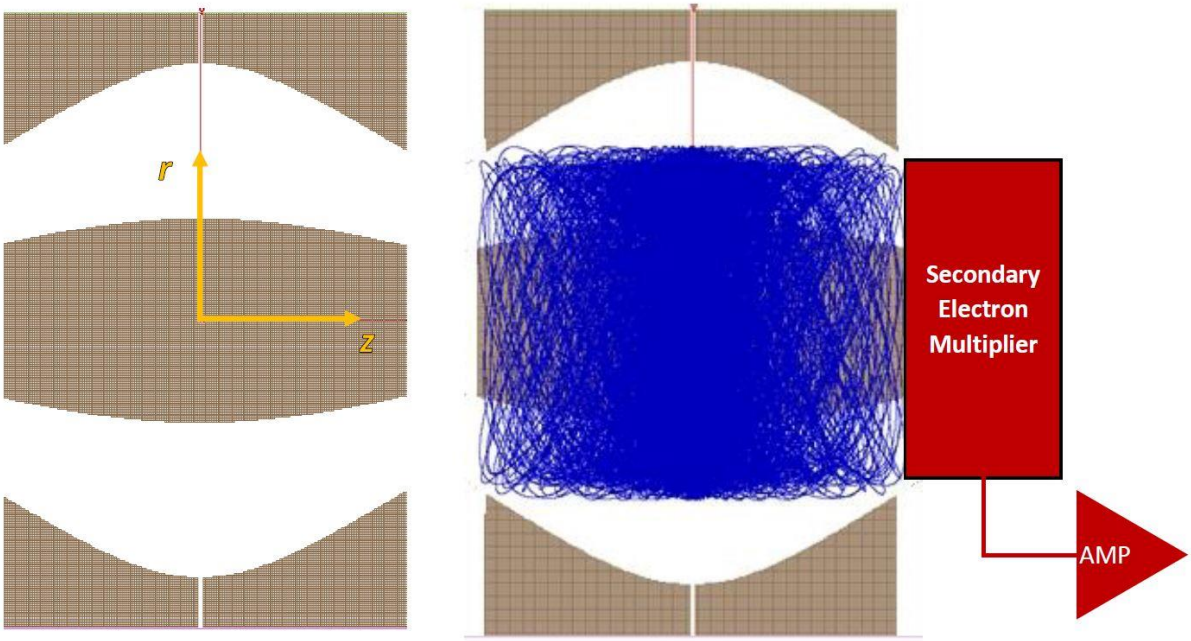

Figure 2.8 – Mass-selective instability mode operation of an orbital ion trap, plot of simulated trajectories prior to ion injection, and at the point of axial ejection

A separate study of resonant excitation of ions with a quadro-logarithmic trap applied the RF voltage as a dipolar signal to the separate external electrodes to excite ion axial motion, (Hu *et al.*, 2006). This was again with the objective of mass-selectively ejecting ions from the trap, with the technique demonstrated over a wide mass range of $100 \leq m/z \leq 6{,}000$, corresponding to a frequency range of 1.1MHz to 142kHz for the orbital ion trap geometry used. The key development made by this 2006 article is the consideration of mass-selective ejection not only for the purpose of ion detection but to remove ions of certain masses from the trap to allow higher resolution analysis of those remaining. Higher mass resolution is possible as space charge effects between ions are reduced due to the lower number of remaining trapped ions, thus causing a reduction in the space charge density in the ion trap.

Some of the same authors produced a further study in 2007 focussing on ion selection using RF excitation waveforms, once again applied to the external electrodes (Hu *et al.*, 2007). In this case, the purpose of the ion selection was for tandem mass

spectrometry, where the benefit of a well isolated parent ion will be seen in isotopically pure fragment ions, allowing unambiguous identification. Mass resolution of the ion ejection was improved by using a 'phase-enhanced' selective ion ejection. This involved estimating the evolution in phase difference between two species over time, calculated from the difference in their oscillation frequency, assuming initially coherent motion. The RF excitation voltage was then applied at the point at which the two species would be 180° out of phase with one another, serving to rapidly eject one species whilst de-exciting, and then re-exciting, the other. This method was able to achieve a mass resolution of greater than 28,000 in terms of ion isolation, at $\sim 517\ m/z$. The retained ions could then be candidates for further fragmentation through collisions with a bath gas for the purpose of tandem mass spectrometry.

In the paper laying out the theory of phase-enhanced selective ion ejection, a method is proposed for estimating the mass resolution with which target ions can be ejected, which is dependent on the frequency difference between two ions with a small difference in mass-to-charge ratio. In much the same way as the mass resolution of a given orbital ion trap spectrum is dependent on the transient length of acquisition, the mass resolving power with which ions can be ejected from the trap depends on the length of the signal which can be acquired before the transient decays. The length of the transient represents the maximum possible delay before a short AC excitation frequency can be applied, thus setting a minimum frequency difference between two ions which are to be retained and ejected respectively. To eject only one of two ions with a small mass-to-charge difference, the ions must be in anti-phase, the time that this takes to happen will depend on the frequency difference between the two ions, which in turn sets the beat period, meaning the time taken for two frequencies to go from being initially in phase, to 180° anti-phase, to being back in phase again. For example, if the maximum transient length without significant decay is 500ms, this would mean two ions could take a maximum of 500ms to become 180° out of phase, corresponding to a 1s beat period, and a 1Hz frequency separation. At m/z 500, ions oscillate with a nominal frequency of ~328kHz in a standard geometry orbital ion trap operated with a 3,500 V internal electrode voltage. In this case, a 1Hz frequency separation represents a frequency resolution of $f/\Delta f \approx$ 328,000, with a corresponding mass resolution of half of this value, $m/\Delta m \approx$ 164,000, for selective ion ejection.

A 2006 study compared simulation models of AC excitation of ions in an orbital ion trap with experimental data, showing reasonable agreement between the two, although ion ejection was found to occur much more quickly in experimental trials than was suggested by simulations, (Wu *et al.*, 2006). The most likely cause of this discrepancy is that the simulations did not accurately represent the initial distribution of ions within the orbital ion trap. Simulations in this study also found that the behaviour of ions under mass selective excitation is dependent on both the amplitude and duration of the applied RF excitation signal.

This form of ion excitation can also be thought of as a type of parametric excitation, referring to the time dependent modulation of a system parameter. Modulating the system parameter at a frequency close to twice the natural frequency of a system causes an effect called parametric resonance (Harish *et al.*, 2008) (Champneys, 2011). This phenomenon can be exploited in the orbital ion trap to dynamically, and mass selectively, manipulate the axial amplitude of ion oscillations. A more thorough examination of the mathematics behind parametric excitation will be covered in the Chapter 3.

Alongside its utility in ejecting ions from the trap, there are other aspects of the performance of an orbital ion trap which can be improved by parametrically exciting ion motion, it could be used to re-phase ion motion once trapped, allowing a potentially wider mass range of ions to be trapped simultaneously, or giving access to higher mass resolution.

Re-phasing of trapped ions was first reported in 2009, using an AC waveform to de-excite ions to the equatorial mid-plane of the orbital ion trap, $z = 0\ \mathrm{mm}$, at which point the amplitude of axial oscillations are negligible, or at least below the limits of detection by the image current amplifiers on the external electrodes (Perry *et al.*, 2009). In this study, an AC voltage with a wide bandwidth compared to the frequency distribution of ions of interest was used, so as to de-excite a wide mass range of ions simultaneously. This would not need to be the case if mass selective de-excitation was being pursued. During de-excitation, space charge effects on the ion packet are stronger, as would be expected for a denser ion cloud. This results in the coalescence of similar frequencies, acting in much the same way as the coalescence phenomenon observed in FT-ICR, which was discussed earlier. This serves to reduce the frequency distribution of the de-excited packet of ions, allowing them to be re-excited with a narrower frequency

distribution than they had upon their original injection, allowing higher mass resolution detection. In the 2009 study, a two to three-fold increase in mass resolution was observed, in an orbital ion trap with an asymmetric, and thus anharmonic axial potential, increasing mass resolution from 40,000 $\leq m/dm \leq$ 60,000 without rephrasing, to $130{,}000 \leq m/dm \leq 170{,}000$ with rephrasing implemented (Perry *et al.*, 2009).

As well as enhancing mass resolution, re-phasing of trapped ions is advantageous in that it allows coherent ion motion to be established after ions have been injected into the trapping volume, allowing the relaxation of the strict injection conditions discussed earlier.

2.3.4 Additional Electrodes

Discussion of further electrodes in addition to the usual internal and split external electrodes forms a particularly interesting facet of the literature surrounding quadro-logarithmic ion traps. There are numerous examples of such electrodes in the literature, such as in (Makarov, 2000) where two further separate electrodes are included. The first of these electrodes is intended to adjust ion entry angle into the trap and the second is to act as a field compensator to minimise electric field distortions introduced due to the injection hole in the external electrodes.

In later literature, the two additional electrodes described by Makarov are rarely referred to separately, but more often as a single ‘deflector’ or ‘compensation’ electrode, with the exact purpose not made clear. Table 2.3 highlights the various additional electrodes discussed in the literature.

Table 2.3 - Summary of Additional Electrodes

Reference	Additional Electrode Discussed	Purpose
(Makarov, 2000)	‘Deflector’	Adjusting ion entry angle
	‘Field Compensator’	Minimising field perturbations from injection slot
(Hu *et al.*, 2005)	‘Deflector’	Minimising field perturbations from injection slot
(Hu *et al.*, 2006)	‘Deflector / Compensator’	Adjusting ion entry angle
(Perry *et al.*, 2008)	‘Deflector’	Minimising field perturbations from injection slot
(Perry *et al.*, 2009)	‘Deflector / Compensator’	Single electrode to deflect ions during injection and also compensate for field perturbations during signal detection
(Zubarev and Makarov, 2013)	‘Deflector’	Minimising field perturbations from injection slot
(Grinfeld *et al.*, 2015)	‘Deflection electrode’	Single electrode to deflect ions during injection and also compensate for field perturbations during signal detection – With different voltages discussed for each usage case

One interesting point raised in (Perry *et al.*, 2009) is the possibility of using a single electrode to perform the function of both a ‘deflector’ during ion injection and a ‘field compensator’ when detection is taking place, this could explain why a number of papers refer to the two seemingly interchangeably.

In (Grinfeld *et al.*, 2015), field imperfections within the trapping volume are mitigated using a combination of altering the voltage on the ‘deflector’ electrode and modifying the gap between external electrodes. This allows quadro-logarithmic ion traps to access higher projected values of mass resolution, as great as several hundred thousand, by virtue of ion trajectories being closer to the ideal. However, the lack of published spectra exhibiting mass resolution of this order suggests that this proposed method of compensating for aberrations is difficult to implement in practice.

2.3.5 Space Charge Effects and Capacity

In orbital ion trapping mass spectrometry, coulombic repulsion forces between trapped ions, referred to as space charge effects, can have an adverse effect on different aspects of the recorded mass spectra, (Kharchenko *et al.*, 2012). Space charge effects can induce frequency shifts in ion harmonic motion, which will reduce the accuracy of mass measurements if unaccounted for. Simulation studies have found a linear dependence between the frequency shift and the number of trapped ions, suggesting this effect could be mitigated by calibration of the orbital ion trap if large ion populations are trapped. An experimental study from 2010 found an empirical calibration relationship to account for space charge induced frequency shifts in orbital ion traps, this relationship also shows linearity with the total number of trapped ions (Gorshkov *et al.*, 2010).

Space charge effects can also lead to degradation of harmonicity, which will reduce the mass resolution of acquired spectra. Collisions between trapped ion clouds can also limit the dynamic range of the orbital ion trap, as ion clouds become out of phase, meaning lower intensity signals are diminished in the mass spectrum. Space charge effects can be effectively minimised by reducing the size of the trapped ion population, this can be achieved by using external ion accumulation prior to injection, or by permitting only a small number of generated ions to enter the orbital ion trap, whilst the rest are transferred to an alternative mass analyser.

However, despite these deleterious effects, it should be noted the space charge capacity of an orbital ion trap is still quite high and compares favourably to FT-ICR instruments, with ion populations up to 10^6 shown to have been trapped (Makarov, Denisov, Lange, *et al.*, 2006). Indeed, ion populations of up to 5×10^6 can be achieved in commercial orbital ion trap instrumentation, where this value is limited by the storage capacity of intermediate ion traps, as will be discussed later (Gao *et al.*, 2015). The increased space-charge capacity compared to FT-ICR is due to multiple factors; the relatively large trapping volume in comparison to FT-ICR cells, the shielding of ion trajectories from one another by the internal electrode, and the independence of the trapping potential on m/z, (Makarov, 2000), (Perry *et al.*, 2008).

It is also worth considering that the advantage in maximum space charge capacity that orbital ion traps are reported to hold over FT-ICR cells will have been eroded to an

extent by increases in FT-ICR magnetic trapping field strengths. As discussed earlier, the maximum number of trapped ions increases quadratically with magnetic field strength, meaning modern FT-ICR cells are predicted to be able to accommodate ion populations in excess of 10^6, although this will only be the case for very high magnetic field strengths, such as the 21T instruments which have recently been developed (Vladimirov *et al.*, 2012), (Hendrickson *et al.*, 2015). Even in this case, a 21T FT-ICR cell could theoretically offer a space charge capacity of only 4.4×10^6 ions for two ion clouds with 0.3u mass difference at m/z 500. This value would still be slightly lower than the maximum reported for an orbital ion trap, despite the 21T FT-ICR being a unique instrument housed in a national-scale laboratory facility, National High Magnetic Field Laboratory in Florida (Hendrickson *et al.*, 2015), whereas orbital ion traps are comparatively inexpensive devices found in analytical laboratories all over the world.

2.3.6 Control Electronics

The precise control of voltages is crucial to the successful operation of a quadro-logarithmic ion trap, this is discussed to some extent in (Makarov, 2000) and (Hu *et al.*, 2006), amongst other papers. Hu et al. offer a timing diagram to show the total experiment duration and the delays between applications of electrode voltages, however a full delineation of the exact shape of voltage ramp applied to the internal electrode is not given. Due to the frequency of ion orbits, ~220kHz for ions of mass 100u, a single rotational orbit will take <5µs, meaning control of voltages in the order of microseconds will be required to coherently trap multiple ion packets as they enter the orbital ion trap.

2.3.7 Detection Electronics

As discussed, the mass-to-charge ratio of trapped ions is discerned from the frequency of their axial oscillations, achieved through image charge detection. For this to be a viable technique, a very sensitive, low-noise differential pre-amplifier is required to be mounted to the constituent external electrodes of the orbital ion trap in vacuum. FT-ICR and orbital ion trapping operate within similar frequency ranges, from approximately 10kHz to several MHz, meaning there is scope to use amplifiers designed for the older Fourier transform technique (Makarov, 2000). The literature on FT-ICR offers much useful research in this area, with pre-amplifiers requiring similarly

demanding performance having already been developed, (Mathur *et al.*, 2007), (Ubieto-Díaz *et al.*, 2009).

Reduction of amplifier noise is particularly important for achieving the ultimate sensitivity capability of an orbital ion trap. Some sources of noise which need to be combatted include (Letzter and Webster, 1970):

1. Thermal noise, also called Johnson-Nyquist noise, is caused by the thermal agitation of electric charge inside a conductor, first measured and described by Johnson and Nyquist, (Johnson, 1927), (Nyquist, 1928).
2. Electrical noise produced in the signal-handling amplifiers themselves, with noise at the front-end pre-amplifier most significant, manifesting as shot noise and flicker noise, first described by Schottky, (Schottky, 1926). Shot noise is caused by the random arrival of discrete electrons at semiconductor junctions. Flicker noise demonstrates a 1/f power spectrum, related to the flow of DC currents and surface defects altering conductivity.
3. Environmental noise, covering a multitude of possible sources, including; interference at the power frequency from other equipment in the laboratory, mechanical vibration causing capacitive changes in cabling, and ambient temperature fluctuations.
4. Statistical fluctuations which result from the quantized nature of any measured quantity.

Noise due to statistical fluctuations tends to be insignificant, and environmental noise can be effectively minimised with relatively simple measures such as appropriate grounding and shielding of amplifier inputs. This leaves thermal noise and amplifier electrical noise as the two primary noise sources which can be minimised by selecting an appropriately designed amplifier, (Letzter and Webster, 1970).

Further noise reductions could be pursued by conducting the experiment at cryogenic temperatures, to drastically reduce thermal noise, providing that all components are specified for this purpose. The detection electronics used in this research project will be discussed in greater detail in Chapter 4 and Chapter 6.

2.3.8 Data Processing

Data is recorded from an orbital ion trap in the form of a time-domain transient of detected image charge, which is then transformed into the frequency domain using a fast Fourier transform (FFT), when it can then be converted into a mass spectrum using the relationship between frequency and mass-to-charge ratio which governs axial oscillations of trapped ions, as discussed earlier. An example of this procedure is laid out in Figure 2.9.

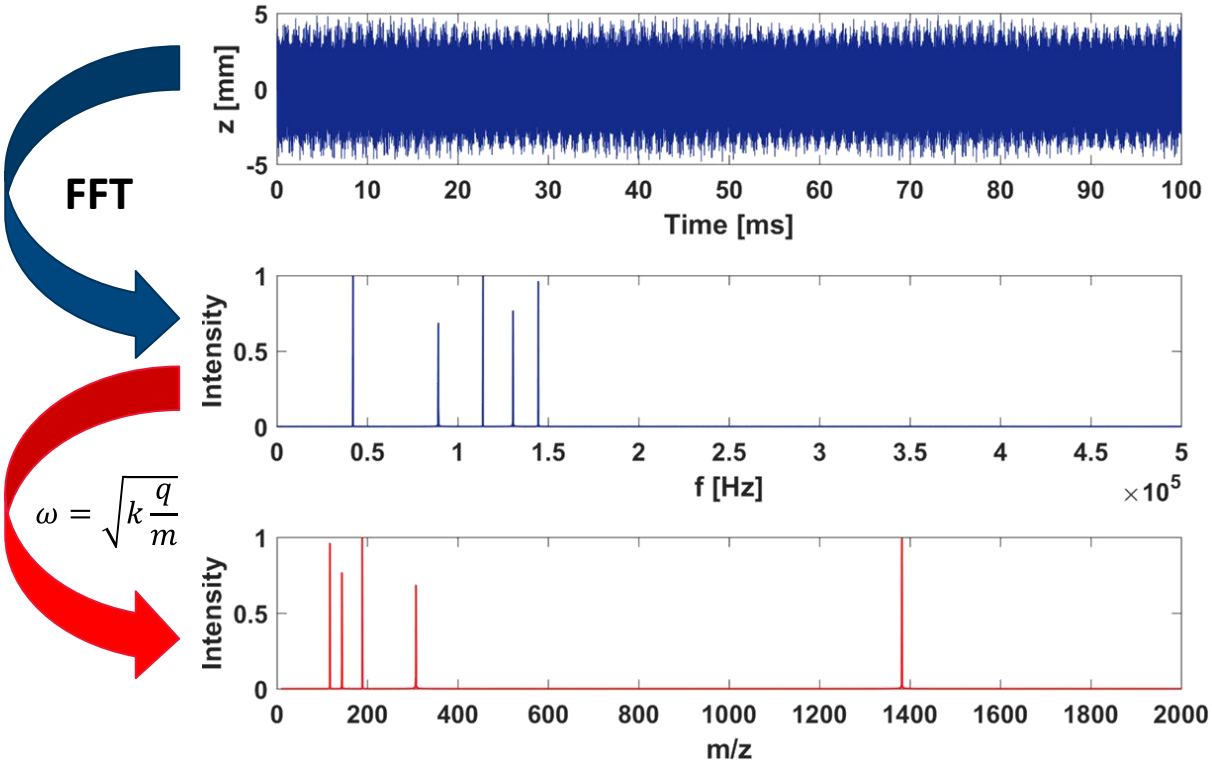

Figure 2.9 - Example data processing steps for orbital ion trapping time-domain transient recording

As can be seen, computational data processing is critical to producing a mass spectrum in Fourier-transform mass spectrometry. As such, methods to improve upon this data processing step are highly sought after. One such method which has been developed for orbital ion trapping FTMS is termed the 'enhanced Fourier Transform' or eFT, which utilises both magnitude and phase information to improve spectral resolution (Lange *et al.*, 2014b). In effect, the eFT is calculating the higher resolution absorption mode spectra, which accounts for phase shifts arising from ion injection, as discussed earlier in terms of FT-ICR instruments.

When the time domain data is transformed into the frequency domain, each data point is represented by a complex value, which can be described by phase and magnitude, or real and imaginary components. Typically in FTMS, a magnitude spectrum is produced which disregards the phase data, as is the case in the process shown in Figure 2.9. In an orbital ion trap, the starting phase of ion motion can be synchronised if ions are injected into the trap simultaneously at an axial offset, allowing excitation-by-injection. However, without any ion bunching to create a time-focus at the entrance to the trap, ions of different m/z will spread out during the time-of-flight of their injection into the trap, causing a phase difference upon excitation. This phase shift can be accounted for using equation (2.15), where t_{inj} refers to the time-of-flight of injection, and L_{eff} is the effective distance travelled during injection. This shows that the phase gained is actually mass independent (Lange *et al.*, 2014b).

$$\Delta\phi = \omega \times t_{\mathrm{inj}} = \frac{L_{\mathrm{eff}}}{\sqrt{2\mathrm{eV}/(m/q)}}\sqrt{\frac{q \cdot k}{m}} = \frac{L_{\mathrm{eff}}}{\sqrt{2\mathrm{eV/k}}} = \mathrm{const.} \qquad (2.15)$$

This allows the phase of ions to be calculated by tracing back their trajectories in the time domain, to a point of minimal phase difference, prior to injection. This step is achieved most accurately if detection begins as close to the time of injection into the trap as possible. Once the initial phase of ion motion is known, the absorption spectrum can then be calculated.

Absorption spectra allow a mass resolving power up to a factor of 2 higher than magnitude mode, as touched upon earlier, with gains in mass accuracy also achieved, (Marshall *et al.*, 1998), (Xian *et al.*, 2010). Greater advantages are gained for short transients, less than one second, as is typically the case in orbital ion trapping, as the detected signal does not decay significantly in this time, assuming that the base pressure in the chamber is sufficiently low to prevent ion collisions with residual gas particles.

Another aspect to consider when calculating ion phase for orbital ion trapping is that ions can be injected into the trapping volume in multiple packets, through the process of electrodynamic squeezing, described earlier. As such, a phase difference can arise between ions within successive packets if their injection is not precisely timed to

correspond to a whole number of rotations around the internal electrode. An alternative to this would be to allow only a single injection of ions per each data acquisition.

A similar method of broadband phase correction has been used to produce absorption mode spectra in FT-ICR mass spectrometry, (Xian *et al.*, 2010). It is difficult to account for phase shifts in FT-ICR spectra, as this phase shift can vary by more than 2π radians across even a single m/z value, making it problematic to deduce the relationship between phase and frequency across a wide frequency range.

A further advantage of absorption mode spectra is that peaks for ions of different m/z can be added together linearly, which is not the case for magnitude mode spectra. This means absorption mode offers a more accurate representation of relative intensities for a peak which contains multiple partially overlapping frequencies. For example, if two separate m/z peaks cannot be completely resolved, the resulting intensity in absorption mode spectra is a true representation of their summed intensity in the region of overlap, which would not be true if magnitude mode were used, (Xian *et al.*, 2010).

Other physical changes were also required to make implementing eFT feasible for an orbital ion trap, including improving voltage stability on the internal electrode, and better matching the capacitances of the two external electrodes. The effect of both changes is to allow detection to begin with as short a delay as possible after ion injection, by faster stabilisation of voltages after all ions are trapped (Lange *et al.*, 2014b).

2.3.9 Alternative Ion Trap Geometries

There is limited discussion in the literature of harmonic electrostatic ion traps with geometry different to the quadro-logarithmic profile described above, one such example is the so called Cassinian trap, (Köster, 2009), (Köster, 2015). The electric potential within a Cassinian trap is a combination of a quadrupolar and logarithmic-Cassinian potential, which permits multiple harmonic modes of ion trapping, including a one-dimensional trapping motion. This 1D motion represents the first time that non-orbital harmonic ion trapping had been theorised for an electrostatic ion trap. A 3D representation of a second order Cassinian trap, also denoted as a classical Cassinian trap, is shown in Figure 2.10. External electrodes are shown as a mesh, and the internal electrodes are depicted with a solid gradient.

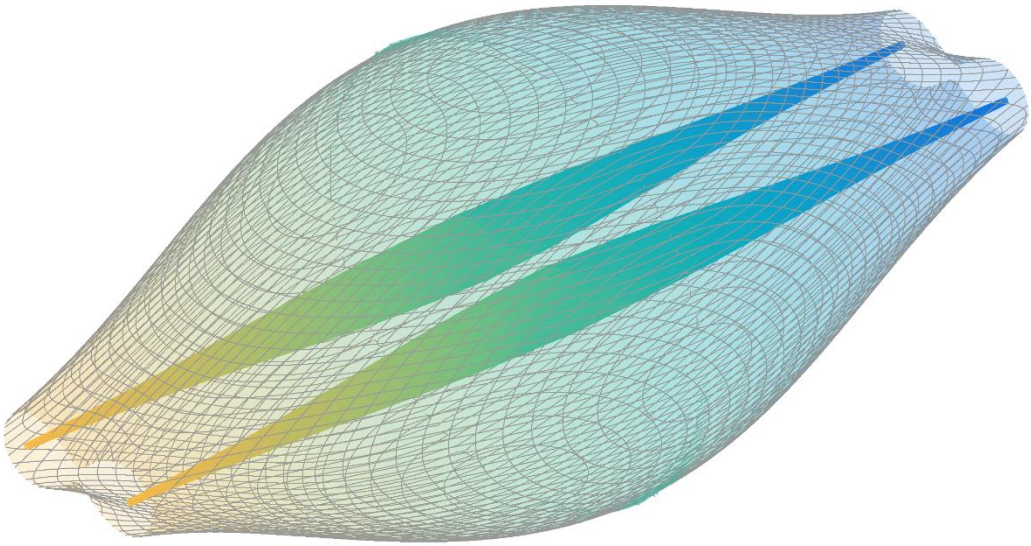

Figure 2.10 - 3D plot of classical Cassinian Trap. The grid represents the external electrodes, the solid gradients represents the internal electrodes.

In fact, the quadro-logarithmic potential used in orbital ion traps is simply a subset of the harmonic potential proposed as the general form of the Cassinian trap, and can be thought of as a first order Cassinian trap. One advantage of quadro-logarithmic traps over Cassinian traps is their rotational symmetry, which allows for more straightforward manufacturing using CNC lathes. A classical Cassinian trap would also require more complex alignment of its internal electrodes, as they are not located concentrically with the external electrode.

One advantage of Cassinian traps over standard geometry orbital ion traps is that ion motion within a Cassinian trap can begin with almost no initial kinetic energy. This means that ionisation of neutral species could take place within the trap itself, for example through laser ionisation. Ions created in such a way would immediately begin their harmonic trapping motion in the z-direction, with the frequency of this motion able to be used to find the ions' mass.

Cassinian traps are also able to accept a wide mass range of analyte ion, with a mass range of a factor of 13 demonstrated, and up to a factor of 50 theorised (Köster, 2009) (Köster, 2015).

As with an orbital ion trap, the mass resolving power that is achievable with a Cassinian trap will depend on the length of the recorded transient, the time for which ions are trapped harmonically. The most important factors which affect the maximum possible transient time, and thus mass resolving power, include; the vacuum within the ion trap,

the precision with which the electrodes have been machined, and the stability of voltages on the component electrodes.

2.3.10 Segmented Orbital Ion Traps

There has been some work towards simplifying the geometry of orbital ion traps, which would allow faster and cheaper manufacture of the component electrodes. Primarily, work in this avenue has focused on accurately replicating the ideal quadro-logarithmic field of an orbital ion trap by using a greater number of electrodes, which each have very simple geometry. One numerical study proposed two alternatives; the first replaced the internal electrode with 35 discs of equal radii, and the external electrode with 35 rings of equal radii, the second replaced both electrodes with stepped geometry approximating the ideal profile (Sonalikar *et al.*, 2015). At the time of writing, only numerical simulation studies have been undertaken to assess the performance of such devices, with significant deterioration expected compared to an ideal orbital ion trap, due to field imperfections induced by the simplified geometry.

A later study proposed a planar variant of an orbital ion trap, consisting of two parallel planar surfaces composed of multiple concentric ring electrodes (Sonalikar and Mohanty, 2017). Such a trap would allow electrostatic orbital ion trapping, in an approximately harmonic quadro-logarithmic field. As with the segmented traps from their 2015 paper, only numerical studies have been undertaken, so real-world performance cannot be definitively stated, although it is again expected that the trap would not be able to achieve as high mass resolution as an ideal orbital ion trap. Whilst both studies propose interesting ideas to simplify the orbital ion trap, which would certainly result in faster and less expensive manufacture, they do not at present represent a realistic proposition for high mass resolution analysis to be coupled with SIMS.

2.3.11 Coupling Orbital Ion Traps to different ion sources

Since its inception, there has been much work to couple orbital ion trapping to different ion sources, to allow its high mass resolution capability to be widely used. Initially, Matrix Assisted Laser Desorption/Ionisation (MALDI) was the preferred ionisation method for orbital ion trapping, (Makarov, 2000). Very briefly, MALDI is the process of generating ions from a sample through ionization with a laser, the sample is mixed with a matrix which absorbs the laser energy and assists the ionization process, the first

experiments of this type were proposed in 1985, and it has since developed into a widely used analytical technique, particularly in life sciences applications, including as a useful diagnostic tool in clinical microbiology (Karas *et al.*, 1985), (Oviano and Bou, 2019). As with SIMS, the choice of mass analyser is of critical importance to the performance of the analytical technique, with time-of-flight analysers having also become popular in the field of MALDI due to their speed of data acquisition, allowing high throughput instruments.

After initial proof-of-concept experiments with photo-ionisation systems, the first commercial orbital ion trap instrumentation utilised an electrospray ionisation (ESI) source. Coupling an orbital trapping mass analyser to a continuous ion source proved to be a significant technological challenge.

One issue that arises when coupling an orbital ion trap to any suitable ion source is the timing of injection pulses into the trap. For optimal trapping behaviour, the orbital ion trap requires a short pulse of ions to be injected into the trapping volume, with narrow spatial and temporal distribution. Once the ion packet enters the trapping volume, the internal electrode voltage can be ramped up to trap the entire packet of ions in orbit (Makarov, 2000). This poses a problem for continuous ion sources, as ions require accumulation outside of the orbital ion trap ahead of injection to ensure all ions can be analysed. Various solutions to this problem have been developed over the past two decades, typically comprising a ‘storage’ or ‘accumulation’ quadrupole ion trap, with ejection from such a trap able to provide the necessary packet of ions for orbital ion trapping. In 2003, a linear accumulation quadrupole was described, operating in RF-only mode to store ions before their pulsed axial ejection from the quadrupole into the orbital ion trap, (Hardman and Makarov, 2003) (Hu *et al.*, 2005).

Such linear quadrupole ion traps have been found to have a compromised space charge capacity, due to the fast extraction required for injection into the orbital ion trap, (Hardman and Makarov, 2003). The result of this is that Coulombic repulsion between accumulated ions cause a variation in ion kinetic energies and spatial distribution, which is detrimental to stable ion motion in the orbital trap. It was found that the space charge capacity of the linear quadrupole which could still achieve suitable focussing of ejected ions was lower than that of the orbital trap itself, meaning an upper limit was enforced on the number of ions which could be successfully injected in a single pulse, reducing the efficiency of acquiring mass spectra.

Due to these limitations, a curved quadrupole ion trap was proposed in 2006, which allows radial rather than axial ejection of ions, providing superior spatial and energy focussing of a large population of a wide mass range of ions at the point of injection into the orbital ion trap (Makarov, Denisov, Kholomeev, *et al.*, 2006). In this curved ion trap, given the name of 'C-trap', ions are retained along the curved axis of the trap by RF trapping plates, and two DC voltage end plates, whilst ion kinetic energy is reduced through collisional cooling with a background gas. Stored ions are then ejected radially in coherent packets by switching off the RF trapping voltages, and rapidly ramping a DC potential to create a potential gradient which forces the ions out of a slot in the 'front' electrode which has a tighter radius of curvature, further lenses are then present to focus ions at the entry to the orbital ion trap. Figure 2.11 shows a CAD representation of a 'C-trap' with approximated trajectories shown for a single pulse of ejected ions.

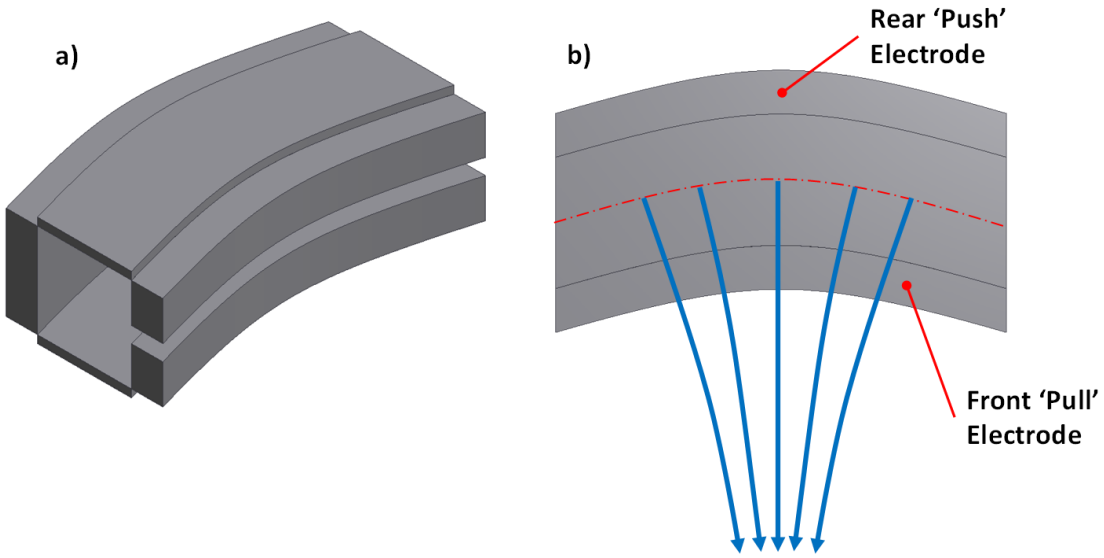

Figure 2.11 - CAD model of curved storage quadrupole 'C-trap', showing;
a) 3D perspective view to show ejection slot in 'front' electrode
b) Top-down view highlighting front and rear electrodes used for DC ejection of ions from the quadrupole, with example ejection trajectories superimposed

Following the development of the C-trap, a hybrid commercial instrument comprising a MALDI source and orbital ion trap was developed, which also utilised an intermediate linear ion trap to decouple the mass spectrometry from the ionisation process, (Strupat *et al.*, 2009). This decoupling serves a similar purpose to the buncher element of the Ionoptika J105, allowing for an increased duty cycle to be used during the ionisation

process, whilst a larger number of ions can be accumulated to make optimal use of space charge capacity the orbital ion trap.

When injecting ions into an orbital ion trap, it is desirable to have a small packet of ions which is narrowly distributed in terms of time, space, and kinetic energy, the C-trap is one way to achieve this. Another method would be to employ an ion buncher, as is present on the Ionoptika J105, which can achieve excellent temporal and spatial focussing of ions across a wide mass-range. However, if a system is being designed with two or more mass analysers, it is possible that an intermediate storage device is not required for an orbital ion trap, as ions which would need to be stored whilst the orbital ion trap is in the detection phase of its operation could instead be directed to the second mass analyser to maximise the efficiency of the system.

2.3.12 Orbital ion trap coupled to SIMS

At the time of writing there is limited published literature documenting the successful coupling of a quadro-logarithmic orbital ion trap with a secondary ion mass spectrometer.

There is known to be a comparable project undertaken as a collaboration between NPL, IONTOF and Themo Fisher, as is mentioned in (Hua *et al.*, 2016), with the first results from their hybrid instrument discussed in (Pirkl, Moellers, Arlinghaus, Kollmer, Niehuis, Horning, Passarelli, Havelund, Rakowska, Race, Gilmore, *et al.*, 2016). The purpose of this collaborative project is to combine the IONTOF TOF-SIMS V instrument with Thermo Fisher's Q Exactive HF, an Orbitrap mass analyser of high-field geometry, designed for high resolution chemical analysis and typically coupled with MALDI or electrospray ion sources. The instrument resulting from this collaboration is referred to as the 3D OrbiSIMS. To an extent, this work is building on (Hardman and Makarov, 2003), in which a Thermo Fisher Orbitrap is coupled with a continuous electrospray ionization source, achieving mass resolution of the order of 150,000 for low mass (<200u) ions.

Inevitably there are compromises when connecting self-contained instruments originally designed to operate differently. In contrast, the aim of this research project was to develop a new mass analyser closely-integrated with an existing Ionoptika J105 SIMS instrument, and indeed our analyser was designed and constructed here at Newcastle University while awaiting delivery of said instrument from the manufacturer.

One of the key challenges arising when attempting to couple a mass analyser of this type to a continuous ion source is the precise timing required to trap ions; the internal electrode voltage needs to be ramped as ions enter the trap and have velocity tangential to the internal electrode, meaning ions can only be trapped in tightly bunched packets (a few millimetres in length) (Hardman and Makarov, 2003). Efficiency of ion injection can be improved with the use of additional electrodes as discussed earlier.

Results from the NPL, IONTOF, and Thermo Fisher collaboration have demonstrated mass spectral imaging data from orbital ion trapping SIMS with 2µm spatial resolution and mass resolution of 240,000 at 200 m/z, with a 512ms transient detection period in the orbital ion trap (Passarelli *et al.*, 2017).

The 3D OrbiSIMS project is based on an IONTOF pulsed time-of-flight SIMS instrument, there are some advantages to be gained by using a quasi-DC SIMS instrument, such as the Ionoptika J105, many of which have already been discussed in this chapter. The decoupling of the sputtering event from the timing of the mass spectrometry allows the use of larger polyatomic primary ion clusters, with water clusters up to sizes of $(H_2O)_n$ where n = 25,000 and n = 40,000 for energies of 40keV and 70keV respectively, having been demonstrated on the J105, (Sheraz née Rabbani *et al.*, 2019), as opposed to argon clusters up to only Ar_{3000} as with the 3D OrbiSIMS, (Passarelli *et al.*, 2017). Such massive polyatomic primary ion sources achieve improved secondary ion yields, particularly for higher masses, as they are able to desorb large biomolecules intact. Identification of these molecules would benefit enormously from the high mass resolving power of an orbital ion trap.

As already discussed, quasi-DC SIMS instruments also offer much faster analysis, as there is a much increased duty cycle without the need to pulse the primary beam. This is particularly beneficial for depth profiling experiments carried out above the static SIMS limit, with the J105 able to deliver ion doses as high as $1 \times 10^{15}\ \mathrm{ion \cdot cm^{-2}}$ over a $100 \times 100\ \mu m^2$ area in as little as 30 minutes, with a 10pA primary beam current, comparable analysis with a pulsed primary ion source would take over a month of continuous operation with 50 ns primary ion pulses running at 10kHz, (Fletcher *et al.*, 2008).

In terms of the 3D OrbiSIMS, the Bi LMIG primary ion source is able to operate in a quasi-continuous mode to speed up orbital ion trap spectrometry, however this primary

ion source would be best suited to inorganic analysis, rather than the analysis of complex biological systems, as discussed earlier in 2.2.6.

Another advantage of orbital ion trapping coupled to a SIMS instrument is the potential for higher order tandem mass spectrometry, MS^n, by way of tandem mass spectrometry in time, as mass analysis takes place in the orbital ion trap whilst retaining the analyte ions. As such, ions can be ejected from the trap after initial mass analysis for fragmentation, before subsequent re-injection for analysis of the product ions.

In summary, there is certainly a niche to be exploited in SIMS by instrumentation which can combine high spatial and high mass resolution analysis. Coupling an orbital ion trap to an existing SIMS instrument represents one way to achieve this aim, whilst also being an efficient solution in terms of the cost of the analyser, and the additional space required. The improved analytical capabilities would be further enhanced by the addition of modern high energy water cluster polyatomic primary ion sources, which would increase the ion yield of the high mass species that would benefit most from increased mass resolution.

Chapter 3. Mathematical Formulation

3.1 Potential Distribution in Orbital Ion Trap

The potential distribution of the electrostatic field within the orbital ion trap is described by equation (3.1) as laid out in (Makarov, 2000).

$$U(r,z) = \frac{k}{2}\left(z^2 - \frac{r^2}{2}\right) + \frac{k}{2}(R_m)^2 \cdot \ln\left(\frac{r}{R_m}\right) + C \qquad (3.1)$$

A graphical representation of this potential distribution was produced in SIMION, a software package used to calculate both 2D and 3D electrostatic or magnetic fields, (SIS, 2015), the resulting potential field is shown in Figure 3.1.

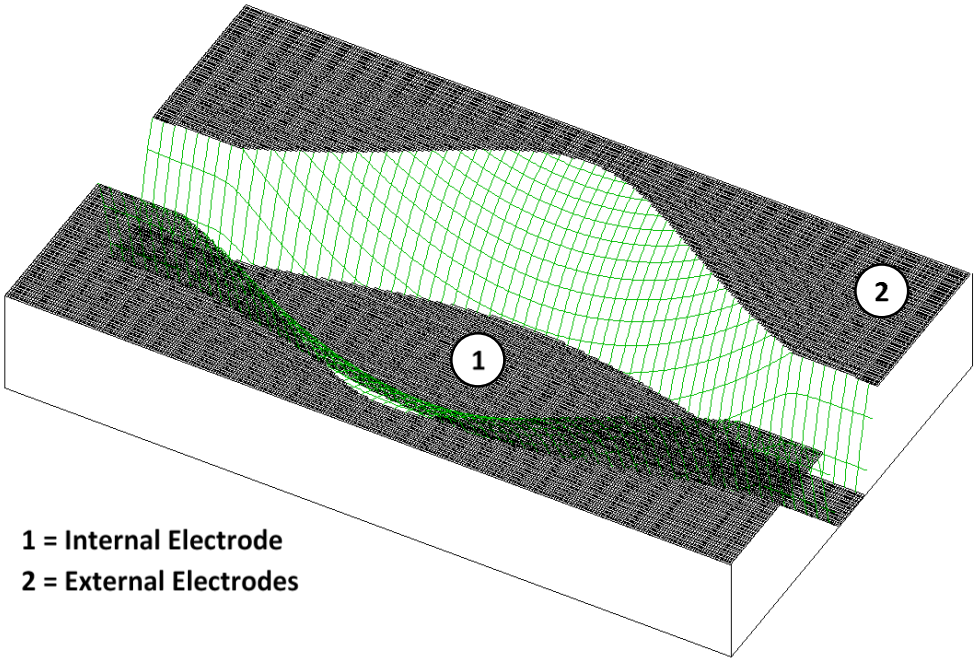

Figure 3.1 - Potential energy distribution in an orbital ion trap, produced in SIMION 8.1.

The component electrodes of the orbital ion trap are defined by equation (3.2), (Makarov, 2000).

$$z(r) = \sqrt{\frac{r^2}{2} - \frac{\left(R_{1,2}\right)^2}{2} + (R_m)^2 \cdot \ln\left(\frac{R_{1,2}}{r}\right)} \qquad (3.2)$$

With R_1 and R_2 referring to the maximum diameters of the internal and external electrodes respectively. The following boundary conditions are set, defining the internal electrode at some voltage, $-U$, and the external electrodes at virtual ground:

$$U(R_1, z) = -U_{\text{int}} \tag{3.3}$$

$$U(R_2, z) = 0 \tag{3.4}$$

From equations (3.1) and (3.4), it follows that:

$$C = -\frac{k}{2}\left[z^2 - \frac{(R_2)^2}{2} + (R_m)^2 \cdot \ln\left(\frac{R_2}{R_m}\right)\right] \tag{3.5}$$

A relationship between the applied voltage, $-U$, and the field curvature, k, can then be found, by substituting (3.3) and (3.5) into (3.1), and re-arranging to give the following, as per (Kharchenko *et al.*, 2012):

$$k = \frac{2U_{\text{int}}}{(R_m)^2 \cdot \ln\left(\frac{R_2}{R_1}\right) - \frac{1}{2}({R_2}^2 - {R_1}^2)} \tag{3.6}$$

Ion energy tangential to the internal electrode, E_ϕ, is related to field curvature by equation (3.7) for circular orbits, (Makarov, 2000), where R_o is the radius of orbit:

$$E_\phi = \frac{k}{4}\,({R_m}^2 - {R_o}^2) \tag{3.7}$$

Combining equations (3.6) and (3.7) gives the following relationship between ion energy and internal electrode voltage to achieve circular orbital trajectories:

$$U_{\text{int}} = \frac{1}{2}\left[{R_m}^2 \cdot ln\left(\frac{R_2}{R_1}\right) - \frac{1}{2}({R_2}^2 - {R_1}^2)\right] \cdot \frac{4E_\phi}{{R_m}^2 - {R_o}^2} \tag{3.8}$$

Equation (3.8) allowed internal electrode voltages to be evaluated for use in SIMION particle simulations of ion trapping, with ions initialised within the trapping volume between the component electrodes, this will be discussed in greater detail in the Simulation chapter of this thesis.

The equation of motion in the axial direction, for which ion motion is decoupled from radial components of motion, is derived in equations (3.9) to (3.14), where (3.9) and (3.10) are Newton's second law of motion and the Lorentz force equation respectively. The derivation follows the simplified example of a single charged particle in a uniform electrostatic field, shown in Figure 3.2.

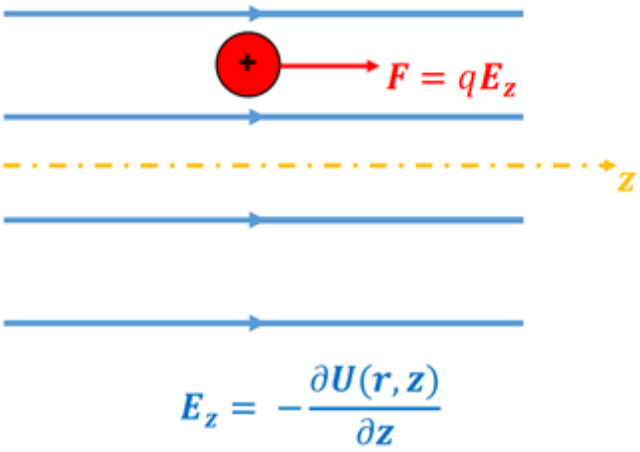

Figure 3.2 - Charge in uniform electric field

$$\boldsymbol{F} = m\boldsymbol{a} \Rightarrow \boldsymbol{F_z} = m\ddot{\boldsymbol{z}} \tag{3.9}$$

$$\boldsymbol{F} = q\boldsymbol{E} + q\boldsymbol{v} \times \boldsymbol{B} \tag{3.10}$$

$$\boldsymbol{B} = 0 \therefore \boldsymbol{F_z} = q\boldsymbol{E_z} \tag{3.11}$$

$$\boldsymbol{E}_z = -\frac{\partial \boldsymbol{U}(\boldsymbol{r},\boldsymbol{z})}{\partial z} = -\frac{k}{2}(2\boldsymbol{z}) = -k\boldsymbol{z} \tag{3.12}$$

Combining equations (3.9) and (3.11) gives:

$$\boldsymbol{F_z} = m\ddot{\boldsymbol{z}} = q\boldsymbol{E_z} = -qk\boldsymbol{z} \tag{3.13}$$

$$\therefore \ddot{\boldsymbol{z}} = -\frac{q}{m}k\boldsymbol{z} \tag{3.14}$$

The solution to the linear homogeneous second-order differential equation (3.14) is of the form shown in equation (3.15).

$$z(t) = A\cos\left(\sqrt{\frac{q}{m}k} \cdot t\right) + B\sin\left(\sqrt{\frac{q}{m}k} \cdot t\right) \tag{3.15}$$

Where the axial oscillation frequency is given as:

$$\omega = \sqrt{\frac{q}{m}k} \tag{3.16}$$

The constants, A and B, can be found using the following initial conditions:

$$\begin{aligned} z(0) &= z_0 \\ \dot{z}(0) &= \dot{z}_0 \end{aligned} \tag{3.17}$$

Alongside the expression for kinetic energy in the axial direction:

$$qE_z = \frac{1}{2}m\dot{z}_0{}^2$$
$$\therefore \dot{z}_0 = \sqrt{\frac{2qE_z}{m}} \tag{3.18}$$

Where the first differential of equation (3.15) is:

$$\dot{z}(t) = -A\omega\sin(\omega t) + B\omega\cos(\omega t) \tag{3.19}$$

Therefore:

$$A = z_0$$
$$B = \frac{\dot{z}_0}{\omega} = \frac{\sqrt{\frac{2qE_z}{m}}}{\sqrt{\frac{q}{m}k}} = \sqrt{\frac{2E_z}{k}} \tag{3.20}$$

Thus, the exact analytical solution to axial motion is:

$$z = z_0\cos(\omega t) + \sqrt{\frac{2E_z}{k}}\sin(\omega t) \tag{3.21}$$

3.2 Parametric Excitation

As discussed in the introduction to this report, a new method of ion excitation has been developed; using the technique of parametric excitation. This is the process of mass selectively exciting ion axial oscillation after injection at the mid-plane of the orbital ion trap, z=0, through the application of an RF voltage to the internal electrode. Axial oscillation is promoted by the contraction and expansion of the axial pseudo-potential. The frequency of ion axial oscillation can be found using (3.16). As discussed in (Makarov, 2000), when an additional RF voltage is applied to the internal electrode, axial ion motion can be modelled using the canonical Mathieu equation, (3.22), as presented in (March, 1997) in reference to RF quadrupole ion traps. Where, ζ is a dimensionless parameter, a_u and q_u are dimensionless variable parameters.

$$\frac{d^2u}{d\zeta^2} + [a_u - 2q_u\cos(2\zeta)]u \tag{3.22}$$

Relevance to the orbital ion trap can be discerned by making the following substitutions, where z represents the co-ordinate axis of the orbital ion trap and Ω is the frequency of excitation.

$$u = z; \quad \zeta = \frac{\Omega t}{2} \tag{3.23}$$

Using the chain rule:

$$\frac{d^2z}{dt^2} = \frac{d^2z}{d\zeta^2}\left(\frac{d\zeta}{dt}\right)^2 + \frac{dz}{d\zeta}\cdot\frac{d^2\zeta}{dt^2} = \frac{d^2z}{d\zeta^2}\left(\frac{\Omega}{2}\right)^2 + \frac{dz}{d\zeta}\cdot 0 = \frac{\Omega^2}{4}\frac{d^2z}{d\zeta^2} \tag{3.24}$$

Substituting equations (3.23) and (3.24) back into equation (3.22) and rearranging, gives:

$$\frac{d^2z}{dt^2} = -\frac{\Omega^2}{4}[a_u - 2q_u\cos(\Omega t)]u \tag{3.25}$$

If the applied excitation voltage has frequency, Ω, and amplitude, P, then the following derivation can be followed, where U_{static} is the potential defined in equation (3.1), and μ is the amplitude ratio of excitation and static voltages.

$$U_{RF}(r,z) = U_{\text{static}}(r,z) - P(r,z)\cos(\Omega t) \tag{3.26}$$

$$\text{Let } \mu = \frac{P(r,z)}{U(r,z)} \tag{3.27}$$

$$U_{RF}(r,z) = U_{\text{static}}(r,z) - \mu\, U_{\text{static}}(r,z)\cos(\Omega t) \tag{3.28}$$

$$U_{RF} = U_{\text{static}}(1 - \mu\cos(\Omega t)) \tag{3.29}$$

$$\frac{\partial U_{RF}}{\partial z} = kz(1 - \mu\cos(\Omega t)) \tag{3.30}$$

The electric field is then:

$$E_z = -\frac{\partial U(r,z)}{\partial z} = [\mu\cos(\Omega t) - 1](kz) \tag{3.31}$$

It then follows that force is evaluated as before:

$$F_z = m\ddot{z} = qE_z = -qkz[1 - \mu\cos(\Omega t)] \tag{3.32}$$

And the equation of motion is thus:

$$\frac{d^2z}{dt^2} = -\omega^2 z(1 - \mu\cos(\Omega t)) \tag{3.33}$$

This allows the Mathieu parameters, a_u and q_u, to be defined as shown in (3.34), by comparing equation (3.33) to (3.25).

$$a_u = 4\left(\frac{\omega^2}{\Omega^2}\right); \quad q_u = 2\mu\left(\frac{\omega^2}{\Omega^2}\right) \tag{3.34}$$

The mass selective nature of parametric excitation can be seen as a result of the dependence of the Mathieu parameters on ω, the natural frequency of ion oscillation,

which itself is dependent only on the mass-to-charge ratio of a trapped analyte ion. Parametric resonance is found at twice the natural frequency of axial oscillation, that is to say; $\Omega = 2\omega$, resulting in values of $a_u = 1$ and $q_u = \frac{\mu}{2}$. Under such parametric excitation conditions, the amplitude of axial oscillations grows exponentially, as will be demonstrated later in this report through simulations. This unbounded oscillation growth can be used to promote larger amplitude ion oscillations for the purpose of detection, or indeed to eject ions from the trap axially, where secondary electron multipliers could be used to detect ion impact upon ejection.

It is useful to note at this point that the mathematical analysis undertaken here does not take into account any mechanism for energy loss, assuming a perfect vacuum where no such damping would be present. Obviously, this is an impossible ideal case, in reality there would be damping provided by space charge repulsion between like charges, as well as collisions between ions and residual gas particles. The validity of a zero damping assumption could be investigated through simulation, where space charge and collisional effects could be introduced. A more rigorous validation of the model would come from experimental data, where the decrease in ion axial oscillation over time could be measured, and used to calculate a damping coefficient which could be introduced into the analytical treatment of ion motion.

Parametric excitation cannot be achieved if the initial amplitude of oscillation is zero, as there would be no initial oscillation to amplify, this would result in the amplitude remaining at zero. In the case of the orbital ion trap this means that any ions injected at z=0 must have some component of velocity in the z-direction for parametric excitation to have the desired effect. In an experimental setup it would be expected that ions would have some axial component of velocity regardless of their initial conditions. This would likely either be due to electric field imperfections present in the manufactured orbital ion trap, or non-ideal injection conditions, such as ions entering the trapping volume at a range of angles as opposed to a single ideal value.

3.2.1 Stability Diagrams

When discussing parametric excitation in the form of the Mathieu equation, it is useful to plot stability diagrams, denoting boundaries within which the amplitude of axial oscillations will remain stable, and outside of which axial oscillation amplitude will grow unbounded and are thus unstable, this being the useful region for parametric

excitation. The typical stability diagram found in the literature is shown in Figure 3.3, (Makarov, 2000).

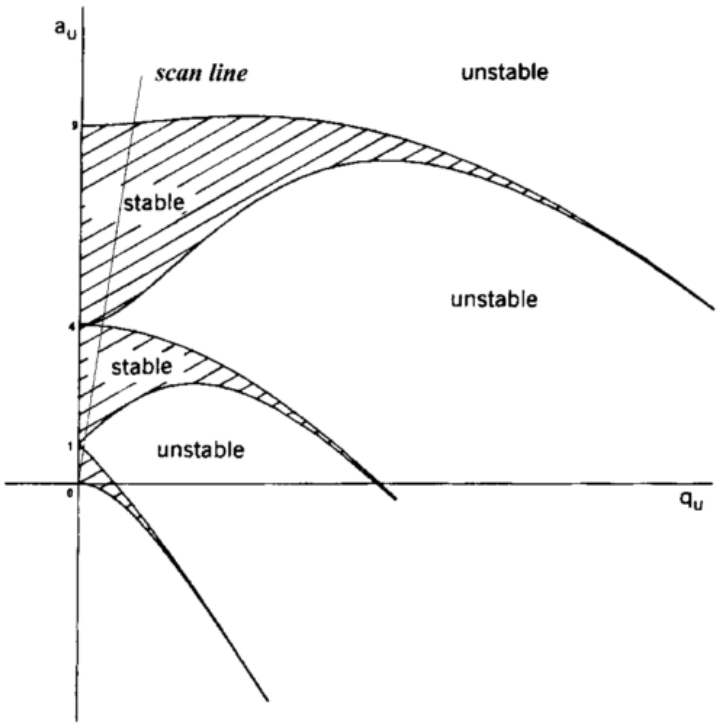

Figure 3.3 - Mathieu stability diagram (Makarov, 2000)

Another method of analytically determining the stability of ions under parametric excitation is to consider which terms in the equations of motion give rise to resonant behaviour. This is laid out in the following equations**,** with treatment similar to that of (Harish *et al.*, 2008).

Initially, assume that the potential field within the orbital ion trap is a superposition of harmonic and DC potentials, where k_p is the time dependent field curvature in the form of a general periodic, and u_0 is the DC component of potential, and u_r and u_r^* the components due to the excitation voltage.

$$\mathrm{U(r,z)} = k_p\left[z^2 - \frac{r^2}{2} + {R_m}^2 \ln\left(\frac{r}{R_m}\right)\right]$$

$$\text{Where} \qquad (3.35)$$

$$k_p = \frac{1}{2}\left[u_0 + \sum_{r=1}^{\infty} u_r e^{ir\omega t} + \sum_{r=1}^{\infty} u_r^* e^{-ir\omega t}\right]$$

This leads to a modification of the axial equation of motion for ions trapped in this field, from (3.14) to that shown in (3.36).

$$\ddot{z} + \frac{2qk_p}{m} z = 0 \tag{3.36}$$

This can then be modified to include a damping term, ζ proportional to the axial velocity:

$$\ddot{z} + 2\zeta\omega_n\dot{z} + \frac{2qk_p}{m} z = 0 \tag{3.37}$$

As the excitation voltage will be small compared to the DC potential, meaning $u_r \ll u_0$, it can be assumed that the effect of damping will be small, with $2\zeta \ll 1$, the small perturbation substitutions of $2\zeta = 2\varepsilon\eta$, and $\varepsilon V_r = u_r/u_0$ can be made, along with the substituting natural frequency under electrostatic trapping ${\omega_n}^2 = qk/m$, to yield (3.45). Where η represents the adjusted damping ratio, and ε the perturbation parameter.

$$\ddot{z} + 2\varepsilon\eta\omega_n\dot{z} + {\omega_n}^2\left[1 + \varepsilon\left(\sum_{r=1}^{\infty} V_r e^{ir\omega t} + \sum_{r=1}^{\infty} V_r^* e^{-ir\omega t}\right)\right] z = 0 \tag{3.38}$$

Perturbation analysis of the form shown in (Gallacher *et al.*, 2006) can now be followed, using the multiple scales expansion method, to give a solution in terms of the slow and fast time scales, where $\bar{t} = \varepsilon t$, $\hat{t} = t + O(\varepsilon^2)$. A full derivation of the solution in the form shown in (3.39) can be found in Appendix A.

$$z(\bar{t}, \hat{t}) = z^{(0)}(\bar{t}, \hat{t}) + \varepsilon z^{(1)}(\bar{t}, \hat{t}) + O(\varepsilon^2) \tag{3.39}$$

This leads to a definition of stability, (3.40), based on two parameters; ν, the ratio of the AC excitation voltage amplitude to the DC internal electrode voltage, and Λ, the difference between the excitation frequency and the natural frequency of a given ion's axial oscillation. Figure 3.4 shows the dependence of Λ on ν, for an excitation frequency of ~156kHz, which would correspond to a target ion mass of 100u, for ions of energy 101eV, trapped by an internal electrode voltage of 175V, with a damping ratio of $\zeta = 10^{-3}$ chosen. It can be seen that there exists a critical voltage ratio, ν_{crit}, below which no parametric excitation is possible as all ion trajectories are in the stable region, this is shown as the point at which the bifurcation begins.

$$\Lambda = \pm\sqrt{{\omega_n}^2\nu^2 - 2({\zeta\omega_n}^2)} \tag{3.40}$$

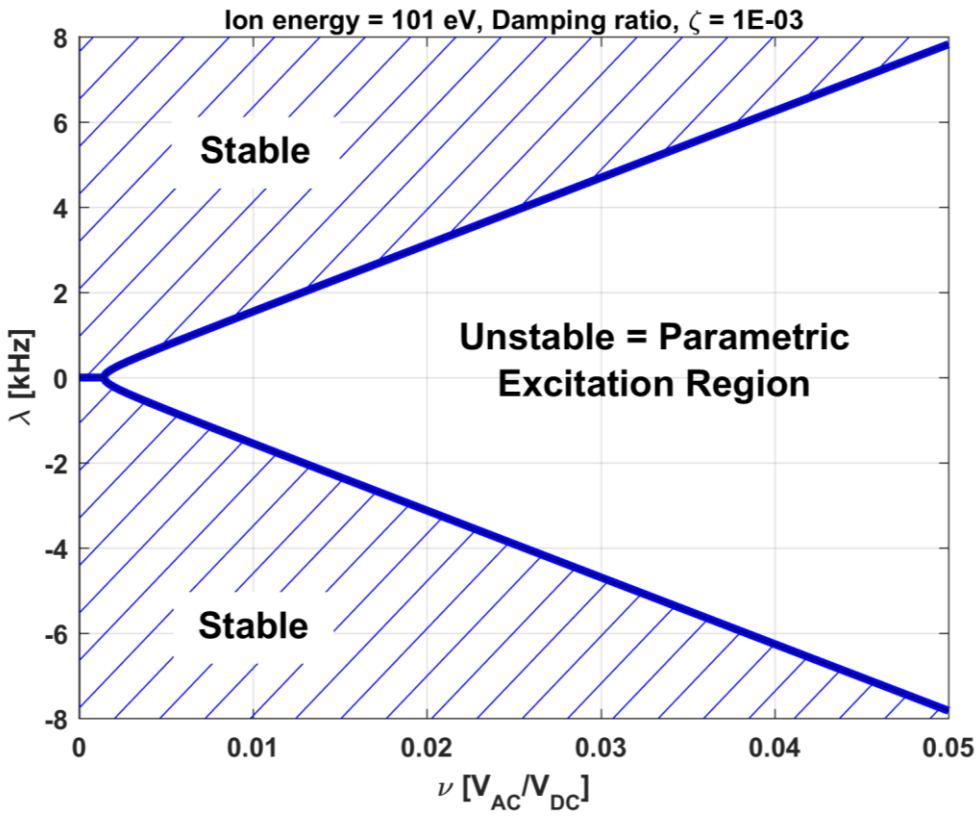

Figure 3.4 - Stability diagram, showing the regions of stability for ions with natural frequencies which differ by Λ from the excitation frequency, against ν, the ratio of AC to DC voltages, for parametric excitation of ions with energy 101eV, trapped by a 175V internal electrode voltage, with a target excitation mass of 100u, corresponding to an excitation frequency of 156.529kHz.

The frequency parameter, Λ, can readily be transformed into a vector of ion masses, using the relationship between ion mass and oscillation frequency of equation (3.16). Doing so gives the stability plot for a range of masses when a particular target mass is excited, as shown in Figure 3.5. A cropped version of the same plot is given in Figure 3.6, showing the region of stability for low voltage ratios, and highlighting the critical voltage ratio of 1.4E-3. This low critical voltage ratio means that parametric excitation can be achieved for very low amplitude AC voltages, requiring only 0.14% of the amplitude of the DC voltage on the internal electrode, in this case a DC voltage of 175V is applied, so the minimum AC voltage amplitude needed to initiate parametric excitation would be <0.25V.

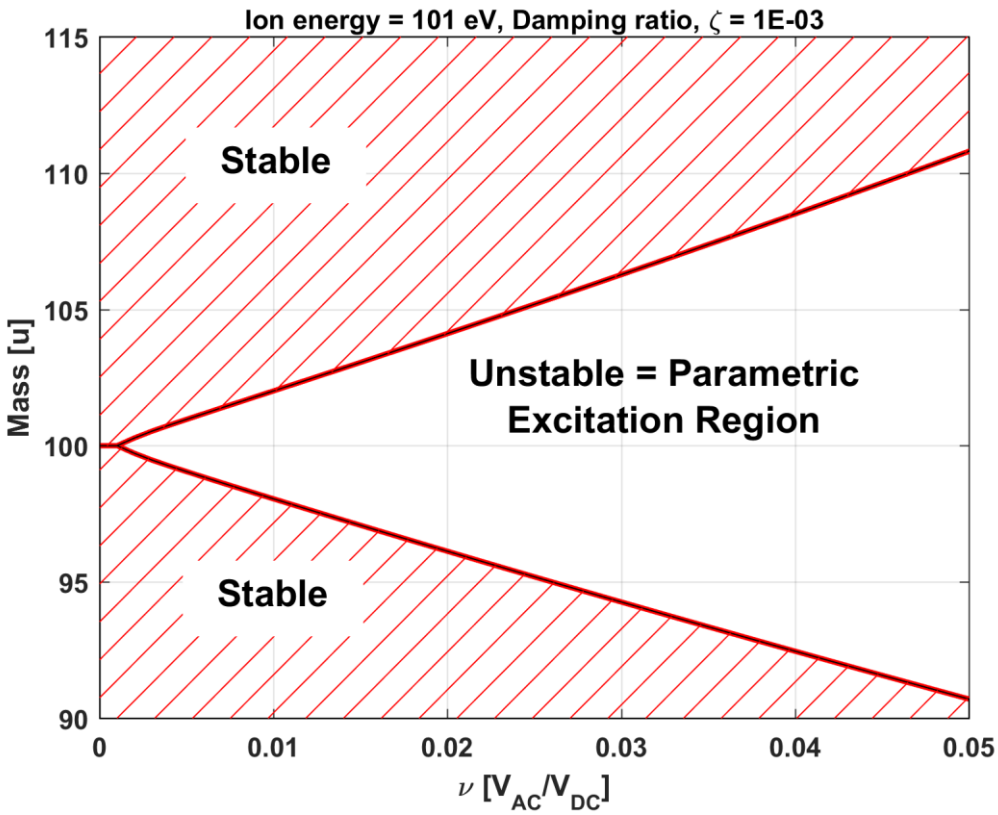

Figure 3.5 - Stability diagram, for parametric excitation of ions with energy 101eV, trapped by a 175V internal electrode voltage, with a target excitation mass of 100u, corresponding to an excitation frequency of 156.529kHz.

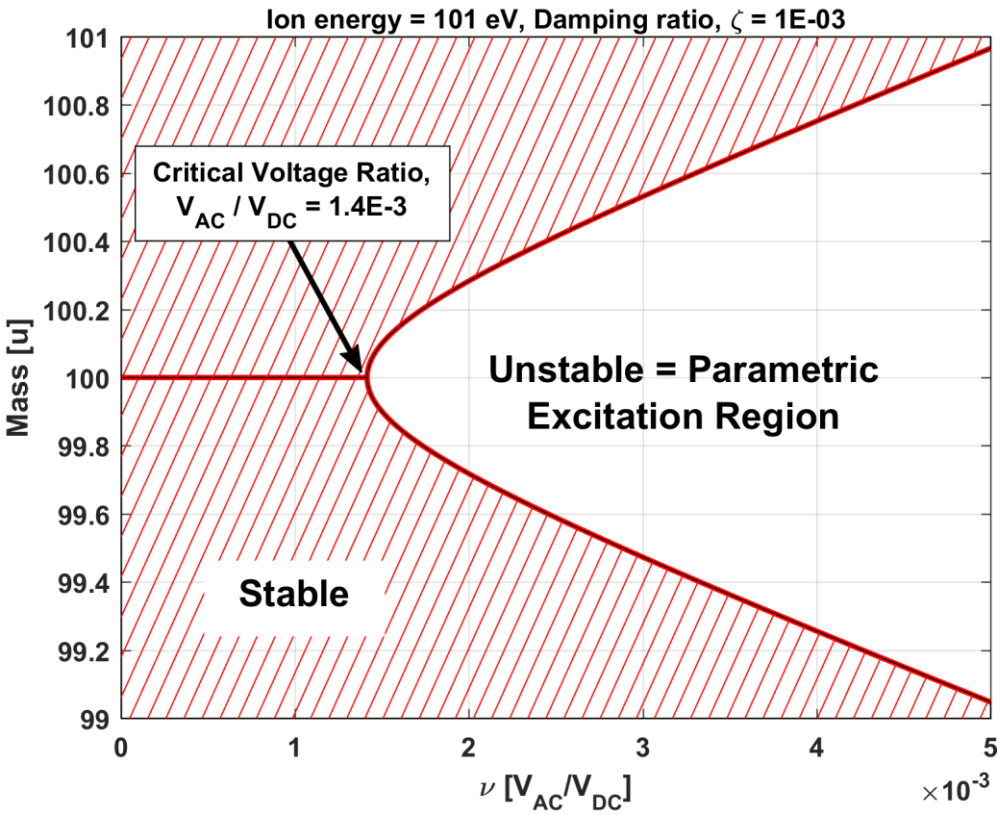

Figure 3.6 - Cropped stability diagram, to highlight critical voltage ratio, with 100u target mass undergoing parametric excitation, for parametric excitation of ions with energy 101eV, trapped by a 175V internal electrode voltage, with a target excitation mass of 100u, corresponding to an excitation frequency of 156.529kHz.

The value of the critical voltage ratio, ν_{crit}, is independent of ion energy and the applied DC voltage. From (3.40) it can be found that in fact, the critical voltage ratio is dependent only on the damping ratio, as shown in the derivation outlined in equation (3.41), by setting $\Lambda = 0$ in (3.40)

$$\begin{aligned} 0 &= \pm\sqrt{\omega_n{}^2|\nu_{\text{crit}}|^2 - 2(\zeta\omega_n)^2} \\ 0 &= \omega_n{}^2|\nu_{\text{crit}}|^2 - 2(\zeta\omega_n)^2 \\ |\nu_{\text{crit}}|^2 &= 2\zeta \\ \nu_{\text{crit}} &= \sqrt{2}\cdot\zeta \end{aligned} \tag{3.41}$$

3.2.2 Stored Waveform Inverse Fourier Transform

Parametric excitation is mass selective, in that the applied excitation frequency is chosen to be twice the natural oscillation frequency of the ions to be excited, where this frequency is dependent only on their mass. Ions of different masses can be simultaneously excited through the application of multiple different excitation frequencies, corresponding to specific masses for excitation.

The process of exciting different masses simultaneously is analogous to the process termed Stored Waveform Inverse Fourier Transform (SWIFT) in Fourier Transform Ion Cyclotron Resonance (FT-ICR) experiments, in which an excitation frequency sweep is generated from an inverse Fourier transform of the frequencies of interest, as described in (Cody *et al.*, 1987), (Scigelova *et al.*, 2011). SWIFT can be used to eject unwanted masses, similar to the mass-selective instability operation of orbital ion traps, discussed in the Literature Survey.

An advantage of coupling an orbital ion trap to an existing SIMS instrument is that the masses of interest can be found quickly at lower mass resolution using the J105 ToF analyser, this information can then be used to selectively operate the orbital ion trap at higher mass resolution. In the case of SWIFT, a program could be devised to take the inverse Fourier transform of the mass spectrum gathered using the ToF, which could then be fed into the orbital ion trap as a parametric excitation waveform to analyse only the ions of interest. This could be achieved quickly if the amplitude of the excitation waveform were to be controlled to move into the unstable region of the stability diagram, promoting unbounded amplitude growth in ions' axial oscillations.

3.3 Alternative Ion Trap Geometries

Alternative style ion trap geometries are also interesting to consider, both from a mathematical, and instrumental standpoint. As discussed in the Chapter 2 the Cassinian ion trap geometry is one such device, being a harmonic electrostatic ion trap where the potential distribution can be described as a combination of quadrupole and logarithmic-Cassinian potentials, (Köster, 2009). In Cartesian co-ordinates, such a potential distribution can be described as laid out in equation (3.42), where U_{Cassini} is the voltage between the internal and external electrodes of the ion trap, A_{ln} and A_{quad} are dimensionless parameters representing the proportion of the potential which is due

to the logarithmic-Cassinian potential and quadrupolar potential respectively, defined in (3.43), a_i is the internal electrode radius, a_o is the external electrode radius, b is the radial distance from the centre of the Cassinian trap to the centre of the internal electrodes, d is a constant related to a DC voltage offset, and B is a constant.

$$U(x,y,z) = U_{\text{Cassini}}\left[\frac{\ln(((x^2+y^2)^2 - 2b^2(x^2-y^2)+b^4))/{a_i}^4)}{A_{\ln}} + \frac{2z^2-(1-B)x^2-By^2}{A_{\text{quad}}} + d\right] \tag{3.42}$$

$$A_{\ln} = \ln\left(\frac{{a_o}^4}{{a_i}^4}\right)$$
$$A_{\text{quad}} = 2({a_o}^2 - {a_i}^2) \tag{3.43}$$

This can be rearranged with respect to z, to yield a function which describes the geometry of the Cassinian trap electrodes, if $U(x,y,z)$ is replaced by the potential of the electrodes, as shown in equation (3.44).

$$z(x,y) = \left[\frac{1}{2}\left((2-B)x^2 - By^2 + A_{\text{quad}}\left(\frac{U}{U_{\text{Cassini}}} - d - \frac{\ln((x^2+y^2)^2 - 2b^2(x^2-y^2)+b^4))/{a_i}^4)}{A_{\ln}}\right)\right]^{\frac{1}{2}} \tag{3.44}$$

This represents a second-order, or classical, Cassinian trap, where a_i controls the radii of the internal electrodes, and b controls the separation of these electrodes. If $b > a_i$ then a second-order trap will have two spatially separated internal electrodes, as shown in Figure 3.7.

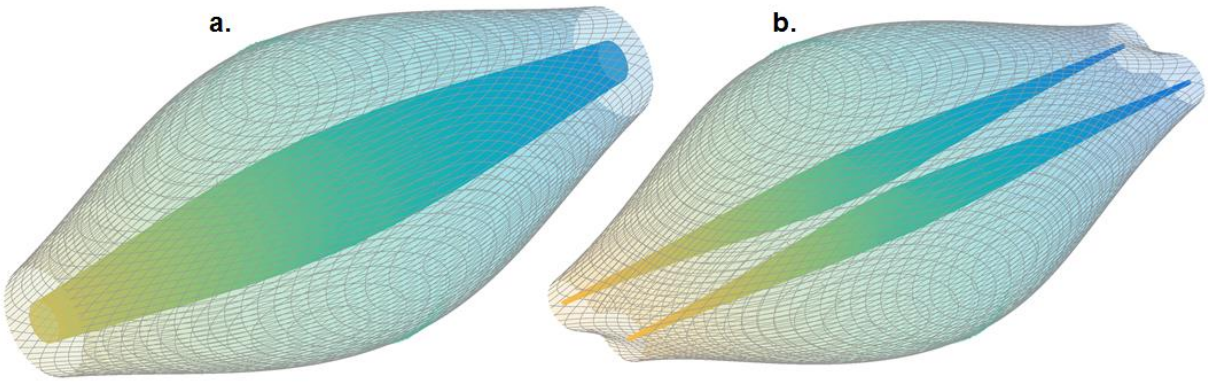

Figure 3.7 – Second-order Cassinian trap 3D plots; **a.** $a_i = 7\ \mathrm{mm}, b = 0\ \mathrm{mm}$, giving a single internal electrode and an orbital ion trap style geometry, and **b.** $a_i = 7\ \mathrm{mm}, b = 6.5\ \mathrm{mm}$, with two internal electrodes, producing a classical Cassinian trap

Potential fields for higher order Cassinian traps can be produced by making the substitution shown in (3.45) for x and y respectively. Equation (3.46) shows the potential field for any even-order Cassinian trap.

$$\begin{aligned} g_x(x, y, \alpha_n) &= x \cdot \cos(\alpha_n) + y \cdot \sin(\alpha_n) \\ g_y(x, y, \alpha_n) &= y \cdot \cos(\alpha_n) - x \cdot \sin(\alpha_n) \end{aligned} \tag{3.45}$$

$$\begin{aligned} U(x, y, z) = U_{\text{Cassini}} \left(\sum_{n/2} \left[\frac{\ln((g_x^2 + g_x^2)^2 - 2b^2\left(g_x^2 - g_y^2\right) + b^4))/{a_i}^4)}{A_{\ln}} \right] \right. \\ \left. + \frac{2z^2 - (2 - B)x^2 - cy^2}{A_{\text{quad}}} + d \right) \end{aligned} \tag{3.46}$$

A 3D plot of a fourth-order Cassinian trap is shown in Figure 3.8, alongside a third-order trap, which cannot be generated from (3.46), but instead can be easily derived in cylindrical co-ordinates, with the potential field in cylindrical co-ordinates shown in (3.47), where the constant B has been replaced by $c = B/2$, and n represents the order of the Cassinian trap.

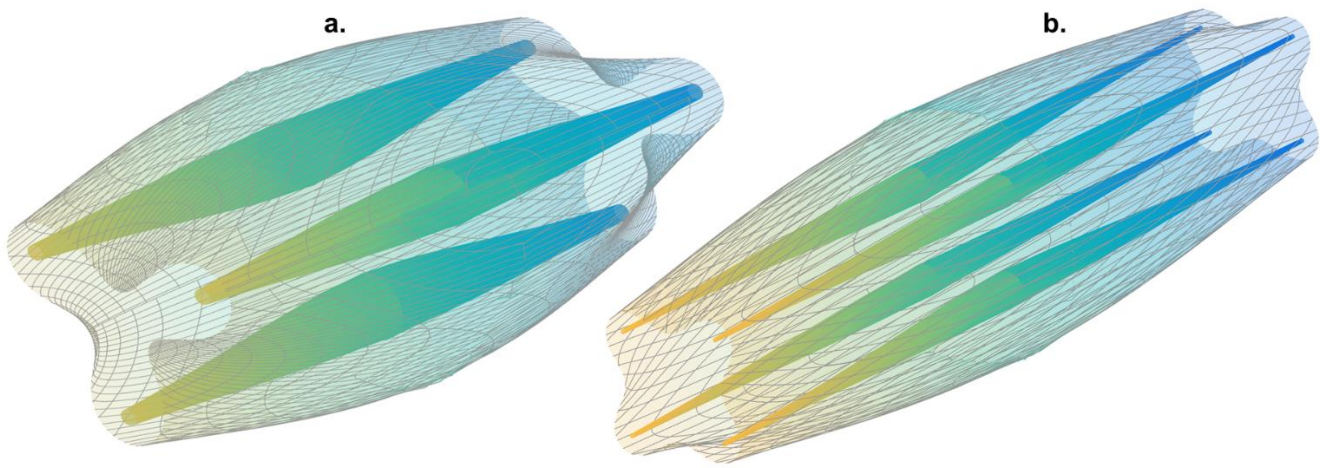

Figure 3.8 - Third and Fourth-order Cassinian trap 3D plots

$$U(r,\alpha,z) = U_{\text{Cassini}}\left[\frac{\ln\left(\left(r^{2n} - 2r^n b^n \cdot \cos(n\alpha) + b^{2n}\right)/a^{2n}\right)}{A_{\ln}} + \frac{z^2 - r^2((1-c)\cos^2(\alpha) + c\sin^2(\alpha)}{A_{\text{quad}}} + d\right] \tag{3.47}$$

This can be re-arranged to define the geometry of a generalised Cassinian trap of any order, as shown in equation (3.48).

$$z(r,\alpha) = \left[r^2((1-c)\cos^2(\alpha) + c\sin^2(\alpha)\,) + A_{\text{quad}}\left(\frac{U}{Uc} - d - \frac{\ln\left(\left(r^{2n} - 2r^n b^n \cdot \cos(n\alpha) + b^{2n}\right)/a^{2n}\right)}{A_{\ln}}\right)\right]^{\frac{1}{2}} \tag{3.48}$$

Ion motion within a second-order Cassinian trap can take the form of multiple different modes, including orbital, lemniscate, and one-dimensional, with higher order traps also able to support further trapping motions. Each mode of trapping can be accessed through changing the initial conditions of the ions, with some trajectories exhibiting much greater stability than others.

The definition of the potential field of a combined logarithmic and quadrupolar field ion trap can be generalised in Cartesian co-ordinates, as shown in (3.49), (Köster, 2009).

$$U(x,y,z) = A_1 \ln\big(f(x,y)\big) + A_2(2z^2 - (2-B)x^2 - By^2) \tag{3.49}$$

Both the logarithmic and quadrupolar potentials must satisfy the Laplace equation, (3.50), which is already true for the latter potential.

$$\Delta U(x, y, z) = 0 \tag{3.50}$$

As such, there are many functions, $f(x, y)$, which would be sufficient, two of which are shown in (3.51), (Köster, 2009).

$$\begin{aligned} f(x, y) &= x^2 + y^2 \\ f(x, y) &= (x^2 + y^2)^2 - 2b^2(x^2 - y^2) + b^4 \end{aligned} \tag{3.51}$$

During the course of this research, a further general function which satisfies the Laplace equation, shown in (3.52), where c is an arbitrary constant. A generalised function of this form has not yet been proposed to form part of the potential field in a harmonic ion trap in the literature at the time of writing.

$$f(x, y) = (x^2 + y^2)^c \tag{3.52}$$

This finding could be used to produce further harmonic ion traps with novel geometry, however further exploration of such devices is beyond the scope of this thesis.

Chapter 4. Design and Manufacture

There have been a number of developments that aim to improve greater mass resolution in SIMS. Examples include an Ion Cyclotron Resonance (ICR-MS) analyser that holds the record to date for SIMS mass resolution to our knowledge (Maharrey *et al.*, 2004; Smith, Robinson, Tolmachev, Heeren, Pasa-Tolic, *et al.*, 2011). However, ICR-MS analysers are prohibitively expensive in comparison to other mass analysers due to the superconducting magnets and associated shielding. ICR-MS instruments are also costly to operate due to the liquid helium required to cool the magnets. Alternative Fourier-Transform mass spectrometers have previously been coupled with SIMS instruments in the past (Castro and Russel, 1984; Amster *et al.*, 1987). More recently the Iontof company has developed a hybrid instrument by connecting an Iontof V ToF-SIMS instrument to a commercially-available Thermo Orbitrap™ mass spectrometer (Pirkl, Moellers, Arlinghaus, Kollmer, Niehuis, Horning, Passarelli, Havelund, Rakowska, Race and Gilmore, 2016). Inevitably there are compromises when connecting different instruments originally designed to operate differently. In contrast, the aim of this research was to develop a new mass analyser closely-integrated with an existing Ionoptika J105 SIMS instrument, and indeed the analyser was designed and constructed here at Newcastle University whilst awaiting delivery of that instrument from the manufacturer.

4.1 Fabrication Challenge

The analyser design is based on the axially-harmonic orbital ion trap proposed by Makarov (Makarov, 2000). This, being an electrostatic trap, does not require expensive high-field magnets of the type used in ICR-MS. Briefly, the ion trap works by applying a potential between an internal “spindle” electrode and two external electrodes held at (virtual) earth potential. Ions injected into the trap follow complex orbits, but Makarov showed that in terms of their axial displacement they follow harmonic paths whose frequency depends on the ion mass-to-charge ratio. These oscillations can be detected and quantified using a sensitive differential charge amplifier connected to the two outer electrodes – essentially measuring the “image charges” induced in those electrodes in response to the ions oscillating in the trap. The disadvantage of this orbital ion trap (compared to ICR-MS for example) is the accuracy of the electric field that needs to be applied between the electrodes, and therefore the high level of accuracy needed in the machining and aligning of those electrodes. As shall be demonstrated, this

accuracy can be on the scale of a few micrometres, or even less, particularly in terms of the manufacturing of the electrodes, as discussed in (Grinfeld *et al.*, 2015).

The precision required in the manufacture and assembly of the ion trap electrodes was determined through ion trajectory simulations, using the commercially available software package, SIMION 8.1 (Dahl, 2000), which employs finite difference methods to calculate the potential fields in which ions are flown, and Runge-Kutta methods to model ion trajectories in three dimensions, (SIS, 2015). These methods by which SIMION evaluates potential fields and simulates ion trajectories, as well as the practice of running simulations, will be discussed in greater depth in Chapter 5 of this thesis.

In total 8 different modes of misalignment were simulated, as listed in Table 4.1, with the axes of the ion trap defined as in Figure 4.1. For each simulation, ten ions were flown, with masses ranging from 100u to 100.9u in 0.1u increments. A greater number of ions would have been too computationally expensive, and ten were sufficient to obtain basic statistics. All ions were modelled with 101eV kinetic energy, and were trapped by a static internal electrode voltage of 175V. The 'output' mass of an ion was evaluated from its axial oscillation frequency, as laid out in equation (3.16) (Makarov, 2000). The mass resolution attainable for various misalignments was found by comparing this calculated 'output' mass with that obtained from an ideal simulation without any misalignment, as shown in equation (4.2), where R is mass resolution, m_{input} is the input mass, m_{ref} is the calculated mass from the reference simulation and $m_{misalignment}$ is the calculated mass from the misaligned simulation.

$$\omega = \sqrt{\frac{q}{m}k} \tag{4.1}$$

Type of Misalignment	Axis of Misalignment / Centre of Rotation	Electrode
Displacement	z-axis	Internal
Displacement	z-axis	External
Displacement	r-axis	Internal
Displacement	r-axis	External
Rotation	Mid-point	Internal
Rotation	Mid-point	External
Rotation	End-point (P)	Internal
Rotation	End-point (P)	External

Table 4.1 - Simulated misalignments

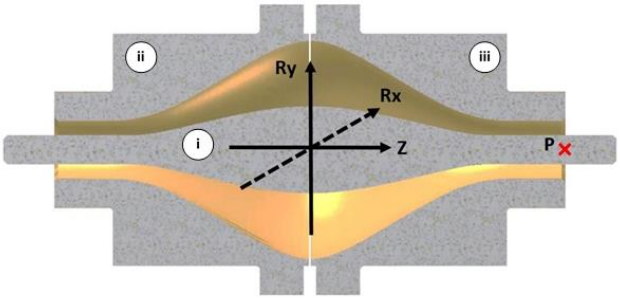

Figure 4.1 - Ion trap axes, where i) is the internal “spindle” electrode, and ii) & iii) are the external electrodes

$$R = \frac{m}{\Delta m} = \frac{m_{\text{input}}}{m_{\text{reference}} - m_{\text{output}}} \tag{4.2}$$

The two principal misalignments examined were axial displacement of the internal and external electrodes relative to one another, results for which can be found in Figure 4.2 and Figure 4.3. Misalignment of this type could arise during machining, for example if an incorrect or imprecise datum is used, or during assembly of the ion trap if component interfaces are damaged or otherwise made to function improperly. It was found that the maximum allowable axial misalignment of the internal electrode was 99.5µm to achieve mass resolution of 10,000, the tolerable axial misalignment for the external electrodes was found to be much lower at only 1.5µm for mass resolution of 10,000, as shown in Table 4.2. Two values of mass resolution were chosen as targets for which to assess the maximum permissible misalignment. Firstly, $m/\Delta m$ = 10,000, was chosen as this is approximately the maximum that can be achieved with the time-

of-flight reflectron mass analyser of the J105 SIMS. A second value of $m/\Delta m$ = 100,000 was selected as resolution in excess of this value has been routinely demonstrated by commercial orbital ion trap variants, (Makarov, 2000).

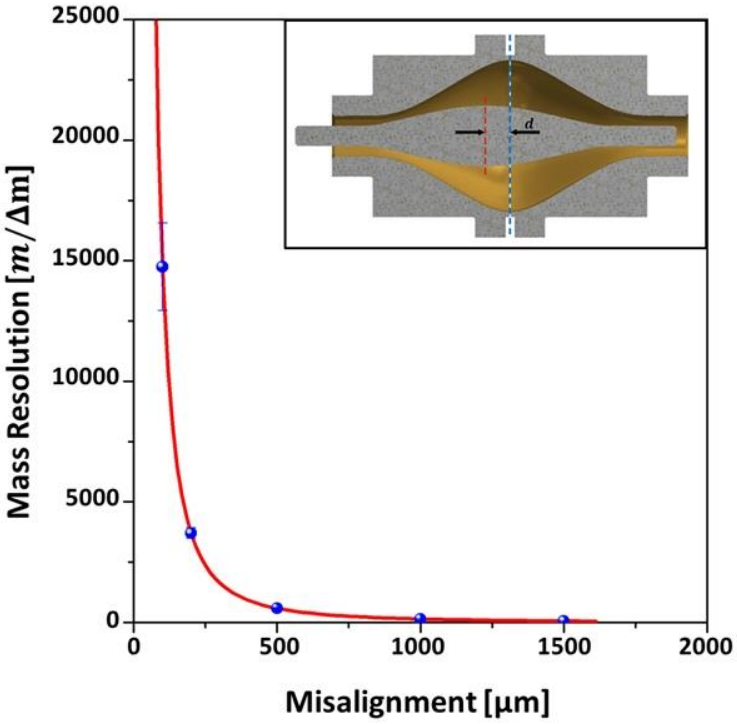

Figure 4.2 - Internal electrode axial misalignment simulated mass resolution results with computer-aided-design (CAD) model of exaggerated misalignment inset.

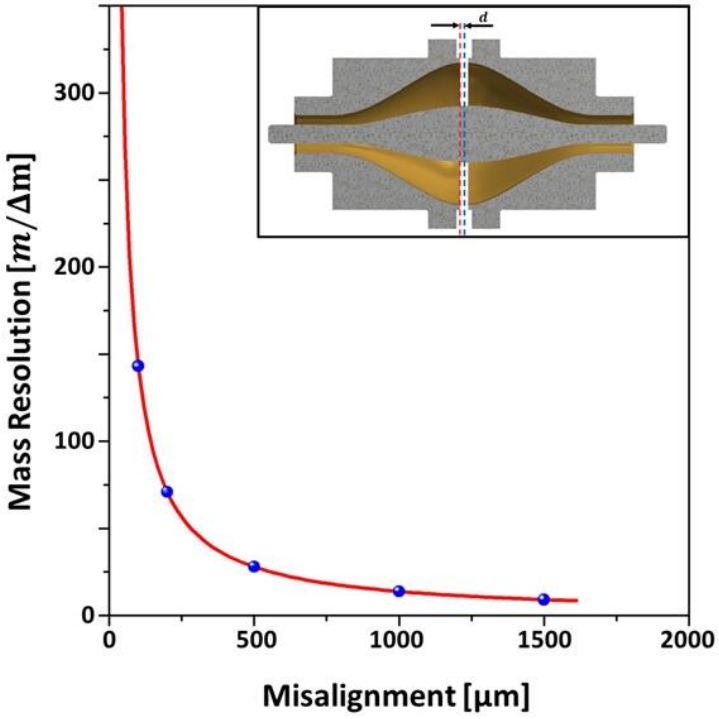

Figure 4.3 External electrode axial misalignment simulated mass resolution results with CAD model of exaggerated misalignment inset.

Axial Misalignment	Misalignment for m/Δm = 10,000	Misalignment for m/Δm = 100,000
Internal Electrode	99.5μm	31.5μm
External Electrode	1.5μm	0.2μm

Table 4.2 - Axial misalignment simulation results, maximum tolerable misalignment for different mass resolving powers.

The increased sensitivity to misalignment of the external electrode can be explained by the increased air-gap, this break in the electric field will cause a much greater perturbation in the ideal electrostatic potential than a simple translation of the internal electrode. The relative insensitivity of the orbital ion trap to axial misalignment of the internal electrode is as predicted by Grinfeld et al. in 2015, in which assembly inaccuracies were anticipated to be tolerable up to tens of micrometres (Grinfeld *et al.*, 2015).

In calculating resolution by comparing the simulated 'output' mass to a reference simulation with no misalignment, the above simulations assume that the reference simulation represents an ideal device in which oscillation frequency maps perfectly to ion mass, as per equation (3.16). In reality, this will not be the case, with all orbital ion traps requiring calibration across its operational mass range. To model this behaviour, further simulations were carried out for ions across a wider mass range, and in this case calculating mass resolution by the shift in mass from the input mass as per equation (4.3), rather than using a reference simulation.

$$\Delta m_{\%} = \frac{m_{\text{input}} - m_{\text{output}}}{m_{\text{input}}} \tag{4.3}$$

In this set of simulations, 19 ions were flown ranging in mass from 100u to 1000u, with an increment of 50u, all ions were given kinetic energy of 101eV, and were trapped by an internal electrode voltage of 175V. Each simulation was carried out with a transient duration of 100ms.

Figure 4.4 and Figure 4.5 show the percentage shift in calculated 'output' mass compared to the ideal input mass, for different amounts of axial misalignment of the internal and external electrodes respectively, where percentage mass shift is equal to the reciprocal of mass resolution. It can be seen that the percentage mass shifts observed are approximately constant across all masses, for a given misalignment.

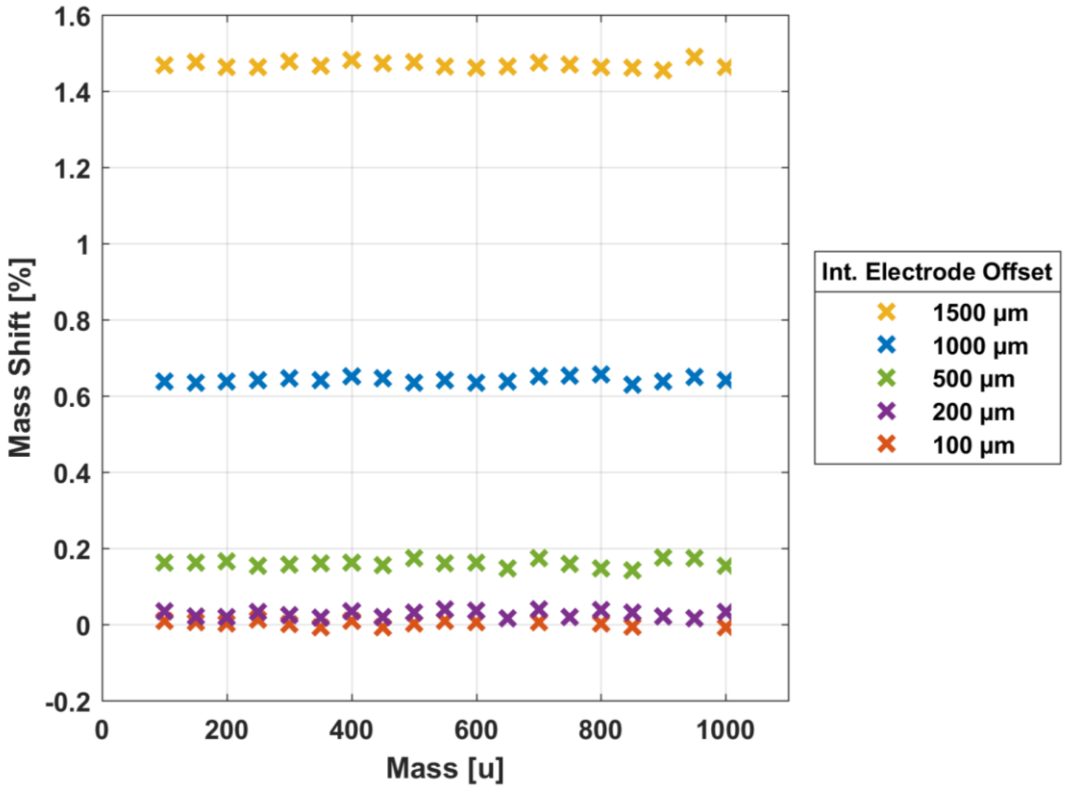

Figure 4.4 - Percentage mass shift plotted against ion mass, as calculated for simulated axial misalignment of the internal electrode. Shown for ions in the range 100u to 1000u.

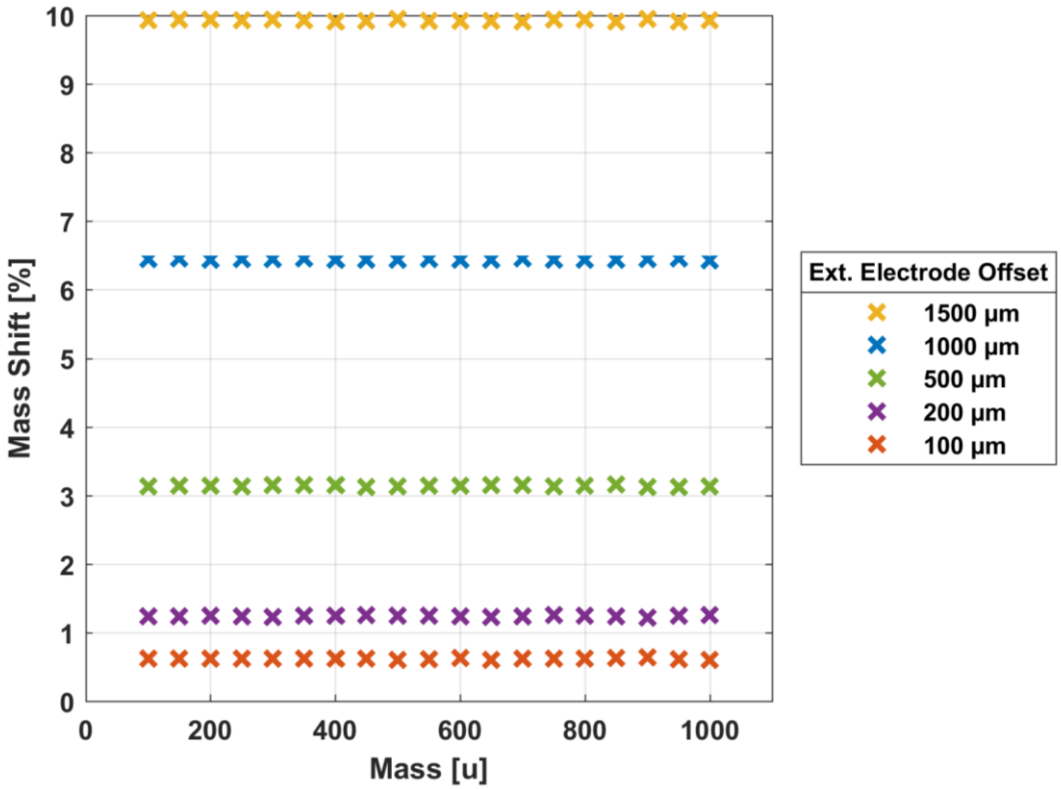

Figure 4.5 - Percentage mass shift plotted against ion mass, as calculated for simulated axial misalignment of one external electrode. Shown for ions in the range 100u to 1000u.

As percentage mass shift did not vary greatly with the mass of the simulated ions, a simple mean of the percentage mass shift was taken, to allow the relationship between mass shift and the amount of axial misalignment to be plotted. Figure 4.6 and Figure 4.7 show these relationships for the internal and external electrode respectively.

It was found that the percentage mass shift for axial misalignment of the internal electrode is proportional to the extent of the misalignment squared. Whereas for axial misalignment of one external electrode, the observed percentage mass shift is linearly proportional to the extent of the misalignment.

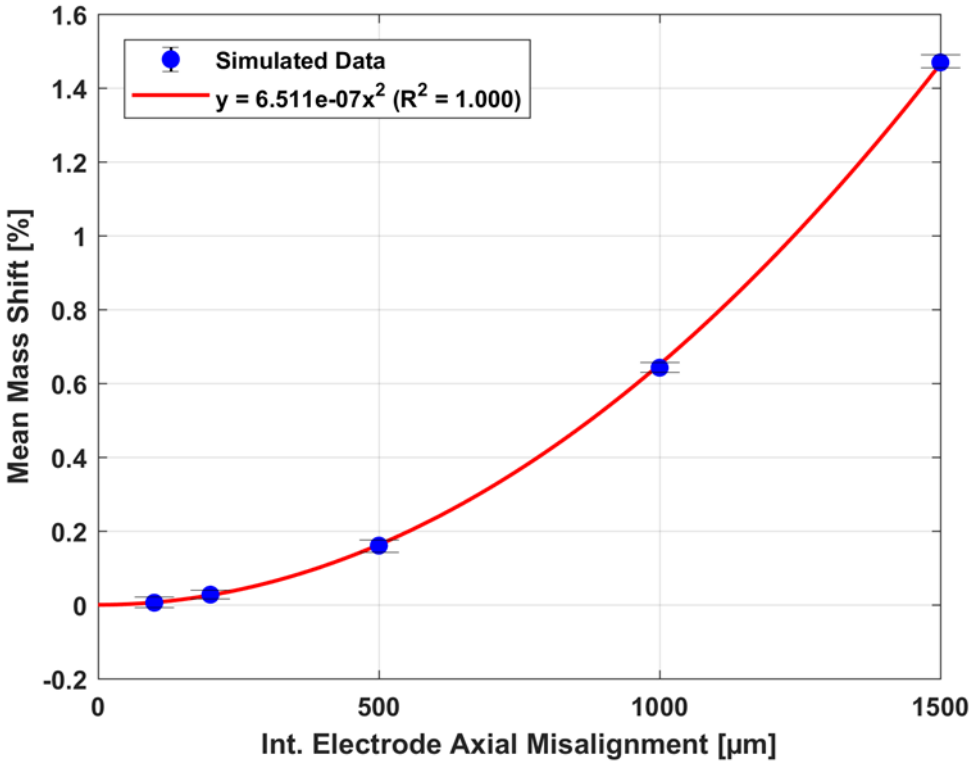

Figure 4.6 - Mean percentage mass shift plotted against axial misalignment of the internal electrode, as observed in simulations of ions in the mass range 100u to 1000u.

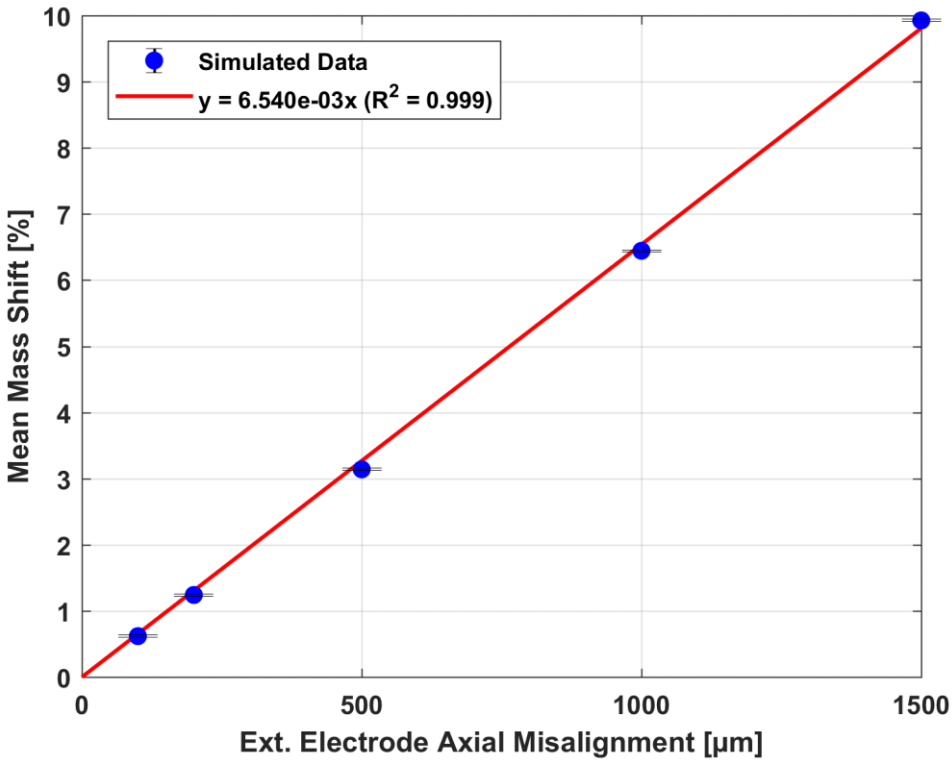

Figure 4.7 - Mean percentage mass shift plotted against axial misalignment of one external electrode, as observed in simulations of ions in the mass range 100u to 1000u.

However, misalignment of the external electrode gives a much larger mass shift for misalignments in the range tested. For example a 3% shift in mass could be expected for a 0.5mm external electrode misalignment, whereas only a 0.2% shift would be expected for an equivalent axial misalignment of the internal electrode.

Due to the square-law dependency of percentage mass shift on internal electrode misalignment, there is a value of misalignment at which the internal electrode would dominate. This value can be calculated by finding the intersection of the two curves presented in Figure 4.6 and Figure 4.7. Figure 4.8 shows this intersection, occurring at a misalignment of greater than 10mm. Such a large misalignment would be impossible due to the physical constraints on the internal electrode of the orbital ion trap imposed by the end cap electrodes. As such, misalignment of the external electrodes would be most detrimental to performance in the expected range of misalignments; of the order of a few tens of micrometres, (Grinfeld *et al.*, 2015).

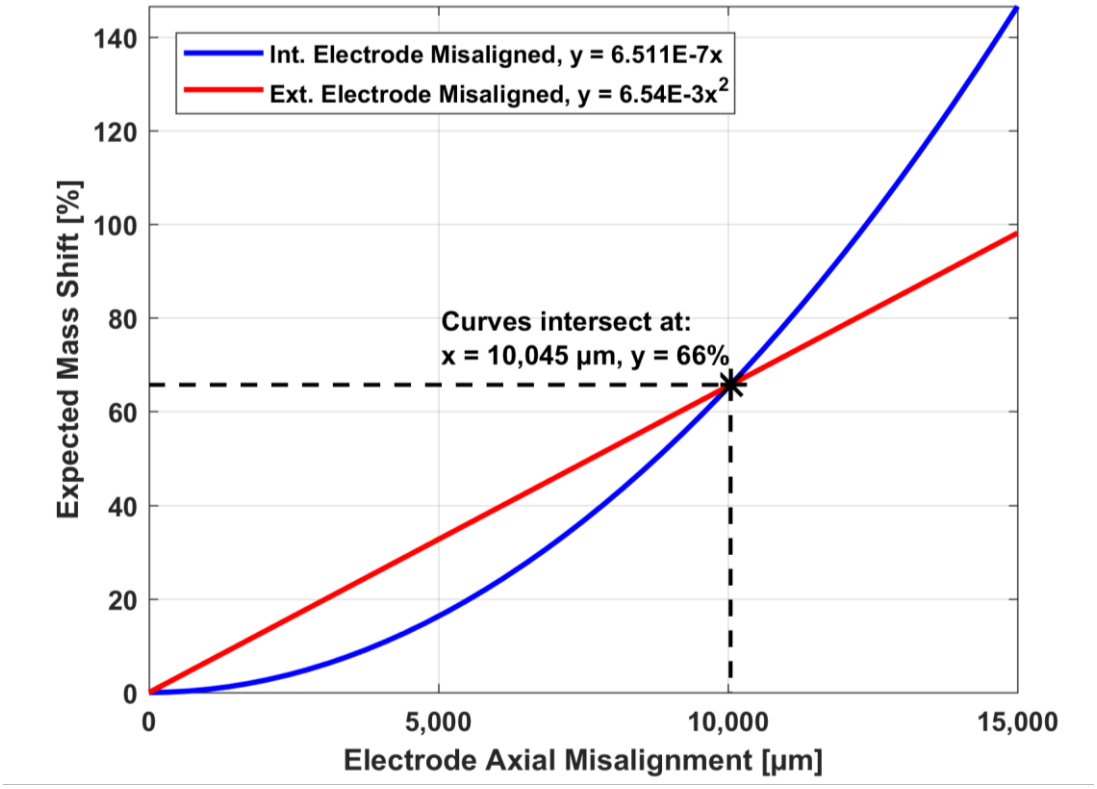

Figure 4.8 - Plot showing the extent of axial misalignment at which internal electrode misalignment would be the dominant cause of shifts in the observed ion mass.

4.1.1 Achieving Alignment in Practice

The method selected to achieve optimal alignment of the component electrodes of the orbital ion trap is quasi-kinematic coupling (QKC).

Aligning components using QKC is achieved using three spheres sitting in holes spaced at 120°, lying on a common pitch circle diameter. This allows the alignment of two components by constraining movement in planar translation, or any possible rotation (Culpepper, 2004). A compressive load which causes the spheres to engage with their contact sites serves to constrain motion in the axial direction, ensuring that all six degrees of freedom for a rigid body in 3D space are constrained.

For aligning the electrodes of the orbital ion trap, synthetic “ruby” balls, composed of sapphire, were chosen as the alignment spheres, as they exhibit good sphericity, of better than 1µm, alongside desirable mechanical properties including hardness of between HK 1525 and 2000 from the Knoop hardness test, according to the manufacturer of the chosen synthetic sapphire spheres, (Dejay Distribution, 2015). Sapphire balls are also suitable for employment in ultra-high vacuum environments due to their low outgassing properties, (LIGO, 2014). Figure 4.9 shows how QKC was implemented using Ø2mm synthetic sapphires to align the two external electrodes of the orbital ion trap.

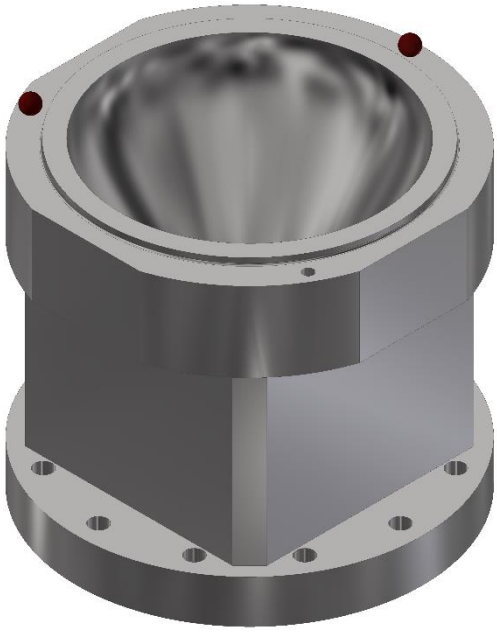

Figure 4.9 - CAD model of one external electrode, prior to final machining of ion injection slot, showing location of QKC sites, with two out of three Ø2mm synthetic sapphires in place.

Figure 4.10 shows the six degrees of rotational and translational freedom which are present before engaging the QKC alignment spheres, and Figure 4.11 shows the remaining axial degree of freedom once engaged.

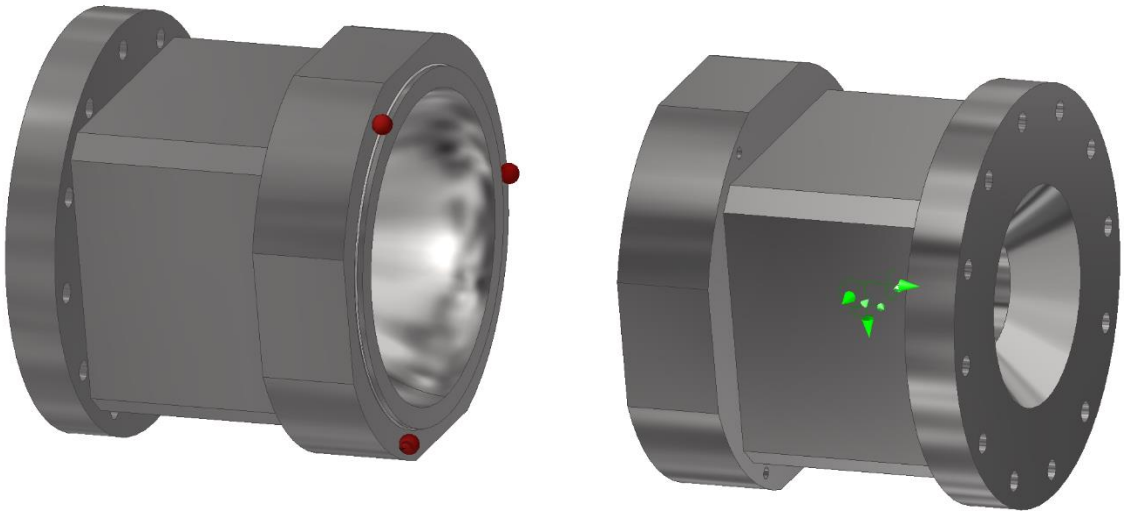

Figure 4.10 - CAD model showing QKC coupling of external electrodes, with the right-hand electrode not yet engaged, green arrows show full six degrees of freedom of the right-hand electrode.

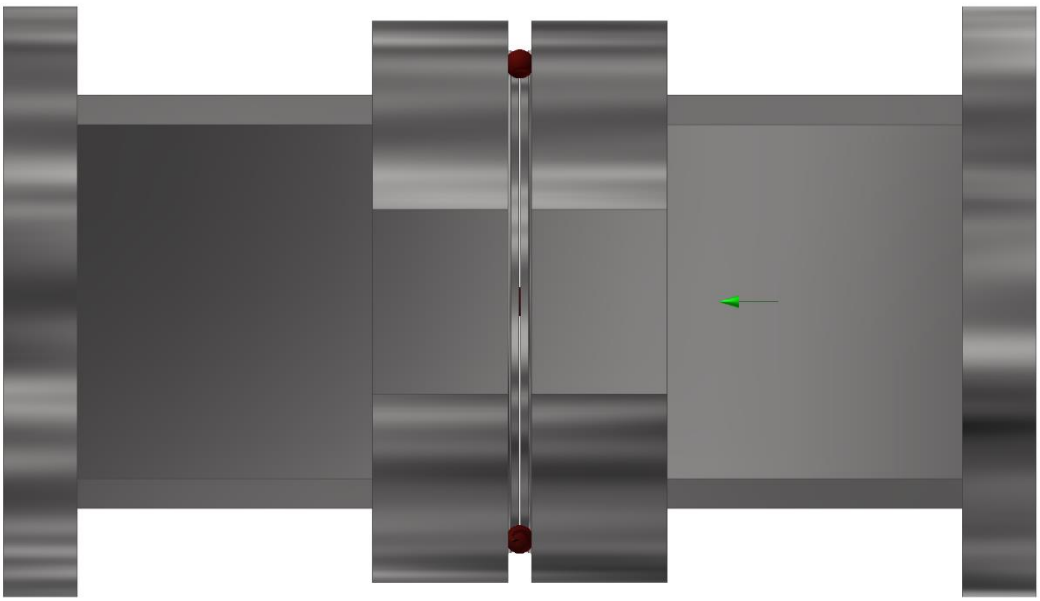

Figure 4.11 - CAD model showing external electrodes aligned using QKC, the green arrow on the right-hand electrode shows the single remaining degree of freedom in the axial direction, which can be constrained using a compressive load.

A compressive axial load is applied by nuts on threaded studs to constrain motion in the axial direction, as shown in Figure 4.12. A fully assembled orbital ion trap with no remaining degrees of freedom can be seen in Figure 4.12, showing the multiple QKC alignment sites used for alignment of the following components; the two external

electrodes, the internal electrode at both ends, and the two end plates which electrically isolate the internal and external electrodes from one another via further QKC sites.

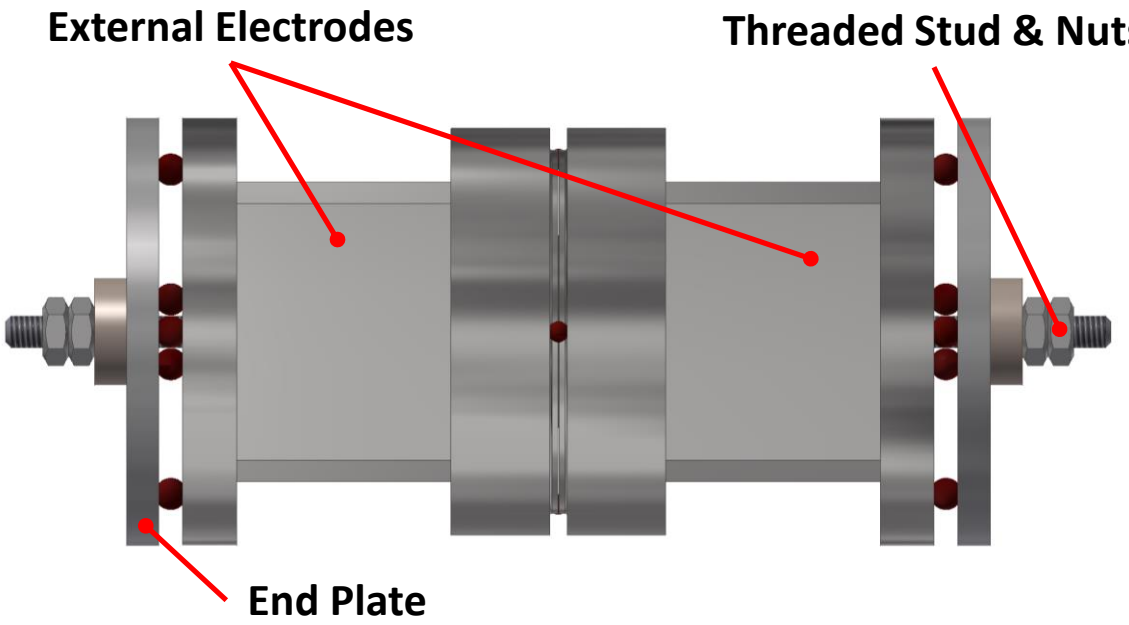

Figure 4.12 - CAD model showing the fully assembled orbital ion trap, with multiple QKC sites, and a compressive load applied using end plates with threaded studs extending from the internal electrode to constrain motion in the axial direction.

4.2 Computer Numerically Controlled Machining

As confirmed by the misalignment simulations, there is very little margin for error in the manufacture and assembly of the ion trap electrodes, therefore accurate machining is of paramount importance. The ideal profile of the electrodes is of a quadro-logarithmic form, as described by Eqn (4.4), from Makarov (Makarov, 2000).

$$z(r) = \sqrt{\frac{r^2}{2} - \frac{\left(R_{1,2}\right)^2}{2} + (R_m)^2 \cdot \ln\left(\frac{R_{1,2}}{r}\right)} \tag{4.4}$$

To translate this relationship into a computer numerically controlled (CNC) machining compatible “G-code” required for manufacture, a number of tools were utilised, including in-house written MATLAB scripts and CAD software. One issue in turning a complex profile such as this on a CNC machine is maintaining the mathematical smoothness of the operation, if G-code is written without considering this it can result in discontinuities in the piecewise representation of the continuous function. Therefore, in this case tangent arcs were used to approximate the ideal electrode profile whilst preserving its smoothness in the form of G^1 continuity (Barsky and DeRose, 1990). An appropriate series of bi-arcs were constructed to represent the profile using Autodesk Inventor, a CAD software package, with a series of tangent arcs fitted to a plot of the ideal profile.

The accuracy of the G-code approximation of the electrode profile was then evaluated using MATLAB. Figure 4.13 shows the ideal orbital ion trap profile overlaid on the profile produced by the bi-arc approximation, at this field of view, almost no discrepancies can be seen between the two. To investigate errors between the curves which are not visible in Figure 4.13, the G-code profile was subtracted from the ideal electrode profile in MATLAB, resulting in the error plot shown in Figure 4.14.

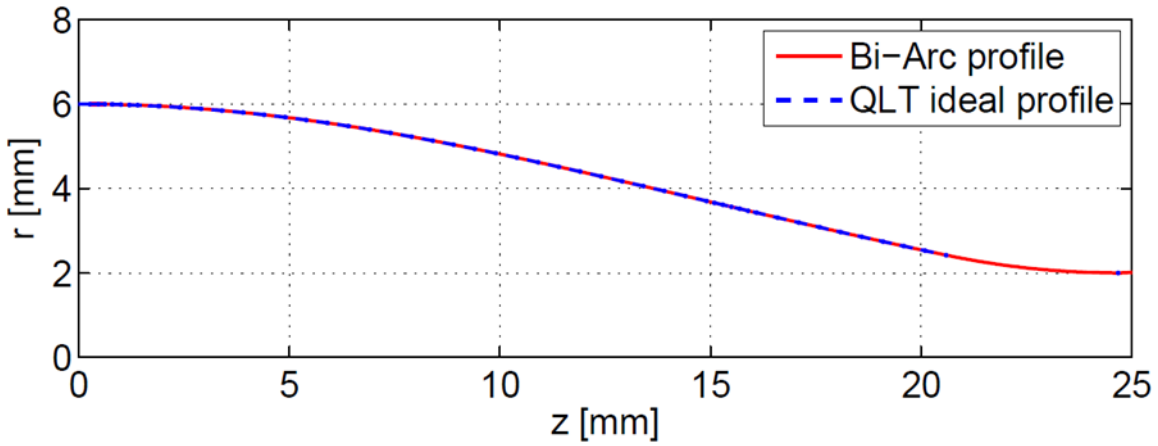

Figure 4.13 - Overlay of ideal internal electrode profile with G-code approximation

To investigate errors between the two curves not visible in Figure 4.13, each bi-arc was represented by one hundred points along its length and corresponding radial values of the ideal profile were interpolated from a table produced of ideal r and z co-ordinates. Interpolation was required as the equation governing the ideal orbital ion trap profile cannot be expressed in terms of r, interpolation was carried out using a piecewise cubic spline. The radial error between the bi-arc approximation and ideal orbital ion trap profile is shown in Figure 4.14.

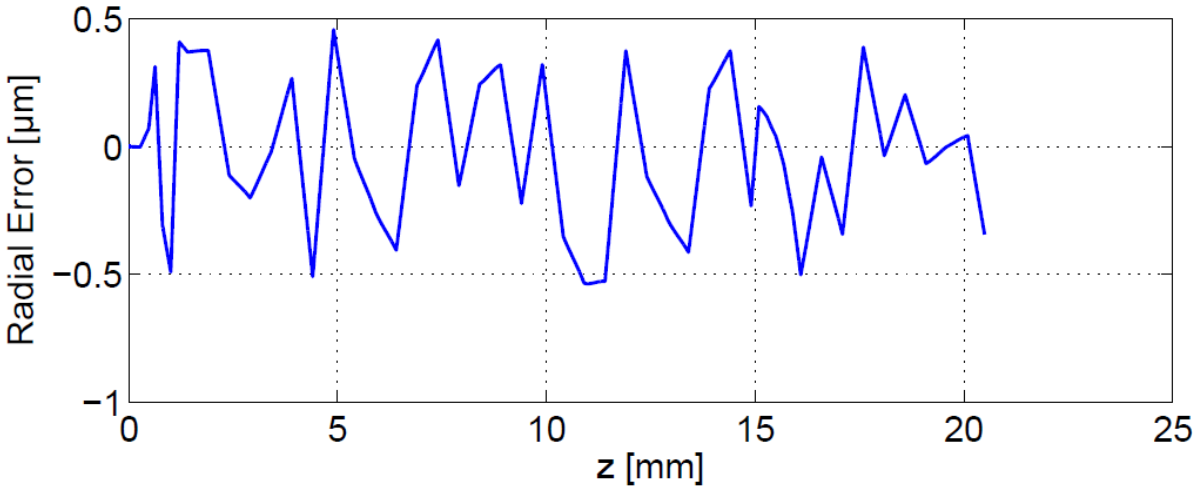

Figure 4.14 - Resulting radial error when G-code profile is subtracted from ideal internal electrode profile

The same process was repeated for the external electrode profile, with maximum radial error values shown in Table 4.3. The maximum error between the ideal profile and bi-arc approximation is of the order of 0.5µm, which was deemed acceptable to proceed with for manufacturing. As surface roughness is expected to be of the order of 5µm, the bi-arc profile error would be negligible in comparison.

	Internal Electrode	External Electrode
Maximum Radial Error	-0.536µm	+0.473µm
Axial Position of Max. Error	z = 11mm	z = 8.5mm

Table 4.3 - Maximum radial error between G-code and ideal electrode profiles

In theory, an arbitrarily small value for radial error could be obtained by increasing the number of arcs used to approximate the ideal profile. However, as the CNC milling machine used accepts input only to the nearest micron, this is not the case in practice. The disadvantage of using an increasing number of bi-arcs would be the increase in time required to evaluate the bi-arcs geometrically, as well as the increase in time required to input co-ordinates into the CNC milling machine, with diminishing returns in the reduction of radial errors.

4.2.1 Bi-Arc Improvements

As discussed, the programming of bi-arc coordinates into the CNC lathe for manufacture is a time consuming process, particularly when compared to the machining time required, with less than 15 minutes active machining demanding over 30 minutes of input to produce an external electrode. An algorithmic approach to choosing bi-arc coordinates has been sought in an attempt to reduce the number of arcs required whilst maintaining the required accuracy.

The desired outcome was an algorithm which could take the following inputs:

- A piecewise continuous function, in this case the quadro-logarithmic profile of either the internal or external electrode, in the form **y(x)**
- Initial coordinate, $\mathbf{P_0}$
- Final coordinate, $\mathbf{P_2}$
- Maximum allowable error tolerance between bi-arcs and ideal profile, **ε**

And produce the following outputs:

- Vector of arc centre-points, $\mathbf{S_i}$
- Vector of arc radii, $\mathbf{r_i}$
- Number of arcs used, $\mathbf{n_{arcs}}$
- Maximum error between bi-arc representation and input function, **error**

Figure 4.15 shows the construction of a pair of bi-arcs between two points, P_0 and P_2, with point P_1 chosen as the joint between arc 0 and arc 1.

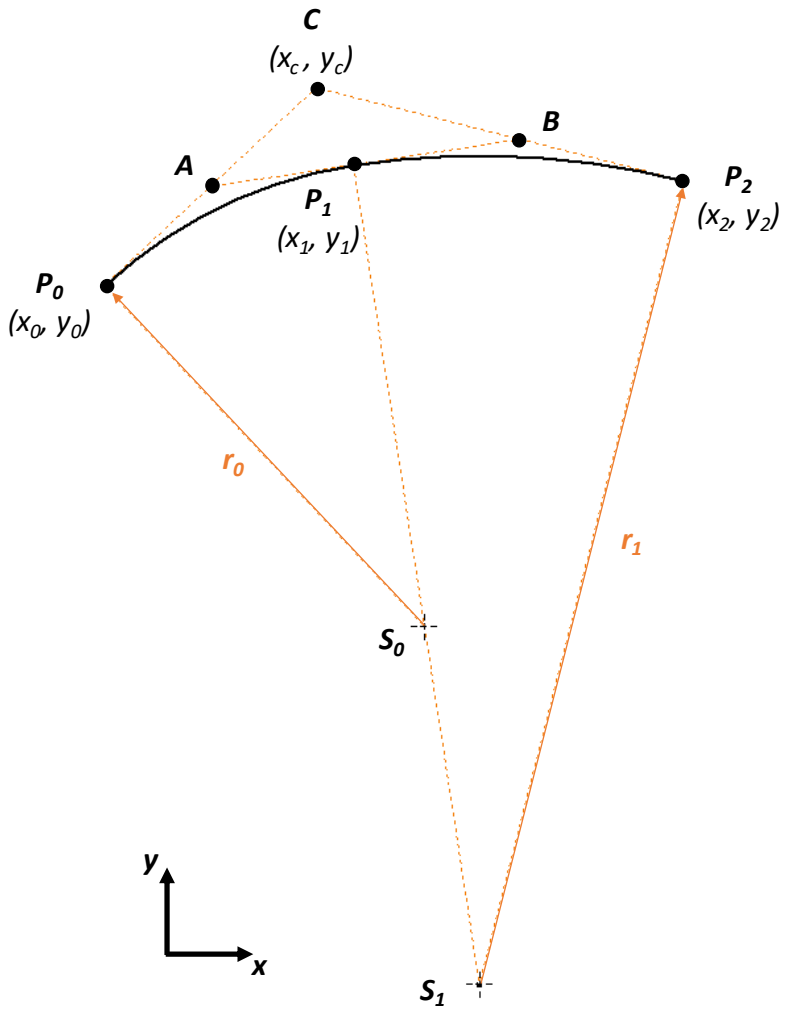

Figure 4.15 - Bi-arc construction diagram

The algorithm was designed to choose a suitable joint, P_1, and construct bi-arcs accordingly, based on the intersection of the tangent vectors at points P_0 and P_2. Point P_1 lies on the line AB, which connects the lines P_0C and P_2C, where C is the intersection of the two tangent vectors at points P_0 and P_2. Initially the x-coordinate of P_1 is selected to lie half way x_0 and x_c, two tangential arcs can then be constructed.

The error between the produced bi-arc and the ideal profile is then estimated, and if this value is greater than the maximum allowed, the region P_0 to P_1 is further sub-divided and another bi-arc pair found, this process is repeated until the estimated error is less than the specified tolerance. A fuller explanation of a similar algorithmic process for producing a bi-arc approximation of a curve can be found in (Jakubczyk, 2012).

The process relies on the input curve function meeting certain criteria in the region to be interpolated:

a) It must be planar
b) It must be piecewise continuous
c) It must be of monotonically increasing or decreasing absolute curvature, where curvature, $\kappa(x)$ as defined in equation (4.5), (Jakubczyk, 2012).

$$\kappa(x) = \frac{y''(x)}{(1 + y'(x)^2)^{\frac{3}{2}}} \tag{4.5}$$

From b) it is necessary that the orbital ion trap profile is written with z = y, and r = x, so that the function z(r) = y(x) is piecewise continuous and planar.

It can be seen in Figure 4.16 that the ideal orbital ion trap profile does not meet condition c) for its full extent, with curvature changing sign at the inflection point, this meant that the profile must be sub-divided into pre and post-inflection regions prior to interpolation.

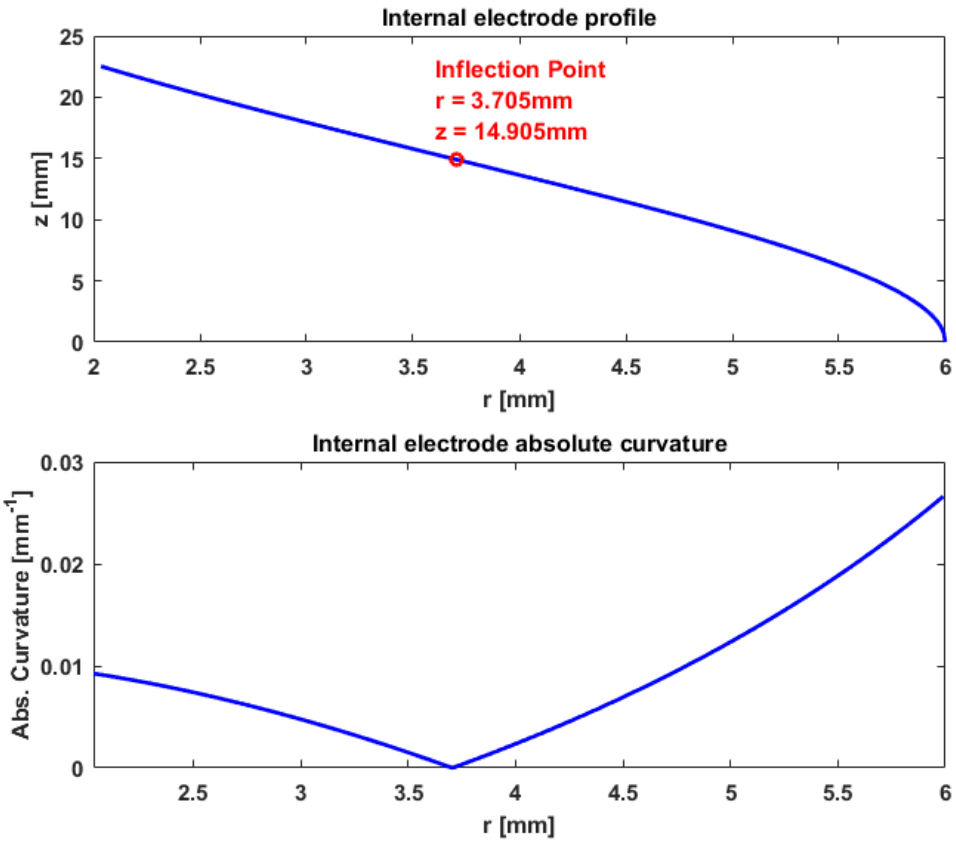

Figure 4.16 - Orbital ion trap profile and curvature, showing inflection point

After interpolation, the two series of arcs for pre and post-inflection regions could be combined to produce a continuous profile, shown in Figure 4.17 for the high-field variant of the internal electrode, with a maximum radius of 9mm rather than 6mm as is standard. This profile was constructed with only 30 arcs required, whereas over 100 arcs were needed when trying to approximate the high-field electrode profile with bi-arcs using Autodesk Inventor as per the previously discussed method.

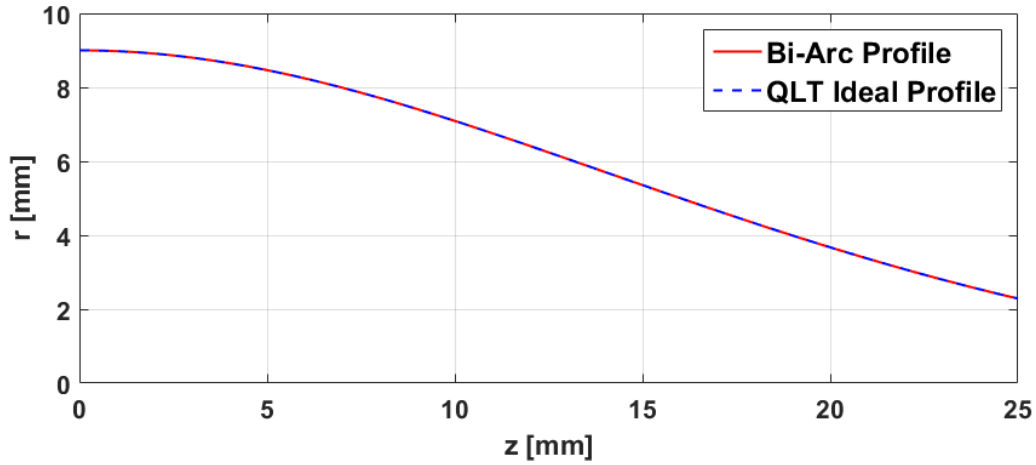

Figure 4.17 - Internal Electrode High-Field Bi-Arc Profile Plot

As is shown in Figure 4.18, the maximal error for this approximation was found to be 0.145µm, a significant improvement over the ~0.5µm error found with manually generated bi-arcs for the standard internal electrode profile.

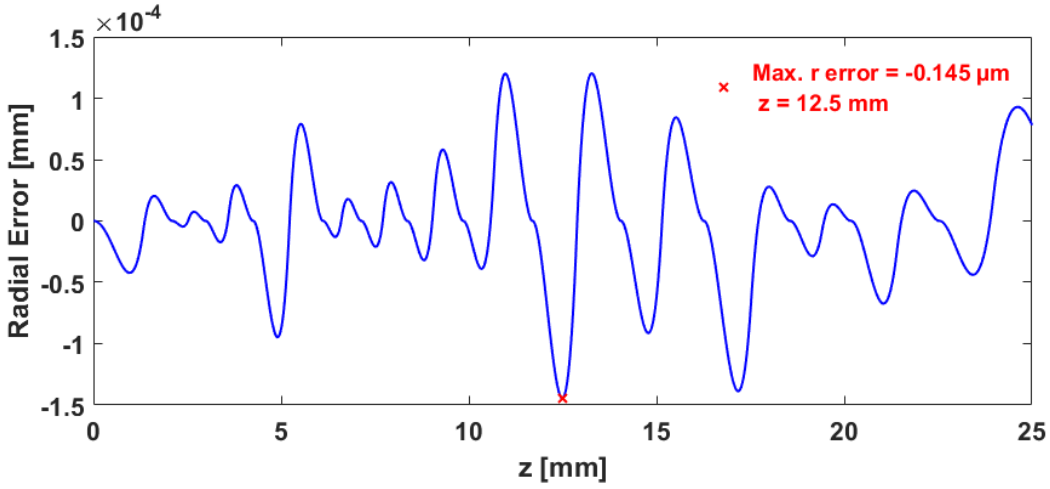

Figure 4.18 - Radial error of Internal Electrode High-Field bi-arc approximation

However, Figure 4.19 shows that this improvement in error is reduced when the bi-arc coordinates are rounded to the nearest micron, as is required for input into the CNC lathe for manufacture.

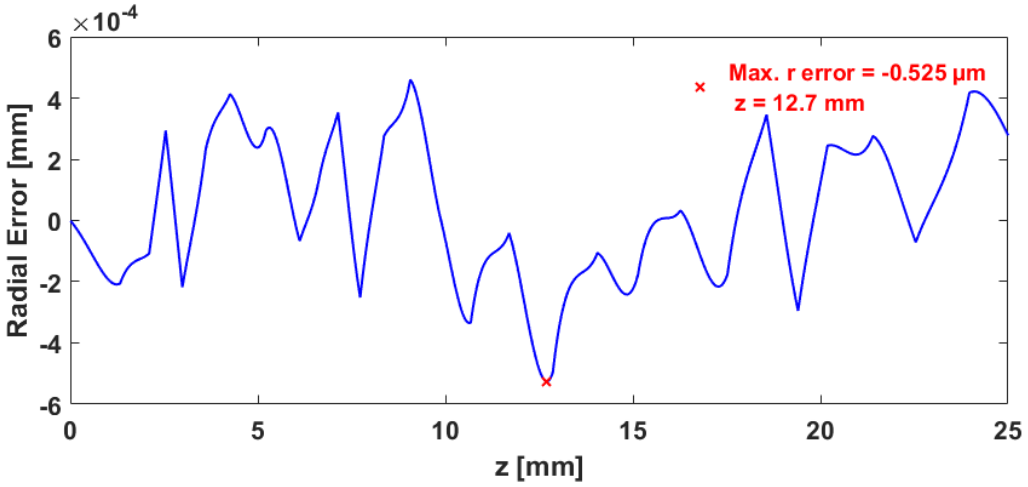

Figure 4.19 - Radial error of Internal Electrode High-Field bi-arc approximation, with co-ordinates rounded to nearest micrometre

The reduction in the number of arcs required still stands as an improvement over manual arc finding methods. The flexibility of the algorithm is also useful and will likely prove time-saving for future iterations of the electrode geometry, for example a bi-arc approximation for altered geometry can be found in under 10s through computation, whereas the process took many hours of trial and error arc allocation using Autodesk Inventor. The algorithm would also be beneficial if more precise co-ordinate input for machining became possible, as arbitrarily accurate bi-arc approximations could be found efficiently. Figure 4.20 shows the relationship between maximum radial error of the bi-arc approximation and the number of arcs used to represent the high-field internal electrode, it can be seen that error of less than 1µm can be achieved with only 16 arcs for the entire profile, and error of less than 0.1µm can be achieved with 40 arcs.

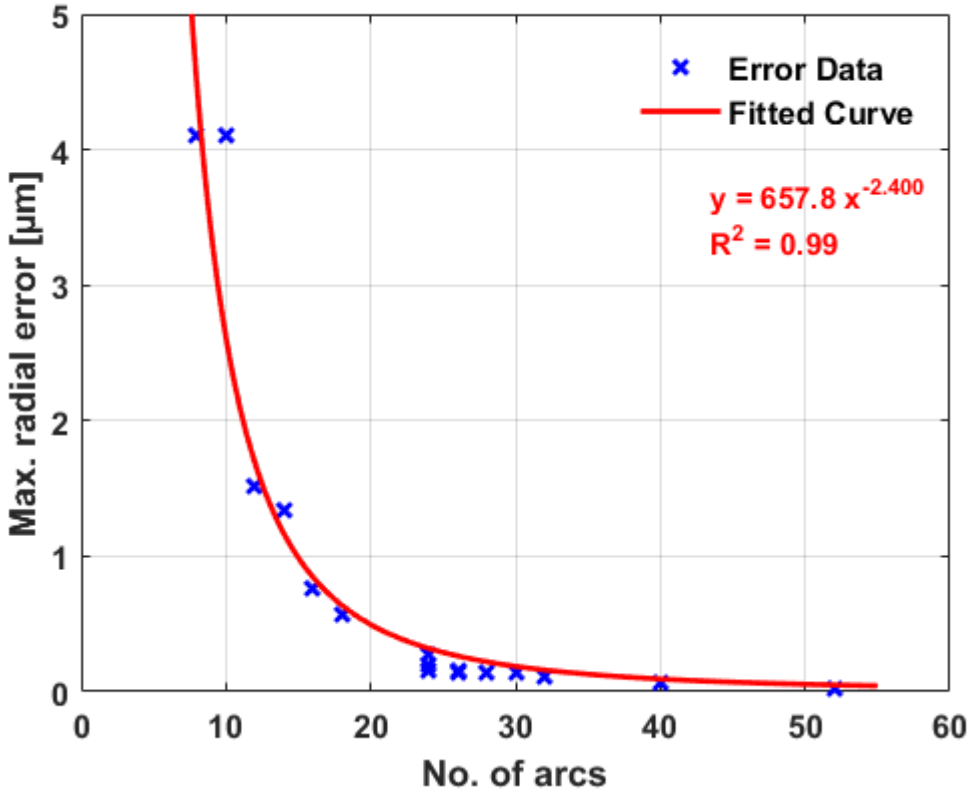

Figure 4.20 - Radial error against number of arcs used in approximation of high-field internal electrode

4.2.2 Bi-Arc Program

A MATLAB function has been written to display a graphical user interface (GUI) to allow bi-arc representations of the ideal profile to be easily generated and assessed, as shown in Figure 4.21. The GUI functions as follows:

1. Select an **Output folder** into which bi-arc data will be saved as an Excel workbook.
2. Select either **Internal** or **External** electrode to generate bi-arc approximation for.
3. If the Internal electrode is selected, **Standard** or **High-Field** geometry configuration can be chosen.
4. Specify an acceptable **error tolerance**, this value is used as an upper bound for allowable deviation between the generated bi-arcs and the ideal profile.
5. Specify an output filename for the Excel workbook containing bi-arc data.
6. Click '**Generate Bi-Arcs**' button to run the bi-arc generation function.

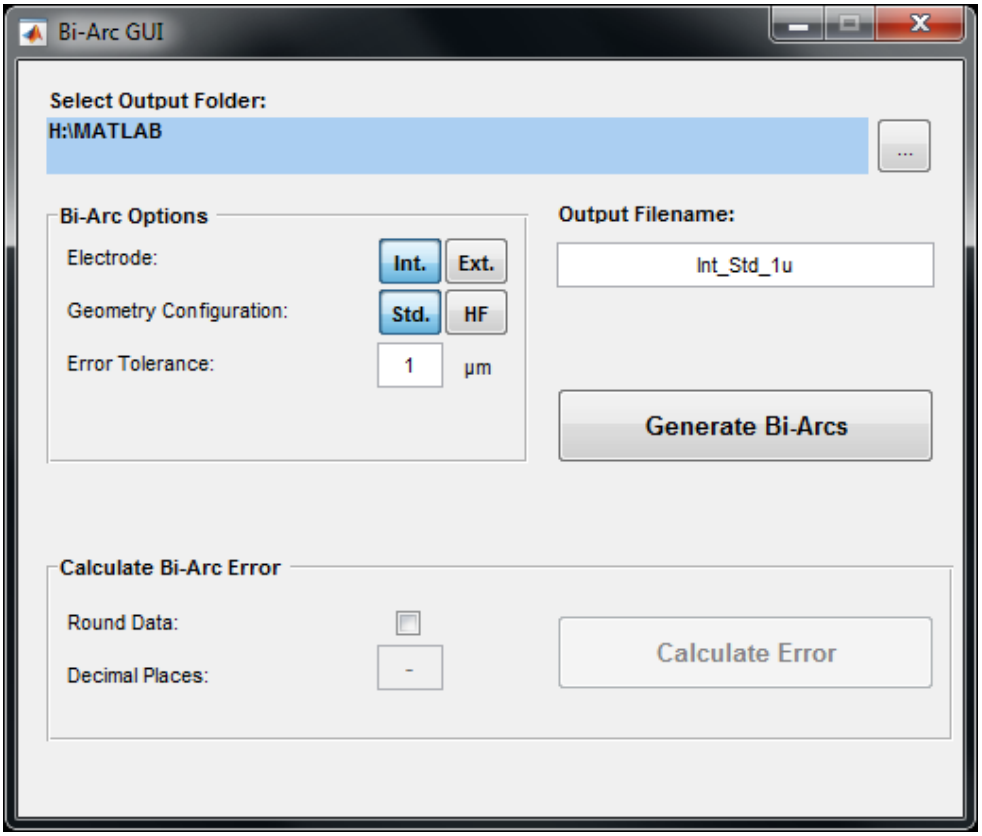

Figure 4.21 - Bi-Arc MATLAB GUI

The Bi-Arc GUI function generates bi-arcs for both pre and post-inflection regions of the parametric profile, this reduces the time taken to generate a full electrode bi-arc profile, ready for input into a CNC lathe, whilst also reducing the possibility of errors which could arise when manually combining multiple sets of bi-arc data.

The generated bi-arcs are saved in the format detailed in Table 4.4, with the curve described by the example data shown in Figure 4.22.

z [mm]	r [mm]	Radius [mm]	Orientation [cw/ccw]
0.009	6.000	37.544	ccw
1.902	5.952	39.782	ccw
3.024	5.879	40.939	ccw
3.654	5.824	43.277	ccw
4.302	5.758	45.014	ccw
5.204	5.650	-	-

Table 4.4 - Bi-Arc example data output

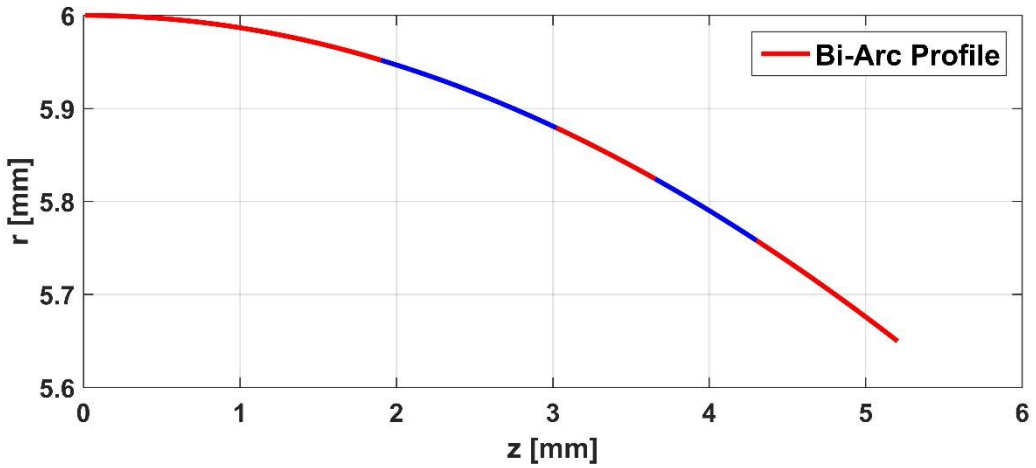

Figure 4.22 - Bi-Arc example plot

Once bi-arc data has been generated and saved to an Excel file, the 'Calculate Bi-Arc Error' section of the software becomes active, this can be operated as follows:

1. Select whether to round the data on import
2. If data is to be rounded, specify the number of **decimal places** to round to, the units of the saved data is [mm], so rounding to 3 decimal places rounds to the nearest micron, which is equal to the smallest input which can be given to the CNC lathe being used for manufacture.
3. Then '**Calculate Error**' can be clicked, to evaluate the error between generated bi-arcs and the ideal parametric profile.

The output of the error calculation part of the program is shown in Figure 4.23. The plot shows the error between bi-arcs and the ideal parametric profile for an internal electrode of standard geometry, for which an error tolerance of 1µm was specified. It can be seen that the maximum radial error of -0.206µm is much less than the specified error tolerance, this is due to the fact that the bi-arc generation minimises error in the axial rather than radial direction. The ideal profile has an axial gradient which is large in comparison to its radial gradient, as shown in Figure 4.24, meaning a given axial error will correspond to a smaller radial error for the same coordinate, an exaggerated example of which is shown in Figure 4.25.

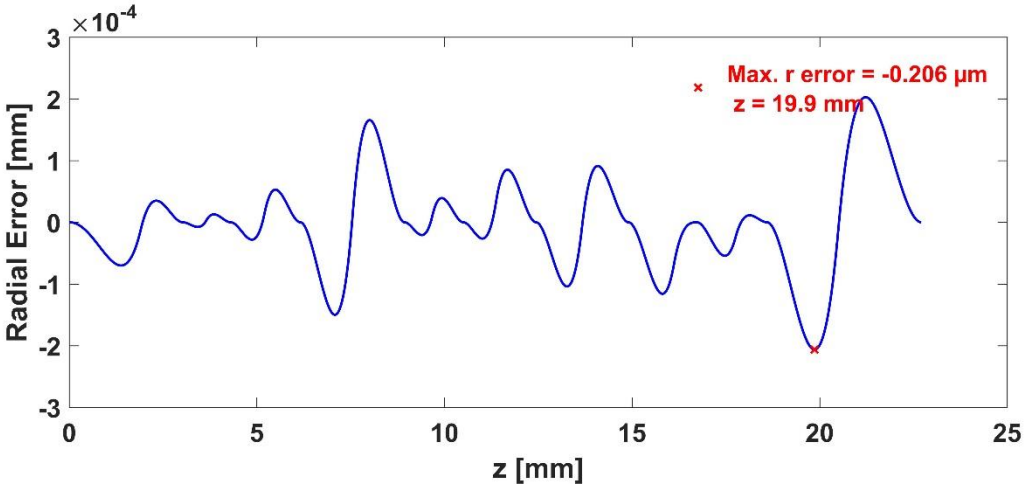

Figure 4.23 - Bi-Arc error output plot, internal electrode, standard geometry

Figure 4.24 shows the plots of Eqn. (4.6) and Eqn. (4.7), which describe the axial and radial derivatives of the ideal parametric profile.

$$\frac{dz}{dr} = \frac{r^2 - Rm^2}{2r\sqrt{\frac{r^2}{2} - \frac{R_{1,2}}{2} + Rm^2 \cdot \ln\left(\frac{R_{1,2}}{r}\right)}} \tag{4.6}$$

$$\frac{dr}{dz} = \frac{2r\sqrt{\frac{r^2}{2} - \frac{R_{1,2}}{2} + Rm^2 \cdot \ln\left(\frac{R_{1,2}}{r}\right)}}{r^2 - Rm^2} \tag{4.7}$$

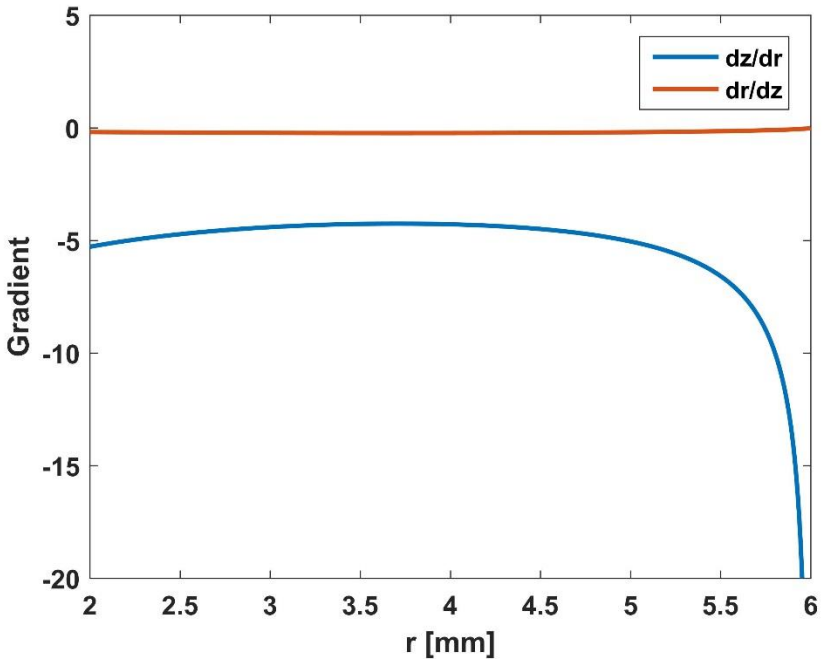

Figure 4.24 - Gradient of ideal parametric profile

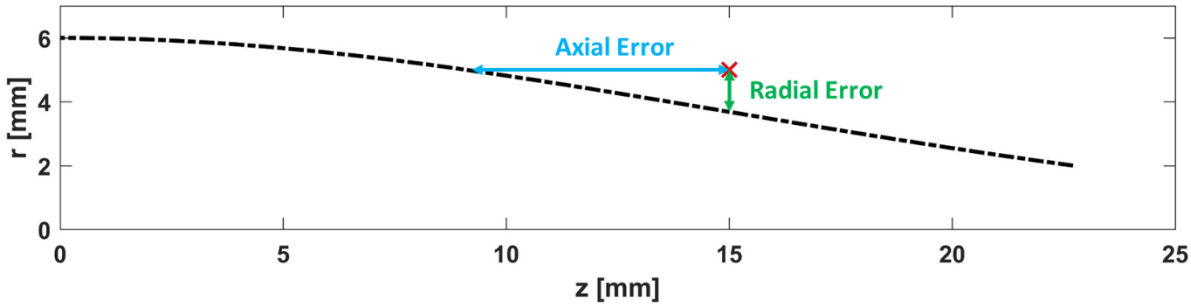

Figure 4.25 - Example of axial error and radial error for parametric profile

4.3 Assembled ion transfer assembly

Once successful ion transfer had been simulated, the CAD model was adjusted to reflect the optimum arrangement of ion transfer components, the transfer assembly was then constructed accordingly. The assembled analyser and associated ion transfer optics are shown in Figure 4.26 mounted onto the J105 SIMS, alongside a CAD model of the transfer and ion trap assembly.

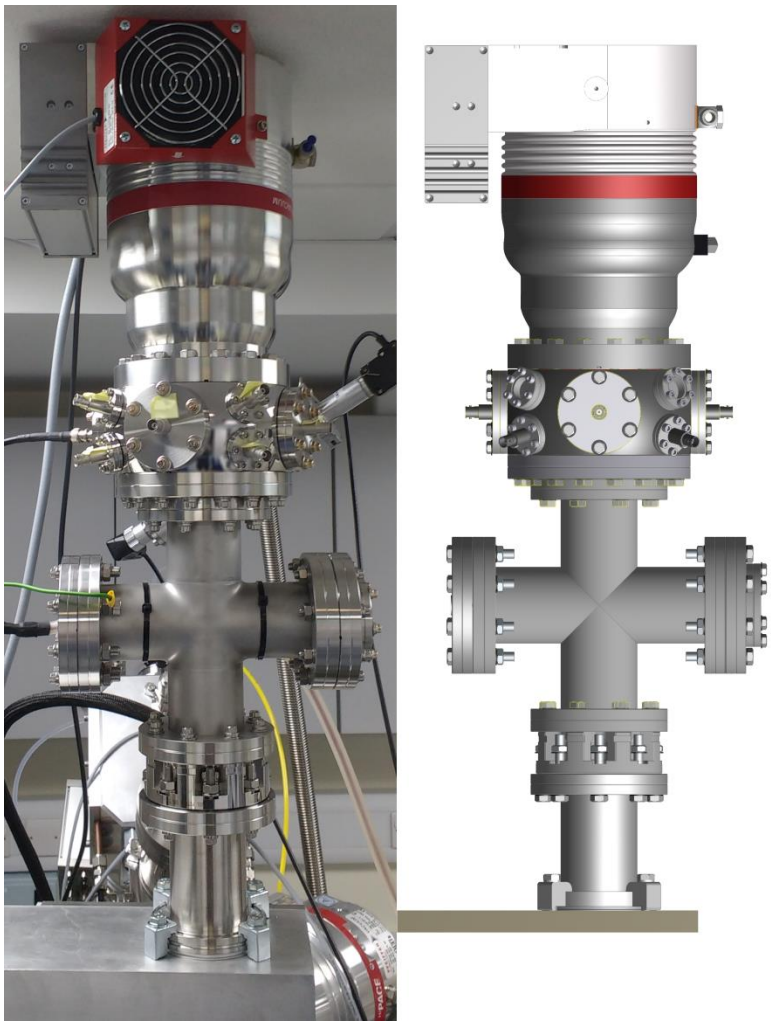

Figure 4.26 - Comparison of assembled analyser mounted on J105 SIMS and CAD model of transfer assembly

4.4 Further Manufacturing

4.4.1 Orbital ion trap Design progression

Over the course of the research project, a number of revisions have been made to the design of the orbital ion trap, which have been grouped into five design iterations, P1 through to P5. Table 4.5 shows the main developments of each generation of the device. Figure 4.27 and Figure 4.28 show CAD images of the different orbital ion trap designs and relevant cross sections to differentiate iterations P3, P4 and P5.

Iteration	Design Changes	Electrode Radii [mm]	
		Internal, R_1	External, R_2
P1	Original Design	6	15
P2	- Loading plate - Integrated end plates - Revised injection pipe	6	15
P3	- Injection electrode - Improved accuracy of bi-arc CNC machining - Revised mounting mechanism - Improved vacuum performance through wider pumping apertures - Simplified assembly	6	15
P4	- As P3 but high-field internal electrode geometry	9	15
P5	- Possibility of ultra-high-field electrode geometry - Further ion lens in injection pipe - Further improvements to vacuum design - Design changes to accommodate faster installation	5	10

Table 4.5 - Orbital ion trap design iterations

Figure 4.27 - Orbital ion trap design iteration CAD images

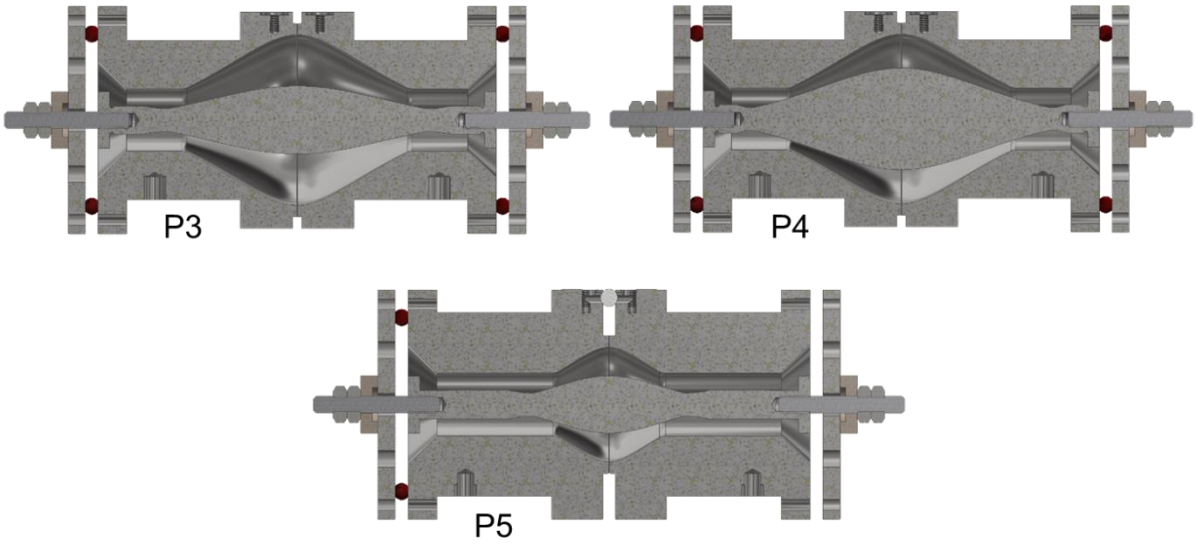

Figure 4.28 - Orbital ion trap design iteration CAD cross sections

4.4.2 Orbital ion trap P3 & P4 – Deflector Electrode

The most significant design change in iterations P3 & P4, not present in P2, is the inclusion of an additional electrode to perform a similar function to the ‘deflector’ or ‘compensation’ electrode as discussed in the Literature Survey. This additional electrode allows ions to be injected at a greater distance from the internal electrode, meaning a greater proportion of the trapping volume is accessible for ion orbits.

The injection electrode itself is a relatively simple construction, as shown in Figure 4.29.

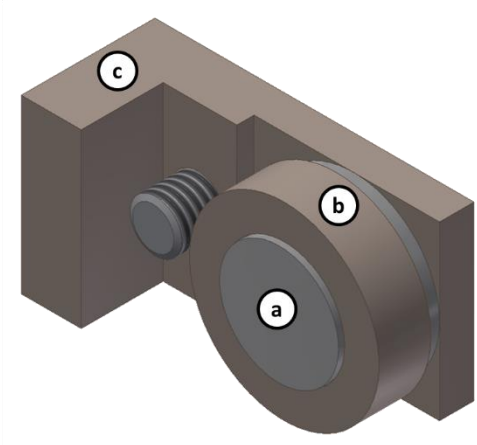

Figure 4.29 - Injection electrode CAD assembly

a) Injection Electrode
b) Insulating PEEK location ring
c) Insulating PEEK retainer

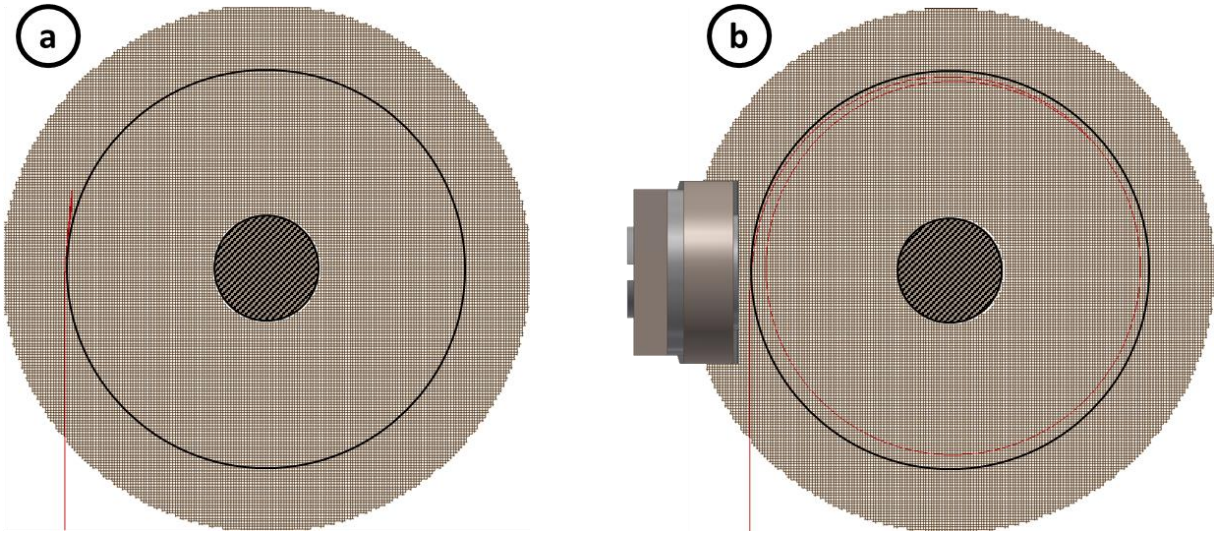

Figure 4.30 - Simulated ion trajectories (red lines)
a) Without injection electrode
b) With injection electrode

Figure 4.30 shows simulated ion trajectories with and without the injection electrode for P3 of the orbital ion trap. It can be seen that without the injection electrode, ions are only slightly deflected by the voltage on the internal electrode, which isn't enough to bring them into the trapping volume. However, with the injection electrode active, ions are pushed into the trapping volume and are retained in orbit around the internal electrode.

4.4.3 Orbital ion trap P5 and beyond – Ultra-high-field

As is true for all design and manufacturing projects, improvements can always be sought. In the case of the orbital ion trap, a fifth iteration, P5 is in the design stage at present, with multiple major and minor improvements or changes being considered, namely:

- **Ultra-high-field geometry of electrodes**, setting R1 = 5mm, and R2 = 10mm as per (Scheltema *et al.*, 2014), would allow an increased electric field to be used, and as a result oscillation frequencies would increase, so spectral acquisition could be achieved more rapidly and with higher mass resolution, as a greater number of oscillations would be recorded in a shorter time. This has already been modelled in CAD software, as shown in Figure 4.31. The manufacturing of ultra-high-field electrodes would require careful consideration, as the required tolerance would be

tighter than the 1µm required for the standard electrodes, the bi-arc approximation algorithm, discussed earlier in this report will be useful in this respect.

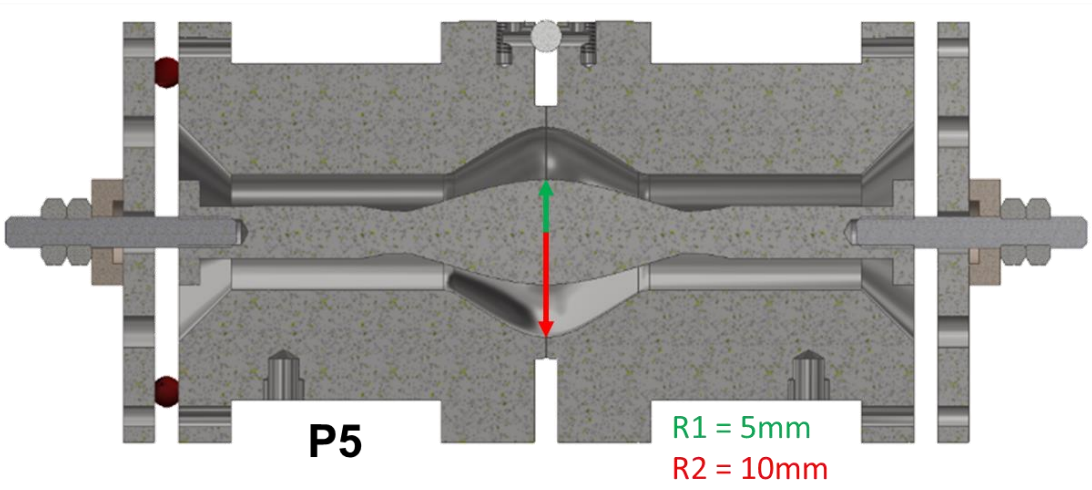

Figure 4.31 - CAD model showing ultra-high-field orbital ion trap geometry

- **Pumping apertures** could be further improved to reduce the time required to pump down to high vacuum. As evident from the cross section of P5 shown in Figure 4.28, there is a reduced volume around the trap, this is advantageous in that less residual gas would need to be pumped away, however it would need to be ensured that apertures are wide enough to permit sufficient flow out of the orbital ion trap whilst the system is being pumped. Pressure simulations could be carried out using Molflow+, a Monte Carlo simulation package developed in CERN for calculating pressures in ultra-high-vacuum systems of arbitrarily complex geometry, (Ady and Kersevan, 2014). This software was used extensively in the initial design of the ion transfer assembly from the J105 to the orbital ion trap.

- **Revised ion injection lens,** including a further focussing lens as part of the injection assembly would allow improved transmission of ions into the trap, as well as offering greater control over their angle of entry. This would require an iterative process of design, simulation and testing to achieve.

- **Faster installation** could be designed for by revising electrical connections, and modifying the mounting platform to remove the need for unfixed ruby balls as locators. At present, the installation or removal of the orbital ion trap from vacuum takes around one hour, once the J105 sample analysis chamber and orbital ion trap

transfer assembly have been vented to atmosphere and the orbital ion trap turbopump demounted. This time could be reduced if the Stahl cryoamplifier did not need to be removed with the orbital ion trap, or if the orbital ion trap could be reduced in size to fit through one of the 2.75” viewports on the chamber – this would mean the turbopump would not need to be removed to install a new ion trap, or make small modifications.

4.4.4 XY Deflectors

As a response to some challenges in obtaining optimal ion transmission from the J105 to the orbital ion trap, a set of deflector electrodes were designed to fit within the constraints of the existing ion transfer assembly, allowing for finer control over ion trajectories immediately prior to entering the ion trap. The deflectors are in the form of two orthogonal pairs of 316L stainless steel deflector plates, housed inside an insulating PEEK cylinder, as shown in Figure 4.32, various similar designs for ion deflectors exist in the literature, such as (Dahl *et al.*, 1999). By applying different voltages to opposing plates, a transverse velocity component is added to each passing ion, thus deflecting ion trajectories in X and Y directions, orthogonal to the axial direction of initial ion trajectories. A plate length of 7mm was chosen, with a gap length of 1mm, to ensure that the electrostatic field between the detector plates is linear by minimising the penetration of external fields into the deflector region, with a length-to-gap ratio of 4.0 or above found to be satisfactory in the literature, (Dahl *et al.*, 1999). An outer diameter of Ø19.05mm (≈0.75”), and an equal length, were required for the PEEK cylinder, so that the deflector assembly could replace an existing 0.75” stainless steel cylinder in the ion optics configuration, without the need for any further alterations.

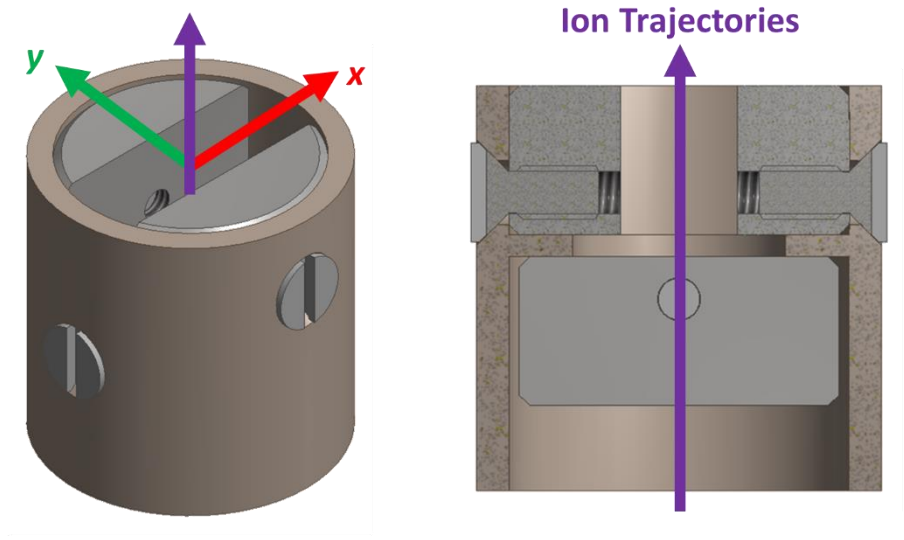

Figure 4.32 - XY Deflectors & Housing CAD model

4.5 Manufacturing Conclusions

We have designed, simulated and constructed a high mass-resolution analyser for the J105 imaging SIMS instrument. Rigorous accuracy requirements for machining the complex surfaces, especially of the inner trapping electrode, were estimated by ion trajectory simulations and have been overcome by careful low-level programming of G-code for CNC tooling. The design and assembly of ion optic components have been informed by ion trajectory simulations to optimise transfer of ions into the mass analyser, with over 90% transmission achieved in simulation.

4.6 Electrical Design

4.6.1 Electrical Connections to Orbital Ion Trap & Transfer Assembly

As discussed in the literature review, precision timing of voltages being applied to the orbital ion trap is critical to its function. The voltages required for operation of the orbital ion trap chamber are shown in Figure 4.33 and Table 4.6. The Stahl amplifier referred to is the Stahl KC 05d differential amplifier (Stahl Electronics, 2015), used to detect image currents on the external electrodes and to be housed in vacuum to reduce noise, a more detailed pin-out for this device is given in Figure 4.33. The counterpart device, to be located outside of vacuum, is the Stahl A3-5b 2-channel amplifier, (Stahl Electronics, 2013), which serves as a room temperature interface and power supply for the in-vacuum amplifier.

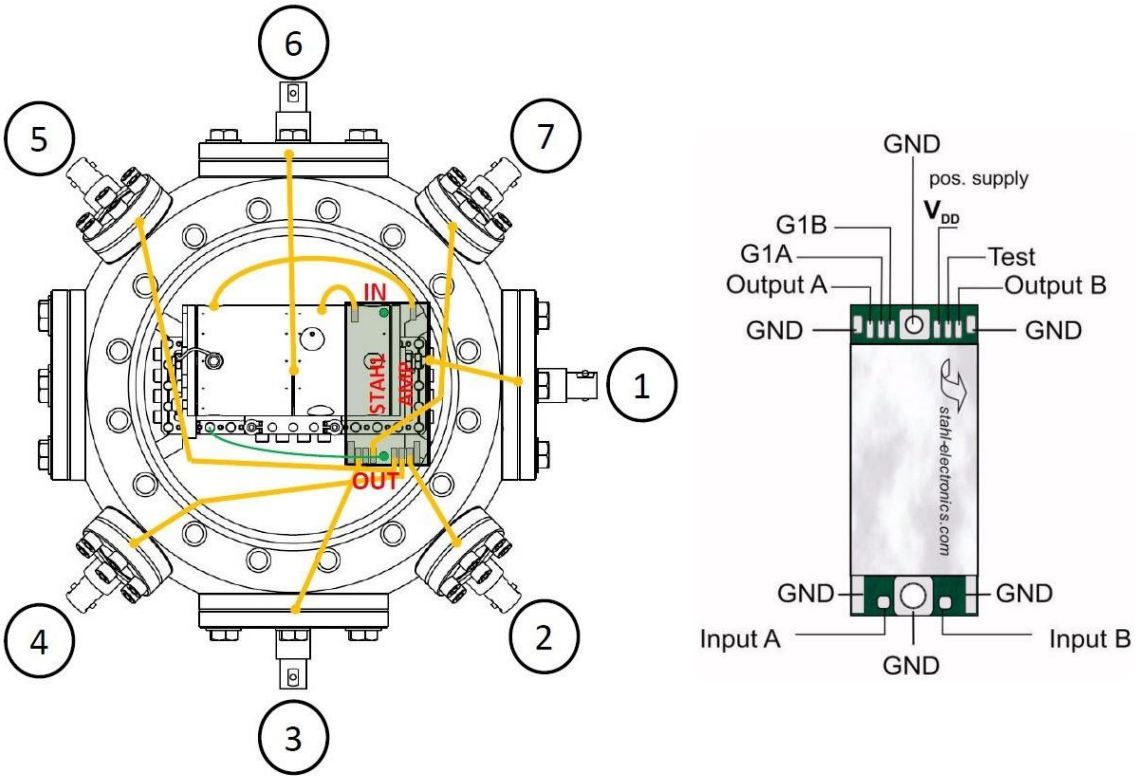

Figure 4.33 - Orbital ion trap Chamber Electrical Connections & Stahl KC05d Amplifier pin-out, (Stahl Electronics, 2015)

The external electrical connections on the vacuum chamber are all standard BNC sockets, except for the internal electrode connection as discussed in the next section, all feedthroughs are housed on either DN16CF and DN63CF flanges, with all in vacuum chamber connections made using Ø1mm Kapton insulated copper wire, rated to 10kV and 10A, (Allectra, 2014).

BNC F/T	Description	Typical Voltage	Operating Limits	Supply
1	Int. Electrode	0 to ±1kV		Trek 623B
2	Stahl Output A	-	-1.2V to +5.3V	-
3	Stahl Output B	-	-1.2V to +5.3V	-
4	Stahl –ve supply G1A	-3.1V @ 4.2K -4.7V @ 300K	+1V to -5.5V	Stahl A3-5b
5	Stahl –ve supply G1B	-3.1V @ 4.2K -4.7V @ 300K	+1V to -5.5V	Stahl A3-5b
6	Float Voltage	0 to ±200V		J105 ToF HV
7	Stahl +ve supply V_{DD}	+3.5V to +4.5V Ideally 4.4V	-1V to +5.3V	Stahl A3-5b

Table 4.6 - Orbital ion trap Chamber Voltages

As stated in Table 4.6, the voltages supplied to the in vacuum Stahl amplifier, via BNC feedthroughs numbers 4, 5 and 7 will be supplied by the aforementioned Stahl A3-5b, which also incorporates a PID feedback loop to adjust negative supply voltages G1A and G1B to ensure a nominal $1.9V_{DC}$ output.

4.6.2 Voltage supply to internal electrode

The supply voltage to the internal electrode is of critical importance to the function of the orbital ion trap, it must have a suitably fast rise-time to trap ions as they enter the trap, whilst also offering low noise to produce stable ion orbits. Of the considered options one of the most promising was a high voltage power amplifier, which would allow fast and easily controlled ramping of voltages with slew rates in excess of 150V/µs, (Trek, 2015). A second option would be to a gallium nitride half-bridge evaluation board, (GaN Systems, 2015), capable of slew rates ≈40V/ns, which would allow incredibly fast voltage ramps. The gallium nitride board would however offer less control over the final voltage of the device, which would be controlled by the set point of a separate high voltage power supply, likely to be the already acquired Applied Kilovolts 0 to ±5kV supply (Exelis Applied Kilovolts, 2013).

From the investigated options, a high voltage power amplifier was preferred, and a ±2kV Trek Model 623B was purchased, with gain of 1,000V/V, slew rate in excess of 300V/µs and $<80mV_{RMS}$ noise according to specifications (Trek, 2015). The amplifier was tested upon arrival with the slew rates up to ~250V/µs measured coarsely using an oscilloscope. A 2kV step was requested and the output had risen by ~500V within

2µs, giving a slew rate of 250V/µs, as shown in Figure 4.34. The discrepancy between specified and measured slew rates could be due to a number of factors, not least that the Trek unit is second-hand and so may be showing reduced performance due to exposure to excess temperature, current or voltage in previous operation. The measured slew rate of 250V/µs is acceptable for supplying the internal electrode voltage for the orbital ion trap.

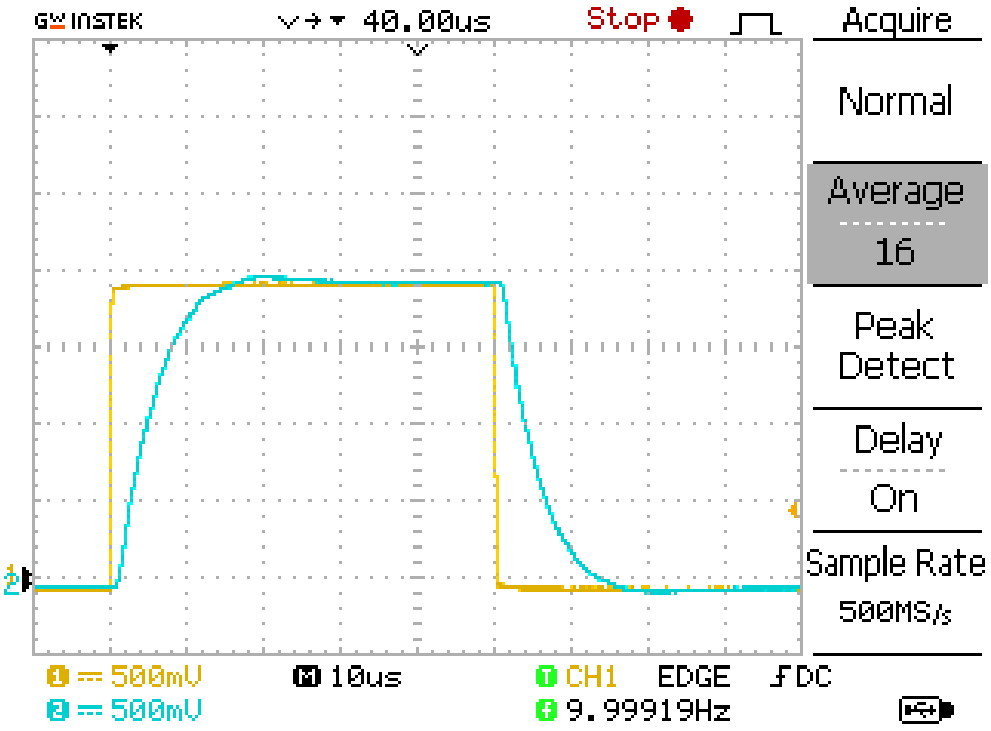

Figure 4.34 - Trek 623B amplifier 2kV step response
1. Input voltage – 0 to +2V Step input
2. Output voltage – Trek voltage monitor
Note: Output voltage is scaled down by factor of 1,000

The connection from the amplifier to the internal electrode is through a safe high voltage (SHV) vacuum feedthrough. An SHV connector is similar to other RF connectors used for terminating coaxial cables, however it is designed specifically designed for high voltage applications with a recessed connector preventing accidental mating with a low voltage plug. The specific feedthrough chosen from Allectra, is rated to 5kV and 5A (Allectra, 2014), these values are in excess of the maximum deliverable voltage and current of the Trek amplifier.

Initial control of the modulation of the voltage sent to the internal electrode was controlled using a National Instruments PXI 5412 arbitrary waveform generator (National Instruments, 2004). The software to control this was written in LabVIEW with

the front panel shown in Figure 4.35 (National Instruments, 2013). The software allows the user to specify the ion energy being trapped, and the geometry of the orbital ion trap being tested. From this, an ideal internal electrode voltage is calculated, with a signal with magnitude of 0.1% of this value sent to be amplified by the Trek 623B unit. The user could also specify an RF waveform to be superimposed on top of the DC voltage, this would the permit parametric excitation of ions, as described in Chapter 3.

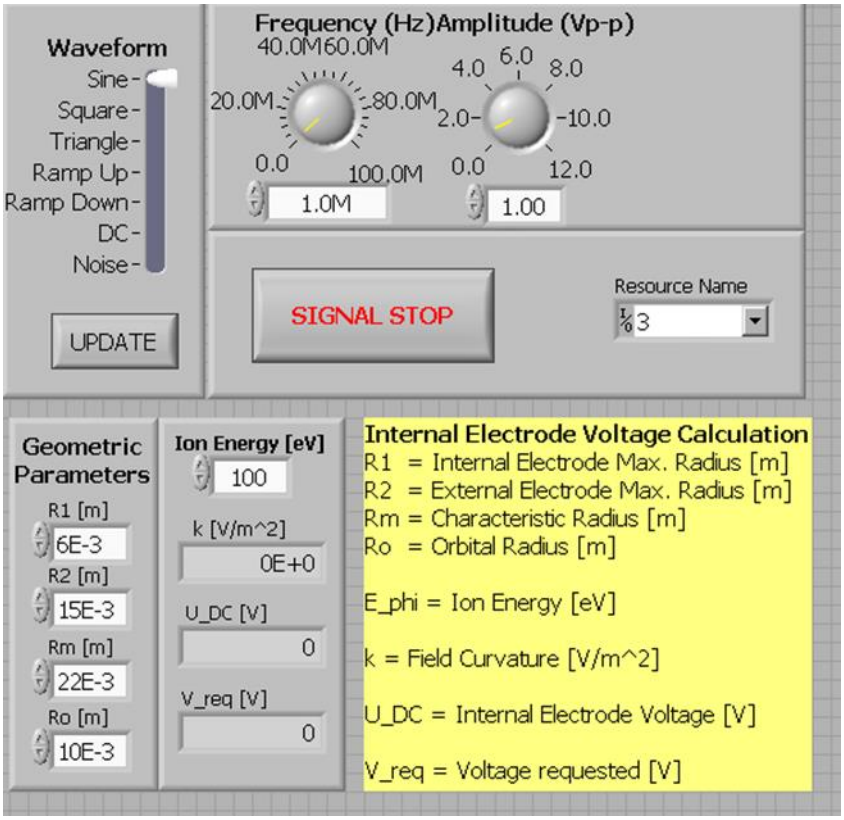

Figure 4.35 - LabVIEW front panel for control of the internal electrode voltage, outputting an arbitrary waveform to the Trek 623B amplifier.

The float voltage applied to the eV float optics and the focussing voltage for the Einzel lens, with connection locations detailed below, was supplied by two spare 0 - ±200V outputs located on the ‘ToF HV’ controller of the J105, controllable through Ionoptika’s SIMS Mainframe software.

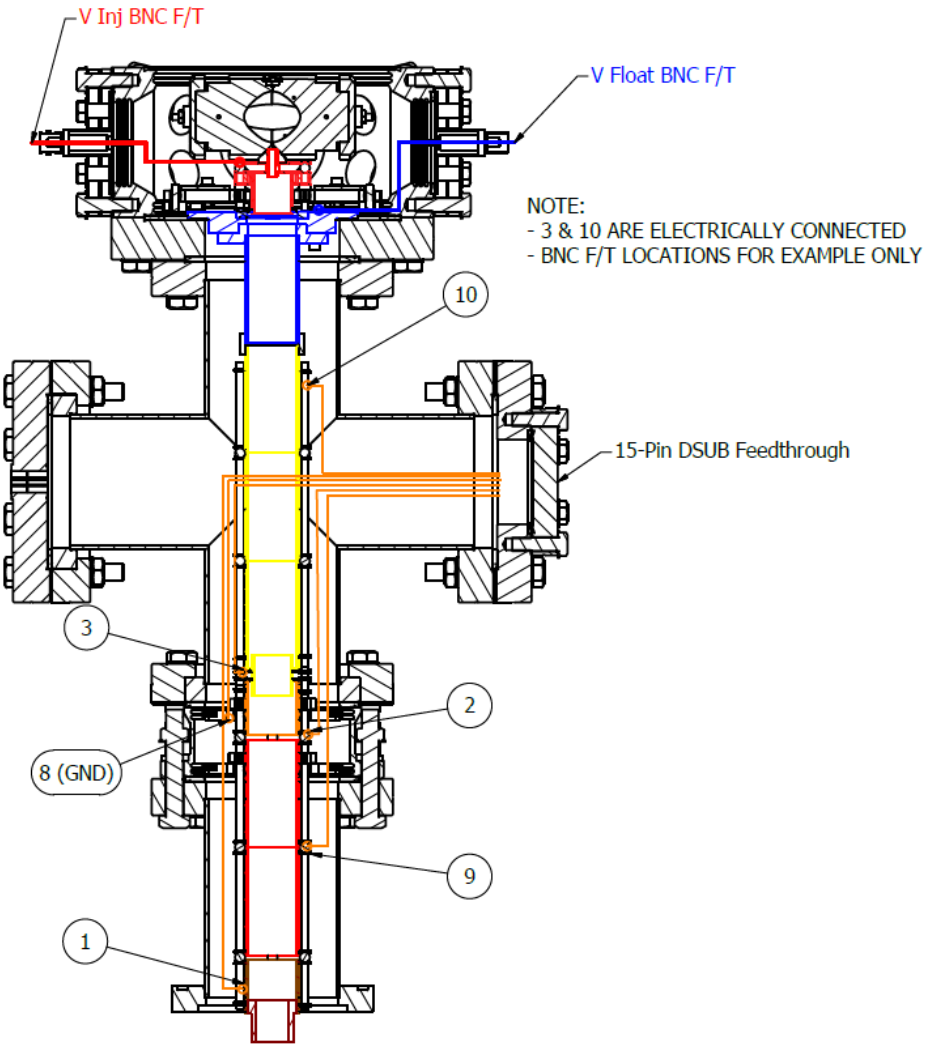

Figure 4.36 – Ion optics Transfer Electrical Connections

The electrical connections to the Transfer Assembly are shown in Figure 4.36. Connection point 9 is the Einzel lens focussing element of the transfer assembly, which will be held at a different voltage from the rest of the assembly components. All other connections, 1, 2, 3, 10, V_{Float} and V_{Inj} will be held at a float voltage of magnitude 50V, 100V, 150V or 200V, as chosen for the ESA of the J105. All connections from the 15-pin feedthrough are made in vacuum with Kapton insulated wire, however as they are connected to the Sub-D feedthrough via ribbon cable they are only rated to 1kV and 2A, (Allectra, 2014). The additional connections made through the orbital ion trap chamber to V_{Float} and V_{Inj} have been electrically isolated from the main ion transfer optics, so as to allow current to be measured at as many different points leading up to the orbital ion trap as possible, making it much easier to tune transfer voltages when initially attempting to detect ions.

4.6.3 Stahl Amplifier KC 05d

The differential amplifier to be used for the detection of induced image currents in the orbital ion trap external electrodes is the Stahl KC 05d, (Stahl Electronics, 2015). The device is a highly sensitive, high input impedance, voltage preamplifier, which has been tested on the benchtop outside of vacuum to assess its noise performance. The covered frequency range of 3kHz to 1MHz comprehensively covers the expected oscillation frequencies of ions in the orbital ion trap.

Noise tests were carried out by connecting the output from the Stahl amplifier into a National Instruments PXI 5122 digitizer (National Instruments, 2003), with the amplifier switched on and powered by a Stahl A3-5b room temperature controller, the amplifier gain was set to 500 unless otherwise stated (Stahl Electronics, 2013). A LabVIEW program was written to record the noise transient, the front panel of which is shown in Figure 4.37, the following parameters are specified by the user:

L = Record Length, the minimum number of data points in each recording
R = Sampling rate of digitizer for recording [Hz]
$\mathbf{t_r}$ = Recording interval, the approximate time between recordings [minutes]
n = Number of loops between recordings, controls $\mathbf{t_r}$

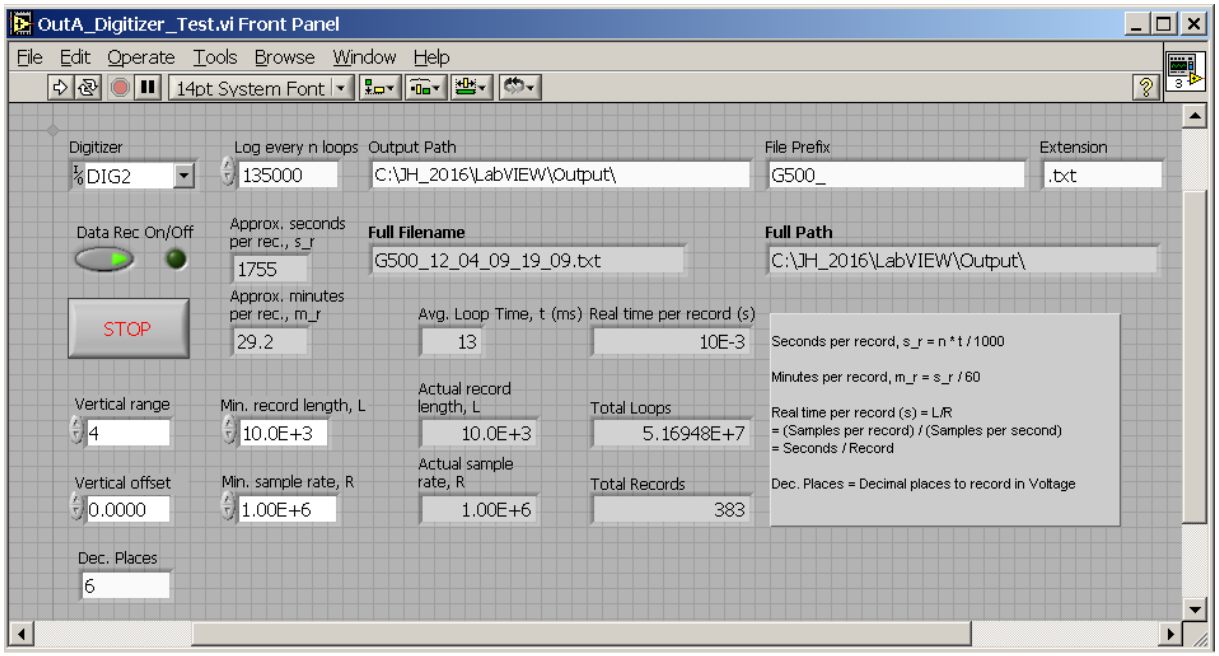

Figure 4.37 - LabVIEW data collection front panel

The LabVIEW program was written in LabVIEW 7.1 as this is the installed variant on the PXI chassis housing the digitizer, and is known to be compatible with the installed PXI modules.

Unless otherwise stated, the noise measurements discussed are of length ~1s, with a sampling rate of 100MHz. Initial recordings were taken over the course of 24 hours at hourly intervals to account for potential variations in lab temperature or localised electrical interference which could affect the amplifier. The recorded data was imported into MATLAB for analysis using a fast Fourier transform (FFT). Figure 4.38 shows the noise spectrum found from the initial recordings overlaid on the same axes, two dominant peaks can be seen at 263kHz and 351kHz, both of which were unexpected and appeared in all of the recorded datasets. The maximum noise intensity was 0.128V. The manufacturer of the amplifier, Stahl Electronics, suggested that noise such as this could be due to a poor grounding of the amplifier, or self-oscillations induced from insufficient shielding between the two input connections.

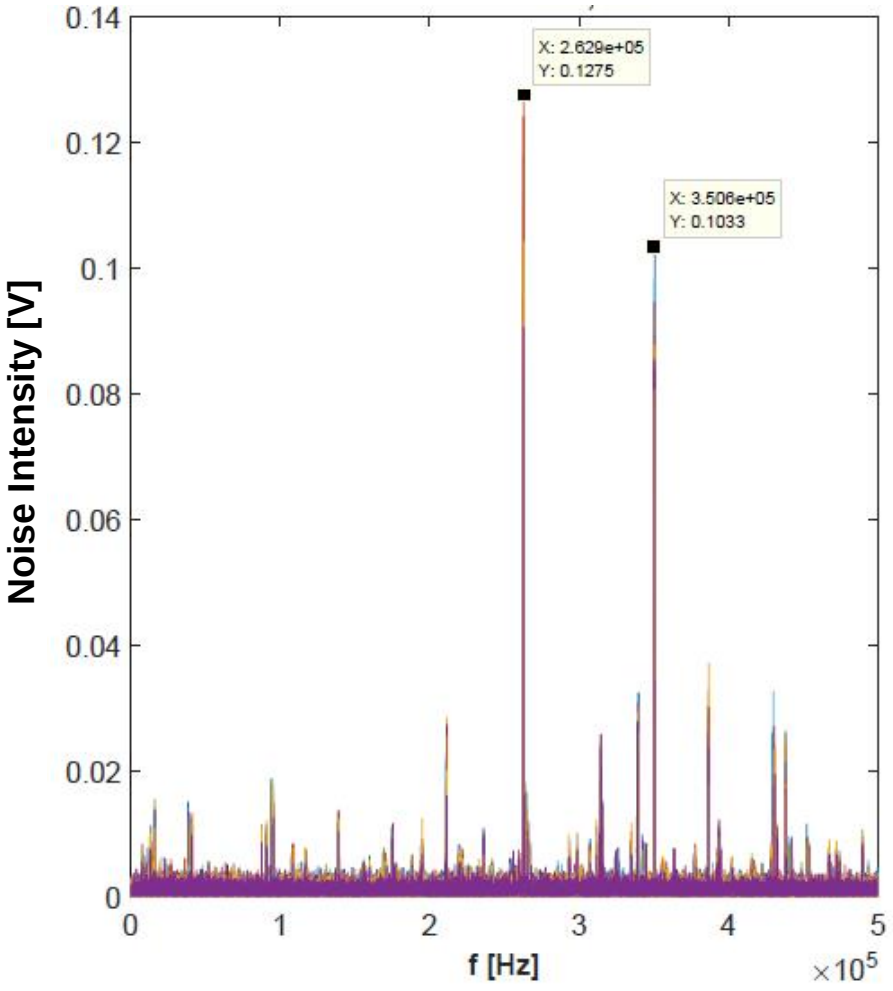

Figure 4.38 - FFT of initial Stahl noise recordings

After the comments from the manufacturer, a simple enclosure was assembled to shield the amplifier from interference, to allow noise characteristics to be assessed in an environment analogous to the orbital ion trap vacuum chamber, but with easier access. A CAD model of the enclosure is shown in Figure 4.39, with a grounded shield also shown covering the two input connections.

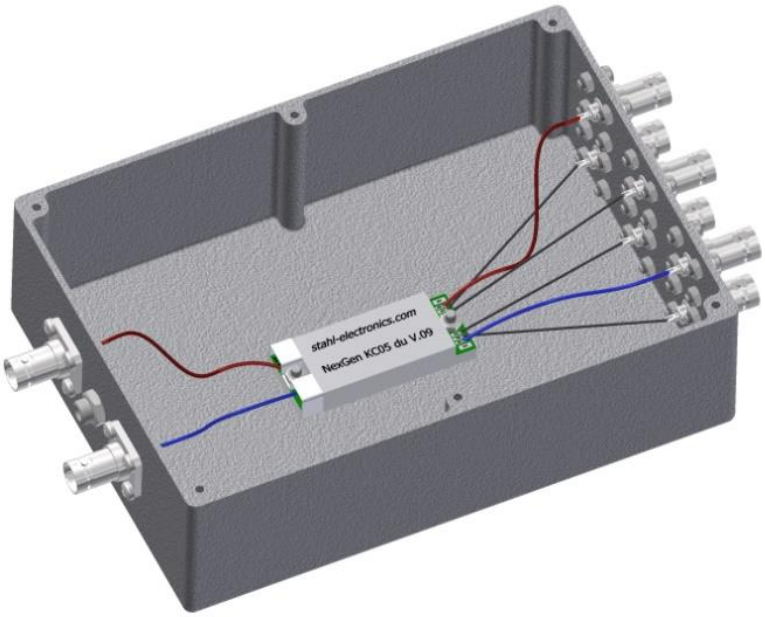

Figure 4.39 - CAD model of Stahl amplifier testing enclosure

After this, further noise recordings were taken, with a significant reduction in noise found, as shown in Figure 4.40, where there are no dominant frequencies in the noise spectra. In this case, the maximum noise intensity was 68.2µV, representing a reduction by more than three orders of magnitude from the initial noise recordings. These recordings were approximately in line with the manufacturer's stated voltage noise density of 1µV/sqrt(Hz) to 10nV/sqrt(Hz) for frequencies of 3kHz to 500kHz. The noise would be expected to further reduce once the amplifier is installed in an ultra-high vacuum environment.

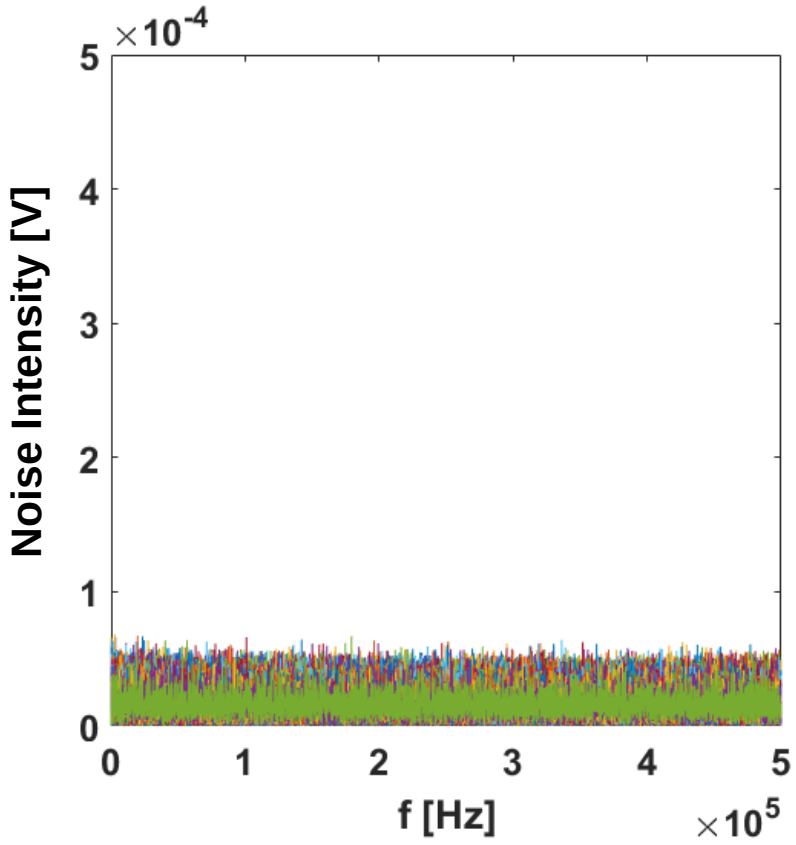

Figure 4.40 - FFT of improved Stahl noise recordings

4.6.4 Ion Detection Electronics & Software

The timing and modulation of the application of the voltage to the internal electrode was controlled using a National Instruments PXI 5412 arbitrary waveform generator and PXI 5122 digitizer, (National Instruments, 2004), (National Instruments, 2003). The software to control this was written in LabVIEW with the front panel shown in Figure 4.41 (National Instruments, 2013). The purpose of the software was to trigger the output of two square waveforms, with user selectable parameters to control their amplitude, DC voltage offset, frequency, duty cycle, relative phase, as well as specifying a desired delay between the two. One of these waveforms was sent to the Trek 623B amplifier to provide the internal electrode voltage, and the other was sent to an ion optical element in the ion transfer assembly, to blank the ion beam after a small packet of ions had been injected into the ion trap.

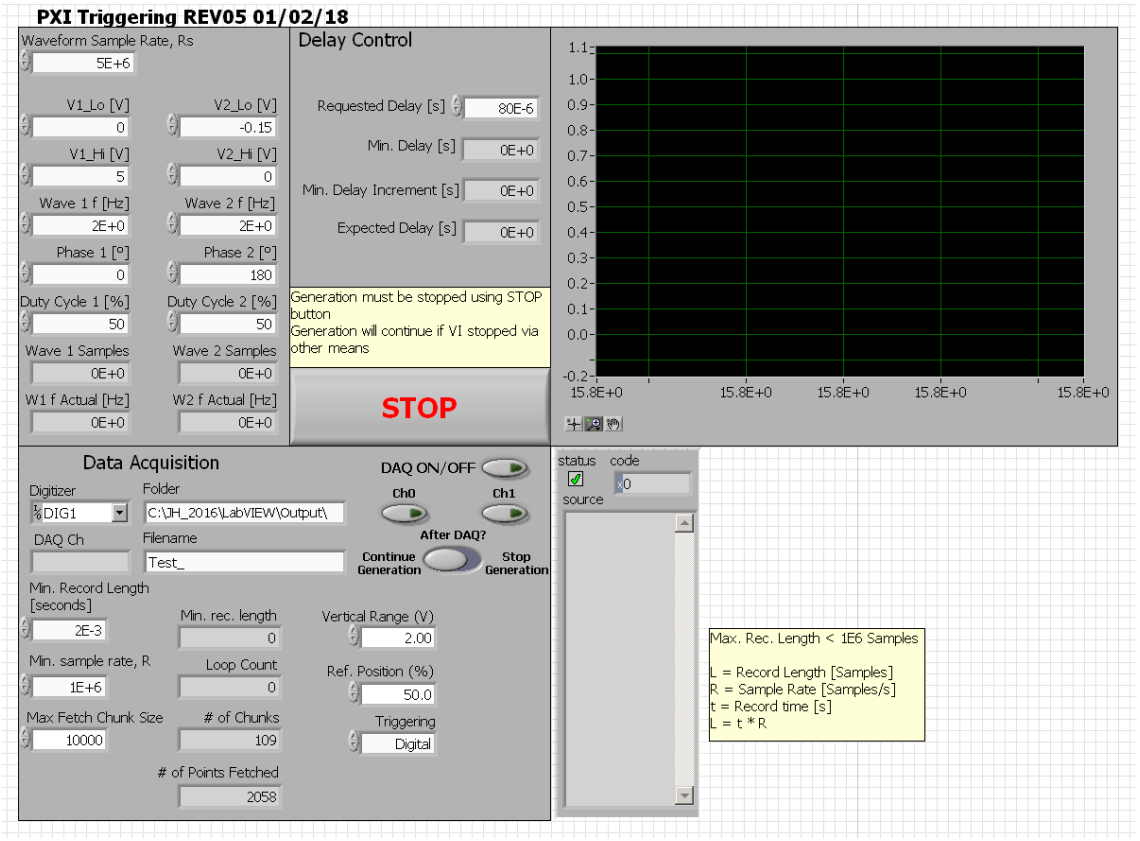

Figure 4.41 - LabVIEW front panel of software written to trigger internal electrode voltage and subsequent data recording.

4.7 Mass Range of Orbital Ion Trap

As with any mass spectrometer, there are limitations in mass resolution and the range of ion masses which can be analysed. One limiting factor of the operational mass range of the orbital ion trap is the range of frequencies which can be used to excite ions, if parametric excitation is employed as described in Chapter 3. This frequency range is directly related to the mass of ions by equation (1.2) found in the introduction to this report.

Figure 4.42 shows the parametric excitation frequencies of ions with different kinetic energies across a mass range from 0 – 2,500u. The effect of restricting excitation frequencies to between 60 kHz and 1 MHz is also shown by the horizontal lines of cut-off frequencies, to give an example of the potential excitable mass range of the orbital ion trap.

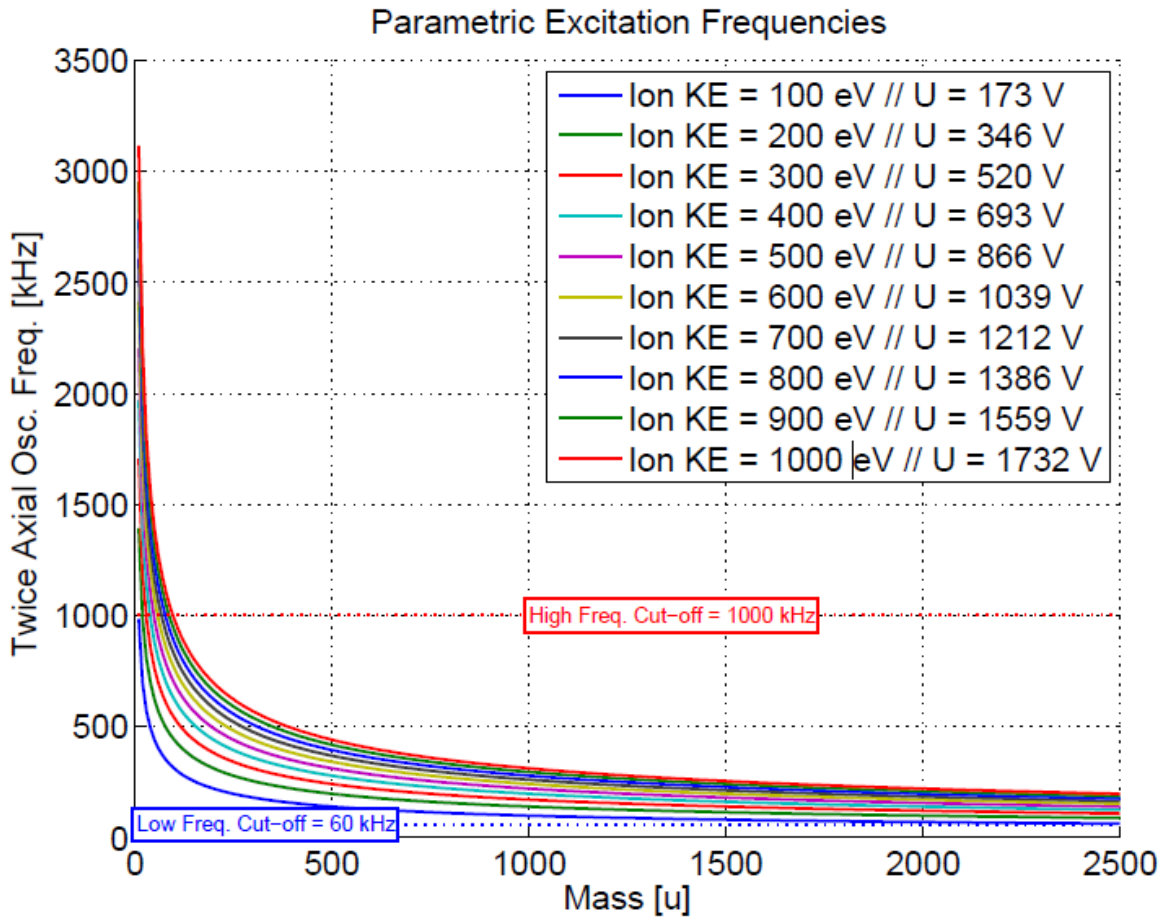

Figure 4.42 - Parametric Excitation Frequencies

These cut-off frequencies were chosen as they correspond to a mass range slightly larger than 10u – 2,500u for ions with 100eV of kinetic energy, (10u = 990 kHz, 2,500u

= 62 kHz). This mass range is comparable to those noted in the literature for quadro-logarithmic ion traps, (Makarov, 2000), (Hardman and Makarov, 2003), (Hu *et al.*, 2005), (Perry *et al.*, 2008). In practice, it is believed that the orbital ion trap will most routinely be used for the analysis of ions with mass in excess of 100u, as this is the region in which high resolution mass spectrometry becomes most useful. One example being the ability to accurately separate hydrides from elemental peaks above 100u, for which the required mass resolution is beyond the 10,000 achievable using the J105, (Stephan, 2001).

A band-pass filter could be designed to attenuate noise outside of the operational region. As the cut-off frequencies lie within two decades of one another, it would be possible to achieve a low ripple pass-band whilst maintaining high roll-off at the cut-off frequencies.

An isolating transformer will be used to couple the DC and RF voltages to be applied to the internal electrode, this will prevent the high voltage DC from travelling back into the low voltage RF supply. The design of such a transformer is dictated by the desired RF frequencies, stated above as between 60 kHz and 1 MHz. A 1:1 transformer will be used in the configuration shown in Figure 4.43 so as to couple the DC and RF voltages without amplification.

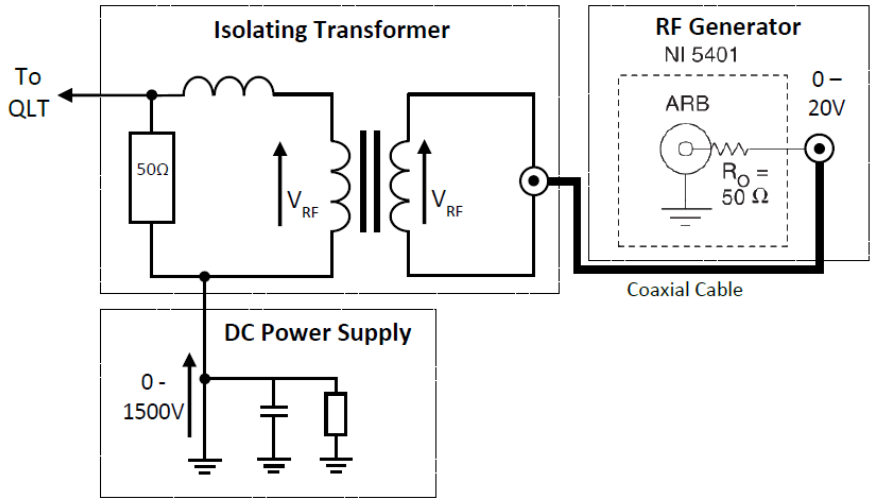

Figure 4.43 - Isolating Transformer Schematic

4.8 Future Design Improvements

During this research project, there have been many small observations which could lead to future improved designs if further generations of ion transfer assembly and orbital ion trap were to be constructed. This section will remark on the feasibility, advantages, and disadvantages of some of these ideas, including:

- Shortening the ion transfer assembly
- Moving the position of the ion deflector elements further from the injection aperture, or add a second pair of deflectors
- Transferring ions at a higher energy
- Adding a gate valve to the assembly

In the case of shortening the ion transfer assembly, this should have the effect of improving ion transmission, whilst also reducing the overall size of the orbital ion trap addition to the J105. This would decrease the total volume required to be evacuated, meaning that either better vacuum could be achieved with the current arrangement, or a less powerful, and less expensive, pumping system could be used to attain the same vacuum performance. This could be achieved by reducing the length of the ion optics, and mounting them on a reduced diameter DN40CF (2.75”) flange coming off the ESA, rather than the present DN63CF (4.5”) flange used. The disadvantage of shrinking the assembly would be the associated reduction in available space in vacuum, which would make routing electrical connections and maintenance more difficult. There would also be an associated cost in re-designing the electrical connections and feedthroughs for smaller flanges. As a result, size reduction should only be considered in the case of installing the instrument in a lab environment where the present height of the extension above the J105 would not be able to fit.

Another potential design improvement would be to move the electrostatic ion deflectors further from the injection aperture of the orbital ion trap. Doing so would increase the effective deflection of the ion beam, as it would have further to travel after passing through the deflectors. However, this would come with the drawback of increased sensitivity to voltage instability, as a small change in deflector voltage would result in a larger beam deflection at the point of injection into the orbital ion trap. Instead, a second pair of deflectors could be added at the base of the ion transfer optics, this would give further control over the position of the ion beam, allowing a parallel shift in the ion beam to be realised, but would come at the expense of a further high voltage

power supply being required for the second set of deflectors. A re-tuning of the focussing elements of the ion optics would also be required, as a second set of orthogonal deflector plates would introduce some beam distortions. These distortions, caused by transition field edge effects at the entrance and exit of the deflectors, would be more significant than those caused by the currently employed deflectors, as the ion beam would travel further after the point of deflection, (Dahl *et al.*, 1999).

As will be discussed in Chapter 5 of this thesis, transferring ions at a higher energy could also be beneficial, as ions trapped at a higher energy will oscillate at a higher frequency, leading to higher mass resolution spectra for the same detection duration. This would require an accelerating ion lens to be located after the exit aperture of the ESA on the J105, as ions leave the ESA with kinetic energy of 50eV, 100eV, 150eV or 200eV, depending on the user selected float voltage, at each energy level a distribution of ion energies of approximately ±1% is expected. Accelerating the ion beam would cause a commensurate widening of the absolute kinetic energy distribution, for example if ions were accelerated from 100 ± 1eV to a nominal energy of 1000eV, and a ±1% energy distribution was maintained, ions would now have a spread of ±10eV. In theory, this should not be a problem in terms of ion trapping, as the orbital ion trap can accept a broad energy range, as demonstrated in ion trajectory simulations in the literature (Hu *et al.*, 2005).

4.8.1 Gate Valve

A further physical improvement which could be made to the ion transfer assembly would be the addition of a gate valve between the J105 ESA and the transfer assembly. This would permit easier maintenance and adjustment of the orbital ion trap as the gate valve could be closed to isolate the ion transfer assembly from the J105 sample analysis chamber, meaning the main analysis chamber of the J105 would not need to be vented to atmosphere as is currently the case.

A suitable gate valve would be the Kurt Lesker SG0250MVIK, which possesses two ISO63-K flanges which could mate directly with the existing transfer assembly, (Kurt J Lesker, 2005). A CAD model of such an arrangement is shown in Figure 4.44.

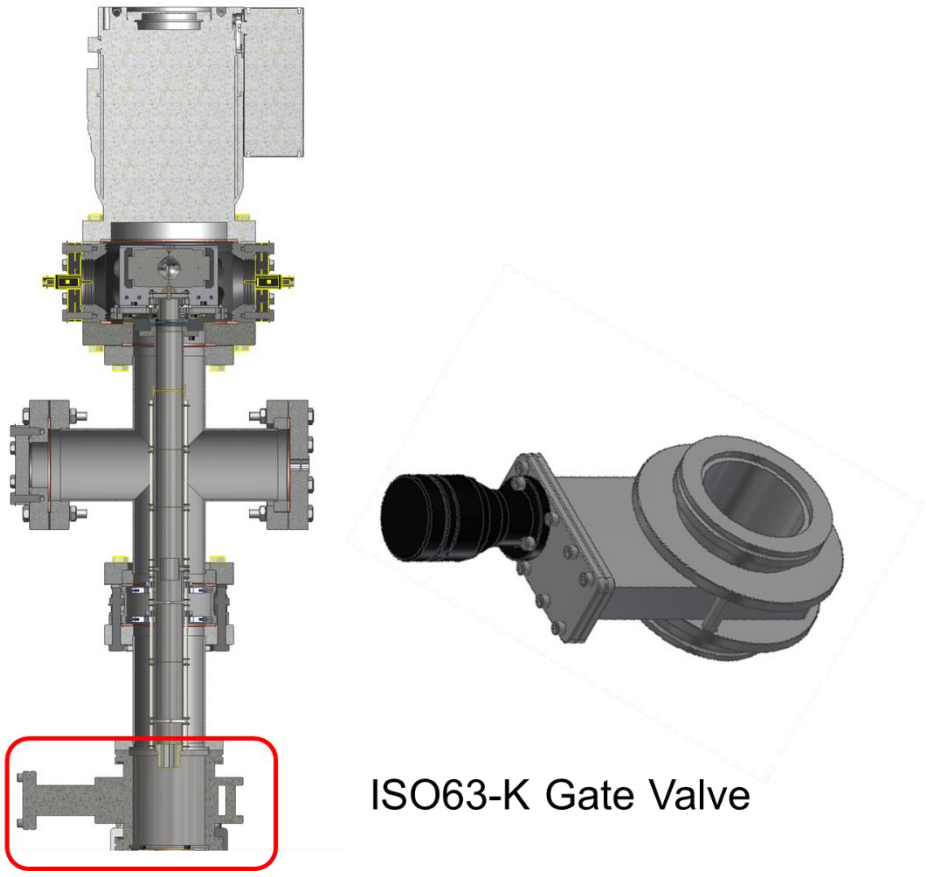

Figure 4.44 - CAD model of ISO63-K gate valve and its position in the transfer assembly

However, the installation of a gate valve would not be without issue, with the biggest concern being the reduction in the transmission of ions to the orbital ion trap, as there would be a large section introduced without any guiding ion optics, where the surrounding region is at ground potential. This could be overcome by modifying the gate valve to integrate ion optics by redesigning the valve blade, as has been done in (Pittman and O'Connor, 2005), although this would be costly and potentially damaging to the sealing integrity of the gate valve. Another option would be to float the entire gate valve at the desired electrostatic float voltage to promote ion transmission, this is feasible if non-conducting ISO-K centring rings are used to isolate the gate valve from the rest of the transfer assembly and the ESA. This would need to be done with caution, as the gate valve would require an earthed electrical safety enclosure to be secured around it to prevent the risk of electrical shock.

Chapter 5. Ion Trajectory Simulations

5.1 Simulation Introduction

Simulations of ion trajectories were carried out using SIMION 8.1, (SIS, 2015). SIMION is a software package used for the calculation of both 2D and 3D electrostatic or magnetic fields, and the simulation of charged particle trajectories within those fields. SIMION employs finite difference methods to solve the required partial differential equations particularly the Laplace equation to evaluate potential fields, whilst using Runge-Kutta methods to solve ordinary differential equations (ODEs) in order to model ion trajectories in three dimensions. The Laplace equation is solved when SIMION calculates the potential field in a potential array (.PA) file.

SIMION is user programmable, allowing electrodes of arbitrarily complex geometry to be defined with geometry (.GEM) files. In this project SIMION has been exploited to create multiple simulations, including; the ion optics required to transfer ions from the Ionoptika J105 into the orbital ion trap, modelling ion motion within the orbital ion trap for various initial conditions, and parametric excitation of ions once trapped.

All simulations were run on a Dell Precision T1700 Windows 7 PC with 16GB of RAM, unless otherwise stated.

Simulation environments in which ions were flown, known as SIMION ion optics workbenches, were initialised by following these steps:

1. An unrefined potential array file (PA#) was created, either by user programmed GEM file, or by converting a 3D CAD model from STL file to a geometry file within SIMION.

   In user programmed GEM files, the geometry was defined either as a series of co-ordinates, or by using the LUA commands built in to SIMION to define geometry using analytical expressions.
2. The created PA# was then refined in SIMION, to accurately evaluate the potential field within the defined geometry. Unless otherwise stated, a refine convergence criterion of 1E-6V was used.
3. The refined potential array file (PA0) was then loaded in a SIMION ion optics workbench, where electrode voltages, ion initial conditions, and simulation parameters, such as ion time markers for data logging, could be set. All of these

parameters were controlled through a mixture of user programmable LUA files, and options included within the SIMION workspace GUI.

4. The simulation of ion trajectories within the workbench could then be run, with output data recorded as specified by the user. During operation user programmed LUA files were used to control dynamic elements of the simulation.

Some uses of LUA files which were developed for simulations presented in this chapter include:

a) Modifying the format of output data, to allow more efficient data processing.
b) Running simulations in batch mode, to programmatically alter ion initial conditions, or initial electrode voltages, between runs without requiring user intervention.
c) Implementing time dependent electric or magnetic fields, such as radio-frequency voltages applied to the orbital ion trap electrodes for modelling the parametric excitation of ions.
d) Imposing a maximum flight time on ions, to prevent simulations running in perpetuity.

5.2 SIMION Calculations

This section will briefly describe the methods used by SIMION to calculate potential fields, and then simulate ion trajectories within these fields.

5.2.1 SIMION Potential Field Calculations

As stated, SIMION uses finite difference methods (FDM) to evaluate the potential fields generated by the specified electrode geometry and associated voltages. Briefly, FDM describes a number of numerical approaches to solving differential equations through discretization. In SIMION, finite difference methods are employed when ‘refining’ a potential array, this is the process of estimating the electrostatic potential produced by user defined electrode geometry, before ion trajectories can be simulated. Finite difference methods are used to solve the Laplace equation, a partial differential equation, given in terms of potential in two dimensions in equation (3.41), subject to the given boundary conditions which constrain the solution. The boundary conditions are; the Dirichlet boundaries imposed by the electrode surfaces, where the potential is specified, and the Neumann boundary conditions imposed by planes of symmetry, or non-electrode surfaces, where the normal derivative of the potential is specified, (Dahl,

2000), (Giglio, 2015). Both planar and rotational symmetry are widely used to reduce the complexity of potential field calculations in SIMION, (Dahl, 2000).

$$\Delta\phi = \nabla^2\phi = \frac{\partial^2\phi}{\partial x^2} + \frac{\partial^2\phi}{\partial y^2} = 0 \qquad (5.1)$$

As applied to the refine process in SIMION, FDM calculations consist of estimating the potential of an unknown point in a 2D or 3D array by the average potential of its nearest neighbours. In two dimensions, this process can be represented using a grid array, as shown in Figure 5.1.

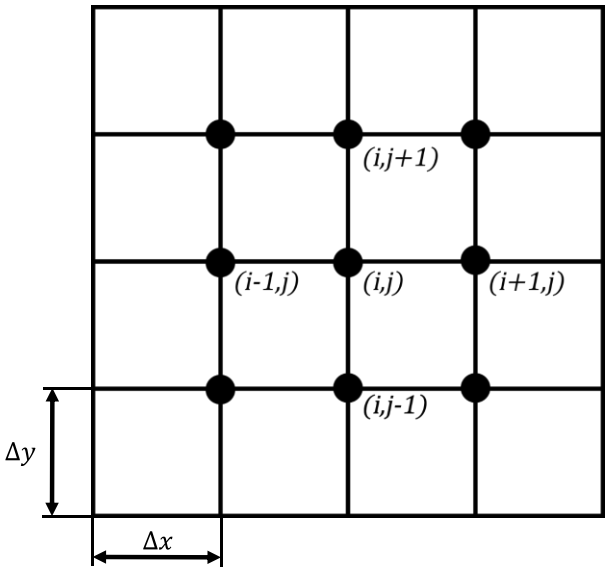

Figure 5.1 - Two dimensional potential grid array, illustrating the notation used for grid nodes during finite difference calculations.

The initial potential of all points not defined as electrode surfaces is set to zero. The expression which calculates the potential of a grid point can then be found using finite difference approximations of the second derivatives in the Laplace equation, derived from the Taylor series expansion, (Sauer, 2006). These approximations are shown for two dimensions in equation (5.2). These approximations can then be substituted into the Laplace equation (3.41), as shown in (5.3), which can then be re-arranged to produce the approximation for the potential of an array point, $\phi_{i,j}$, based on the average of its nearest neighbours, assuming that the grid spacing is equal in both directions, $\Delta x = \Delta y$.

$$\left.\frac{\partial^2\phi}{\partial x^2}\right|_{i,j} \approx \frac{\phi_{i+1,j} - 2\phi_{i,j} + \phi_{i-1,j}}{(\Delta x)^2}$$
$$\left.\frac{\partial^2\phi}{\partial y^2}\right|_{i,j} \approx \frac{\phi_{i,j+1} - 2\phi_{i,j} + \phi_{i,j-1}}{(\Delta y)^2} \quad (5.2)$$

$$\frac{\phi_{i+1,j} - 2\phi_{i,j} + \phi_{i-1,j}}{(\Delta x)^2} + \frac{\phi_{i,j+1} - 2\phi_{i,j} + \phi_{i,j-1}}{(\Delta y)^2} = 0 \quad (5.3)$$

$$\phi_{i,j} = \frac{1}{4}(\phi_{i-1,j} + \phi_{i-1,j} + \phi_{i-1,j} + \phi_{i-1,j}) \quad (5.4)$$

Repeat iterations of this calculation are then carried out across the entire potential array to refine the solution, with each point eventually converging to a value within the tolerance of the user selected convergence criteria, (Dahl, 2000).

5.2.2 SIMION Trajectory Calculations

Once a potential grid array has been refined, SIMION is then able to model ion trajectories within this 2D or 3D space based on the initial conditions of each ion, encompassing; mass, charge, position, velocity direction vector, kinetic energy and time of birth, which allows for ions to be initialised after the simulation has begun.

Ion trajectories are calculated in SIMION by an iterative process, solving ordinary differential equations through numerical integration using a fourth-order Runge-Kutta method, which has the advantage of allowing adjustable time step sizes, whilst maintaining accuracy (Dahl and Appelhans, 2000).

Initially, the potential at the current location of the ion must be found, this is done by taking a 4x4 array of grid points around the ion in question, and constructing a four-point “spider” extending ±0.5 grid units in orthogonal directions from the position of the ion, as shown in Figure 5.2, and described in (Dahl, 2000). The potential at each end-point of the spider is then linearly interpolated from the nearest four grid array points surrounding it, with the potential at the location of the ion taken as the average of these four results. The potential gradient in x and y directions at the ion location is taken as the difference between horizontal and vertical spider end-points respectively.

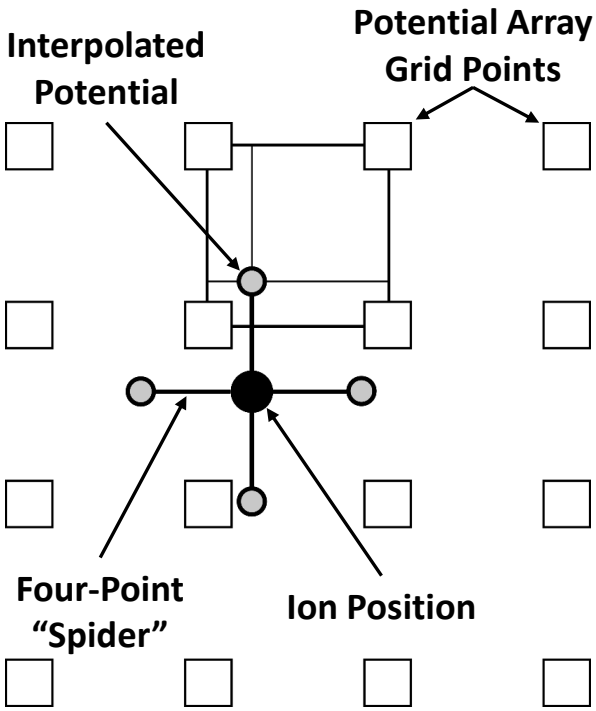

Figure 5.2 - Diagram showing how the potential field and potential gradient are found for an arbitrary ion position, using a 2D 4x4 array of grid points.

The ion acceleration can then be calculated at this time step by combining the Lorentz law, equation (5.5), and Newton's second law of motion, equation (5.6), as shown in (5.7).

$$\mathbf{F} = q(\mathbf{E} + \mathbf{v} \times \mathbf{B}) \tag{5.5}$$

$$\mathbf{F} = m\mathbf{a} \tag{5.6}$$

$$\mathbf{a} = \frac{q}{m}(\mathbf{E} + \mathbf{v} \times \mathbf{B}) \tag{5.7}$$

From this point, the ion velocity and position at the next time step can be found using numerical integration, with the fourth-order Runge-Kutta method. The first step is to rewrite the second-order differential equation of (5.7) as a system of coupled first-order differential equations, as shown in (5.8).

$$\text{Let } \frac{d\mathbf{x}}{dt} = \dot{\mathbf{x}} = \mathbf{v}, \text{and } \frac{d\mathbf{v}}{dt} = \dot{\mathbf{v}} = \mathbf{a}$$
$$\begin{bmatrix} \dot{\mathbf{x}} \\ \dot{\mathbf{v}} \end{bmatrix} = \begin{bmatrix} \mathbf{v} \\ \frac{q}{m}(\mathbf{E} + \mathbf{v} \times \mathbf{B}) \end{bmatrix} \tag{5.8}$$

The fourth-order Runge-Kutta algorithm can then be applied, as shown in (5.9), adapted from (Sauer, 2006).

$$
\begin{aligned}
&x_{i+1} = x_i + \frac{1}{6}(s_1 + 2s_2 + 2s_3 + s_4) \\
&\text{Where} \\
&s_1 = \Delta t \cdot f(t_i, x_i) \\
&s_2 = \Delta t \cdot f\left(t_i + \frac{\Delta t}{2}, x_i + \frac{\Delta t}{2} s_1\right) \\
&s_3 = \Delta t \cdot f\left(t_i + \frac{\Delta t}{2}, x_i + \frac{\Delta t}{2} s_2\right) \\
&s_4 = \Delta t \cdot f(t_i + \Delta t, x_i + \Delta t s_3)
\end{aligned}
\tag{5.9}
$$

Where Δt refers to the time step used, t_i is the time at the current time step, and x_i and x_{i+1} are the solutions to the differential equation at the current and next time steps respectively. The intermediate terms, s_1, s_2, s_3 and s_4, are incremental increases in the solution, based on the product of the interval width, Δt, and an estimate of the gradient specified by the original function, $f(t, x)$. A solution to the differential equation can be found using this method given an initial value of the solution, x_0. To use this method for a coupled system of differential equations, for example those presented in (5.8), the formulae laid out in (5.9) should be vectorised, with $\boldsymbol{x}$, $\boldsymbol{f}$, and $\boldsymbol{s_n}$ in this case representing vectors of length two, with elements corresponding to variables relating to velocity, $\dot{x}$, and acceleration, $\dot{v}$, respectively, with initial conditions of $\dot{x}_0$ and $\dot{v}_0$ specified to allow solutions to be found. Vectorisation would also permit the formulae to be scaled up a system of n coupled differential equations, although that is not necessary for SIMION calculations of ion trajectories.

The total accumulated truncation error arising from a fourth-order Runge-Kutta numerical solution is $O(h^4)$. This allows greater accuracy for a given time step than would be achieved using lower order approximations. The time step is allowed to vary throughout the simulation, typically maintaining a fixed integration step distance of approximately one grid unit between time steps. The time step is reduced by SIMION in regions of high field curvature, to maintain the accuracy of trajectory calculations.

5.3 Simulating Ion Transmission

Ion trajectory simulations were performed in SIMION to optimise the transfer of ions into the orbital ion trap mass analyser and confirm the conditions required for their

successful trapping, as demonstrated in the simulations screenshots in Figure 5.3. These screenshots represent an ideal capture of a single ion, resulting in the perfectly circular radial orbit as shown in Figure 5.3 ii). For this set of simulations, the key criteria being investigated were the static voltages applied to the ion optics used to transfer ions from the J105 into the orbital ion trap.

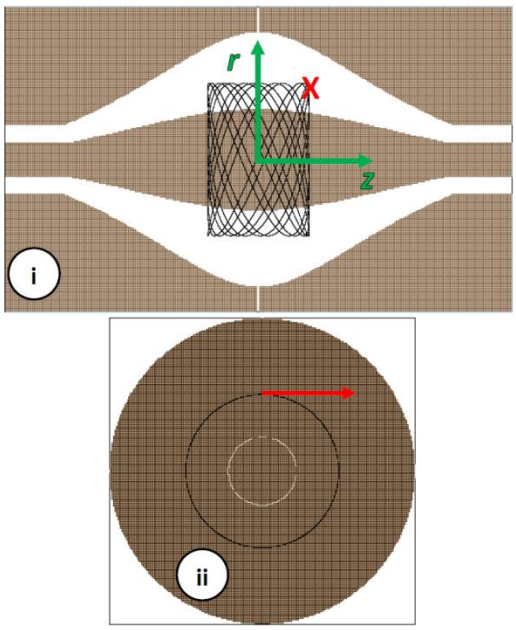

Figure 5.3 - Simulated ideal ion trajectories within ion trap; i) axial view ii) radial view

The simulation of different voltages applied to elements of the ion transfer optics was an essential step in predicting the optimal conditions to successfully transfer ions from the J105 instrument to the mass analyser. A simplified model showing successful ion transfer and capture is shown in Figure 5.7. In the simulations used to model ion transfer, 300 ions were flown in each run so as to account for multiple ion initial conditions simultaneously, thus giving an estimate for the percentage of ions successfully transferred into the mass analyser. This large number of simulated ions, compared to the number used in earlier studies on misalignment, was possible due to a coarser simulation time-step being used than for the misalignment simulations. A larger time-step was permissible as mass resolution was not being evaluated from ion trajectories in this instance. The ions were grouped into 3 distinct sets of initial conditions exiting the J105 SIMS, each with different starting co-ordinates. Each group was given a random distribution of initial velocities within a prescribed cone, of 10° half-angle. As each group of ions were given equal kinetic energy, the velocity

distribution only affected their initial direction. Ions were modelled leaving the tertiary beam optics (TBO) of the J105, passing through the ESA, into the transfer assembly to the orbital ion trap, as can be seen in the 3D rendering from SIMION in Figure 5.4. Figure 5.5 shows a potential energy representation of the simulation set-up, showing that the ESA was operated with all electrodes set to the float voltage, with no change in potential energy as ions pass through the ESA. The potential energy well of the orbital ion trap is also shown in this figure, which would only be present once the trapping voltage has been ramped up from ground during ion injection.

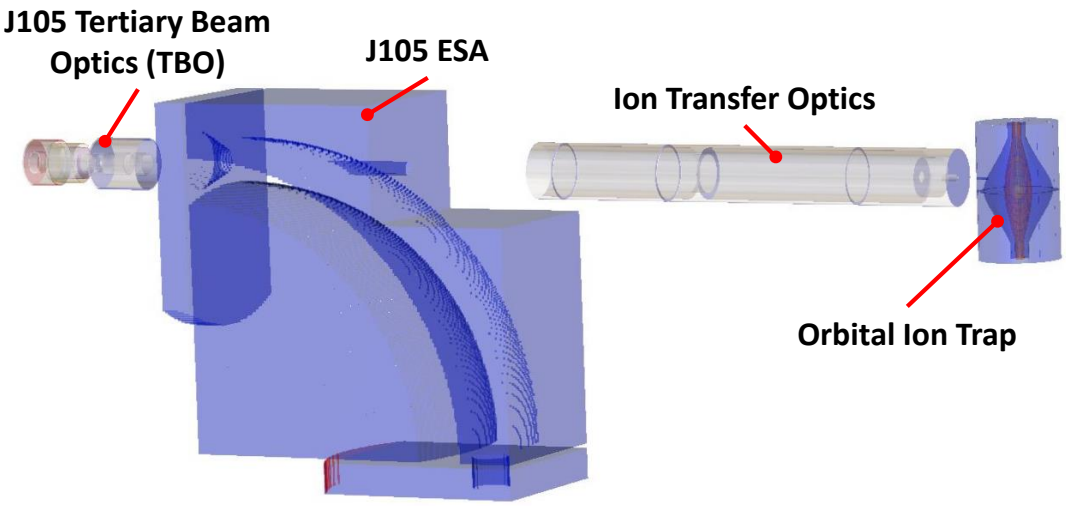

Figure 5.4 - Partially transparent 3D view from SIMION, showing the ion optics elements modelled for ion transfer from J105 to orbital ion trap.

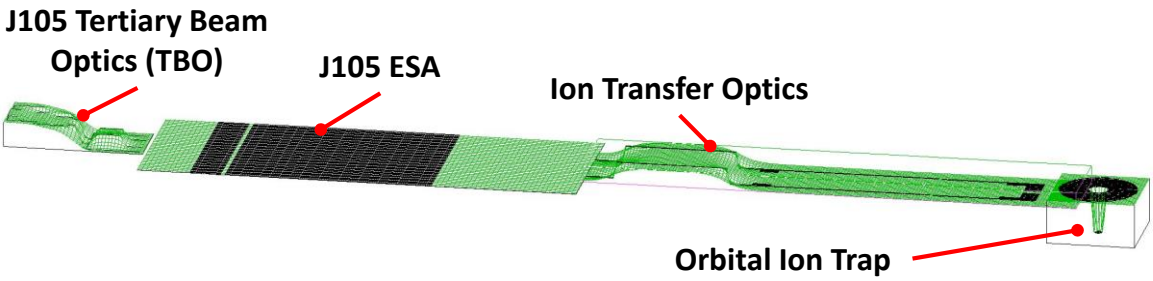

Figure 5.5 - Potential energy 3D representation from SIMION, showing the ion optics elements modelled for ion transfer.

In total, over 300,000 simulations were run to optimise transfer voltages, with maximum simulated ion transmission from the J105 SIMS to the mass analyser in excess of 90%.

Figure 5.6 shows the flight of ions through the entire SIMION model, from the TBO through to the orbital ion trap, with the first few orbits of successfully trapped ions also shown. Figure 5.7 shows a magnified view to highlight the focussing of the ion beam

upon injection into the ion trap. Transmission of an ion was deemed to be successful if it crossed the plane x = 495mm, indicated by the red centre-line along the z-axis of the orbital ion trap in Figure 5.7. All simulations were carried out assuming ideal vacuum conditions, with no collisions between ions and residual gas molecules modelled. This assumption is certainly valid for ion transmission simulations, as the mean free path would be orders of magnitude larger than the distance travelled. For example, in the case of benzene, which has a kinetic diameter of approximately 585pm, the calculated mean free path would be greater than 250m at a vacuum of 10^{-7} mbar, and a temperature of 293K. A value for mean free path can be estimated using a relationship derived from kinetic theory, shown in equation (3.1), adapted from (O'Hanlon, 2003), where k represents Boltzmann's constant, T is temperature, d_m is the particle diameter, and p is pressure.

$$\lambda = \frac{kT}{\sqrt{2} \cdot \pi \cdot d_m^2 \cdot p} \qquad (5.10)$$

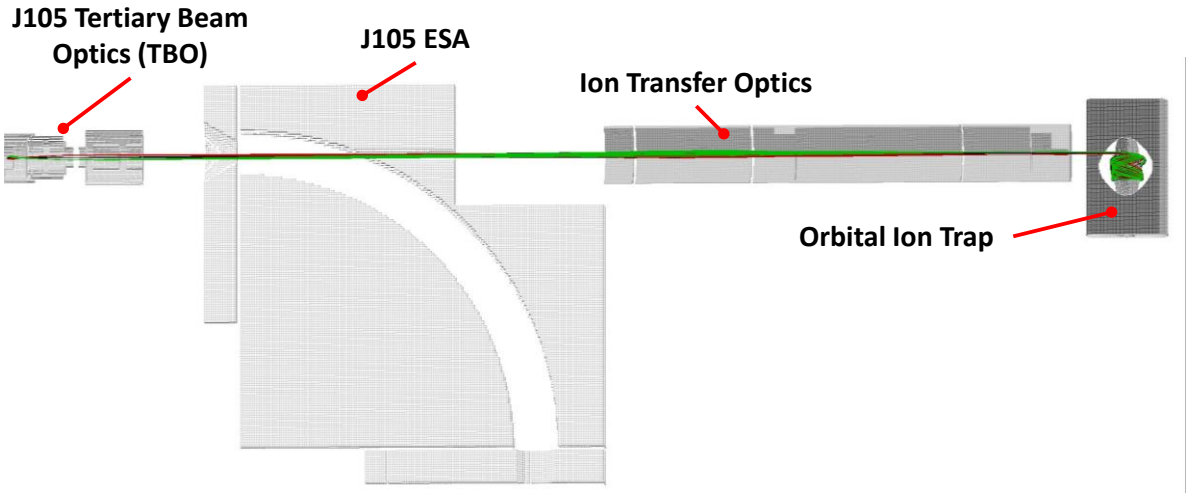

Figure 5.6 - SIMION model of ion transfer from the J105 into the orbital ion trap, showing ions travelling from the tertiary beam optics of the J105, with initial orbits for ions trapped in the orbital ion trap shown. Red, black and green ion trajectories represent ions simulated with different initial co-ordinates.

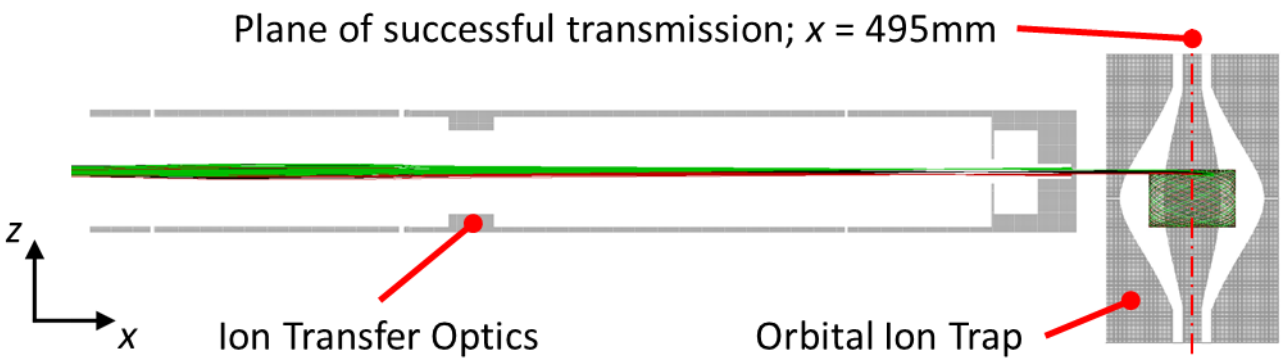

Figure 5.7 – Magnified SIMION model of ion transfer optics and orbital ion trap. Red, black and green ion trajectories represent ions simulated with different initial co-ordinates.

Three critical transfer voltages were tuned via simulation; float voltage V_f, lens voltage V_l, and injection voltage V_i, the ranges of simulated values are shown in Table 5.1.

Voltage	**Minimum [V]**	**Maximum [V]**
Float Voltage, V_f	-500	+500
Lens Voltage, V_l	-500	+500
Injection Voltage, V_i	-50	+0

Table 5.1 - Transmission voltages simulated

The output voltage of the ESA was also varied, with eight set-points possible of 50V, 100V, 150V or 200V, and their negative equivalents, as per the discrete settings available for selection in the J105 high-voltage software controller. It was assumed that for any of these settings ions would retain a kinetic energy spread of no larger than ±1%, for example for a 100V ESA output voltage, ion energies would range from 99eV to 101eV, this follows from advice given by the manufacturer.

Simulations were run in batch mode, controlled by an in-house written user program; ESA-Transfer.lua, which is made accessible along with other used LUA, GEM, and MATLAB scripts via a public GitHub repository (Hood, 2019). This script iterated through the desired ion optics voltages, simulating ion transmission for every permutation. Output data from SIMION was saved as individual CSV files for each simulation, containing the mass, charge, and kinetic energy of ions which were successfully transmitted, as well as the voltages simulated and the ion flight times at which transmission occurred. These files were then imported into MATLAB for further analysis. Simulations were not carried out as a single batch, but rather as smaller

subsets, to allow multiple simulation sets to be run in parallel, whilst also allowing the incremental voltage change to be varied to examine areas of higher transmission in greater detail.

The results of simulations were plotted as surfaces, with transmission represented as both height and colour to allow a two dimensional view of the relationship between three variables, to highlight the voltage space in which optimal transmission could be found, as shown in Figure 5.8. Figure 5.9 shows the MATLAB GUI created to visualise the output of multiple transmission simulations in 3 dimensions.

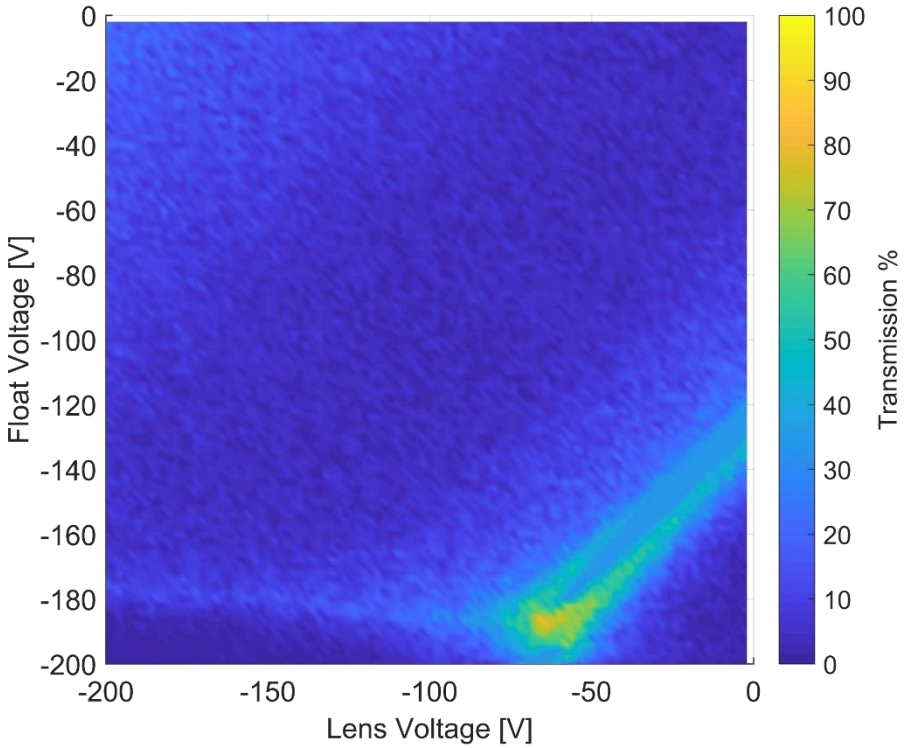

Figure 5.8 - Subset of results of simulated ion transmission, with the percentage of ions successfully transferred indicated by colour.

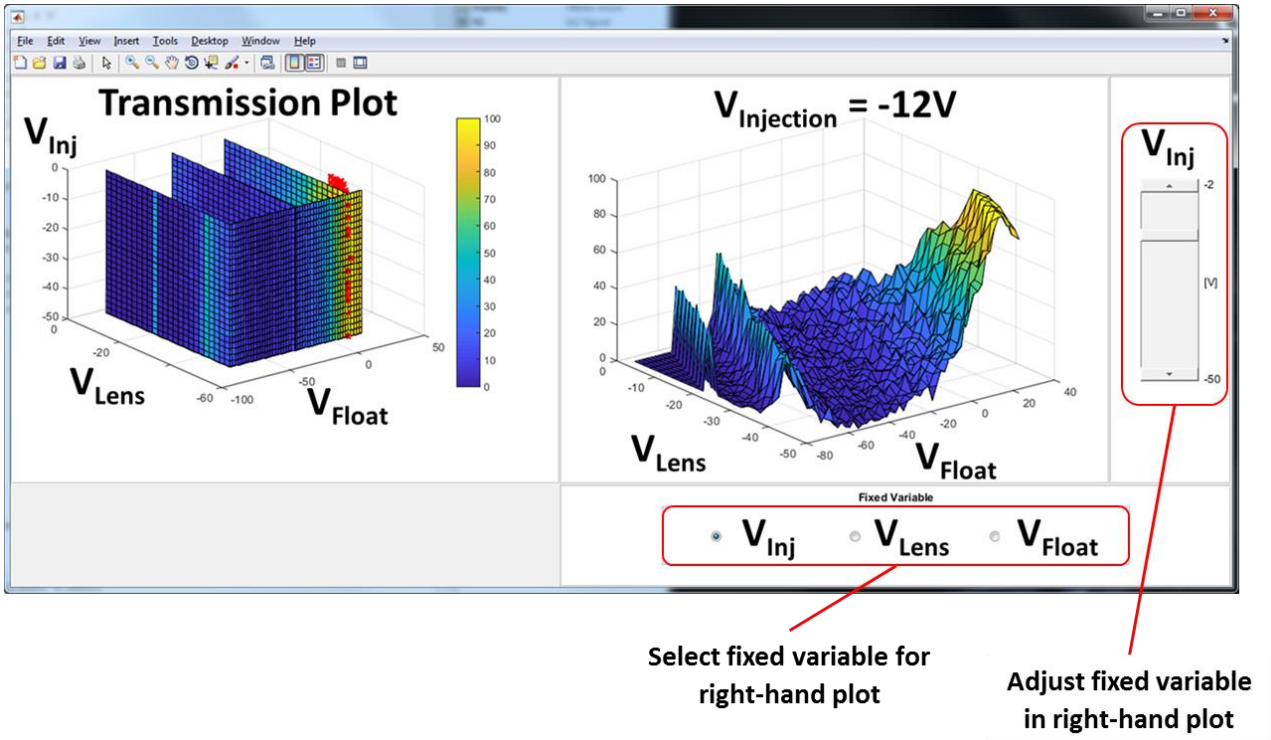

Figure 5.9 - Ion transmission GUI, showing; on the left-hand side a 3D model of the simulated voltages, with transmission encoded as colour, on the right-hand side a surface plot is shown where one voltage is fixed, in this case the injection voltage, with the remaining two voltages being the x and y axes, with transmission the z axis, whilst also being represented by colour. Text was added to this figure outside of MATLAB to improve legibility.

5.3.1 Space Charge Effects on Ion Transmission

A simple model of space charge effects, which simulates electrostatic repulsion between like charges within the ion beam itself was trialled, and found not to have a significant effect on simulation results. It should be noted that this consideration of space charge did not model the effect of ion charge density on the local electric field distribution. Although, this would not be expected to be significant in the case of the secondary ion beam in question, as the ion beam is neither exceptionally bright, nor being focussed to a small spot size, (Appelhans and Dahl, 2005). Repulsion between ions was set to either 0pA, 0.5pA or 1pA, to approximate the effect of space charge on ion transmission, it was found to have only a small effect in most cases, so was typically neglected as calculating repulsion lengthened simulation run time by a factor of more than 4.

Figure 5.10 shows the transmission results of two simulations which were identical except for the inclusion of 1pA of beam repulsion included in the second simulation. As discussed, transmission is encoded as colour, with float and lens voltages shown

on the x and y axes respectively. It can be seen that the areas of highest transmission are the same for both simulations with and without space charge effects. The main difference between the two datasets is a steeper decline in transmission around areas of peak transmission for the simulations which did include space charge effects, as shown by the larger areas of 0% transmission in plot b) of Figure 5.10.

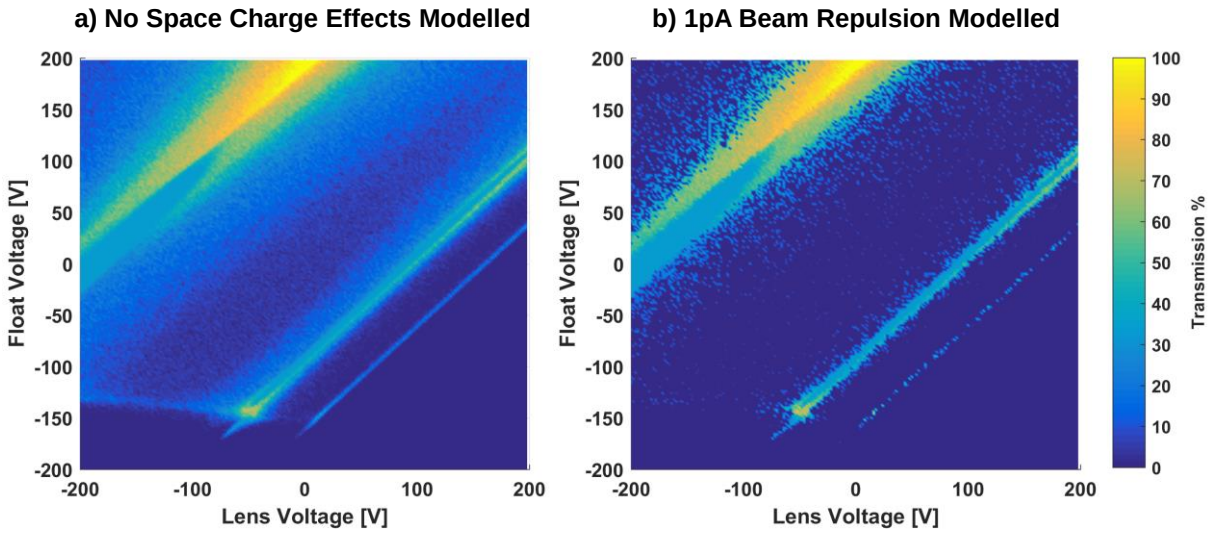

Figure 5.10 - Transmission plotted as a function of float voltage and lens voltage for simulations undertaken with a) no space charge effects incorporated, b) 1pA beam repulsion space charge effect modelled. Injection lens voltage set to -10V.

To further examine the differences between simulations with and without space charge repulsion, the magnitude of the differences between the two sets of transmission values was found, as per equation (5.11), resulting in the surface plotted in Figure 5.11.

$$\Delta\text{Transmission} = \left|\text{Transmission}_{1\text{pA}} - \text{Transmission}_{\text{No Space Charge}}\right| \quad (5.11)$$

It is obvious from Figure 5.11 that there are no large differences between simulations with and without space charge repulsion. Indeed, around the areas of highest transmission in Figure 5.10, there are almost no differences at all, shown by the areas indicating a difference in transmission of 0% around those areas.

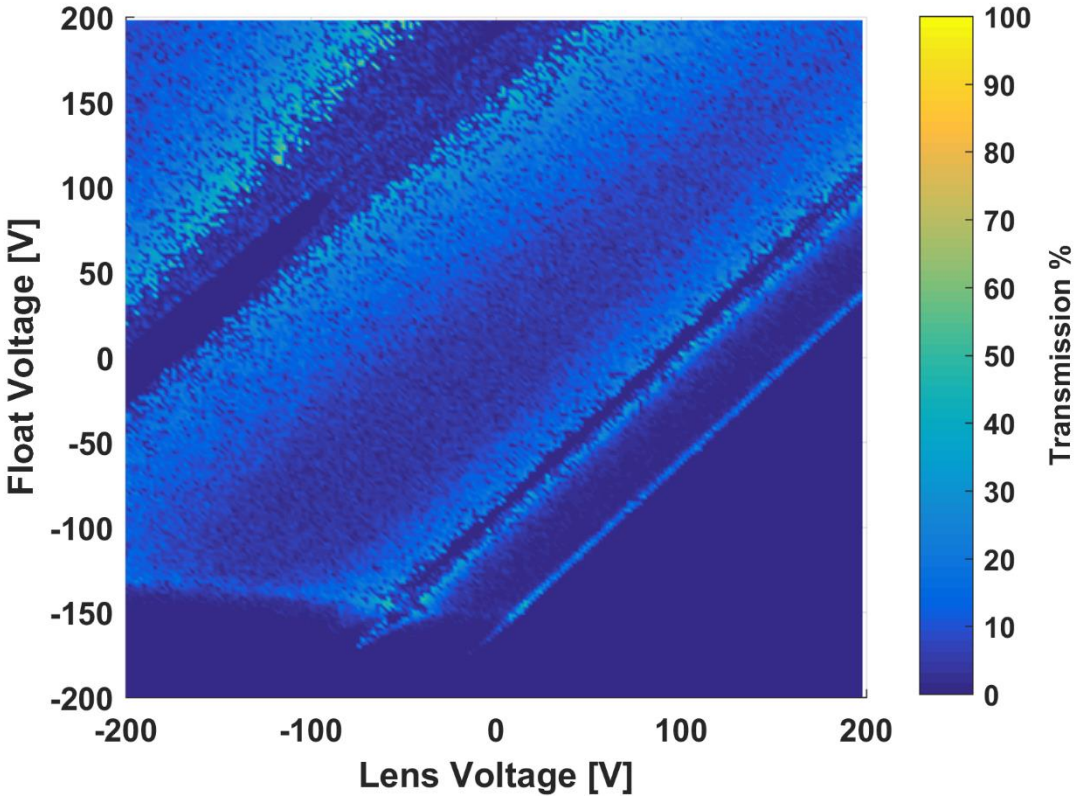

Figure 5.11 - Absolute difference in transmission between simulations shown in Figure 5.10, in which one simulation incorporated no space charge effects, and the other modelled 1pA of beam repulsion. The difference in transmission is plotted as a function of float voltage and lens voltage. Injection lens voltage set to -10V.

Figure 5.12 shows a histogram of the differences in transmission between simulations which did and did not incorporate space charge effects. It can be seen that the most common difference is 0%, underlining the minimal effect of space charge effects in most cases. The negatively skewed distribution is evidence of the steeper drop-off in transmission which was found in simulations including space charge repulsion.

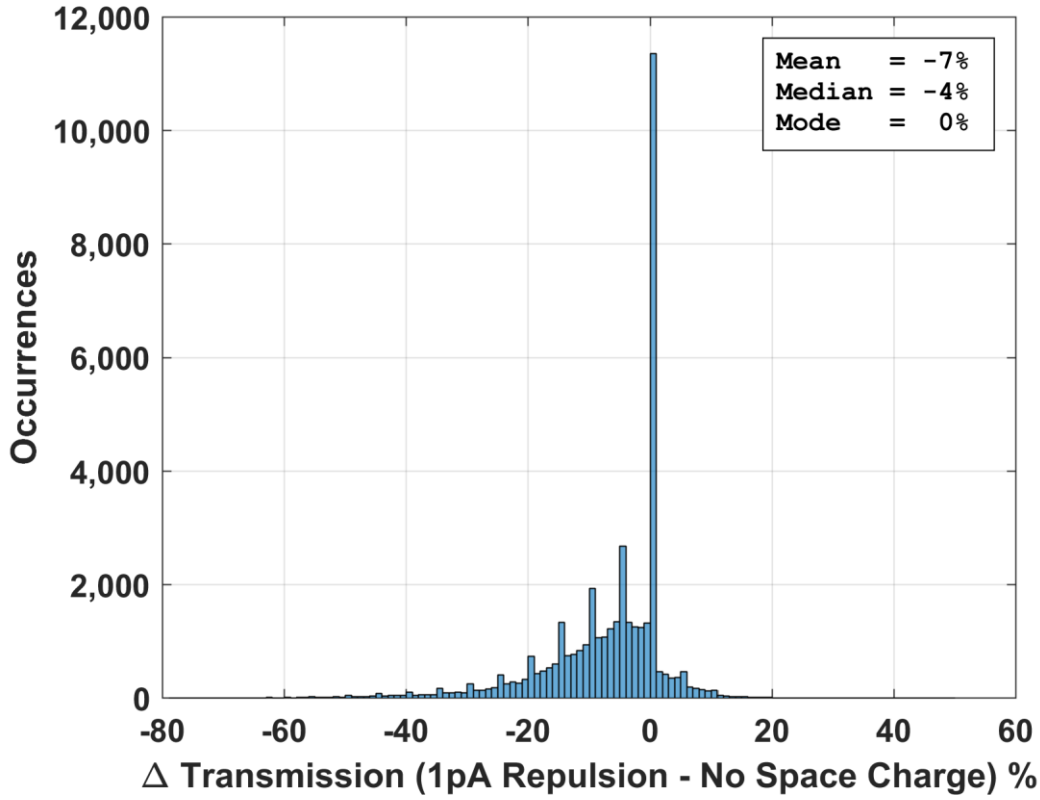

Figure 5.12 - Histogram of the differences in transmission between those simulations which incorporated space charge repulsion and those which did not. Simulations covered lens and float voltages from -200V to + 200V, with the injection voltage fixed at -10V, and ESA voltage fixed at -150V.

The goal of these simulations was simply to find the combinations of voltages which gave peak transmission, in order to give initial conditions from which manual tuning of voltages could be conducted on the ion transfer assembly when mounted to the J105. As such, the regions in voltage space between areas of peak transmission were not of primary interest. As it has been shown that there is little impact caused by the inclusion of space charge repulsion in simulations, it was decided that these effects would not be included in further simulations of ion transmission, as to include repulsion would be computationally expensive without significant benefits.

5.3.2 Impact of Injection Voltage

Across different simulations of ion transmission, it was observed that the injection voltage value did not have a significant impact on the achieved transmission percentage. To investigate this further, plots were created of transmission percentage against injection voltage for a series of different conditions.

Figure 5.13 shows how the percentage of ions successfully transmitted varies with injection voltage for four different combinations of float and lens voltages. These results were from simulations with the ESA voltage set to 100V, meaning ions entered the ion transfer assembly with kinetic energy equal to approximately 100 ± 1eV. A selection of float and lens voltage combinations were chosen to show the behaviour of transmission against injection voltage across a broad range of ion transmission values, showing that the injection voltage has little effect on transmission at both low and high transmission percentages. It can be seen that the transmission percentage does not vary a great deal as the injection voltage increases, with the standard deviation of each plotted transmission series less than 5%.

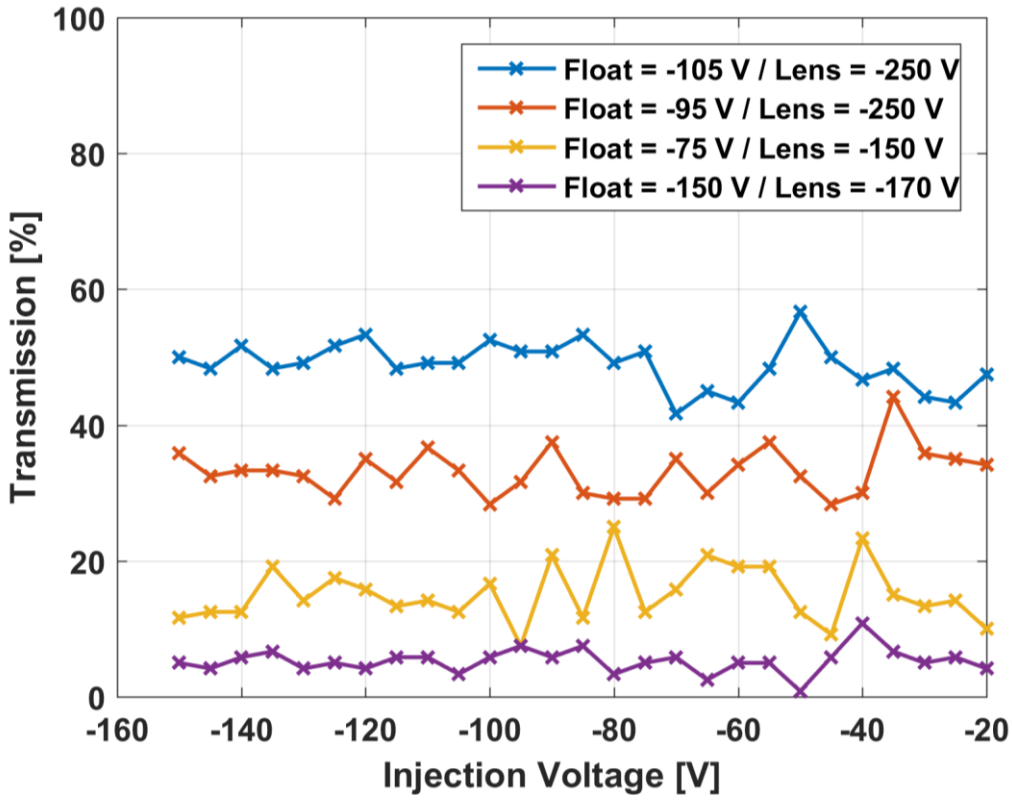

Figure 5.13 - Transmission percentage against injection voltage for ions simulated with an ESA voltage of 100V, resulting in a kinetic energy of 100eV at the entrance aperture of the ion transfer assembly. Four different combinations of float and lens voltages are shown.

The stability of transmission percentage across the entire range of injection voltages is illuminated particularly when compared to Figure 5.14. This plot uses data from the same simulation dataset as Figure 5.13, but with transmission plotted against lens voltage for four combinations of float and injection voltages. It can be seen that successful transmission percentage varies much more widely across different float

voltage values. The standard deviations of the plotted transmission series are much greater than for the previous figure, here ranging from 7% to 14%.

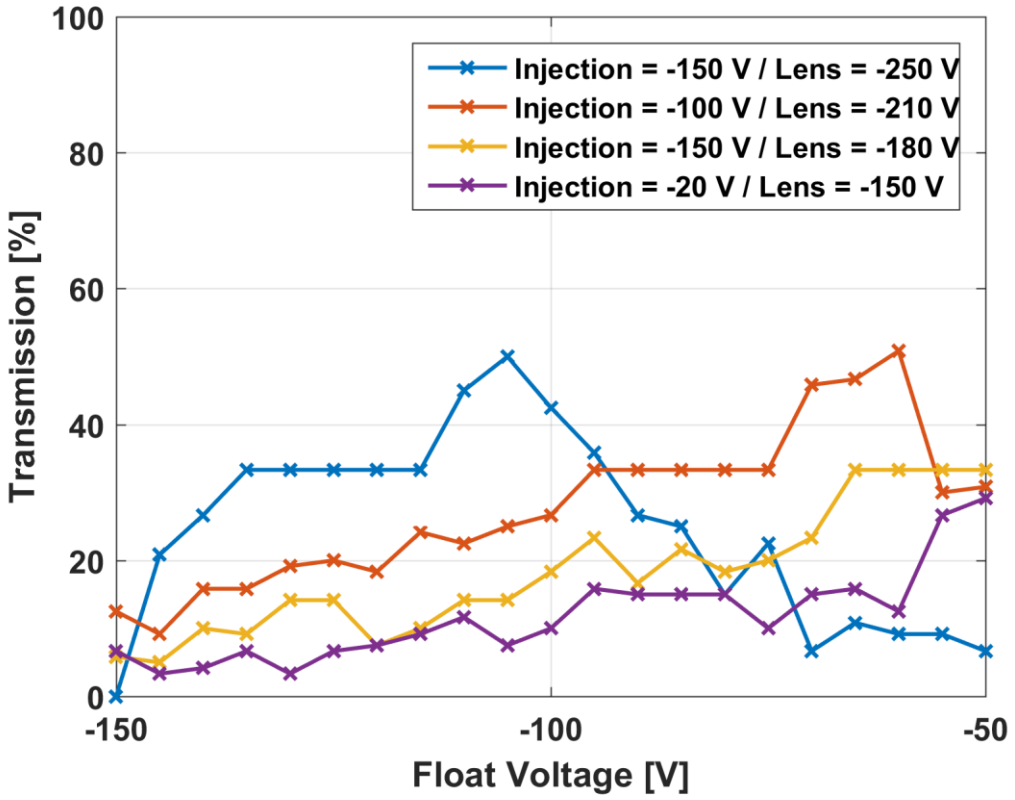

Figure 5.14 - Transmission percentage against float voltage for ions simulated with an ESA voltage of 100V, resulting in a kinetic energy of 100eV at the entrance aperture of the ion transfer assembly. Four different combinations of injection and lens voltages are shown.

A similar effect was seen in different simulation datasets, with transmission not dependent on the injection electrode voltage. Figure 5.15 shows a plot of transmission against injection voltage for simulations with an ESA voltage of 50V. The particular combinations of float and injection voltages chosen were again to highlight the stability of transmission against injection voltage across a wide range of ion transmission percentages. As in Figure 5.13, the standard deviation of each transmission series is again less than 5%.

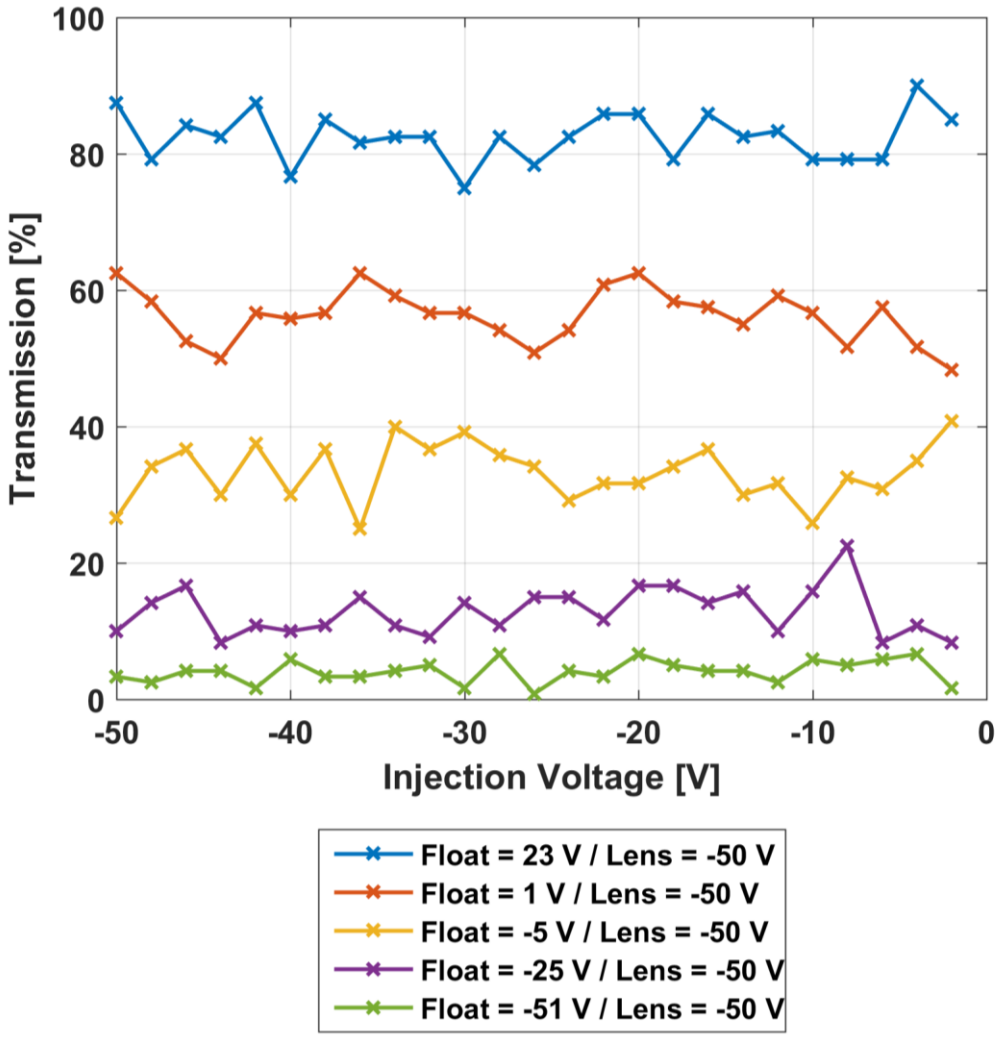

Figure 5.15 – Transmission percentage against injection voltage for ions simulated with an ESA voltage of 50V, resulting in a kinetic energy of 50eV at the entrance aperture of the ion transfer assembly. Five different combinations of float and lens voltages are shown.

An alternative way to observe the stability of transmission for different injection voltages across a broader range of conditions is to add a third dimension to the plot, in the form of colour representing transmission, as used earlier in this section. The following two figures use the same simulation dataset used for Figure 5.14 and Figure 5.15, with an ESA voltage of 50V.

Figure 5.16 shows the variation of transmission plotted for injection voltage against float voltage, with lens voltage fixed. Figure 5.17 shows the variation of transmission plotted for injection voltage and lens voltage, with float voltage fixed. In both cases, it can be seen that there is little transmission variation in the horizontal direction, showing that transmission is not dependent on injection voltage.

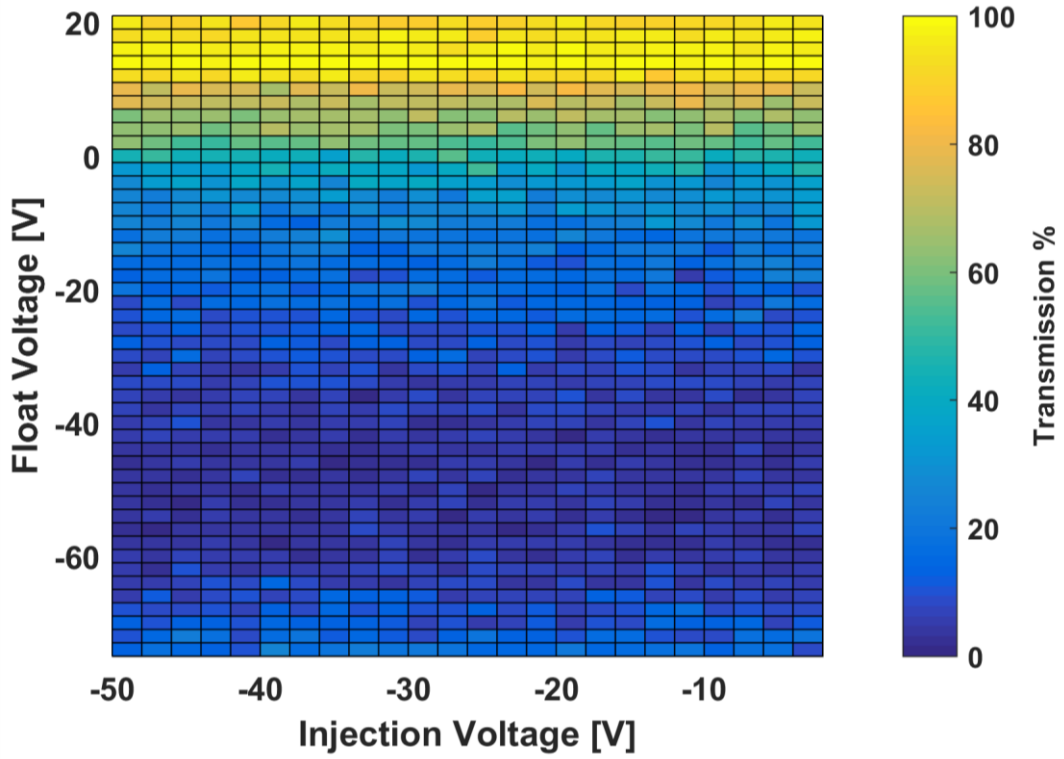

Figure 5.16 - Plot of transmission percentage for varying float and injection voltages, with a fixed lens voltage of 50V. All simulations in this dataset were undertaken with a fixed ESA voltage of 50V, resulting in a kinetic energy of 50eV for ions entering the ion transfer assembly.

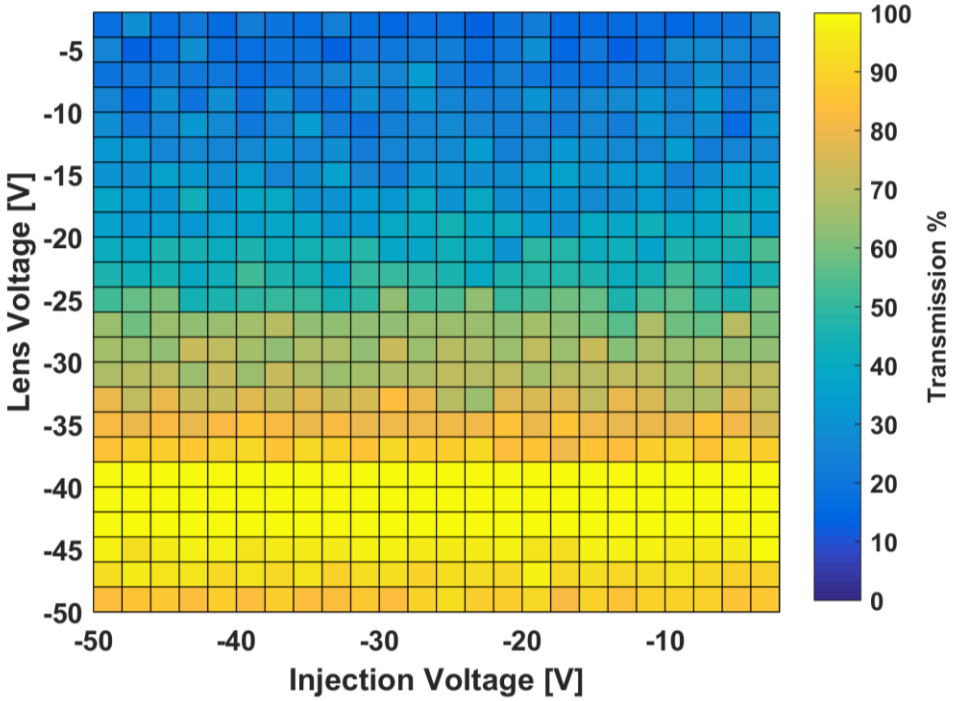

Figure 5.17 - Plot of transmission percentage for varying lens and injection voltages, with a fixed float voltage of 21V. All simulations in this dataset were undertaken with a fixed ESA voltage of 50V, resulting in a kinetic energy of 50eV for ions entering the ion transfer assembly.

Figure 5.18 shows a similar plot for lens voltage against float voltage, with a fixed injection voltage. As can be seen, transmission varies significantly in the directions of both variables for this plot, indicating that both lens and float voltage affect ion transmission.

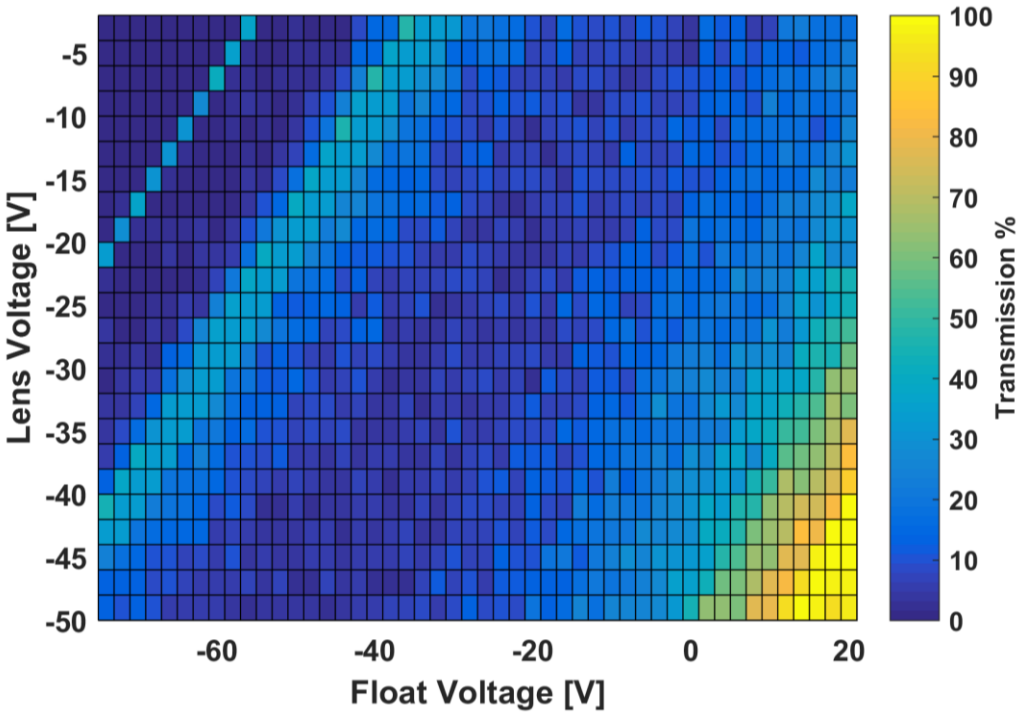

Figure 5.18 - Plot of transmission percentage for varying lens and float voltages, with a fixed float voltage of -50V. All simulations in this dataset were undertaken with a fixed ESA voltage of 50V, resulting in a kinetic energy of 50eV for ions entering the ion transfer assembly.

5.4 Orbital Ion Trapping Simulation – Timing

Alongside transmission of ions through the ESA, successful trapping of ions within the orbital ion trap was also modelled. Ions were trapped by precisely timed voltage ramp on the internal electrode programmed in SIMION using LUA code. Ions were found to take ~42µs to reach the central axis of the ion trap, 495mm from their origin. When the internal electrode voltage was ramped to its final value within 1µs of this time, successful ion capture was achieved, as demonstrated in Figure 5.19. As would be expected, if the internal electrode voltage was applied too early ions were found to collide with the internal electrode, and if it was applied too late ions struck the external electrodes.

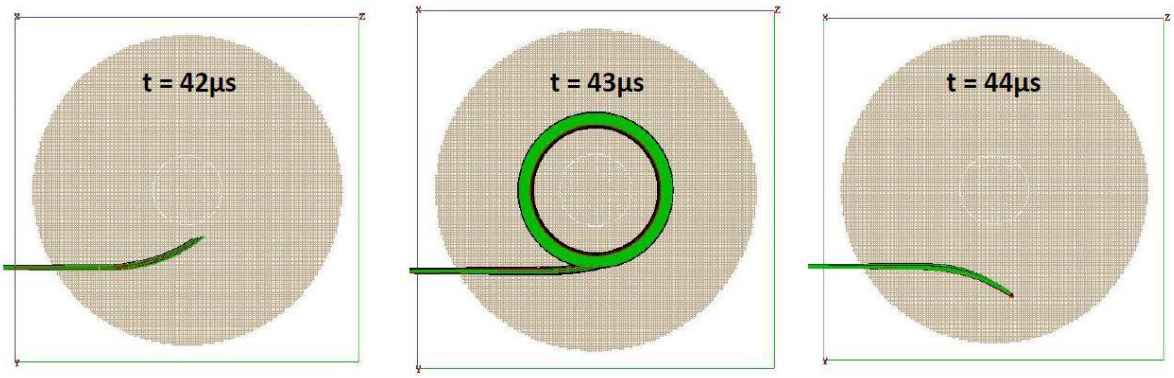

Figure 5.19 - Ion trajectories for different times of internal electrode voltage activation

5.5 Orbital Ion Trap Performance – Mass Resolution

Simulations were also used to evaluate the performance of the orbital ion trap under various conditions, including how the spread in ion kinetic energy affects mass resolution, or how long ions need to be trapped to attain a desired mass resolution.

An analytical approach can be used to give an upper bound of the mass resolution which can be achieved for a given ion trapping duration, also known as the transient time. If it is assumed that a standard fast Fourier transform (FFT) method is to be used, without any zero-padding, or other pre-treatment of the data, the frequency resolution of the transformed data will be dependent linearly on the length of the transient, as shown in equation (5.12), (5.13), and (5.14). The variables used in these equations are defined as follows:

$\boldsymbol{N}$	Number of data points acquired in the recorded transient.
$\boldsymbol{t_{\max}}$	Duration of the recorded transient acquisition, in seconds.
$\boldsymbol{f_s}$	Sampling frequency at which the signal is recorded, in hertz.
$\boldsymbol{\Delta f}$	Smallest difference in frequency which can be detected, in hertz.
$\boldsymbol{f}$	A recorded frequency, in hertz.
$\boldsymbol{f_{\text{res}}}$	Maximum possible frequency resolution for a given recorded frequency.

It should be acknowledged that this upper limit on frequency resolution can be exceeded, if the data undergoes pre-processing before applying the FFT algorithm, although this is not possible for all frequencies simultaneously.

$$N = \frac{t_{\max}}{T} = \frac{t_{\max}}{{f_s}^{-1}} = f_s \cdot t_{\max} \tag{5.12}$$

$$\Delta f = \frac{f_s}{N} = \frac{f_s}{f_s \cdot t_{\max}} = \frac{1}{t_{\max}} \tag{5.13}$$

$$f_{\text{res}} = \frac{f}{\Delta f} = f \cdot t_{\max} \tag{5.14}$$

From this relationship, the theoretical limit of frequency resolution can be plotted against frequency for different transient times, as shown in Figure 5.20, these can then be transformed into plots of mass resolution against mass, as per Figure 5.21. This

transformation is possible due to the relation between mass and frequency inherent in the design of the orbital ion trap, as described by equation (5.15), (Makarov, 2000).

$$\omega = \sqrt{\frac{q \cdot k}{m}} \tag{5.15}$$

The relationship between mass resolution and frequency resolution can be found in a few short steps, starting by rearranging equation (5.15) in terms of m, as shown in equation (5.16).

$$m = \omega^2 \cdot \sqrt{q \cdot k} \tag{5.16}$$

The partial derivative of m, with respect to ω, can then be found.

$$\frac{\partial m}{\partial \omega} = 2\omega \cdot \sqrt{q \cdot k} \tag{5.17}$$

By dividing (5.16) by (5.17), the relationship between $m/\partial m$ and $\omega/\partial\omega$ can now be found.

$$\begin{gathered} \frac{m}{\left(\frac{\partial m}{\partial \omega}\right)} = \frac{\omega^2 \cdot \sqrt{q \cdot k}}{2\omega \cdot \sqrt{q \cdot k}} = \frac{\omega}{2} \\ \therefore \frac{m}{\partial m} = \frac{1}{2}\left(\frac{\omega}{\partial \omega}\right) \\ \Rightarrow m_{\mathrm{res}} = \frac{1}{2} f_{\mathrm{res}} \end{gathered} \tag{5.18}$$

This is in agreement with the statement made by Makarov that the mass resolution achieved in an orbital ion trap will be half of the frequency resolution, (Makarov, 2000). As such, the theoretical maximum mass resolution for an ion of any mass can easily be found by substituting equations (5.14) and (5.15) into (5.18). The required variables for the calculation are; the mass of an ion, m, with units of kilograms, its charge, q in coulombs, the field curvature, k in Vm^{-2}, and the transient duration, $t_{\max}$ in seconds. The field curvature can be found from the internal electrode voltage, and the geometry of the orbital ion trap electrodes, using the equation presented by Kharchenko, as discussed in Chapter 3 (Kharchenko *et al.*, 2012).

$$m_{\text{res}} = \frac{1}{2} \cdot f_{\text{res}} = \frac{1}{2} \cdot f \cdot t_{\max}$$
$$= \frac{1}{2} \cdot \frac{\omega}{2\pi} \cdot t_{\max} \qquad (5.19)$$
$$= \frac{t_{\max}}{4\pi} \cdot \sqrt{\frac{q \cdot k}{m}}$$

The relationship between ion mass and oscillation frequency is demonstrated in Figure 5.22 for ions of different kinetic energies in the range 100eV to 1000eV. All of the plots in this section are for standard orbital ion trap geometry, with an internal electrode radius, R_1 = 6mm, and an external electrode radius R_2 = 15mm. Behaviour for ions with masses in the range 50u to 2,500u is shown in these plots, to reflect the approximate mass range of secondary ions generated by the cluster ion sources on the Ionoptika J105 SIMS. Although with the new 40keV water cluster primary ion source, some fragments larger than m/z 2,500 can be desorbed intact.

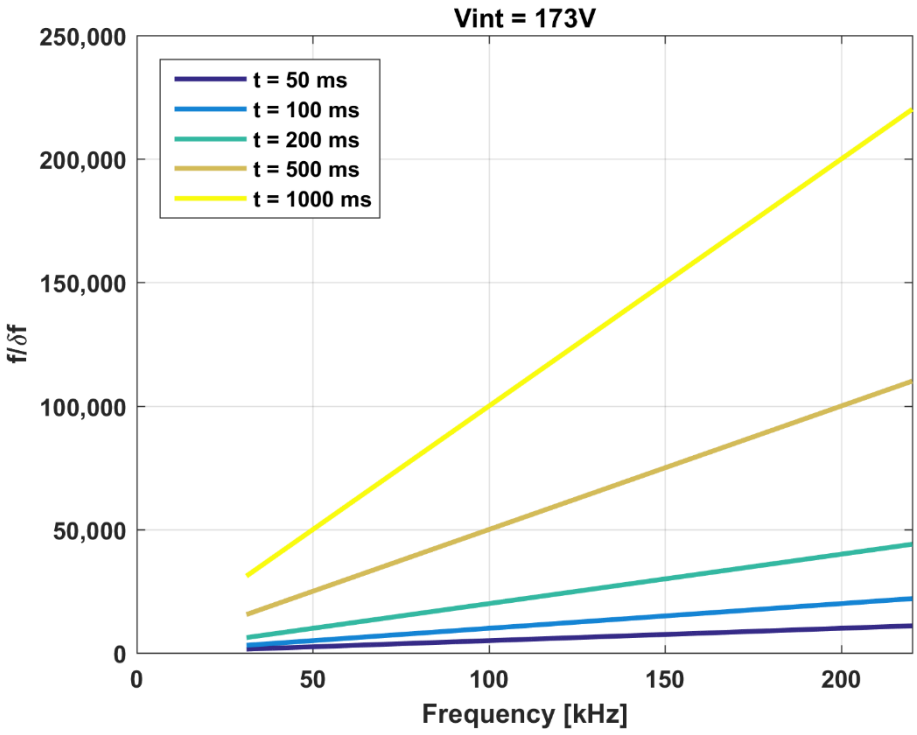

Figure 5.20 - Frequency resolution against frequency for different transient lengths, for ions with kinetic energy of 100eV, trapped by an internal electrode voltage of 173V.

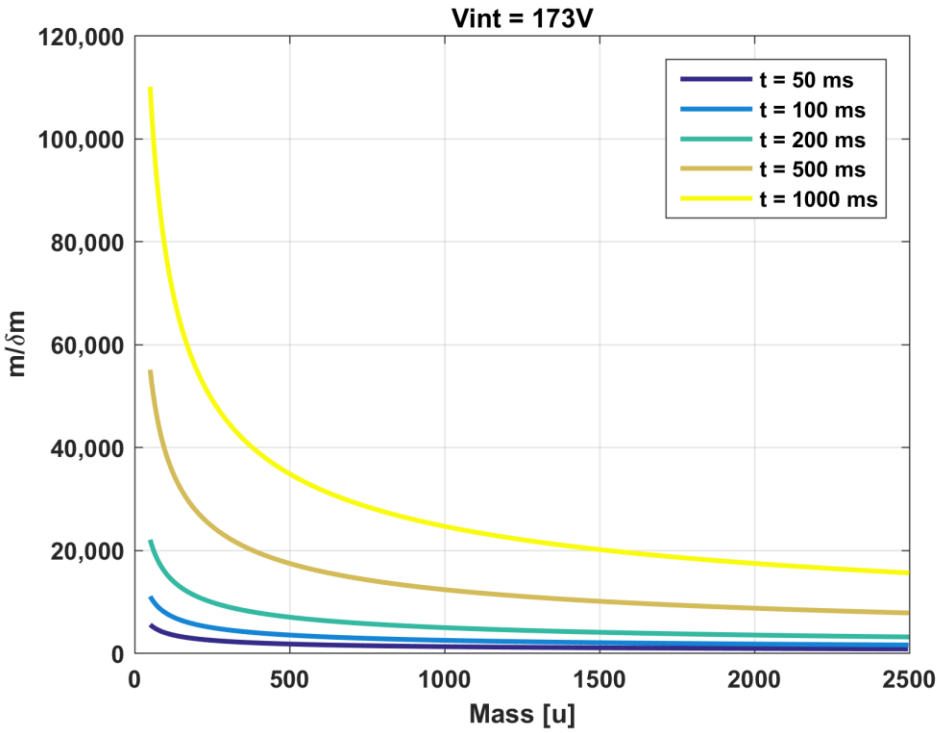

Figure 5.21 - Mass resolution against mass for different transient times, for ions with kinetic energy of 100eV, trapped by an internal electrode voltage of 173V.

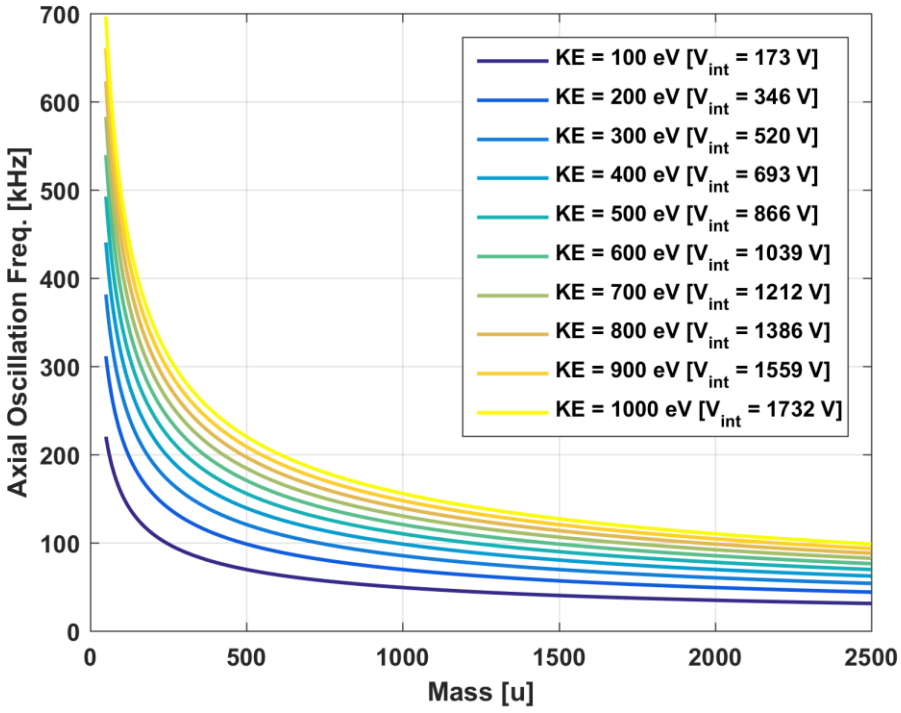

Figure 5.22 - Axial oscillation frequency against mass for different trapping energies, in a standard geometry orbital ion trap, mass range from 50u to 2,500u.

It can be seen from Figure 5.21 that the highest values of mass resolution can only be accessed for the lower portion of the mass range, below about 200u. Higher mass resolution is more desirable however at higher masses, where specific chemical identification is often more difficult. To increase the mass resolution of the orbital ion trap, without requiring a longer transient time, one could increase the ion trapping voltage. This would be suitable for trapping higher energy ions, which would increase the axial oscillation frequency and thus the mass resolution, for a given transient duration. Figure 5.23 shows that mass resolution in excess of 100,000 can be achieved for a wide mass range, if ions are trapped at higher energies. Increases in mass resolution could also be sought by increasing the internal electrode radius to further increase the field curvature experienced by trapped ions, as per (Makarov *et al.*, 2009). However, in doing this, ions will orbit closer to the internal electrode, meaning that the effect of any distortions in the ideal electric field caused by small surface defects will be magnified. This means that greater accuracy would be required in the manufacture and alignment of a higher field orbital ion trap.

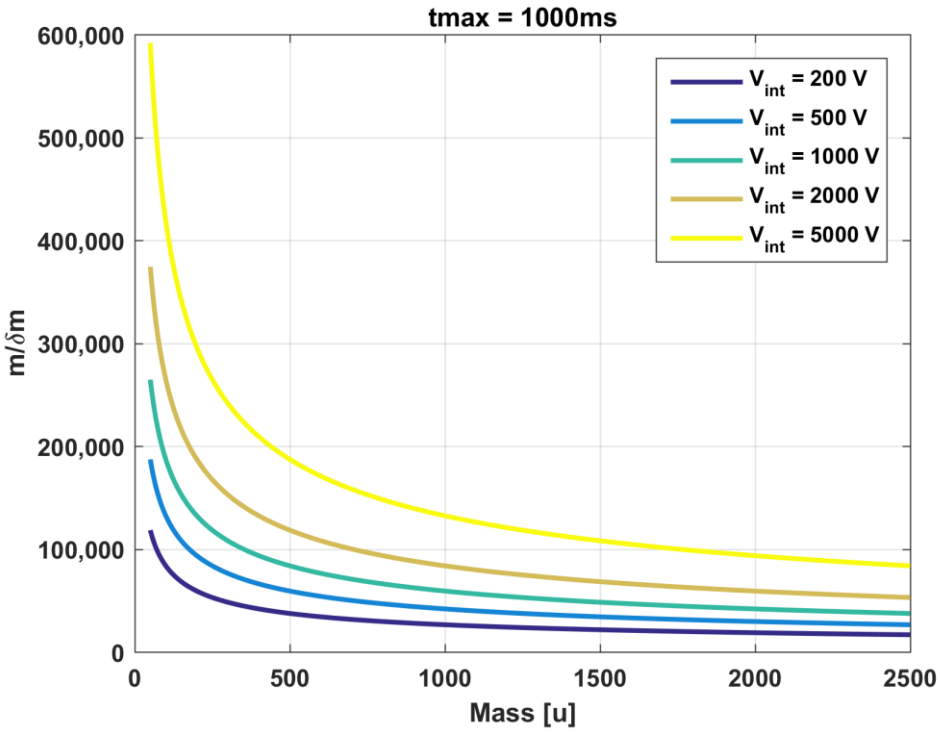

Figure 5.23 - Mass resolution for a 1s transient time, for different ion trapping voltages between 200V and 5000V.

In SIMION, simulations were run with ions trapped for different transient acquisition times, to produce data which could be analysed using FFT to validate the above analytical relationships found between trapping time and mass resolution. Output data from SIMION was recorded at regular time steps to ensure its suitability for FFT. A recording time step of 1µs was chosen, equivalent to a sampling frequency of 1MHz, giving a Nyquist frequency of 500kHz. This allowed all ions with masses greater than 100u to be detected for ion energies up to 1000eV, as 100u ions have an axial oscillation frequency of ~493kHz when trapped at 1000eV in a standard geometry orbital ion trap. Ions trajectories were defined as beginning inside the trapping volume, at a radius of 9mm, with an initial axial offset of 6mm, so no further excitation was required to promote harmonic trapping. To compute the FFT of the data, an average was taken of only the ions' axial positions, to mimic the behaviour of a differential image current amplifier, which would be positioned to record only the axial oscillations of trapped ions.

A plot of mass resolution against internal electrode voltage for different fixed masses gives an indication of the advantage which can be gained by trapping ions at higher energies. Presented in Figure 5.24 for a transient of 200ms, it can be seen that mass resolution follows a power law relationship with internal electrode voltage, with mass resolution proportional to the square-root of internal electrode voltage. This means that increases in internal electrode voltage give diminishing returns in terms of mass resolution. There would also be further technical challenges in applying higher internal electrode voltages at the slew rate required to trap a packet of ions. A higher internal electrode voltage would require higher energy ions to be trapped, thus the ion packet would be travelling faster, giving a shorter window in which the internal electrode voltage must be ramped up to its final value to achieve successful trapping. There are consequently two factors which would cause a higher slew rate to be required; a higher final voltage, and a shorter ramp time for effective trapping.

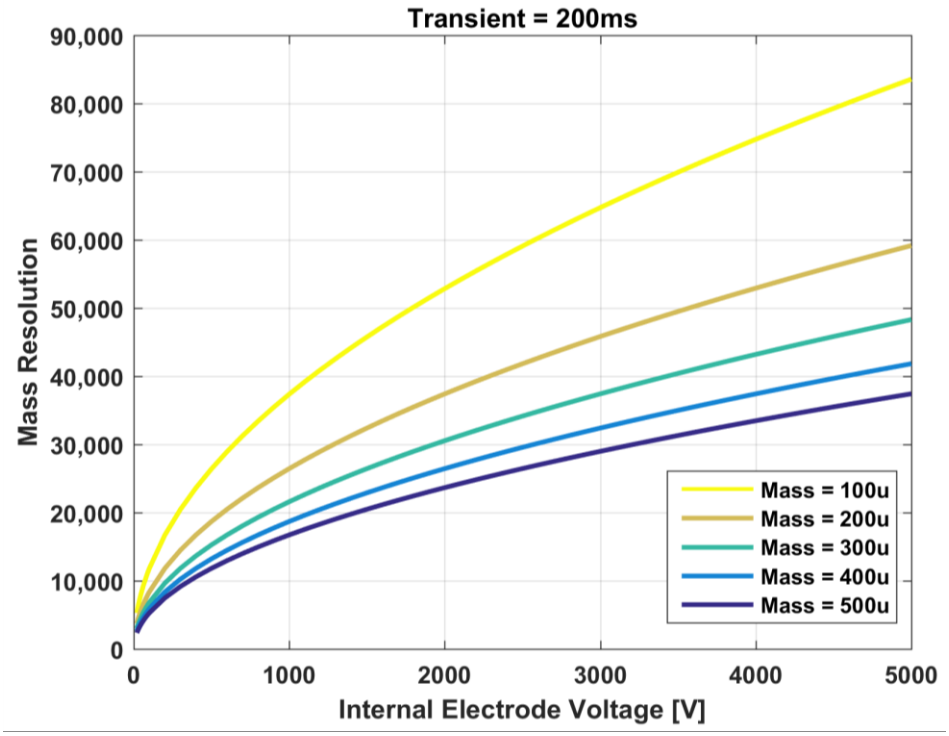

Figure 5.24 - Mass resolution against internal electrode voltage for 5 separate masses, transient = 200ms

It is also instructive to investigate the relationship between mass resolution and transient detection time, while holding ion mass and kinetic energy constant. Figure 5.25 shows the linearity between mass resolution and transient duration for a given ion mass, this can be used to reduce the computational expense of simulations, as short transient times can be simulated, with mass resolution for longer transients able to be extrapolated from the resultant data.

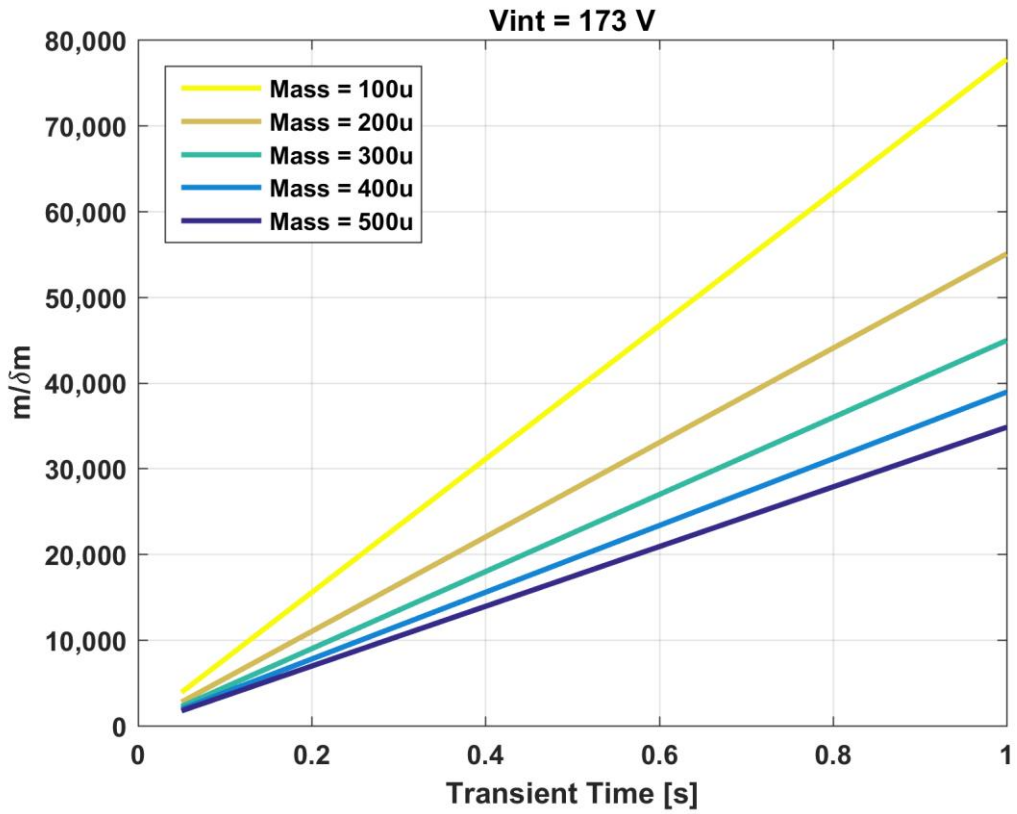

Figure 5.25 - Mass resolution against transient time for ions of mass 100u to 500u, with kinetic energy of 100eV, trapped by a 173V internal electrode voltage.

Similarly, linearity between mass resolution and transient duration can be found for different ion kinetic energies, when mass is constant, as shown in Figure 5.26. This relationship can also be used to extrapolate mass resolution for longer transient durations than those simulated.

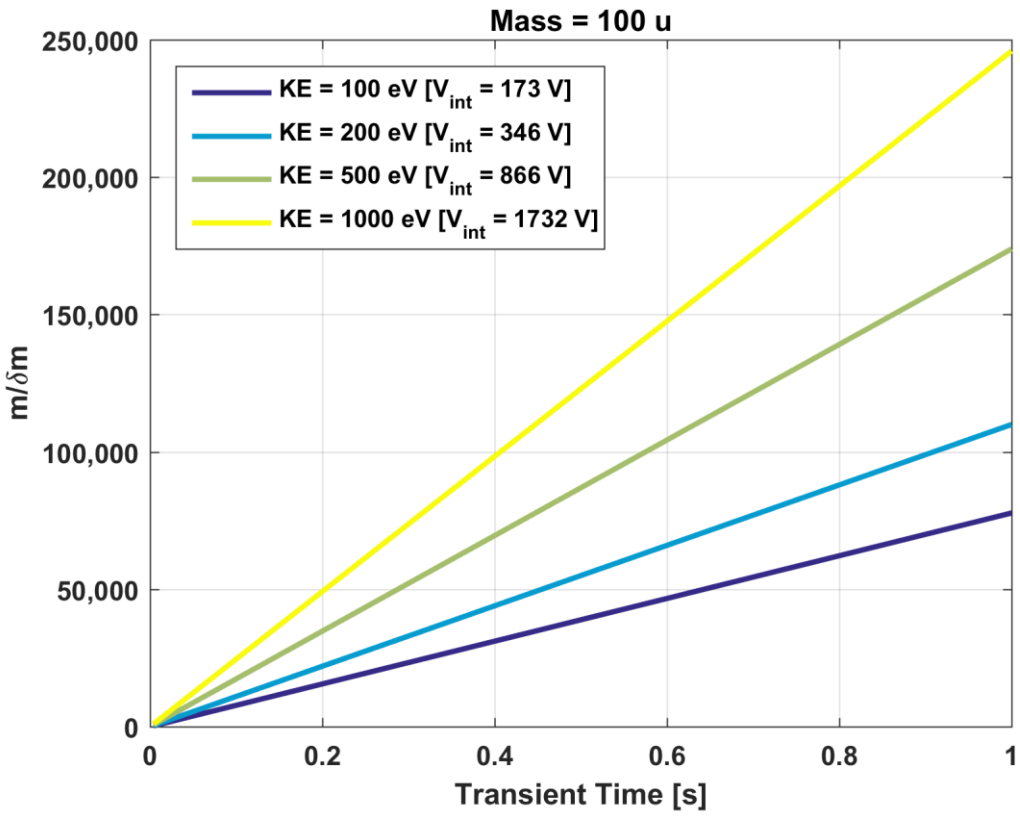

Figure 5.26 - Mass resolution against transient time for ions with kinetic energy 100eV to 1,000eV, with a fixed mass of 100u.

5.5.1 Mean Free Path, Distance Travelled, & Vacuum

As stated earlier, all simulations were carried out with the assumption of a perfect vacuum, which is to say that no collisions between ions and residual gas molecules were modelled. This assumption is valid providing that the mean free path of an ion is significantly longer than the distance travelled while the ion is trapped. Obviously, this will not always be the case, particularly if ions are trapped for longer periods of time, as is required to achieve maximal mass resolution. To approximate the distance travelled by ions whilst trapped, a MATLAB script was written to analyse simulation data and sum the distance travelled for ions across a series of fixed time steps. The distance travelled in a single time step was calculated simply using the Cartesian co-ordinates recorded for each ion, as laid out in equation (5.20). This assumes that the time step used is sufficiently small for ion motion to be approximated as linear during the interval. To test this assumption, different ion time marker steps of 2, 1, 0.1, 0.01 and 0.001µs were used, to investigate the effect these different time steps had on the calculated distance travelled by an ion flown under identical conditions. Where the term time marker step refers to the fixed time increment at which simulation data is recorded.

$$d = \sqrt{(x_{n+1} - x_n)^2 + (y_{n+1} - y_n)^2 + (z_{n+1} - z_n)^2} \qquad (5.20)$$

It can be seen in Figure 5.27 that for time marker steps below 0.1µs there was little change in the calculated flight distance, for ions of mass 100u and 150u with 101eV kinetic energy over a flight time of 200ms. This suggests that a time step of 0.1µs is sufficiently small for ion motion to be considered linear during this interval. It should be noted that the distance travelled by ions in a real orbital ion trap would be slightly larger than given by this calculation, even for a small time step, as SIMION itself uses a finite time step to calculate ion motion, assuming linear motion during this period, which would not be the case in a real device, although this difference will be negligible.

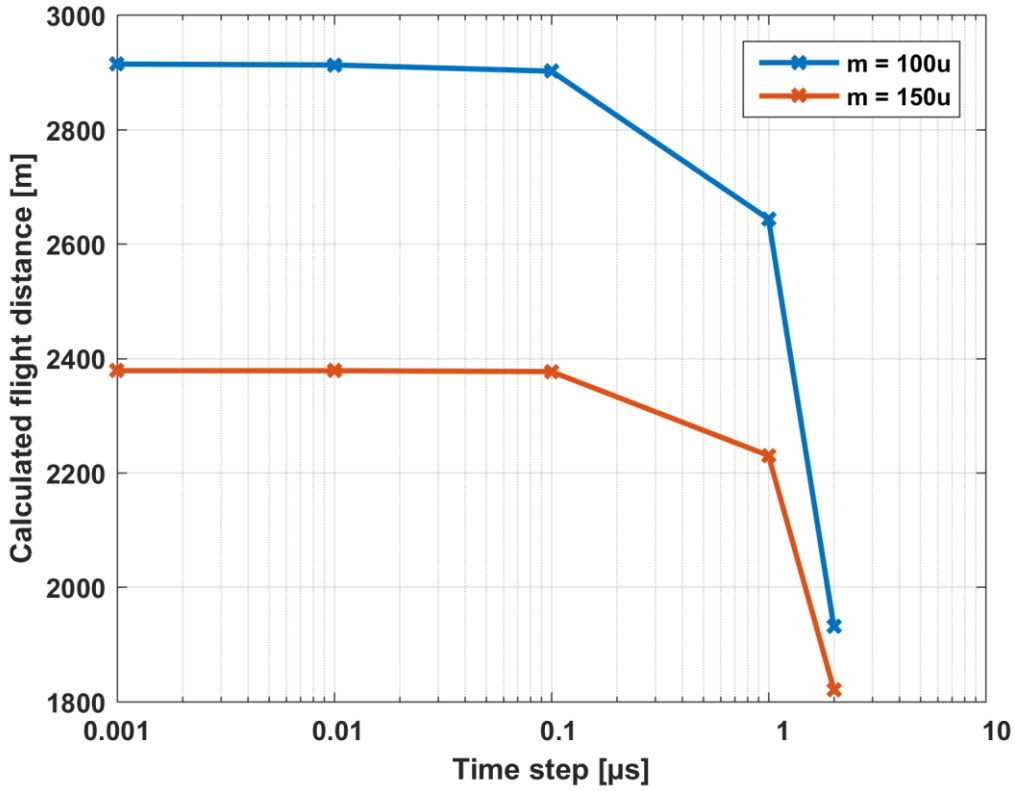

Figure 5.27 - Calculated flight distances for ions with mass 100u and 150u, and kinetic energy 101eV, using different discrete time marker steps, with a flight time of 200ms.

As would be expected, it was found that the distance travelled was linearly proportional to the ion flight time was trapped, this is evident from Figure 5.28. It was also seen that less massive ions travel further for a given transient time, with an inverse square proportionality, due to their higher oscillation frequency, as shown in Figure 5.29, again this is as would be expected from the equations which govern motion in an orbital ion trap.

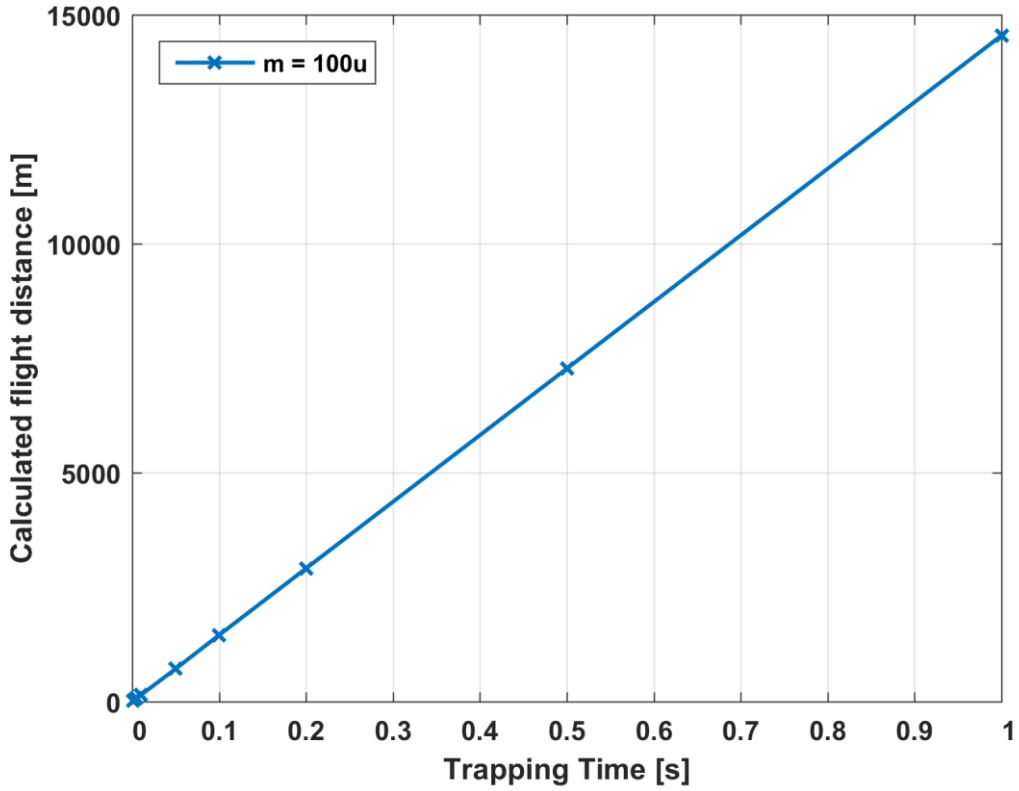

Figure 5.28 - Calculated flight distances for ions with mass 100u, and kinetic energy 101eV, calculated using discrete time steps of 0.1µs, across different trapping times.

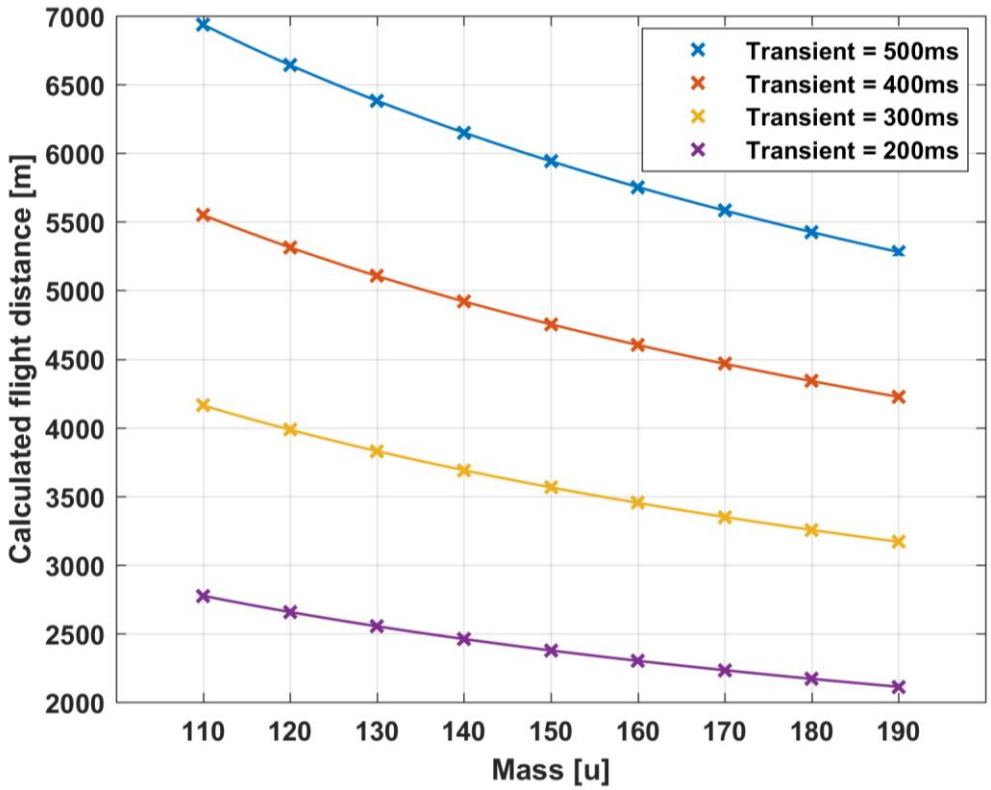

Figure 5.29 - Calculated flight distances for ions with mass 110u – 190u, and kinetic energy 101eV, calculated using discrete time steps of 0.1µs, for trapping times of 200ms – 500ms, solid line represents MATLAB curve fit, of the form $y = A_1 x^{b_1}$ with coefficients listed in Table 5.2.

Figure 5.29, showing the relationship between mass and distance travelled also gave rise to a general relationship between mass, transient trapping duration, and distance travelled, for a fixed ion kinetic energy of 101eV. This was possible as the coefficient, A_1, of the curve fits found for distance as a function of mass were seen to be linear with transient duration, as can be seen from the fit coefficients in Table 5.2, with the additional term A_1/t found to be constant for any length transient, as would be expected for flight distances linearly proportional to the flight duration.

Transient, t [s]	A_1	b_1	A_1/Transient
0.2	29,012.93	-0.5	145,064.6
0.3	43,519.39	-0.5	145,064.6
0.4	58,025.85	-0.5	145,064.6
0.5	72,532.32	-0.5	145,064.6

Table 5.2 - Fit coefficients for Figure 5.29

Equation (5.21) shows the relationship found to estimate distance travelled from the mass of an ion, m, in atomic mass units, and the transient duration, t, in seconds.

$$d(m,t) = 145064.6\, t \cdot m^{-0.5} \qquad (5.21)$$

This relationship can be adjusted to also model the effect of ion kinetic energy on the distance travelled. To do this, a relationship was found between the flight distance and ion kinetic energy, for a series of different ion masses, whilst holding the transient duration constant. This can be seen in Figure 5.30, which shows how the calculated flight distance varies with ion kinetic energy, for masses of 100u to 1000u, with each mass flown for a transient duration of 200ms.

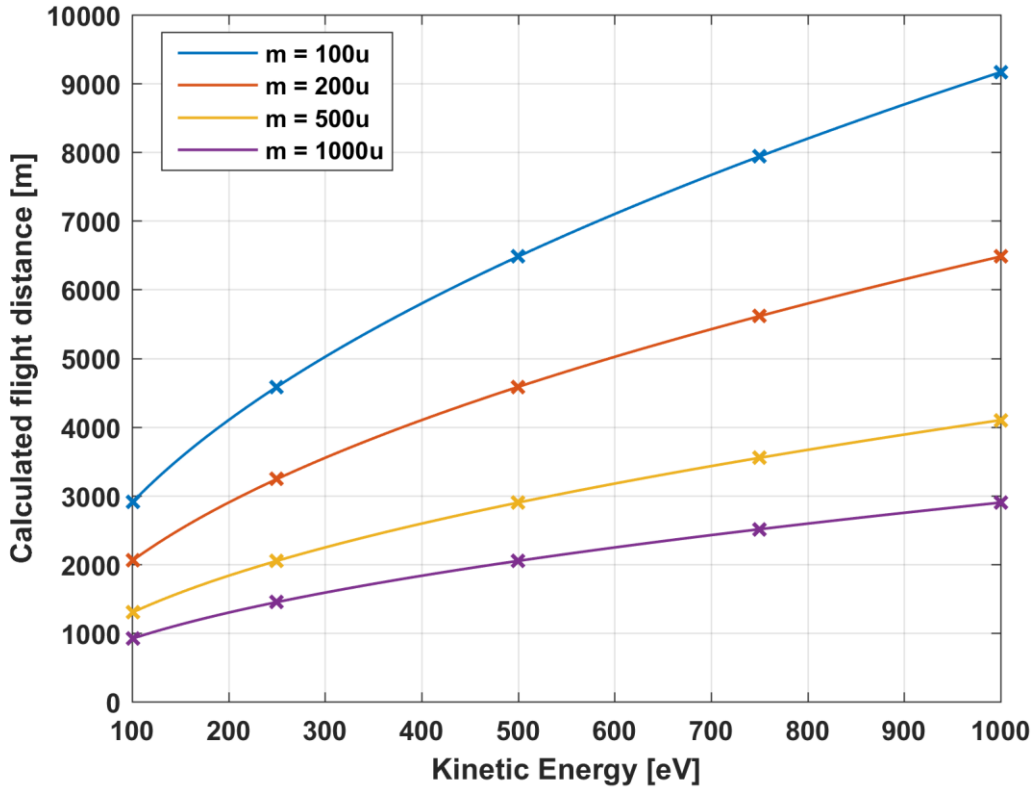

Figure 5.30 – Calculated flight distance plotted against kinetic energy for different ion masses in the range 100u to 1,000u, for transient duration of 200ms, with solid lines representing MATLAB curve fits of the form $y = A_2 x^{b_2}$, with a value of $b_2 = 0.5$ found for all data in this plot.

Using MATLAB, power law curve fits of the form $d(E_k) = A_2 \cdot {E_k}^{b_2}$ were found for the relationship between calculated flight distance, d, and ion kinetic energy, E_k, for each mass and exponent of $b_2 = 0.5$ was found, suggesting a relationship of $d \propto \sqrt{E_k}$. As the variables, m, t and E_k are all independent of one another, this can be combined with equation (5.21), to give a relationship of the form shown in equation (5.22), where A_3 was calculated to be $14{,}491.6\ \mathrm{J}^{0.5}$. This value was found by rearranging equation (5.22) for A_3 and substituting in values of d, m, t and E_k from simulated ion trajectories.

$$d(m, t, E_k) = A_3 \cdot t \cdot m^{-0.5} \cdot {E_k}^{0.5} \qquad (5.22)$$

The validity of this relationship can be seen in Figure 5.31, where flight distance is plotted against the derived parameter $t \cdot m^{-0.5} \cdot {E_k}^{0.5}$, with a linear prediction of flight distance of the form of equation (5.22) overlaid. In total, the results of 90 simulations are plotted, resulting from combining the following simulation parameters: 9 different masses; 100u to 1,000u with increments of 100u, 5 different ion kinetic energies; 101eV, 250eV, 500eV, 1000eV, and 2 different transient durations of 20ms and 200ms.

The largest deviation between the calculated and simulated flight distances is less than 0.005%. An R^2 value of 1.000 suggests that the relationship is an excellent reflection of the simulated data.

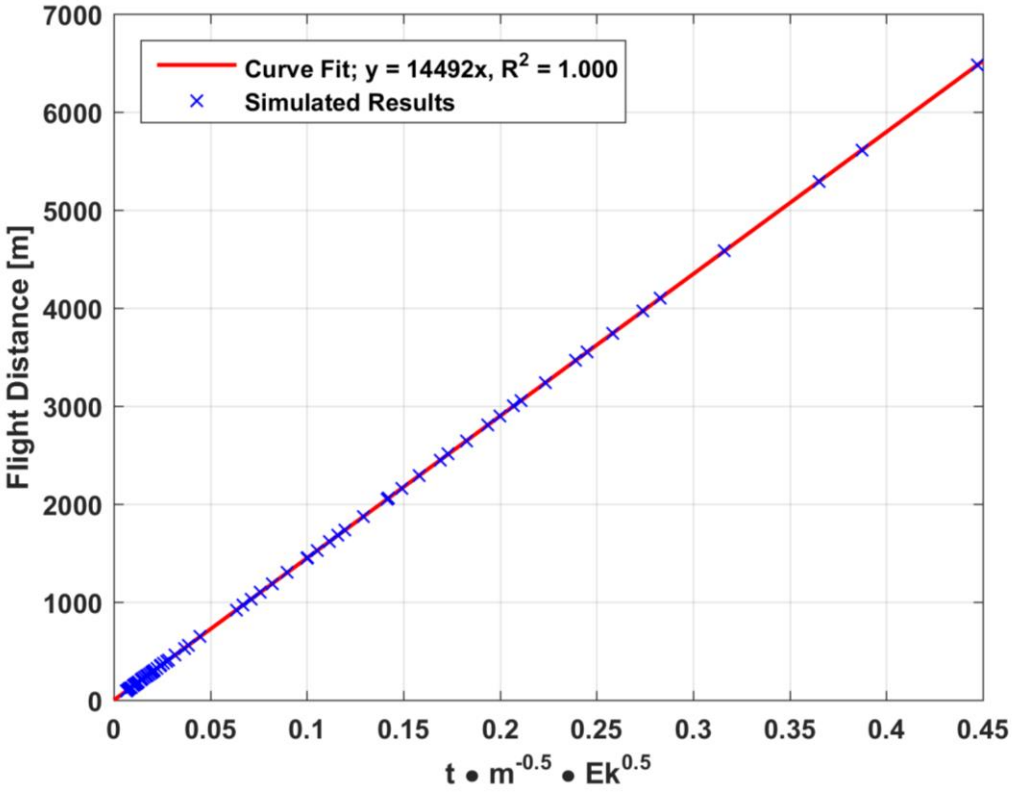

Figure 5.31 - Flight distance against derived parameter, $t \cdot m^{-0.5} \cdot {E_k}^{0.5}$, showing simulation results, and a curve fitted overlaid of the form $d(m, t, E_k) = A_3 \cdot t \cdot m^{-0.5} \cdot {E_k}^{0.5}$, where $A_3 = 14{,}491.6\ \mathrm{J}^{0.5}$, for m given in atomic mass units, t in second, and E_k in electron-volts.

Flight distances can now be calculated for any arbitrary combination of ion mass, kinetic energy, and transient duration. Values found by this method can then be compared to the expected mean free paths for particles under vacuum to confirm the pressure required for the orbital ion trap to operate, and to validate the assumption made of there being no collisions between ions and residual gas particles in simulations.

Figure 5.32 shows the relationship between mean free path and pressure, as given earlier in equation (5.10), with dashed lines added to indicate the approximate distance that an ion with mass 100u, and kinetic energy of 101eV would travel for different length transients. This shows that a pressure of 10^{-9} mbar would be sufficient for transients up to 1s. Ions of mass 100u were chosen as representative of the lowest mass for which the high mass resolving power of the orbital ion trap would be desirable over

that of the time-of-flight reflectron of the J105, with heavier ions travelling shorter distances in the same transient duration. With the differential pumping set-up of the ion transfer assembly, a pressure of 10^{-9} mbar is achievable in the orbital ion trap chamber, meaning an assumption of no collisions between ions and residual gas particles is valid for simulation models, in the case of transient durations up to 1s for ions with energy of 101eV. If ions are to be trapped at higher energies, the distance travelled will increase, which will require higher vacuum, or reduced transient durations.

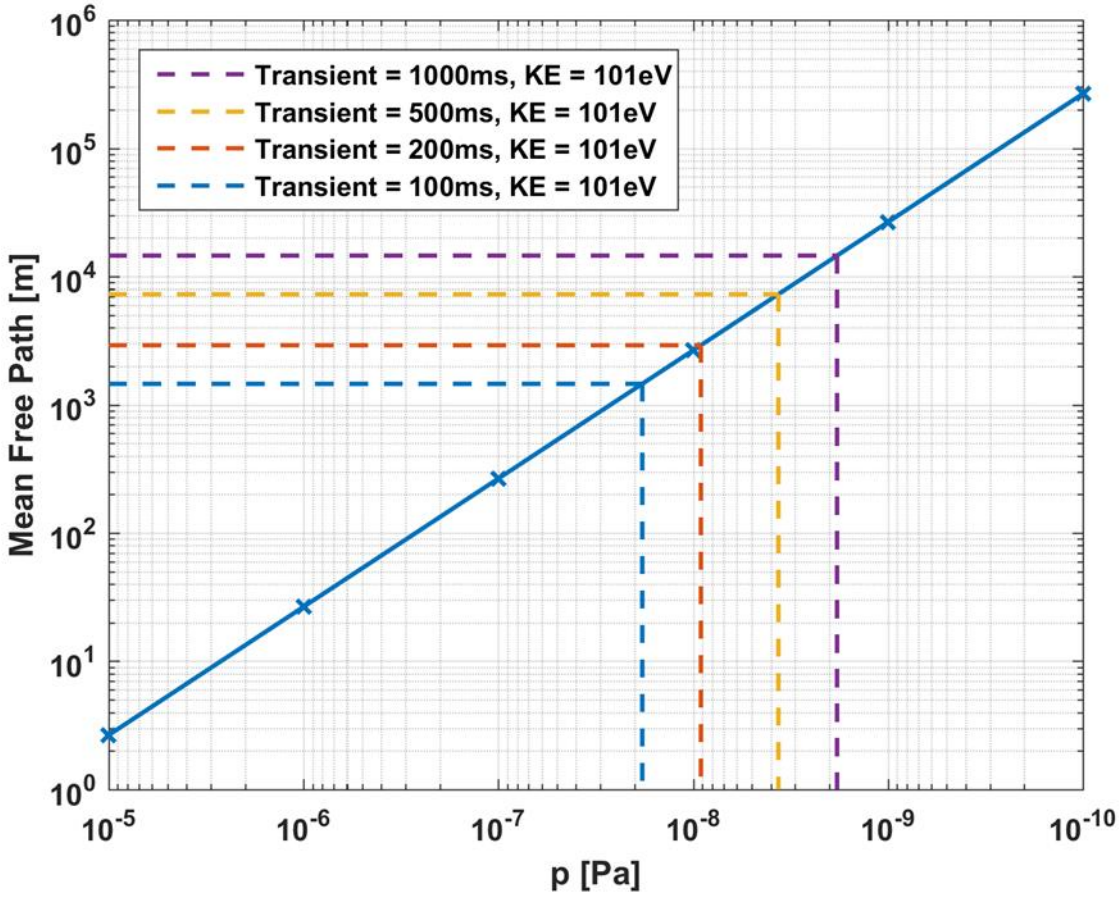

Figure 5.32 - Mean free path plotted against pressure, for 585pm particles at an ambient temperature of 293.15K, with dashed lines showing the approximate flight distances and thus pressures required for ions over different transient recording times, for ions with mass of 100u, and kinetic energy 101eV.

Figure 5.33 shows the relationship between mean free path and the pressure required to permit this mean free path, for ions with 1000eV kinetic energy, and mass 100u. Again, the mean free paths expected for four different transient durations in the range 100ms to 1s, are indicated, showing the pressures required for each transient duration. The advantage of using higher energy ions would be that higher mass resolution could be achieved for a given transient duration. Higher energy ions will travel faster than

lower energy ions of the same mass, meaning they will travel further for the same transient duration, and thus a lower pressure would be required to acquire the same length transient without signal decaying due to collisions with residual gas particles.

It can be seen that in the case of 1000eV ions, the required pressure for transients of 1s duration drops below 10^{-9} mbar. Pressure as low as this would require a bake-out of the instrument if it were to be achieved in the orbital ion trap chamber. As ions are currently not accelerated in the ion transfer assembly, the pressures indicated in Figure 5.32 should be sufficient for operating the orbital ion trap.

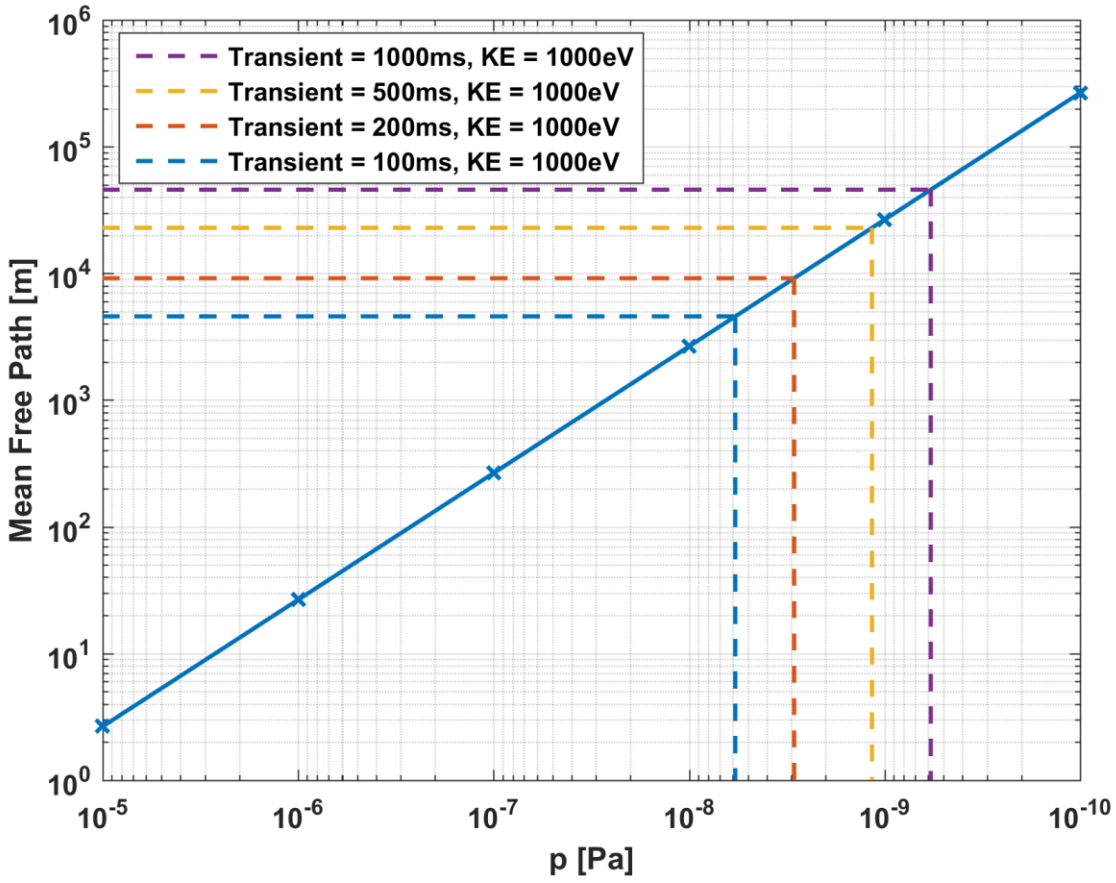

Figure 5.33 - Mean free path plotted against pressure, for 585pm particles at an ambient temperature of 293.15K, with dashed lines showing the approximate flight distances and thus pressures required for ions over different transient recording times, for ions with mass of 100u, and kinetic energy 1000eV.

5.5.2 Mass Resolution Simulations

This section will present the mass resolving performance found by simulating trajectories of ions in an orbital ion trap of standard geometry; internal electrode radius, R_1 = 6mm, external electrode radius, R_2 = 15mm.

Firstly, Figure 5.34 shows an example of the time domain transient data which has been recorded from simulations. To produce this plot, the axial co-ordinate of the location of each ion was extracted from simulation data. The mean of these values was then calculated, to replicate the signal which would be passed to the differential amplifier in vacuum. The positions of all simulated ion were recorded at fixed time intervals, so as to permit straightforward FFT analysis of the data. This interval is referred to as the simulation time-marker step, which is set by the user in SIMION. The significance of this parameter has already been discussed with respect to accurately finding the distance travelled by trapped ions, where a 0.1µs time marker step was found to be required. The impact of the chosen time marker step on calculated mass resolution will be investigated later.

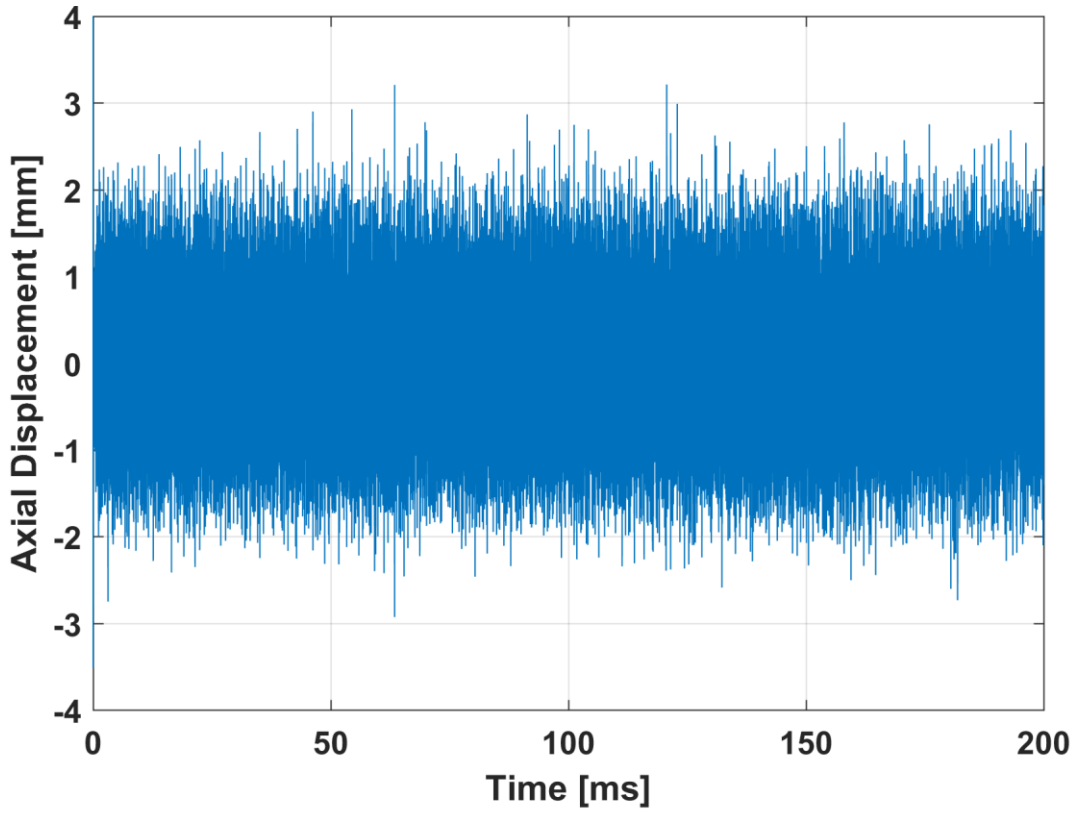

Figure 5.34 - Time domain transient signal for a simulation of 37 trapped ions, showing the average axial displacement of all ions against time. Ions were simulated with mass 100u to 1,000u, with increments of 25u, ion kinetic energy of 101eV, and internal electrode voltage of 175V.

This time domain transient can then be converted into the frequency domain using a fast Fourier transform in MATLAB, producing the frequency spectrum shown in Figure 5.35, with some peaks annotated with their frequency resolution. The relationship between frequency and mass is evident, as although the simulated ions were evenly spaced in mass, an uneven distribution of frequency peaks is seen, due to the inverse square-root dependency, shown earlier in equation (5.15).

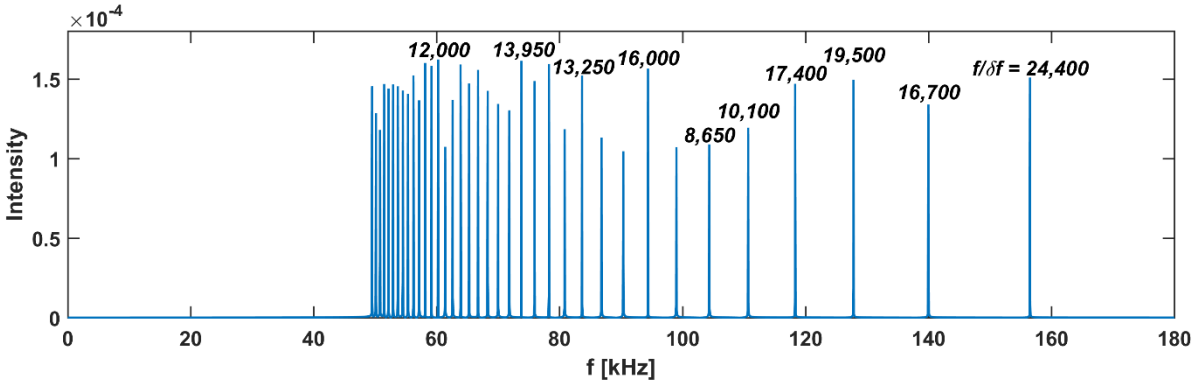

Figure 5.35 - Frequency spectrum for a simulation of 37 trapped ions. 10 peaks are annotated with their frequency resolution. Ions were simulated with mass 100u to 1,000u, with increments of 25u, ion kinetic energy of 101eV, and internal electrode voltage of 175V.

Once a frequency spectrum had been acquired, this can be translated into a mass spectrum using the relationship between frequency and mass-to-charge ratio which is central to the operation of the orbital ion trap, shown in equation (5.15). An example of a simulated mass spectrum, with peaks annotated with their mass resolution, can be seen in Figure 5.36. The values for mass resolution can be compared to the corresponding frequency peaks in Figure 5.35 to see that the achieved mass resolution is approximately half of the corresponding frequency resolution, as expected as oscillation frequency is inversely proportional to the square-root of mass.

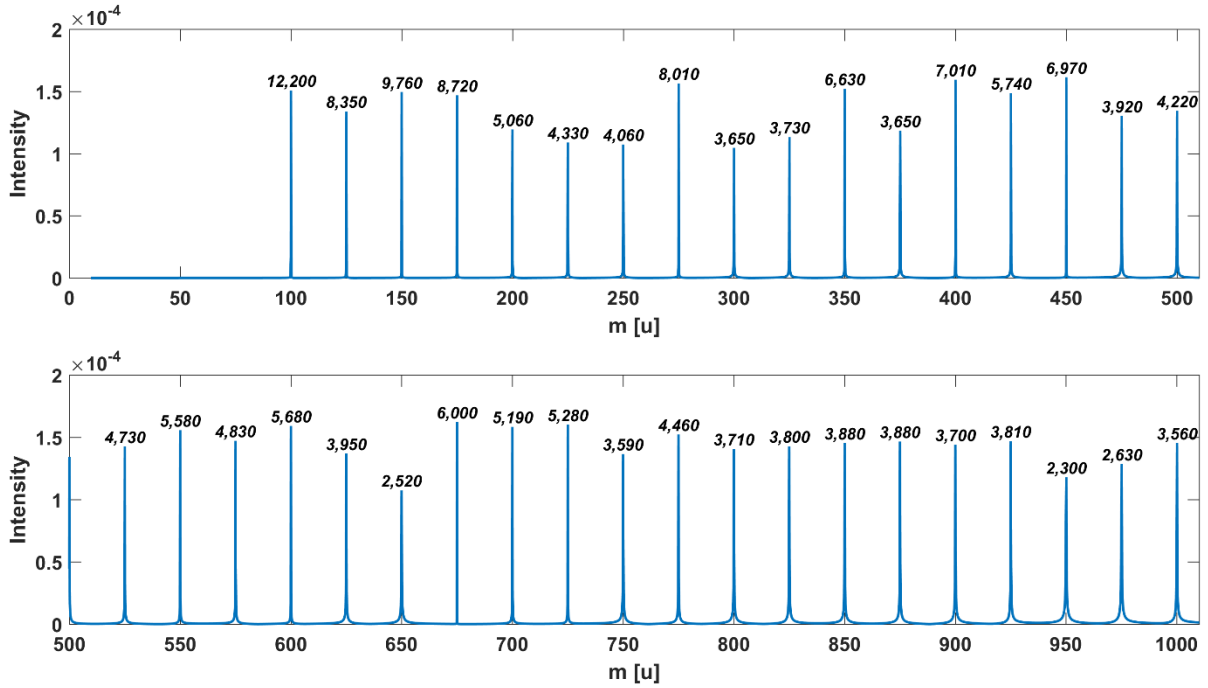

Figure 5.36 - Mass spectrum generated from SIMION data, with every peak annotated with its respective mass resolution. Simulation carried out using 37 ions ranging from mass 100u to 1,000u, with an increment of 25u. All ions were given kinetic energy of 101eV, and the transient duration was 200ms.

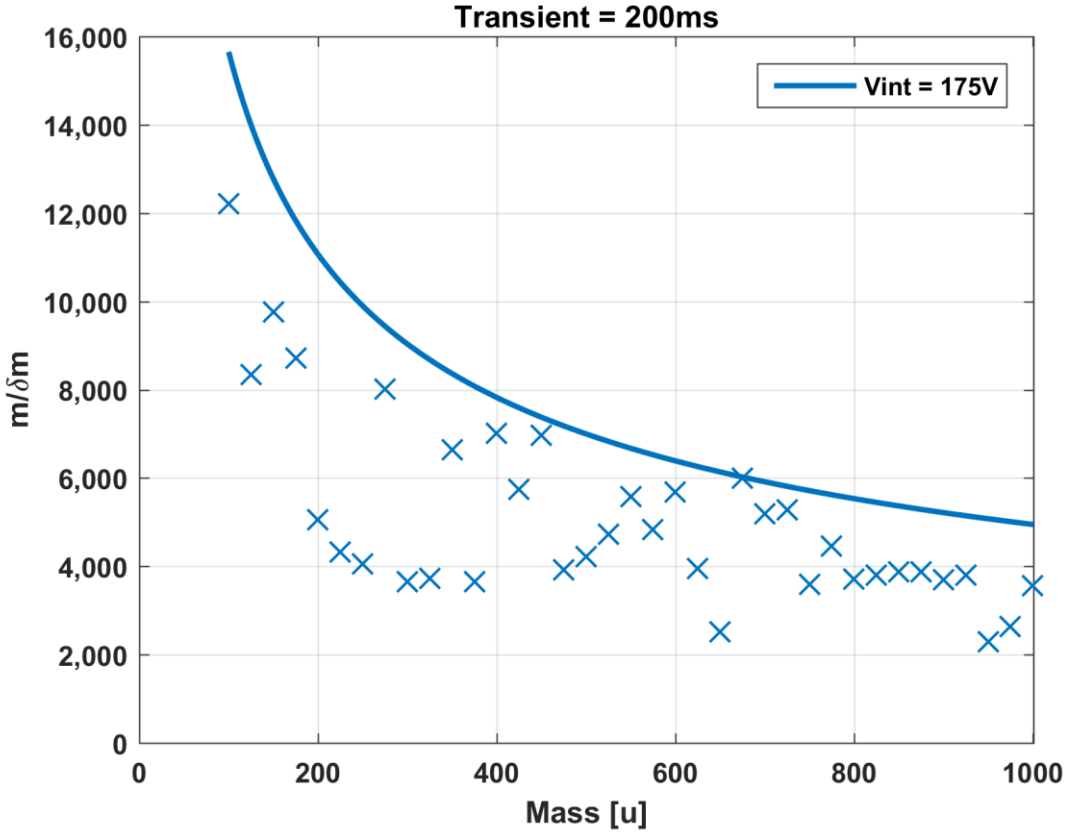

Figure 5.37 - Mass resolution against ion mass, for theoretical performance (solid line) and simulated data (markers), for ions with kinetic energy 101eV, and a transient duration of 200ms.

Figure 5.37 shows a plot of mass resolution against mass, where the solid line is the maximal expected value, calculated using the method described earlier, as per equation (5.19). In this case, for a transient of $t_{\max} = 200ms$, with an internal electrode voltage of 175V, giving an associated field curvature of $k \approx 10^6\ \mathrm{Vm}^{-2}$. The data-points overlaid show the values of mass resolution calculated from SIMION output data of the same trapping conditions for ions of mass 100u to 1000u, with increments of 25u. The length of the transient was capped at 200ms, as simulations of this length for the 37 masses chosen took approximately 24 hours to complete, choosing a longer transient would have limited the number of permutations which could be investigated. A 200ms transient is comparable to some of the shortest transients used in existing orbital ion traps, although typically longer transients are used to achieve higher mass resolution. Although as shown earlier in Figure 5.25 and Figure 5.26, mass resolution varies linearly in proportion to the duration of the transient, for a fixed ion mass or kinetic energy, so the mass resolution which would be expected for longer transients can be extrapolated from the simulation data presented. Figure 5.36 shows the mass spectrum produced from the simulation data, with mass resolution annotated above each peak. It can be seen that simulated data gives values for mass resolution below the predicted theoretical maximum, which is as would be expected. It is evident from Figure 5.36 that the relative abundance of each ion is not reflected in the mass spectrum, as each mass was present with the same abundance during simulation. This could be improved by zero-padding data before performing the FFT.

It is encouraging that simulation results give values of mass resolution in broad agreement with the estimated theoretical maxima, and it gives confidence that the higher mass resolutions predicted for longer transients and higher trapping voltages would hold.

Simulations were carried out to confirm that higher trapping voltages give rise to higher mass resolutions, with ion energies of 500eV and 1000eV trapped with internal electrode voltages of 866V and 1732V respectively, as shown earlier in the theoretical curves of mass resolution against mass in Figure 5.23.

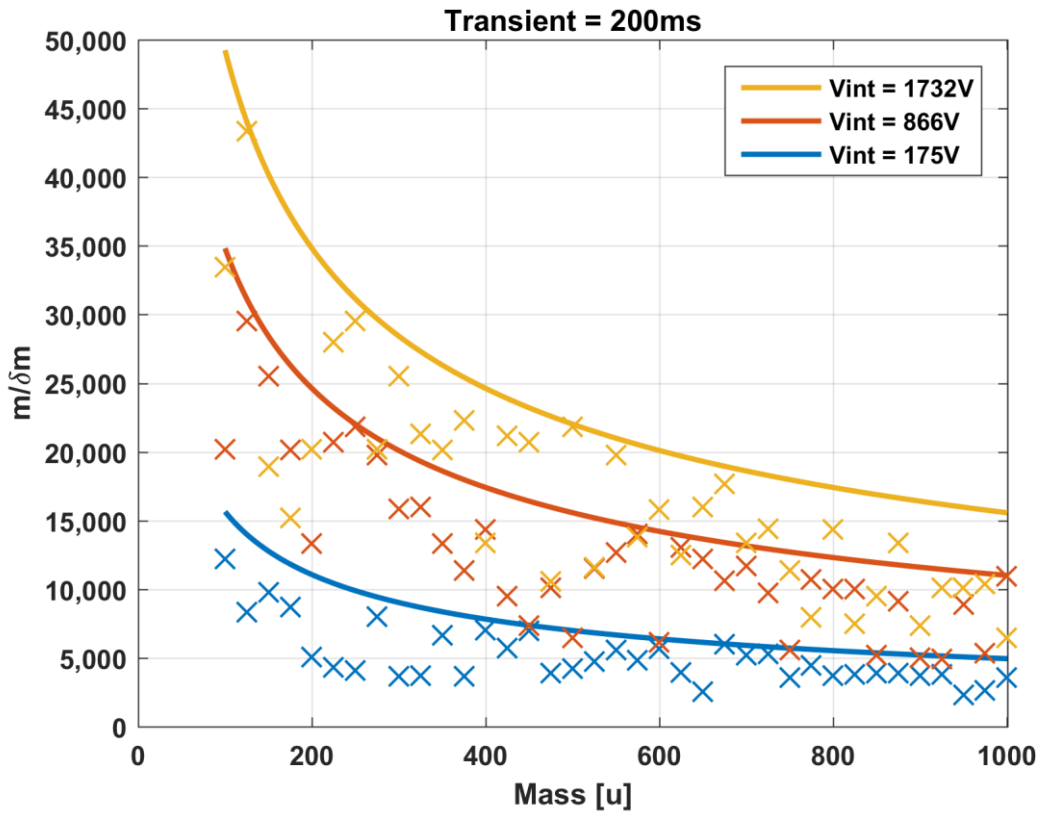

Figure 5.38 - Mass resolution against mass for theoretical (solid line) and simulated data (markers) for different internal electrode voltages

Figure 5.38 shows theoretical and simulated mass resolution data for the three internal electrode voltages simulated, it can be seen that mass resolution does increase for higher internal electrode voltages. This can be shown more clearly if the data for each simulated voltage is replaced by a fitted curve. Curves of the form shown in equation (5.23) were fitted to the simulated results for mass resolution, as this is the expected relationship between ion mass and mass resolution, where A is a constant.

$$R = \frac{m}{\delta m} = A \cdot \sqrt{\frac{1}{m}} \qquad (5.23)$$

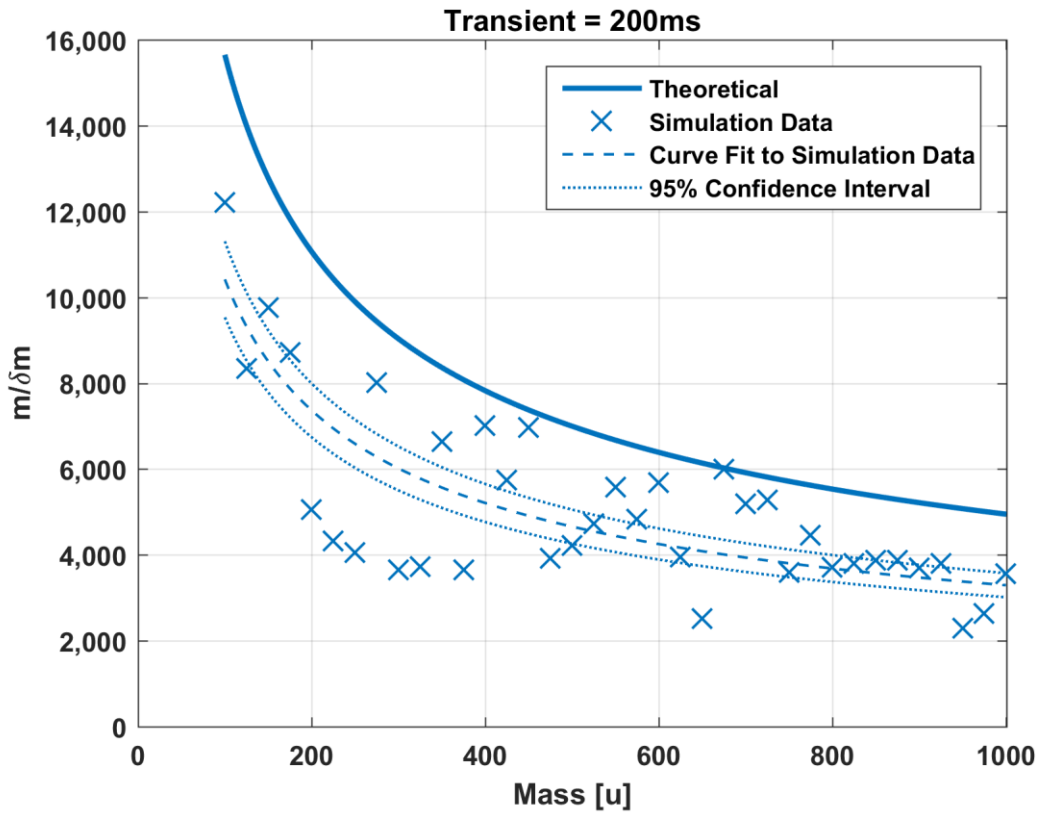

Figure 5.39 - Simulated mass resolution data with curve fit, 200ms transient, 175V internal electrode voltage, ion kinetic energy of 101eV.

Figure 5.39 is equivalent to Figure 5.37, with the addition of a curve fit for the simulated data, it is evident that the curve fit does not perfectly capture the simulated values of mass resolution, but it is useful nevertheless to highlight the typical difference between simulated and theoretical maximum mass resolution. The curve fit was found in MATLAB using a non-linear least squares regression model. Figure 5.40 shows a plot of the residuals of the curve fit against mass, alongside a histogram of the values of the residuals. It can be seen that there is no obvious pattern in the residual plot, residuals are reasonably symmetrically distributed about zero, suggesting that the error is random, and that the chosen model is valid, although imperfect.

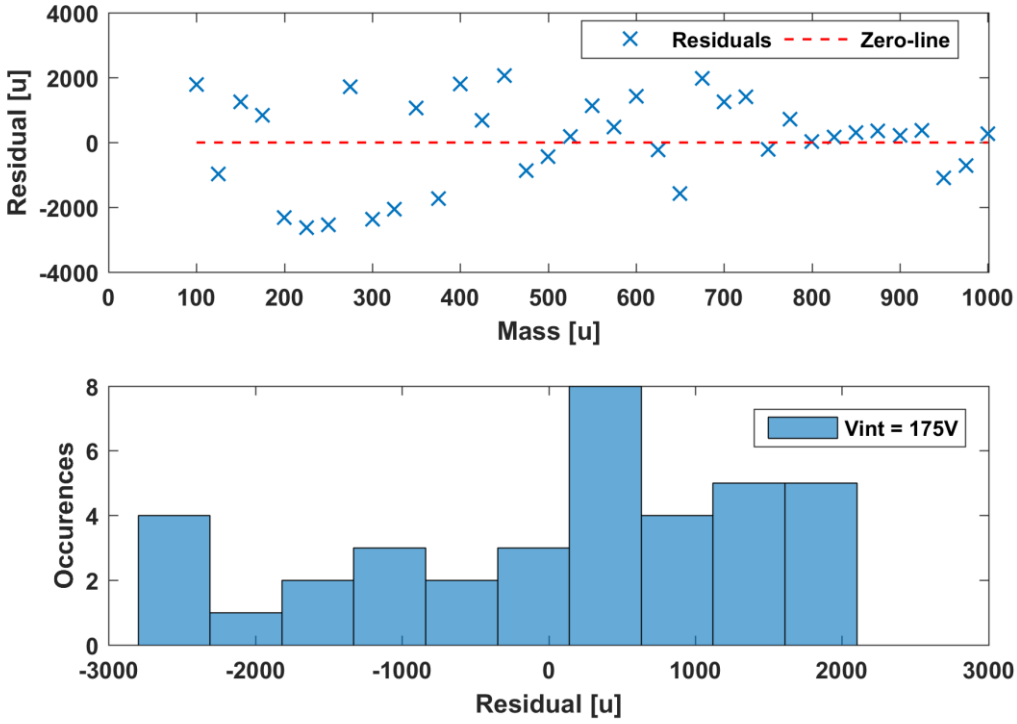

Figure 5.40 - Residuals for curve fitted to simulated mass resolution data, 200ms transient, 175V internal electrode voltage, ion kinetic energy of 101eV.

Figure 5.41 shows the theoretical maximal curves and curve fits for simulation data for all three internal electrode voltages investigated. This plot makes it apparent that simulated mass resolution does increase with internal electrode voltage, but still lags some way behind the maximum theoretical values.

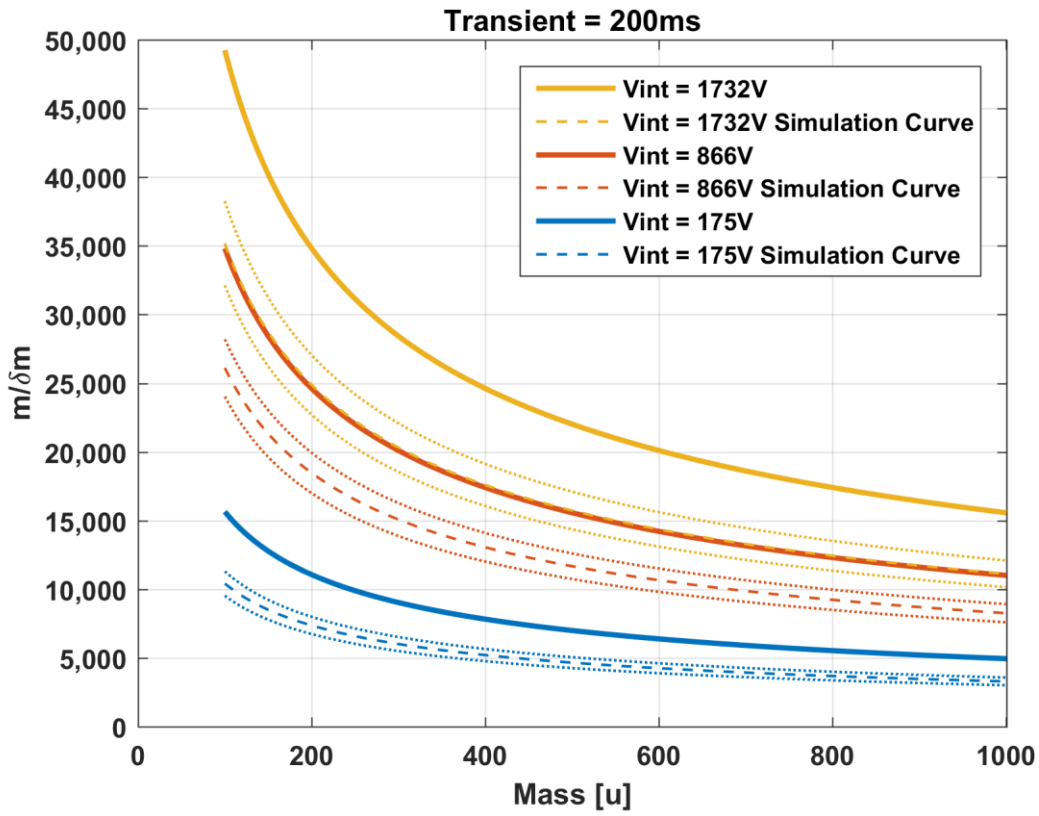

Figure 5.41 - Curve fits for simulated mass resolution values, with theoretical maxima shown as solid lines, all for 200ms transients

The residual plots for internal electrode voltages of 866V and 1732V are shown in Figure 5.42 and Figure 5.43 respectively. Once again, the residuals exhibit random behaviour, with reasonably symmetric distribution about zero, giving more confidence to the validity of the choice of model.

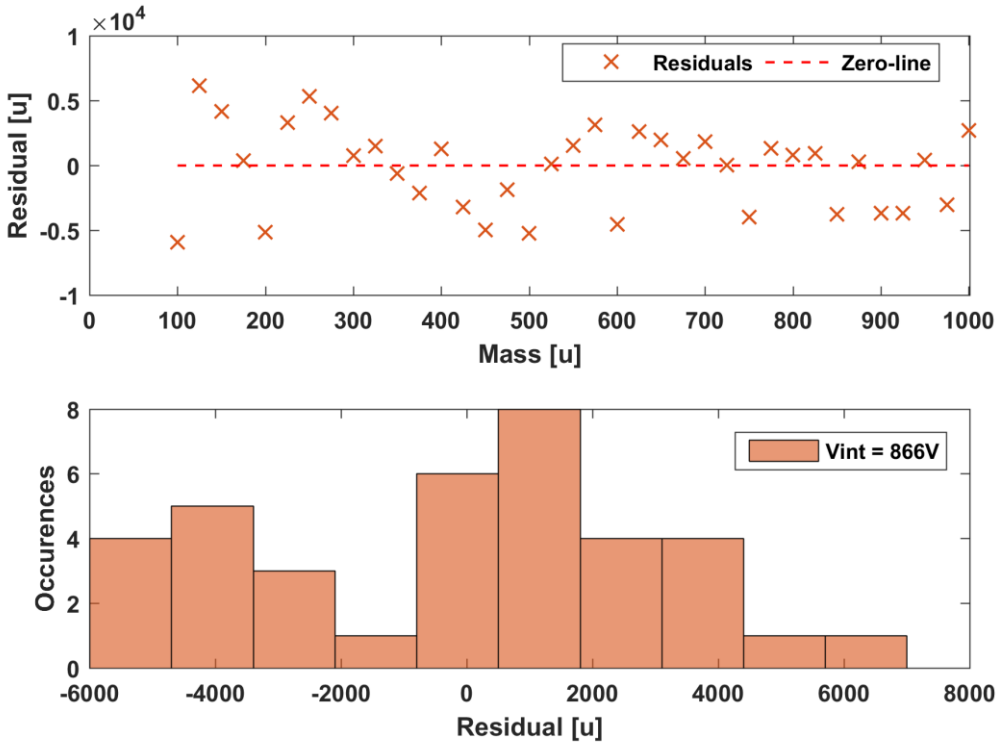

Figure 5.42 - Residuals for curve fitted to simulated mass resolution data, 200ms transient, 866V internal electrode voltage

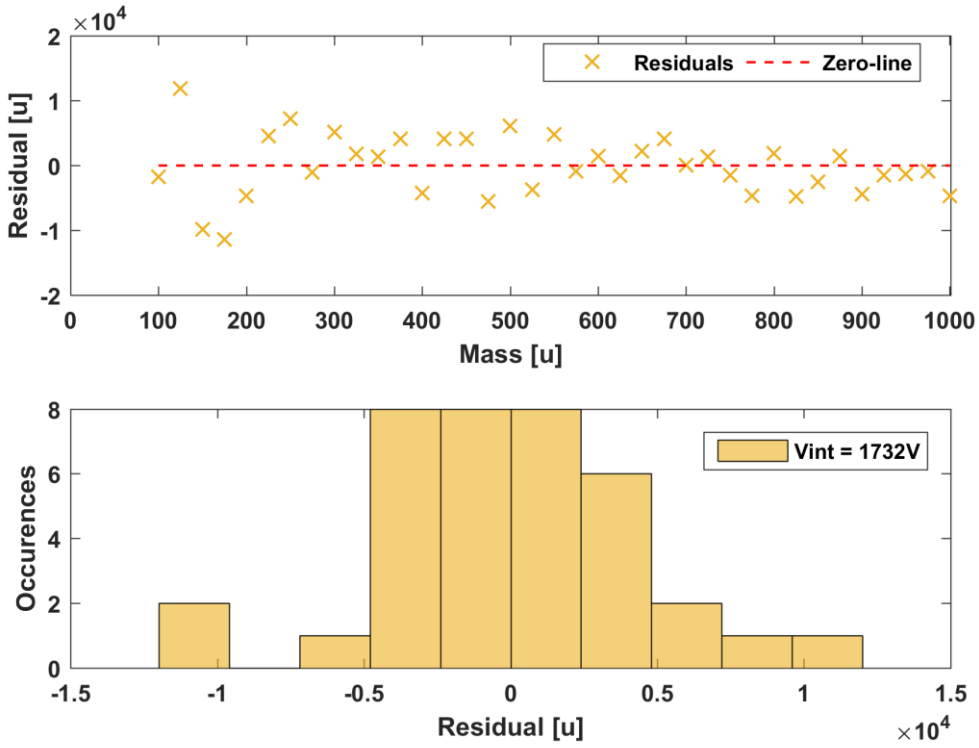

Figure 5.43 - Residuals for curve fitted to simulated mass resolution data, 200ms transient, 1732V internal electrode voltage

Figure 5.44 shows the simulated mass resolution for two different transient durations of 500ms and 1,000ms, for masses in the range 50u to 1,000u. It can be seen that in some cases there were quite large discrepancies between the maximum predicted curves for mass resolution and the simulated values. However, the expected dependency of mass resolution on the inverse square-root of mass is followed.

Figure 5.45 shows the residuals of the fitted curves for the two different length transients. It can be seen that these residuals are randomly dispersed around zero. A histogram of the residuals for both 500ms and 1000ms transient simulations is shown in Figure 5.46. It can be seen that the residuals for the 1000ms transient are not normally distributed about zero, with the fitted curve tending to overestimate mass resolution compared to simulated values.

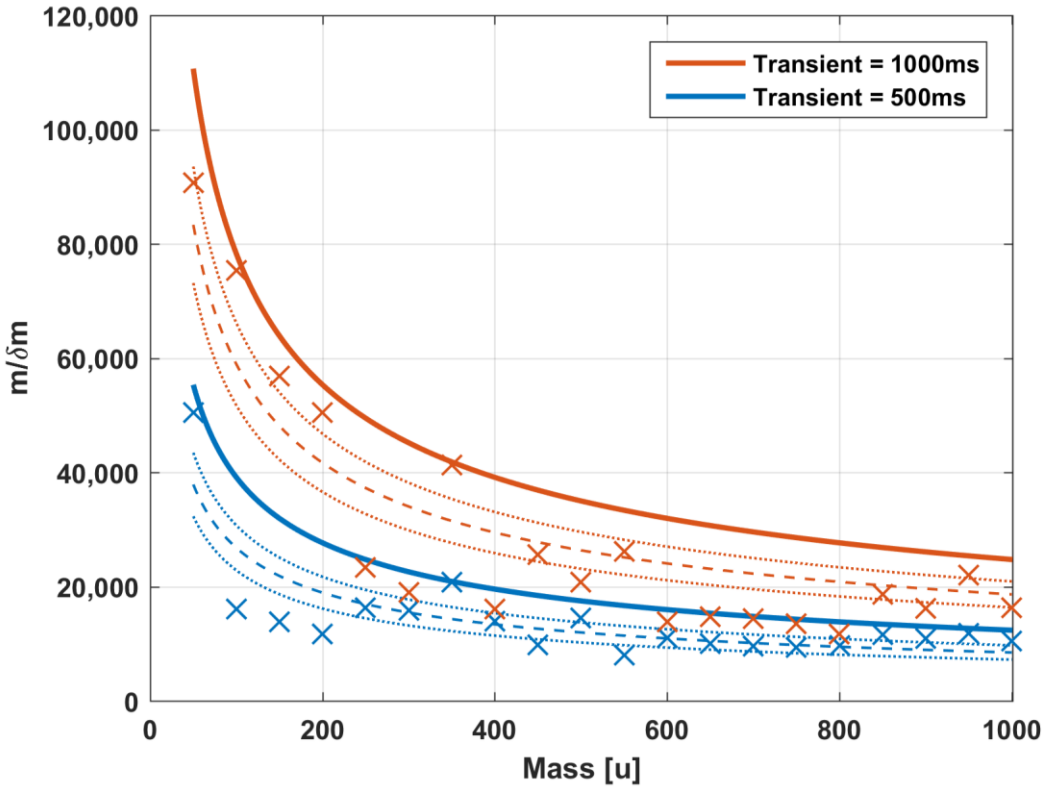

Figure 5.44 - Mass resolution against mass for different transient durations. Simulations consisted of 5 ions from mass 100u to 500u, with an increment of 100u. All ions were given 101eV of kinetic energy, and were trapped with an internal electrode voltage of 175V.

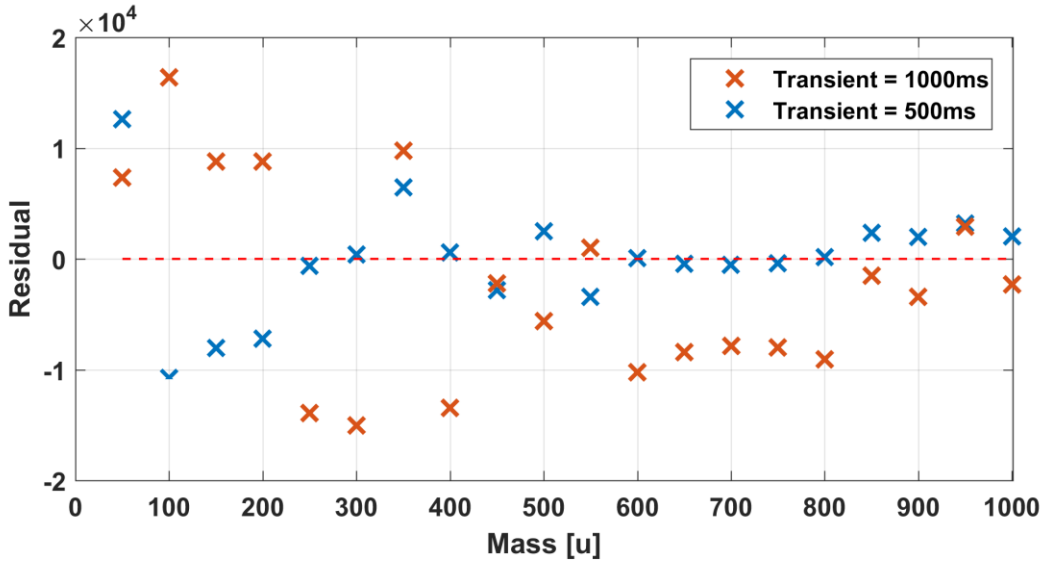

Figure 5.45 – Residuals for curves fitted to simulated mass resolution data, 500ms and 1000ms transients, ions with 101eV kinetic energy and trapped by a 175V internal electrode voltage.

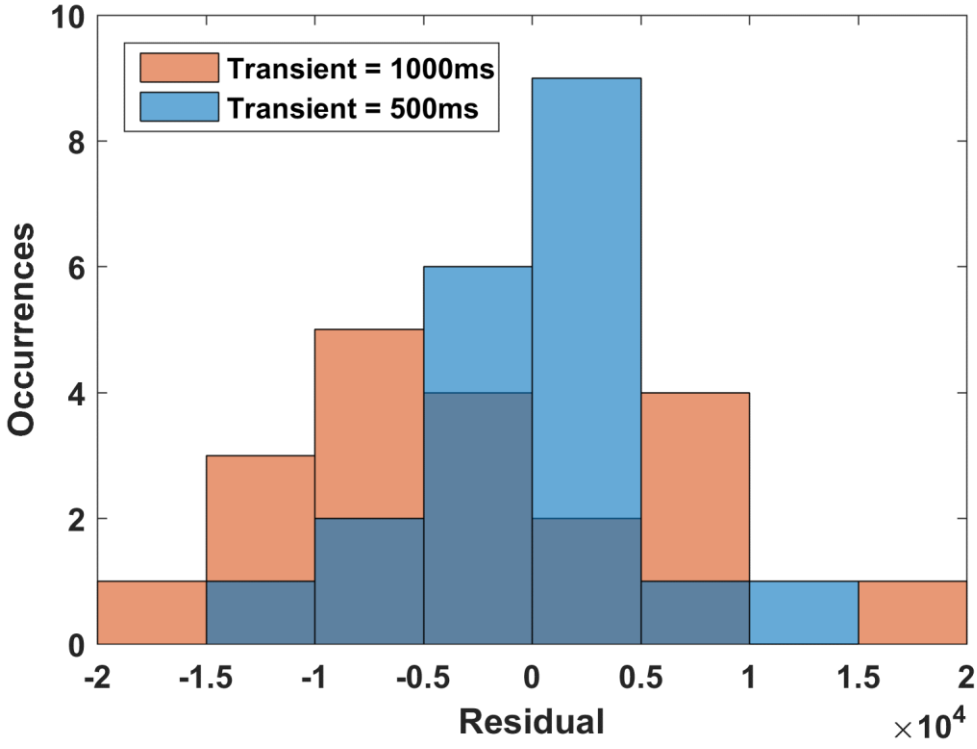

Figure 5.46 - Histogram of residuals for curves fitted to simulated mass resolution data, 500ms and 1000ms transients, for ions with 101eV kinetic energy trapped by a 175V internal electrode voltage.

As a more robust verification of the linear dependence of mass resolution on transient duration, multiple transient durations were simulated for different mass ions, with the results shown in Figure 5.47 as a plot of the simulated mass resolution against transient duration. Ions of mass 50u, 200u, and 500u were simulated for transient

durations of 20ms, 50ms, 100ms, 200ms, 800ms, 1000ms. Linear curve fits passing through the origin were found for each mass, of the form $m/\Delta m = A \cdot t$, with R^2 values of 0.95, 0.94, and 1.00 respectively for masses 50u, 200u and 500u, showing that a linear relationship between simulated mass resolution and transient duration is valid.

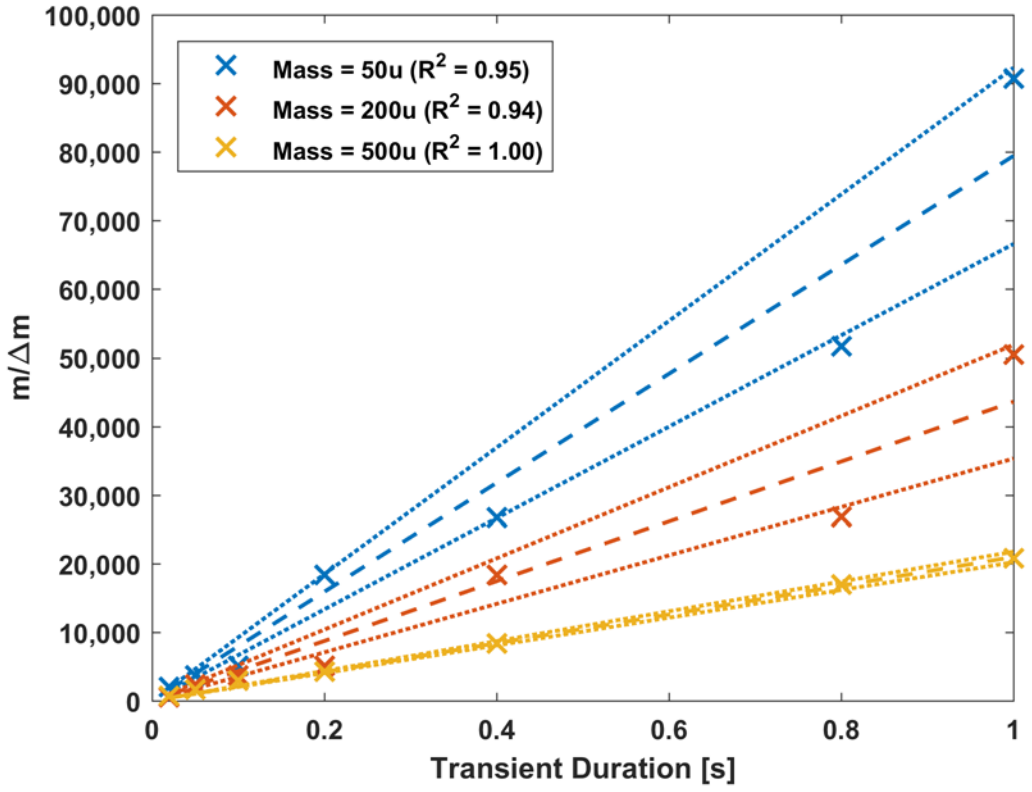

Figure 5.47 - Simulated mass resolution against transient durations in the range 20ms to 1s, for ions with 101eV kinetic energy, trapped by an internal electrode voltage of 175V. Linear fits of the form $m/\Delta m = A \cdot t$ were found, shown as dashed lines, with 95% confidence intervals shown as dotted lines.

5.5.3 Validation of Mass Resolution Simulations

Typical transient durations in the literature for orbital ion traps are of the order of hundreds of milliseconds so as to achieve high mass resolution spectra, (Makarov, 2000), (Makarov, Denisov, Kholomeev, *et al.*, 2006), (Makarov *et al.*, 2009). Simulating transients of this length is computationally expensive, due to the small simulation time steps which are needed in SIMION because of the high field curvature in the orbital ion trap. As such, the linearity between mass resolution and transient duration can be used to simulate shorter duration transients, and proportionally scale up the resultant mass resolving powers to allow comparisons to mass resolution reported in the literature.

It should be noted that as simulations were run with all ions injected immediately into the trapping volume, there would be no phase shifts accrued due to ion injection. As a result, the spectra and calculated mass resolution found from simulations are effectively equivalent to absorption mode spectra, often referred to in the orbital ion trap literature as 'enhanced Fourier transform' or eFT spectra, (Lange *et al.*, 2014a). As discussed in Chapter 2, absorption mode spectra can exhibit mass resolution up to twice that of magnitude mode spectra in the ideal case of accounting for all phase shifts in ion motion, (Marshall *et al.*, 1998). This means that simulated mass resolution would be expected to be twice higher than those reported for magnitude mode spectra, which would encompass most spectra published prior to the first public description of the eFT method in 2014.

Finding studies in the literature which give sufficient information to run comparison simulations is not straight forward, as many papers do not accurately report the transient acquisition duration used, but simply quote the scan cycle time, such as (Makarov, Denisov, Kholomeev, *et al.*, 2006). This scan cycle time value also incorporates the time required to fill any intermediate ion traps, and the time required for ion transfer to the orbital ion trap, so an accurate transient duration cannot be determined.

There is also the matter of the internal electrode voltage and ion energy used to consider. Although it can be assumed that any study using a standard geometry orbital ion trap, that is internal electrode radius, R_1 = 6mm, and external electrode radius, R_2 = 15mm, would use an internal electrode voltage of 3.5kV. This value is widely reported as standard for the first commercial orbital ion traps with standard geometry, (Makarov, Denisov, Kholomeev, *et al.*, 2006), (Makarov *et al.*, 2009), (Kharchenko *et al.*, 2012).

In Makarov et al.'s 2009 paper evaluating the high-field orbital ion trap geometry, a plot of the mass resolution obtained from a 0.76s duration transient, acquired using a standard geometry orbital ion trap is shown, for spectra acquired in magnitude mode. Mass resolution is given for ions across a mass range of 100u to 10,000u trapped with an internal electrode voltage of 3.5kV, (Makarov *et al.*, 2009). This voltage would correspond to ideal trapping behaviour for ions with kinetic energies of approximately 2,021 eV. A comparison simulation was run for ions with the following masses; 100u, 500u, 1,000u, 5,000u, 10,000u, but with a transient length of 7.6ms, only 1% of that used in the literature. The mass resolution values reported in the literature could then

be reduced by a factor of 50 to allow for comparison. This reduction accounts for the transient duration being 100 times shorter, and also for the simulated data being absorption mode spectra, with twice the expected mass resolution of magnitude mode.

Other useful comparison data was found in a 2006 paper exploring the dynamic range of mass accuracy of orbital ion traps, as such mass resolution was presented across a broad mass range from a single acquisition (Makarov, Denisov, Lange, *et al.*, 2006). Mass resolution was reported for a 0.38s magnitude mode transient, with $m/\Delta m = 30{,}209$ for m/z 524, and $m/\Delta m = 19{,}245$ for m/z 1422. These values would correspond to mass resolutions of $m/\Delta m = 604$ and $m/\Delta m = 385$ respectively for a 7.6ms transient duration, in magnitude mode, scaling to $m/\Delta m = 1{,}208$ and $m/\Delta m = 770$ for absorption mode.

A further study which offers a useful comparison is the 2014 paper which detailed the eFT method for processing orbital ion trap spectra. This paper reported mass resolution of approximately $m/\Delta m = 56{,}000$ for m/z 345, acquired over a 256ms transient, with eFT processing active. The expected equivalent mass resolution for a shorter transient of 7.6ms would be approximately $m/\Delta m = 1{,}600$.

Figure 5.48 shows the mass resolution figures from the literature, all scaled to be equivalent to absorption mode, or eFT processed, spectra, for a transient duration of 7.6ms, overlaid on a plot of comparable simulation data.

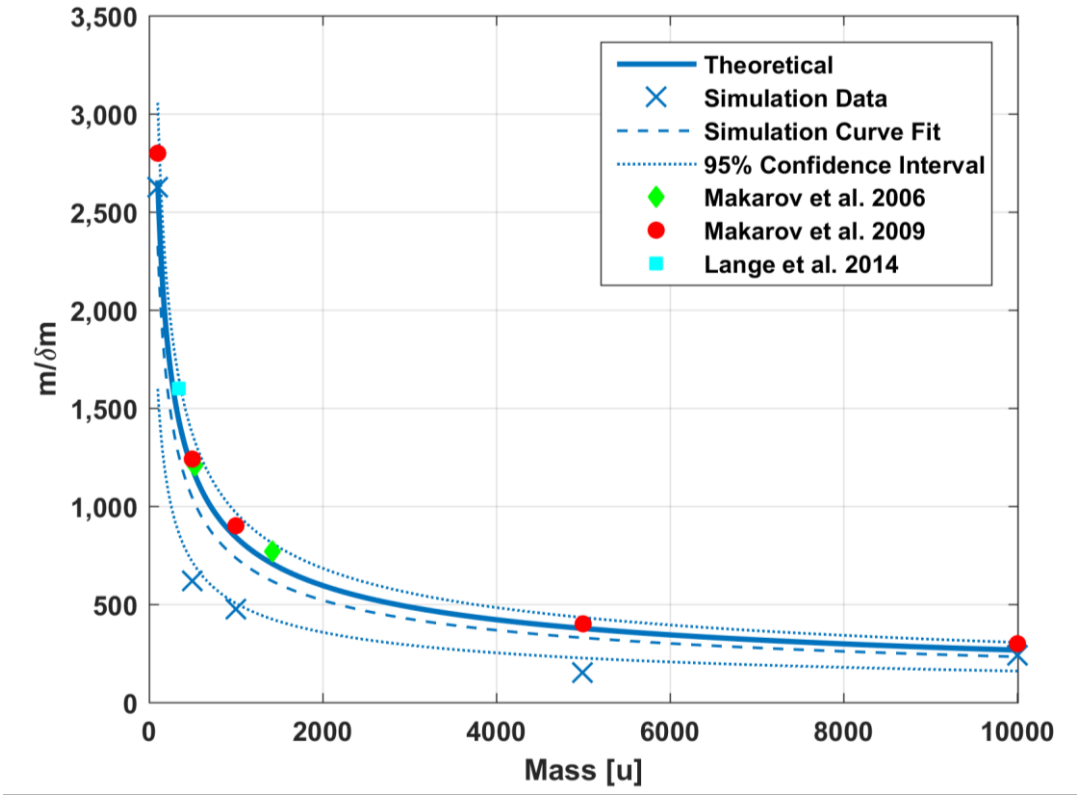

Figure 5.48 Mass resolution against mass for simulated ions in the mass range 100u to 10,000u, with 2,021eV kinetic energy, trapped by a 3.5kV internal electrode voltage, with a transient duration of 7.6ms. Overlaid are comparative experimental values of mass resolution from the literature, scaled to be equivalent to absorption mode mass resolution for a transient duration of 7.6ms.

It can be seen that all of the experimental results from the literature lie within the 95% confidence interval of the curve fitted to simulation mass resolution data. As such, simulations can be seen to be good approximations of experimental results of mass resolution from orbital ion traps.

5.5.4 Impact of Simulation Time Marker Step

The time marker step chosen in ion trajectory simulations refers to the fixed interval at which data is recorded for post-processing outside of SIMION. A fixed interval is particularly useful as it permits FFT analysis of recorded simulation data, as is required for generating mass spectra from orbital ion trap simulations, from which mass resolution can be evaluated.

The time marker step is distinct from the calculation time step, which is the interval for which ion position and velocity are calculated whilst simulations are running, and can vary dynamically within a simulation depending on factors such as; the field curvature in the region through which the ions are flying, or how close ions are to an electrode surface. The calculation time step is primarily controlled by the trajectory quality parameter, as discussed later.

Figure 5.49 shows the simulated mass resolution found using time marker steps of 1µs, 0.1µs, 0.01µs and 0.001µs. It can be seen that each time marker step produced identical mass resolution data, this is as would be expected for any time marker step size less than the period of oscillation of a trapped ion. From Figure 5.22 it can be seen that for ion energies up to 1000eV, no ion with mass greater than 50u will have an oscillation frequency in excess of 1MHz, that being the frequency at which a 1µs time marker step would become unsuitable. This means that the coarsest time step of 1µs is sufficient for further simulations concerned with mass resolution. This will serve to reduce the file size of simulation output data, allowing for faster data analysis.

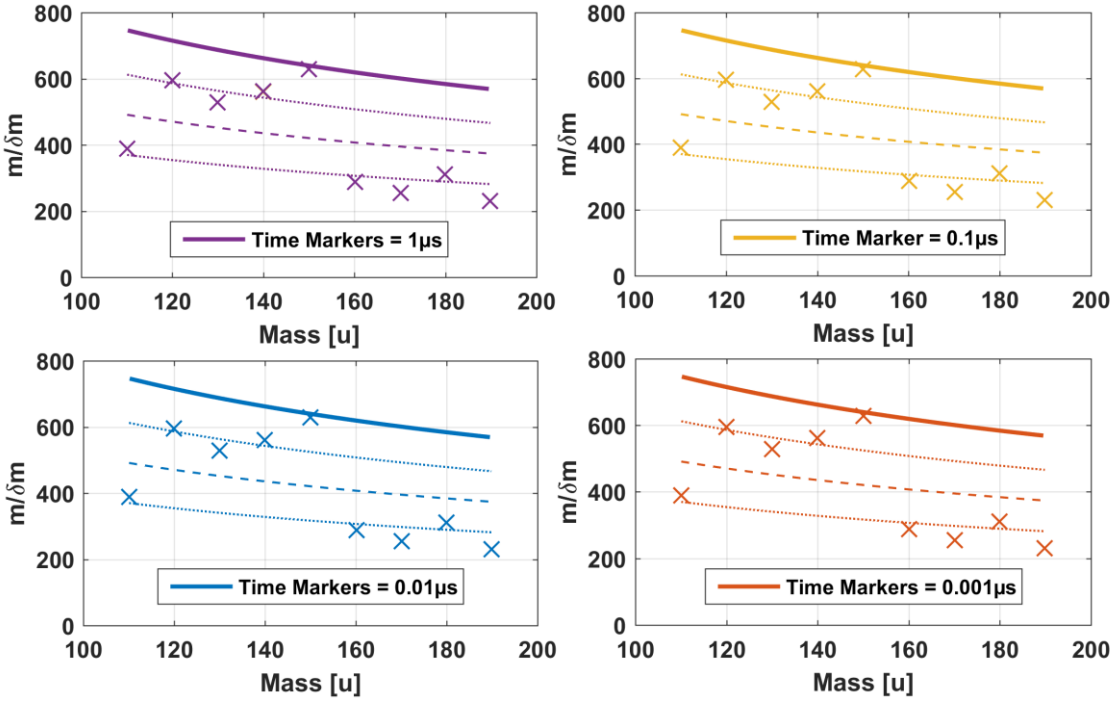

Figure 5.49 - Comparison of mass resolution against mass, found for different time marker steps of 1µs, 0.1µs, 0.01µs, and 0.001µs, all for ion kinetic energy 101eV, and internal electrode voltage of 175V. Plots are not overlaid as they were found to give identical results.

5.5.5 Impact of Refine Convergence Criterion

As noted in the introduction to this chapter, all simulations were carried out using a 1E-6V refine convergence criterion, this was initially chosen to allow potential array files to be refined within a reasonable time frame on an average desktop PC, whilst also maintaining a good degree of accuracy. To give some context, a typical cylindrical array used to represent the orbital ion trap contained over 21E6 grid points, and took approximately 20 minutes to refine on a Dell Precision T1700 PC with 16GB of RAM. If a lower convergence criterion had been chosen, the time taken to refine arrays would have reduced the number of different arrays which could be simulated in the available time.

To test the impact of the convergence criterion on simulation results, one potential array was refined to 1E-7V, which is the limit permitted in SIMION 8.1. Comparative simulations were then performed to judge whether this gave significantly different results compared to a potential array refined to 1E-6V.

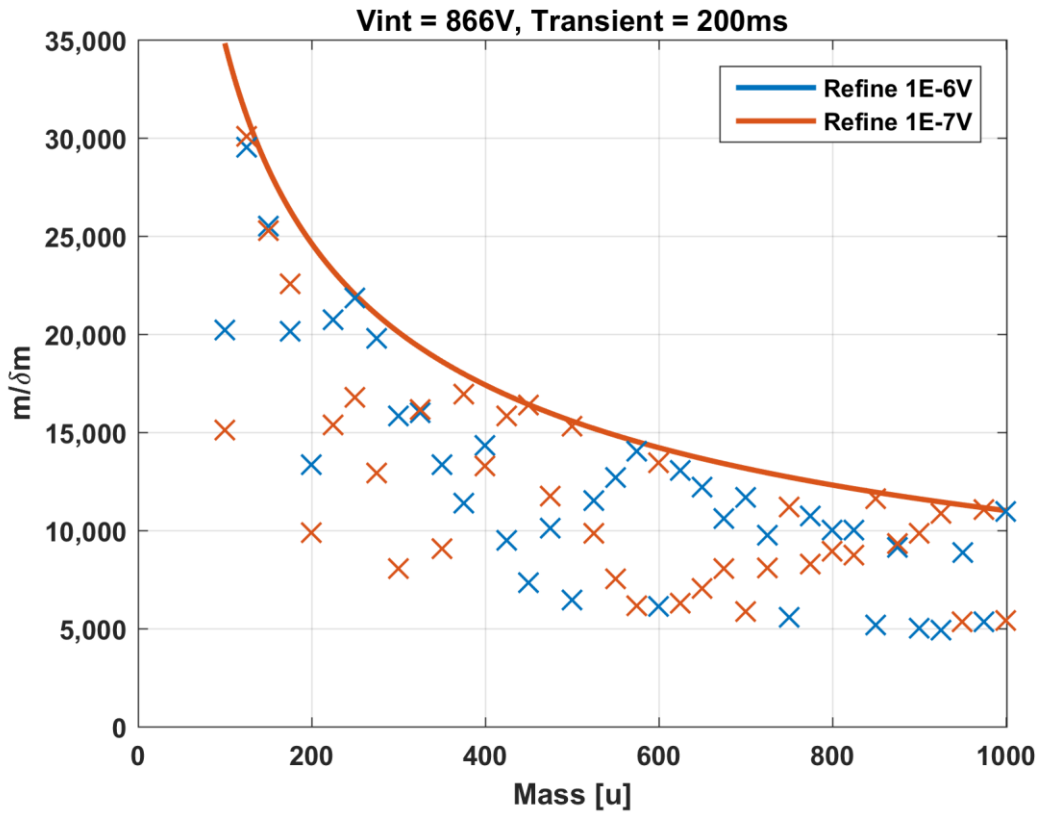

Figure 5.50 - Comparison of simulated mass resolution for potential arrays refined with different convergence criteria, for a 200ms transient. 37 ions simulated in each case, from mass 100u to 1000u with increment of 50u, ion kinetic energy of 500eV, trapped by an internal electrode voltage of 866V.

Figure 5.50 shows that there is little to distinguish between simulated mass resolution values for two arrays refined to 1E-6V and 1E-7V convergence criteria. Figure 5.51 shows curves fitted to the simulated mass resolution data, it can be seen that there is significant overlap in both curve fits, with the 1E-6V refined array giving slightly higher mass resolution data. This was reversed when ions were trapped at 1732V, with the 1E-7 refined array giving greater mass resolution, again with significant overlap in the two curve fits as shown in Figure 5.52.

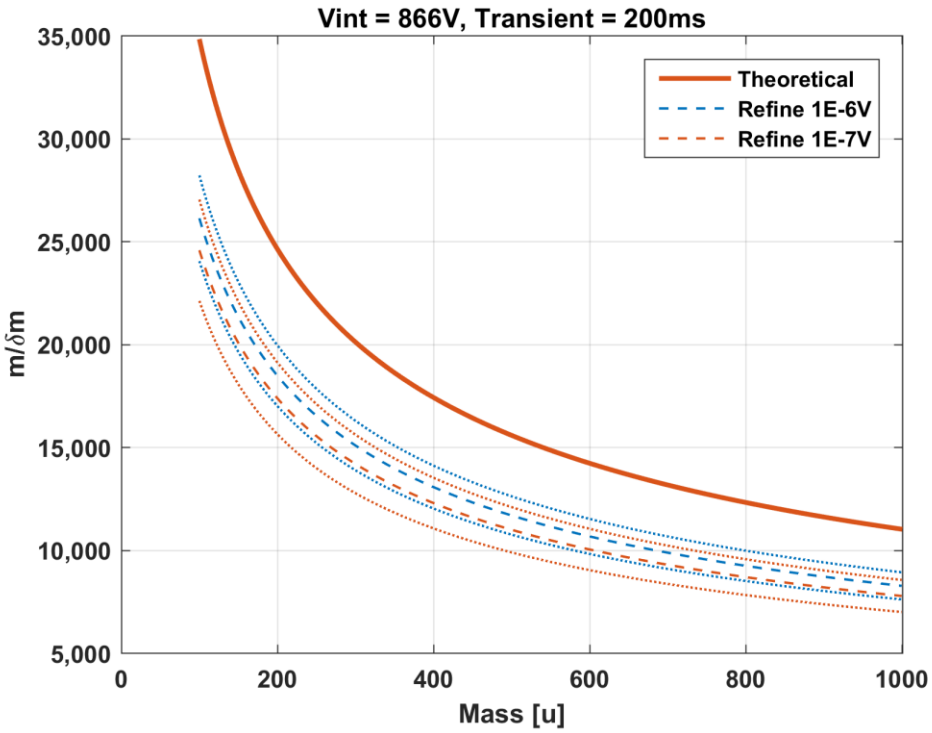

Figure 5.51 - Curves fitted to simulated mass resolution data for potential arrays refined to 1E-6V and 1E-7V convergence criteria, 200ms transient, 866V internal electrode voltage

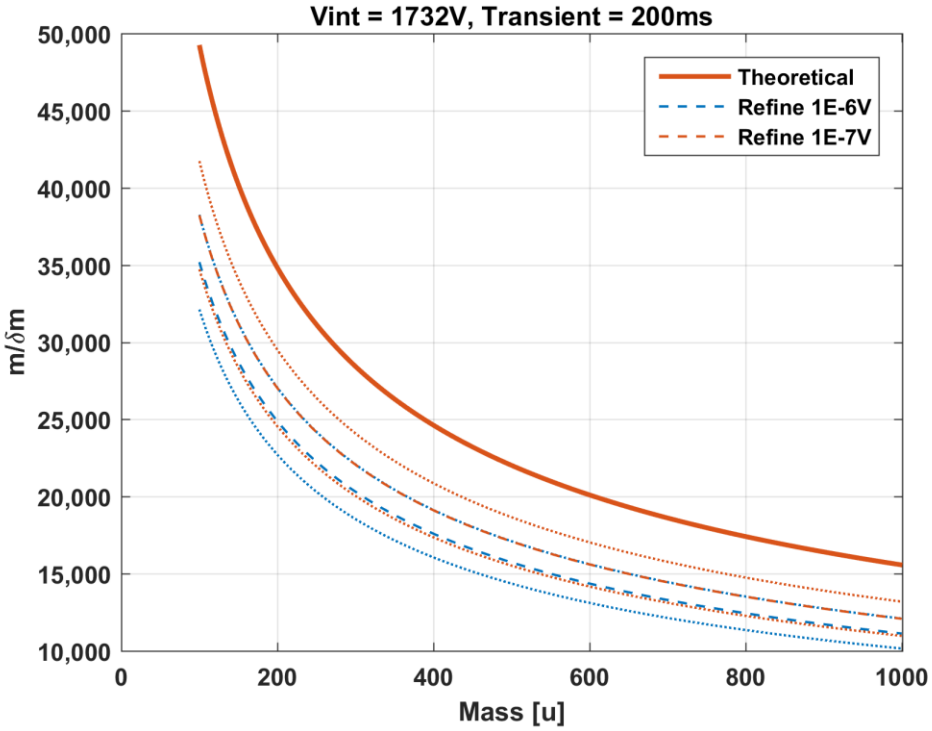

Figure 5.52 - Curves fitted to simulated mass resolution data for potential arrays refined to 1E-6V and 1E-7V convergence criteria, 200ms transient, 1732V internal electrode voltage

The residuals of the curves fitted to both 1E-6V and 1E-7V refined arrays for ions trapped at 866V are shown in Figure 5.53. The residuals are once again randomly distributed and centred around 0u, suggesting that both curve fits are suitable models, with random errors of a similar magnitude found for each.

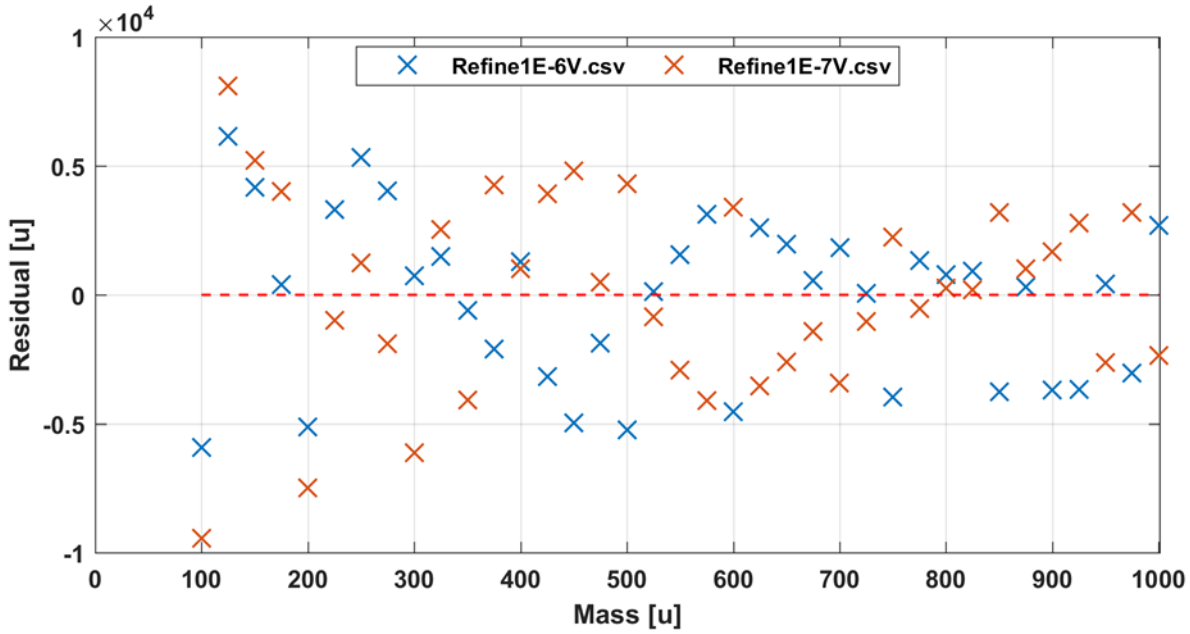

Figure 5.53 - Residual plots for curves fitted to 1E-6V and 1E-7V refined potential arrays, 200ms transient, 866V internal electrode voltage, ion kinetic energy of 500eV.

Figure 5.54 shows histograms of the residuals plotted in Figure 5.53, where it can be seen that those for a refine criteria of 1E-7V are approximately normally distributed, whereas those for 1E-6V are skewed slightly towards positive values. This is due to there being 5 positive residuals which were within 500 of being zero, if some of these values had been slightly lower, then the distribution would appear more normally distributed, a similar effect can be achieved by allowing the bins for both histograms to be misaligned, as shown in Figure 5.55. The histograms of residuals show minimal difference between the results of the two convergence criteria.

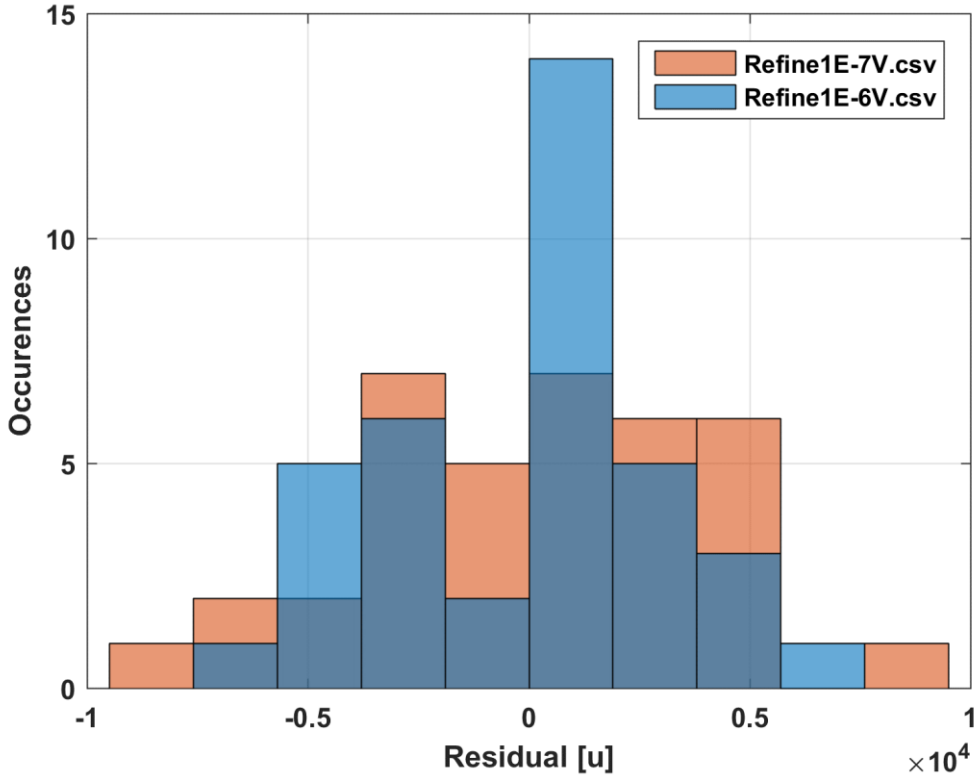

Figure 5.54 – Overlaid histograms of residuals for curves fitted to 1E-6V and 1E-7V refined potential arrays, 200ms transient duration, 866V internal electrode voltage, ion kinetic energy of 500eV. Histogram bins chosen to be aligned.

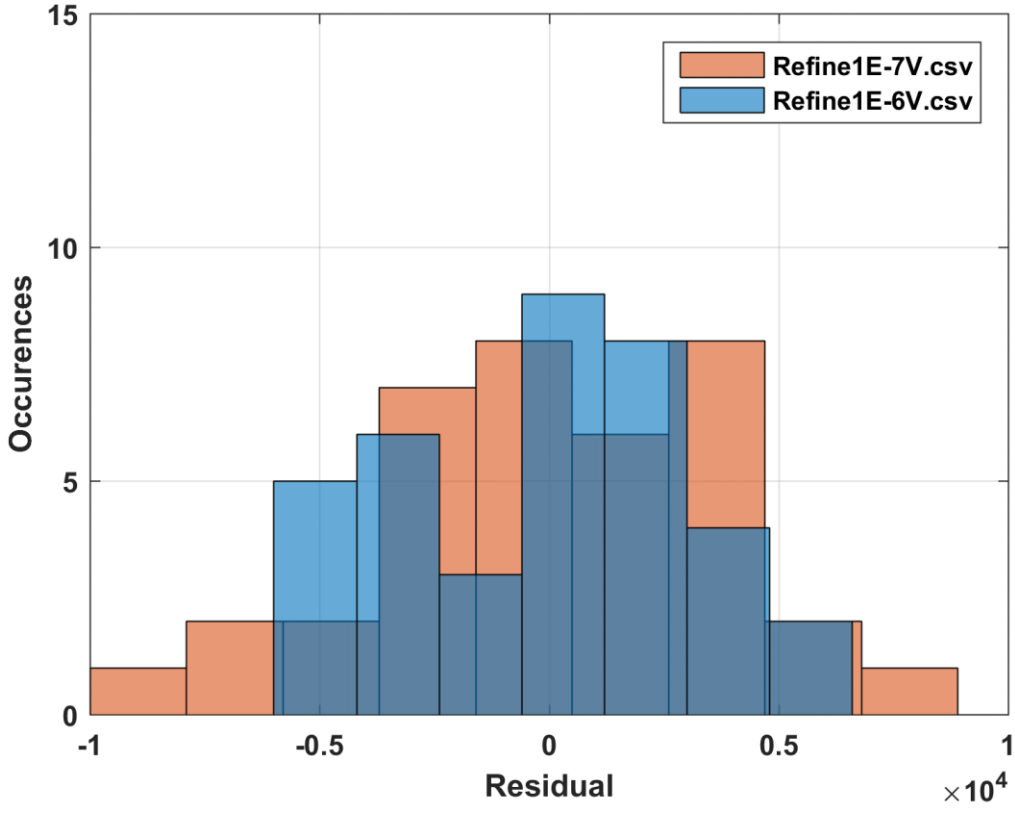

Figure 5.55 – Overlaid histograms of residuals for curves fitted to 1E-6V and 1E-7V refined potential arrays, 200ms transient duration, 866V internal electrode voltage, ion kinetic energy of 500eV. Histogram bins not aligned.

As there was no significant difference between 1E-6V and 1E-7V convergence criteria, 1E-6V was deemed an acceptable choice, as it allowed new simulations to be built and tested at lesser computational expense.

5.5.6 Impact of Trajectory Quality

In SIMION, the user can define the parameter trajectory quality, which controls the time steps at which ion trajectories are calculated, these time steps can vary non-uniformly across the trajectory. Trajectory quality can be set to any integer from -500 to +500. A larger value for trajectory quality reduces time step sizes where applicable to improve accuracy, for example in areas of high field curvature or velocity reversal, both of which are found for ions in an orbital ion trap. Typically a trajectory quality value of +3 is used, this sets the typical step distance equal to one grid unit of the potential array, and dynamically reduces this as required.

Simulations were carried out to assess the impact of higher trajectory quality on mass resolution. The cost of higher trajectory quality is more expensive computations, with initial simulations suggesting that setting trajectory quality to +500 would result in simulations approximately 400 times slower than for trajectory quality of +100.

Figure 5.56 shows the simulated mass resolution data for trajectory quality set to +3 and +100, both of which produced identical data, suggesting that increasing trajectory quality did not affect the SIMION calculations in this instance. The SIMION documentation states that positive trajectory quality values from +1 to +100 cause the time step to default to 1 grid unit, with more aggressive reduction of time step in high field curvature regions as the trajectory quality increases. In this case, the time step is evidently sufficiently small to accurately calculate the ion motion that increasing this value above +3 would be of no benefit. Simulations for trajectory quality of +3 and +100 were completed in similar amounts of time, approximately 24hrs for a 200ms transient of 1000eV ions with masses 100u to 1000u in 25u increments. That no greater computational expense was required for trajectory quality of +100 also indicates that simulation accuracy was not improved over trajectory quality of +3.

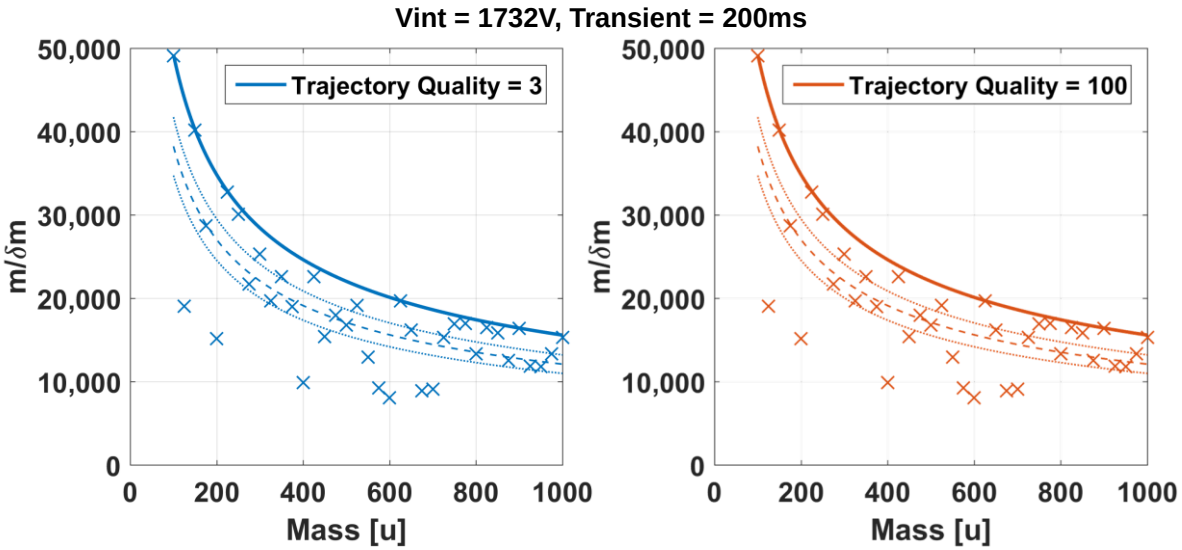

Figure 5.56 - Simulated mass resolution data with fitted curves for different trajectory quality settings, 200ms transient, 1732V internal electrode voltage ion, ion kinetic energy of 1000eV. Trajectory quality was not found to affect mass resolution, as both datasets produced identical data, hence why they are shown side by side, rather than overlaid on a single plot.

5.5.7 Potential Array Grid Spacing

Potential arrays with finer grid spacing were also simulated, although no advantage was found when compared to the 5µm per grid unit array which was used for the above simulations. It was found that trajectory quality was a more significant determinant of the behaviour of ions than potential array grid size, as the SIMION time step is automatically reduced to be less than one grid unit in areas of high field curvature. Potential arrays with finer grid spacing would have increased the RAM burden of running simulations, reducing the number of simulations which could be carried out simultaneously. The potential array files used here were created using a rotationally symmetric 2D profile, meaning RAM usage is dependent on the square of grid resolution, for example reducing grid spacing by a factor of two to 2.5µm per grid unit, would result in a four-fold increase in RAM usage.

RAM usage in SIMION can be estimated by considering the number of points in the potential array, in the simulations discussed here, a 2D array of 30mm in the x-direction and 18mm in the y-direction with a grid resolution of 5µm per grid unit was used. This array contains 6,000 points in the x-direction and 3,600 points in the y-direction, giving a total of 21.6E6 points. Each grid point requires 10 bytes in RAM, so this would require 216E6 bytes (206MB) of RAM for a single potential array. Each electrode with an adjustable voltage requires a separate potential array file to be held in RAM whilst simulations are being run, so in the case of the orbital ion trap, three potential arrays are required with a RAM burden of 618MB in total.

In much the same way, an estimate of the maximum possible grid resolution can be found from the amount of available RAM. The PC used for this study had 16GB of RAM, if it is assumed that all of this RAM is available, this would mean SIMION could operate a single array of up to 1.7E9 points, or three arrays of 572E6 points in the case of the orbital ion trap. This would correspond to a grid resolution of slightly better than 1µm per grid unit (0.971µm/gu) for three 18mm by 30mm 2D potential arrays. It is unrealistic to assume that all of the installed RAM would be available to SIMION, but it is useful to highlight the upper limit of grid resolution which could be simulated on the hardware used.

As evidence that finer resolution potential arrays did not alter the calculated mass resolution, a series of short trial simulations were run with grid resolutions of 2µm, 5µm and 10µm per grid unit, with only a 10ms transient simulated. Figure 5.57 shows the

results of these simulations, the data is almost perfectly overlaid for all three datasets, making it difficult to distinguish them from the plot. As such, Table 5.3 is presented, highlighting the minimal difference in mass resolution found for different grid resolution across the mass range tested.

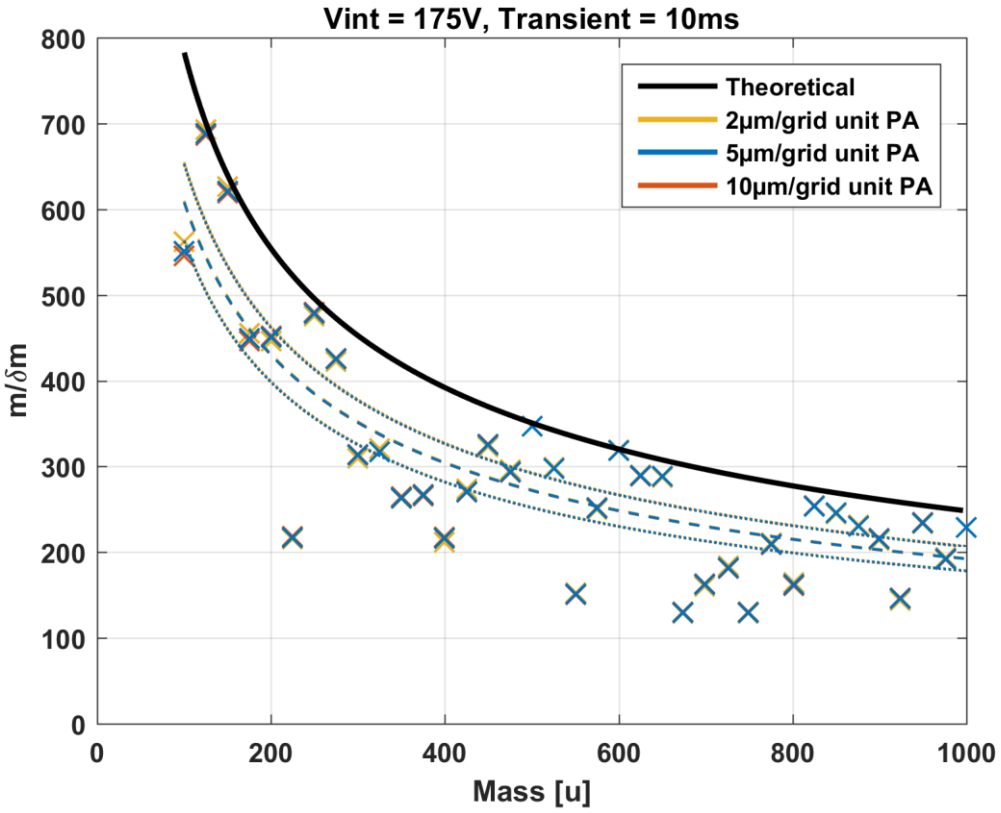

Figure 5.57 - Simulated mass resolution data for 10µm, 5µm, and 2µm per grid unit potential arrays, 10ms transient, 175V internal electrode voltage. Note that many data-points are closely overlaid, as there was little difference between results acquired using different grid resolutions.

Nominal Mass [u]	Simulated Mass Resolution		
	2µm per grid unit	5µm per grid unit	10µm per grid unit
200	446	451	452
400	212	216	218
600	319	318	319
800	164	162	161
1000	229	229	229

Table 5.3 - Simulated mass resolution for 10µm, 5µm, and 2µm per grid unit potential arrays at example masses, 10ms transient, 175V internal electrode voltage.

As demonstrated earlier, mass resolution varies linearly with transient duration for a fixed mass, therefore the values of mass resolution shown in Table 5.3 could be scaled up to predict expected mass resolution for longer transients. In this case, this is useful

to note, as it means that although the simulated mass resolutions are very low due to the short transient used, the parity in mass resolution between different grid resolutions would be expected to hold for longer transients.

5.6 Parametric Excitation Simulations

Parametric excitation is a mass-selective method of exciting ions within an orbital ion trap after their initial injection into the trapping volume, as discussed in greater detail in Chapter 3.

Parametric excitation is useful in two scenarios. Firstly, if trapped ions have already been excited in the axial direction, for example by injecting them at some distance from the mid-plane of trap, parametric excitation can further excite ions within a chosen mass range so that they are no longer present in any mass spectra gathered. Secondly, ions can be injected at the mid-plane of the trap, where z = 0mm, and parametric excitation can excite only the masses of interest, to allow a mass spectrum to be gathered only for these excited masses.

One situation in which the first mode of operation of parametric excitation would be useful is MS-MS, or tandem mass spectrometry, in which large molecules are fragmented to reveal their constituent components for more precise identification. For example, a wide mass range could be allowed to enter the ion trap, and then all masses except that of a large molecule of interest could be over-excited to remove them from the trap. At this point, the large molecule could be fragmented, and an MS-MS spectrum could be gathered consisting of only the daughter ion fragments.

To simulate parametric excitation, a SIMION workbench was set up comprising only the three component electrodes of the orbital ion trap. This was generated using a user written GEM file. In this geometry file, a series of points lying on the ideal orbital ion trap profile are defined with a radial spacing of 1µm. These points are then connected using straight line approximations and the resulting profile is revolved around the z-axis, as shown in Figure 5.58**.**

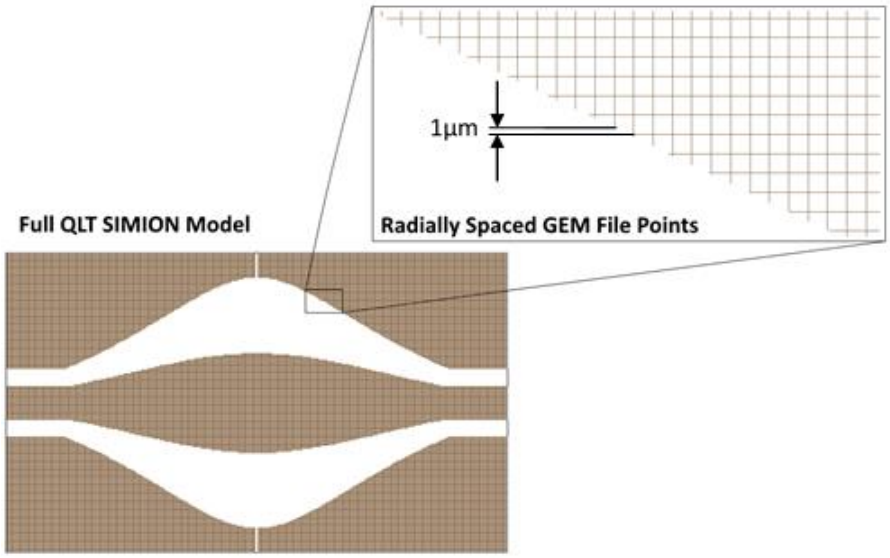

Figure 5.58 - SIMION GEM file representation

For this simulation, ions of mass, m = 100u, and kinetic energy, T = 101eV, were chosen, corresponding to an ideal internal electrode of U = 174.925V and an axial oscillation frequency of $\omega = 983.5 \times 10^3$ rad/s (f = 156.5 kHz).

In the simulation of parametric excitation, ions were injected at z=0 with a small velocity component in the z-direction, approximately 1% of that in the radial direction. Without an axial component of velocity, parametric excitation would not be possible, as discussed in Chapter 3. The RF excitation voltage was applied 1ms after ion injection, this timing was chosen to reduce the size of ion trajectories to be stored in RAM, with trajectory data before excitation not used in the below analysis. In a real experiment, a longer delay between injection and excitation would be used to allow trapping of a greater number of ion packets.

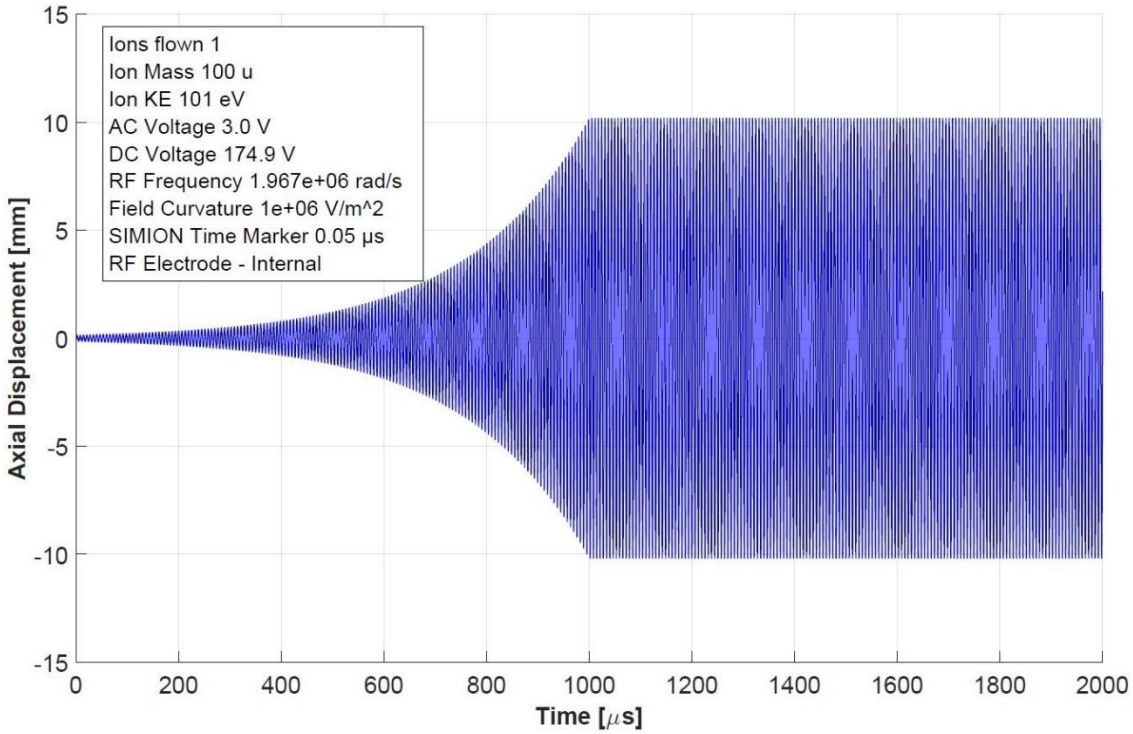

Figure 5.59 - Ion trajectories during parametric excitation

The development of ion trajectories whilst undergoing parametric excitation are shown in Figure 5.59; the increase in axial oscillation amplitude follows an exponential relationship with time, as discussed in Chapter 3. In this case, $t = 0\mu s$ is the time at which the RF excitation voltage was first applied.

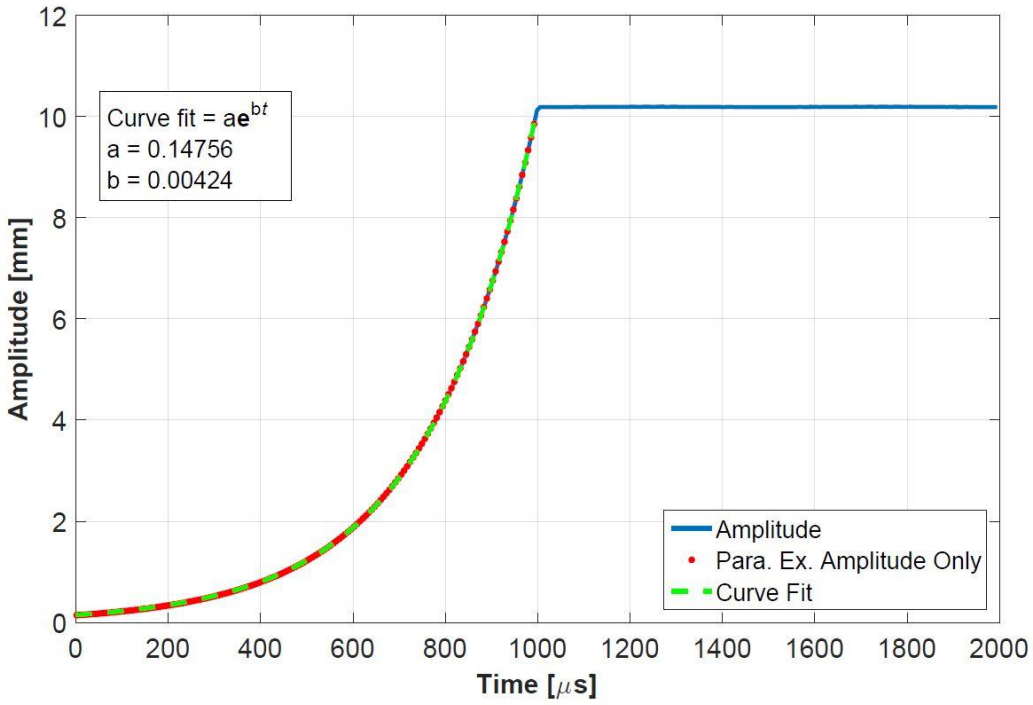

Figure 5.60 - Curve fit to parametrically excited oscillation amplitudes

This relationship can be better interrogated when looking only at positive axial oscillations, as shown in Figure 5.60.

In Figure 5.60, the peaks of positive oscillation amplitudes were plotted as a continuous function, with a curve fit found for $0 < t < 1{,}000\mu s$; the time during which an RF excitation voltage was applied to the internal electrode. The exponential fit was of the form shown in equation (5.24), with 95% confidence intervals for fit coefficients a and b given:

$$\text{Oscillation Amplitude [mm]} = ae^{bt}$$
$$a = 0.14756 \pm (5 \times 10^{-4}) \qquad (5.24)$$
$$b = 0.004242 \pm (4 \times 10^{-6})$$

This voltage will be applied to the orbital ion trap using an RF generator as described earlier. Simulated predictions for how ion axial oscillations will develop inside the orbital ion trap are useful to give an initial estimate for the length of time excitation voltages need to be applied. In practice, the duration of excitation will be tuned based on the detected signal, starting with approximately 1ms of excitation as used in these simulations.

As discussed in Chapter 3, parametric excitation of ions can be modelled using the Mathieu equation. To this end, a SIMION workbench has been written with Mathieu parameters, a_u and q_u given as user adjustable variables, to allow simulations to be carried out using various combinations of these parameters. This was used to simulate the stability or instability of ion axial oscillation amplitude and compare this to the predicted analytical stability boundaries of the Mathieu equation.

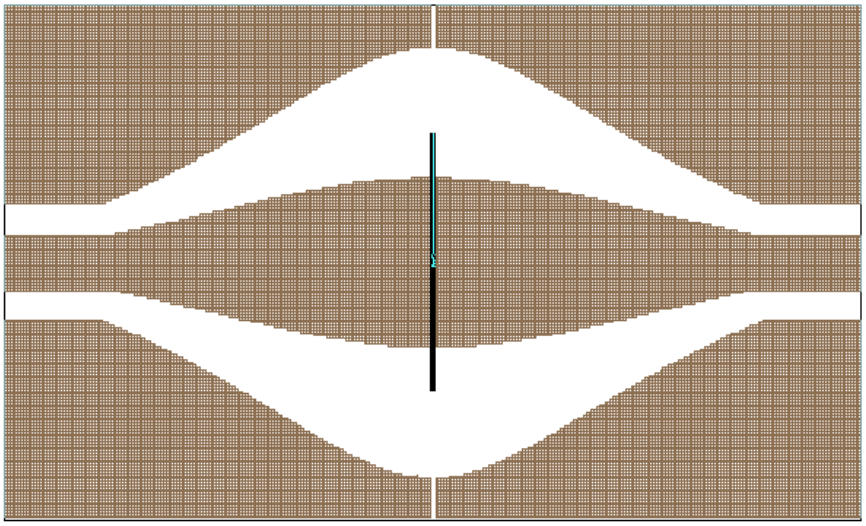

Figure 5.61 - Stable ion trajectories under parametric excitation

In these simulations, ion trajectories were deemed stable if their axial oscillation amplitude remained constant under parametric excitation, and unstable if axial oscillation amplitude increased. This can easily be distinguished visually, with the ion trajectories shown in Figure 5.61 counted as stable, and those in Figure 5.62, deemed unstable. It can be seen in Figure 5.62 that the radial amplitude of ion trajectories reduces once parametric excitation has finished (green trajectories).

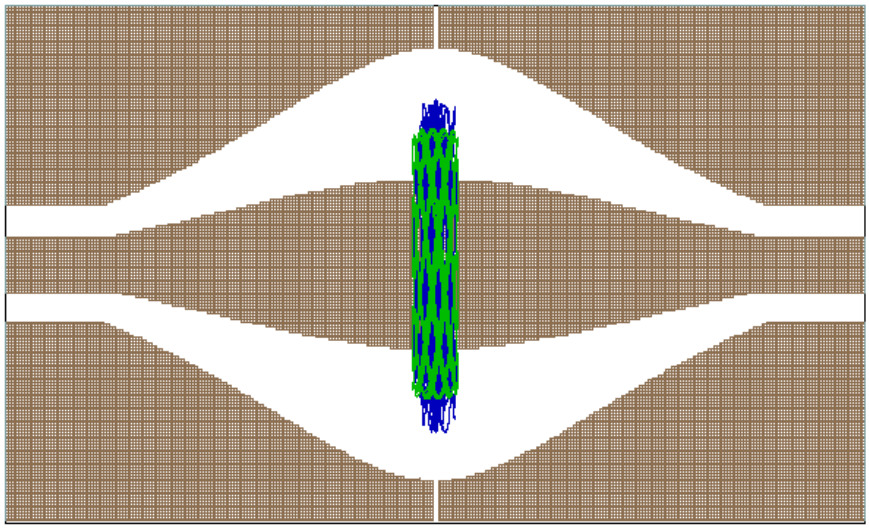

Figure 5.62 - Unstable ion trajectories under parametric excitation (blue trajectories), and after parametric excitation (green trajectories)

Table 5.1 shows some example Mathieu parameters which were simulated, and whether the resulting ion trajectories were stable, akin to Figure 5.61, or unstable with unbounded axial oscillation amplitude growth, as per Figure 5.62. The analytical model

discussed in Mathematical Formulation predicted that values of $a_u = 1$ and $q_u = \frac{\mu}{2}$, would produce unstable ion trajectories and cause parametric excitation, where $\mu = P(r,z)/U(r,z)$ which is the ratio of AC excitation voltage, to DC trapping voltage. With this description, when $a_u = 1$, q_u determines the speed of axial oscillation amplitude growth, if q_u is too low, ions will not be sufficiently excited to be detected, if q_u is too high, ions will be excited too much, causing collision with the external electrodes of the orbital ion trap. Simulations were in agreement with this prediction, meaning a tuneable mass-selective excitation model has been developed.

Mathieu Parameters		**Resultant Trajectory Description**
a_u	q_u	
0.5	0.0050	Stable
0.5	0.0075	Stable
0.5	0.0100	Stable
0.5	0.0125	Stable
0.5	0.0150	Stable
1.0	0.0050	Unstable – Minimal excitation (<0.4mm)
1.0	0.0075	Unstable
1.0	0.0100	Unstable
1.0	0.0125	Unstable
1.0	0.0150	Unstable – Collision with External Electrodes
1.5	0.0050	Stable
1.5	0.0075	Stable
1.5	0.0100	Stable
1.5	0.0125	Stable
1.5	0.0150	Stable
2.0	0.0050	Stable
2.0	0.0075	Stable
2.0	0.0100	Stable
2.0	0.0125	Stable
2.0	0.0150	Stable

Table 5.4 - Simulated Mathieu parameters, and stability of resulting ion trajectories, for an excitation duration of 1ms, for ions of mass 100u with an internal electrode voltage of 175V. Cells highlighted in green are those for which unstable ion trajectories were found.

5.7 Simulation Conclusions

Transmission of ions from the Ionoptika J105 to the orbital ion trap have been optimised using ion optics simulations. These voltages provided the starting point for physical testing of the ion transfer assembly.

A wide array of simulations have also been carried out to investigate the effect of trapping time and internal electrode voltage on the mass resolution which can be achieved with an orbital ion trap. An analytical model in which frequency resolution is dependent linearly on the time for which ions are trapped was found to agree with simulations. This in turn means that mass resolution is also linearly dependent on the transient trapping time. Mass resolution was also found to be linearly dependent on the frequency of ion axial oscillation, which is proportional to the square root of the internal electrode voltage used. Combining these results means that higher mass resolutions can effectively be pursued down two avenues; increasing the transient time, or increasing the ion oscillation frequency.

Simulations of the mass-selective parametric excitation of trapped ions were carried out. It was found that the Mathieu parameters derived analytically in Mathematical Formulation which define the stability boundaries for ion excitation are in agreement with simulated results. Building on this, a method of exciting only specific masses of interest for high mass resolution analysis can be developed.

Chapter 6. Orbital Ion Trapping

This chapter will detail the practical experiments undertaken to maximise ion transmission to the orbital ion trap through the ion transfer assembly designed and mounted on the J105.

6.1 Primary Ion Conditions

Initially, when simply proving transmission from the J105, through the transfer assembly and to the orbital ion trap, the maximum possible secondary ion current was required to be generated from a sample in the J105. This was in order to maximise the number of ions transmitted, for ease of detection. To achieve this, the 40keV C_{60} primary ion source was used, with primary ion beam current typically tuned to a value of up to 2nA, by using the Ø1mm aperture in the primary column, with the source temperature set to 400°C, and de-focussing the ion optics lenses in the C_{60} column. On occasion, the beam current was increased to a higher value, up to 3.5nA, this was only ever done for a short period of time as such high emissions currents are detrimental to the life of the ion source. The primary ion currents used were much higher than typically chosen for SIMS experiments on the J105, and as would be expected had an adverse effect on the primary ion beam spot size, with spot size increasing to greater than Ø20µm, as opposed to the minimum spot size of better than Ø300nm which can be achieved with the ion beam under optimal tuning. Spatial resolution was not a significant concern at this stage, as the aim was only to demonstrate any transmission of ions from the J105 to the orbital ion trap.

6.2 Transferring Ions from Ionoptika J105

This section will briefly cover the practical aspects of transferring ions from the J105 into the orbital ion trap, and diverting them from their usual course through the buncher into the reflectron time-of-flight analyser.

As the orbital ion trap transfer assembly is located on top of the ESA of the J105, ions can be made to transfer directly upwards into this assembly simply by setting both plates of the ESA to equal DC voltage. This can be done easily by selecting an option in the ‘ToF HV Control’ software provided by Ionoptika, options of 50, 100, 150 or 200V are available for the ESA float voltage. The voltage chosen is assumed to be the

nominal initial kinetic energy of the ions upon their entry into the transfer assembly, with ions having an approximate energy distribution of ±1%.

6.3 Procedure for Measuring Ion Transmission

Ion transmission was measured using the current meters built-in to the Ionoptika J105, and externally with a Keithley 6514 programmable electrometer, capable of measuring currents of 100fA to 21mA (Keithley, 2003). Beam currents were typically measured in four locations to assess transmission:

1. At a Faraday cup located on the sample stub, to measure incident primary ion beam current.
2. At the entrance to the buncher to assess the typical number of secondary ions which are typically transmitted through the ESA.
3. At the entrance aperture of the ion transfer assembly.
4. At the desired measurement point, for which transmission was being determined. Measurement points were located at various locations; at an ion optical element part way along the ion transfer assembly, at the aperture separating the ion transfer assembly from the orbital ion trap chamber, at the injection aperture, or on one of the component electrodes of the orbital ion trap itself.

Figure 6.1 shows some of the intermediate points in the ion transfer assembly at which the beam current could be measured to assess ion transmission. The input to the Keithley electrometer was biased by between 30V and 60V with opposite polarity to that of the ion beam being measured, so as to deflect the ion beam towards the measurement point.

Figure 6.1 also shows the ion optics elements which could be tuned to improve ion transmission through the transfer assembly, with the brown, red, and yellow elements, connections 1, 9, and 3 respectively, forming an einzel lens to focus the ion beam at the entrance to the ion trap.

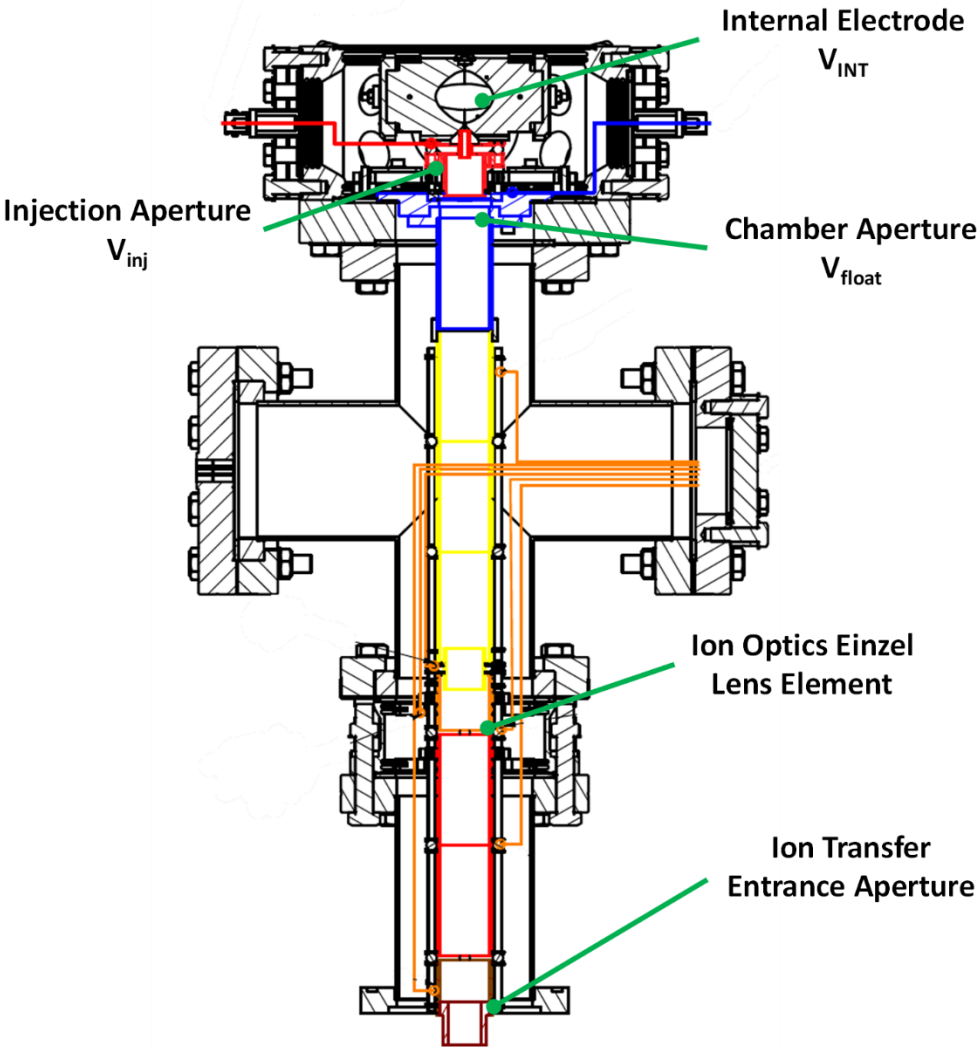

Figure 6.1 – Ion optics transfer electrical connections, with key points for measuring ion beam current annotated.

6.4 Tuning Ion Optics

The ion optics of the J105 played an important role in optimising the ion transmission into the orbital ion trap, as they defined the condition of the ion beam at its entry into the ion transfer assembly. There were four main ion optic elements from the J105 which affected ion transmission, and were thus chosen for tuning; tertiary beam optics (TBO) lens 1, TBO X/Y deflectors, TBO extract, and ESA X/Y deflectors. Drawings of these components are not provided as they are intellectual property of Ionoptika. The tertiary beam optics are located prior to the entrance to the ESA, and control the divergence and location of the ion beam before any energy filtering has taken place in the ESA. The ESA X/Y voltages control two pairs of orthogonal electrostatic deflector plates located at the two exits from the ESA; with one pair located after a 90° bend of

the ion beam before entering the buncher, the other pair located vertically upwards, before the beam is passed to the ion transfer assembly.

Initial values for the ion optics voltages were found from SIMION simulations, and used as a starting point for tuning to optimise transmission through the ion transfer assembly. With a float voltage of 150V, simulations suggested that an einzel lens voltage of approximately -50V would give optimal transmission, as suggested in the simulation results shown in Figure 6.2. In reality, optimal transmission to the orbital ion trap was found with a voltage of -90V applied to the lens element. This discrepancy is likely due to space-charge repulsion effects in the ion beam, which would lead to beam spreading, thus altering the required focussing voltage. Attempts were made to include such effects in simulations, although only a small effect was observed. This is likely because only a small number of ions were simulated, with 300 trajectories modelled, it would have been prohibitively computationally expensive to simulate a larger number of ions, for which space-charge effects would have been more evident.

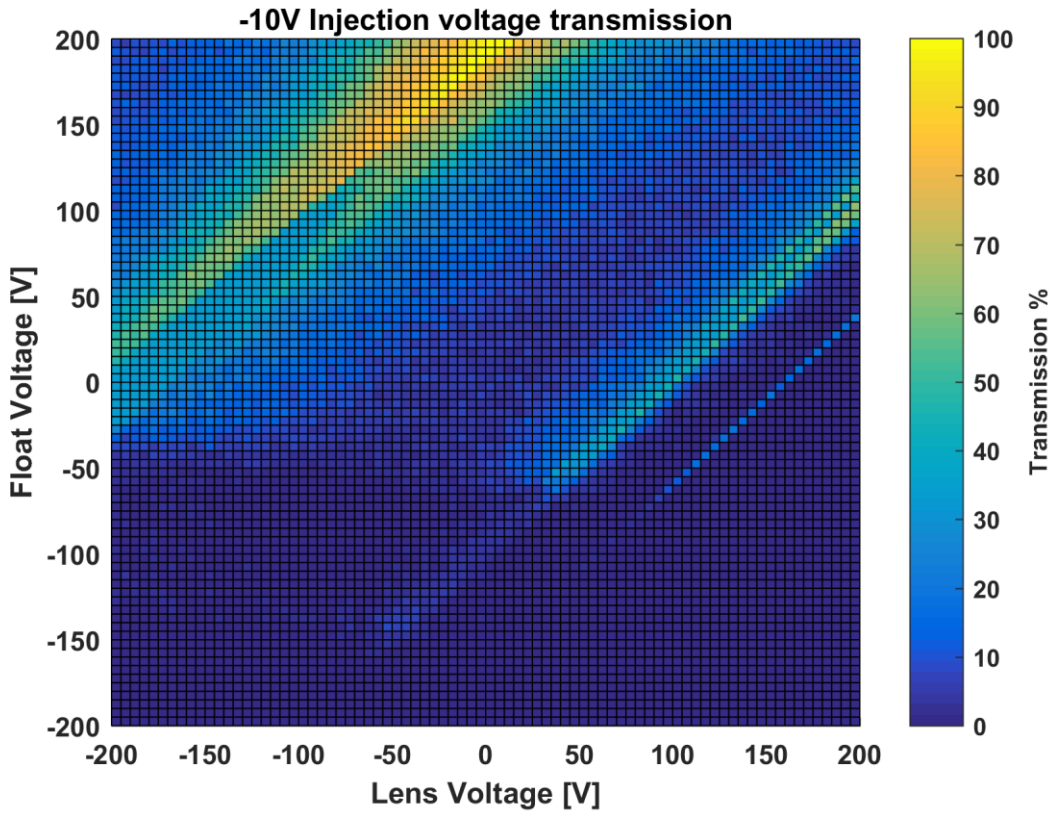

Figure 6.2 – Ion optics simulation results for transfer of ions from J105 to orbital ion trap, showing a region between -40V and -60V which would achieve optimal ion transmission for a float voltage of 150V, and an equivalent ESA voltage. Colour indicates ion transmission percentage.

As stated, initial experiments were conducted with the C_{60} ion beam set to produce the maximum possible current at the sample, this value varied depending on the age of the source being used, and the chosen operating temperature. A new source, or one heated above its standard operating temperature is able to give beam currents in excess of 2nA, when measured using a Faraday cup on the sample stub.

6.5 Ion Transmission

This section will discuss the results of ion transmission measurements taken over more than 100 separate experiments, with ion optics tuning attempted for each, to maximise transmission wherever possible.

6.5.1 Ion Transmission: Up to the Ion Transfer Assembly

Secondary ion current was first measured at the usual exit of the ESA, which is also the entrance to the buncher, using a picoammeter built in to the J105 buncher controller software. For this test, the ESA was operated in its normal mode, with ions deflected through 90° and transferred to the buncher as per time-of-flight SIMS on the J105. This value likely represented an upper estimate for the secondary ion beam current which would be available to transfer to the orbital ion trap. Measured values were in the range of 1pA to 350pA, depending on; the primary ion beam current, and the ion optics voltages chosen. The primary ion beam current being the key determinant of the measured secondary ion current at the buncher, as would be expected. It was found that secondary ion current at the entrance to the buncher was approximately 10% of the primary ion beam current measured at the sample, with this transmission percentage encompassing the secondary ion yield from indium, and the transmission of the extraction optics, quadrupole mass filter, and electrostatic analyser of the J105. Evidence of the relationship between primary ion current measured at the sample, and the secondary ion current measured at the ESA can be seen in Figure 6.3, showing results for 82 experimental runs using C_{60} as a primary ion source.

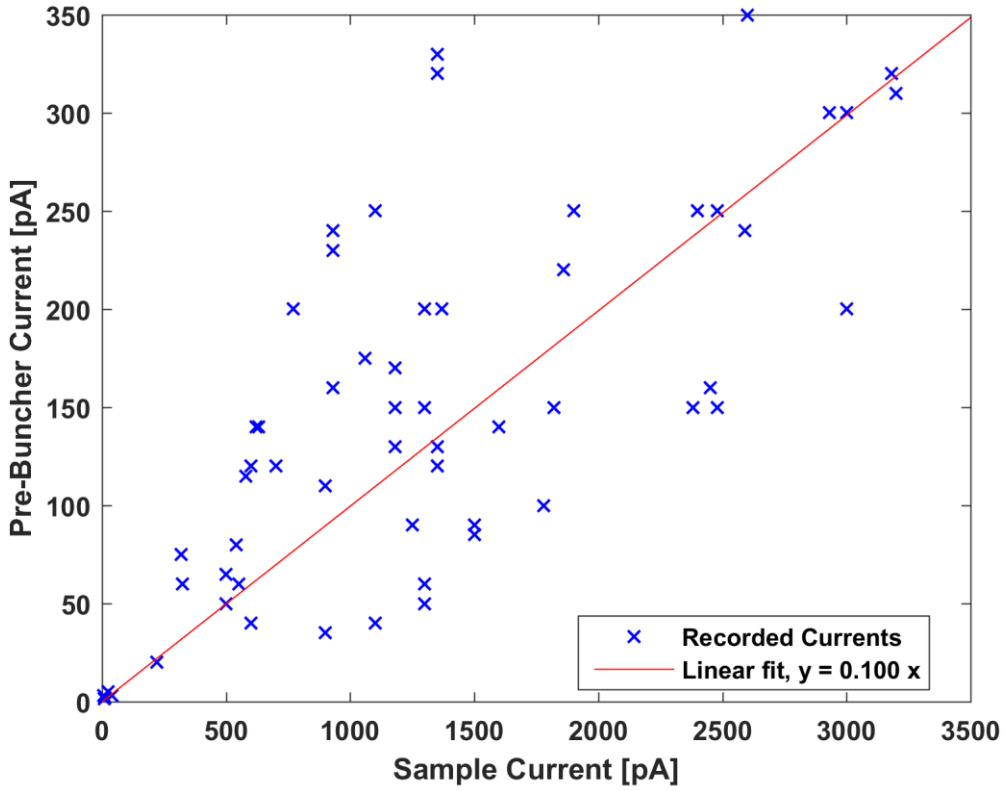

Figure 6.3 - Currents measured experimentally at the sample in the Faraday cup, and at the current monitor prior to the buncher, with a linear best fit found by MATLAB non-linear least squares regression, $y = 0.1x$ also plotted. Results are from 82 separate experiments using a C_{60} primary ion beam.

The next step was to prove ion transmission to the second ESA exit aperture, located at the entrance to the ion transfer assembly, shown as point 1 in Figure 6.1. This was done in much the same way as for the pre-buncher ion current measurements, with multiple recordings taken in the range 1pA to 140pA at the entrance to the ion transfer assembly. Results from 60 different experiments are shown in Figure 6.4. It can be seen that the current measured at the entrance to the ion transfer assembly is much lower than that measured at the pre-buncher current monitor. It was found that the secondary ion current entering the ion transfer assembly was only approximately 3.4% of the primary ion current measured at the sample.

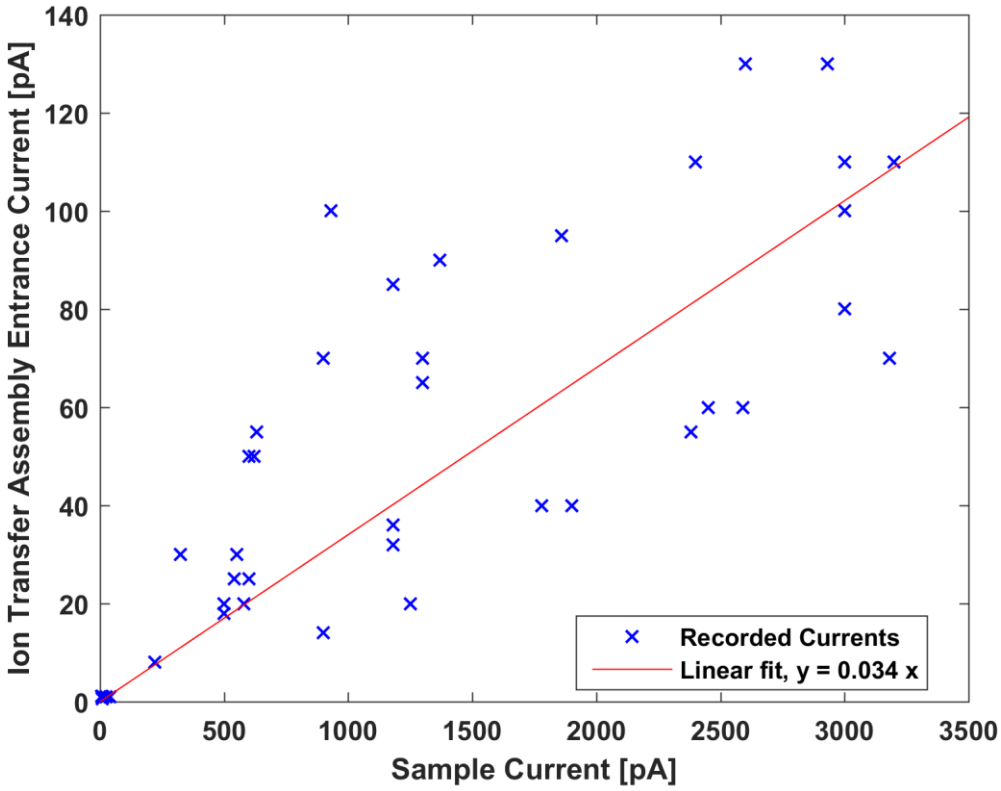

Figure 6.4 - Currents measured experimentally at the sample in the Faraday cup, and at the entrance aperture to the ion transfer assembly atop the ESA, with a linear best fit found by MATLAB non-linear least squares regression, $y = 0.034\,x$ also plotted. Results are from 60 separate experiments using a C_{60} primary ion beam.

Figure 6.5 shows the relationship between currents measured at the pre-buncher current monitor and at the entrance to the ion transfer assembly, when both were measured in a single experiment with identical primary ion conditions. It can be seen that the ion current entering the transfer assembly is typically only equal to 36% of that measured prior to the buncher. This lower transmission represents the losses accrued when the ESA is operated in non-deflecting mode, with ions travelling straight upwards to the ion transfer assembly. The reasons for such losses could include; misalignment of the ion optics elements within the ESA which allow vertical transmission of ions, sub-optimal tuning of the tertiary beam optics causing poor transmission. The low transmission could also be caused by the method of beam current measurement, with the ion current measured at point 1 of the ion transfer assembly likely to be an underestimate for the true beam current at this point. To measure the current, the ion beam is simply deflected onto the walls of a cylinder, by a small biasing voltage of magnitude 60V, which was the limit of the permissible float voltage input to the Keithley

electrometer for the triaxial to BNC adapter used in these experiments. As a result there could be insufficient deflection of the ion beam, meaning that a portion of the beam will travel beyond this point and will not be detected by the picoammeter.

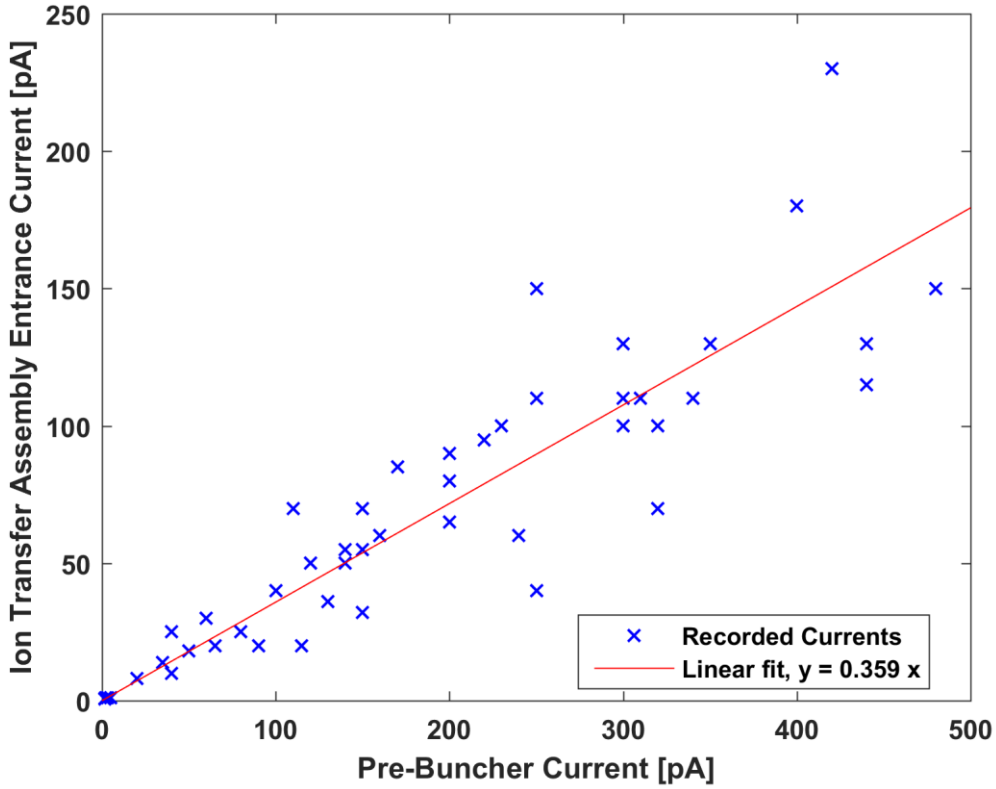

Figure 6.5 - Currents measured experimentally at the pre-buncher current monitor and at the entrance aperture to the ion transfer assembly atop the ESA, with a linear best fit found by MATLAB non-linear least squares regression, $y = 0.359\,x$ also plotted. Results are from 71 separate experiments using a C_{60} primary ion source.

6.5.2 Ion Transmission: Within the Ion Transfer Assembly

Once ion transmission to the entrance of the ion transfer assembly had been proven, the next step was to transfer ions upwards towards the orbital ion trap. Again, this section will refer back to ion current measurement points shown in Figure 6.1. Rather than giving a single current measurement to represent the ion transmission to different points, this section will present plots of the current measured over time. These results were recorded whilst the primary ion beam was blanked and un-blanked via electrostatic deflection controlled by the J105 software. The reason for this was to assess the difference in measured current which can be attributed to the secondary ion beam, rather than any electrical noise which may have been adversely affecting

measurements. Electrical noise could have been due to multiple factors, such as triboelectric effects arising from friction due to motion within the measurement cables themselves. Noise from such effects can be of the order of 10pA, (Keithley, 2001). Noise of this magnitude would account for some of the difficulties found in measuring successful ion transmission to the internal electrode of the orbital ion trap.

Figure 6.6 shows the current measured against time at point 10 of the ion transfer assembly, where point 10 is connected to the electrostatic cylinder located after the three element Einzel lens used to focus the ion beam. It can be seen that the difference in measured current attributable to the secondary ion beam is greater than 20pA, representing a transmission of between 6% and 8% of the ion beam as measured prior to the buncher. For this experiment, no record was made of the current measured at the ESA aperture at the entrance to the ion transfer assembly.

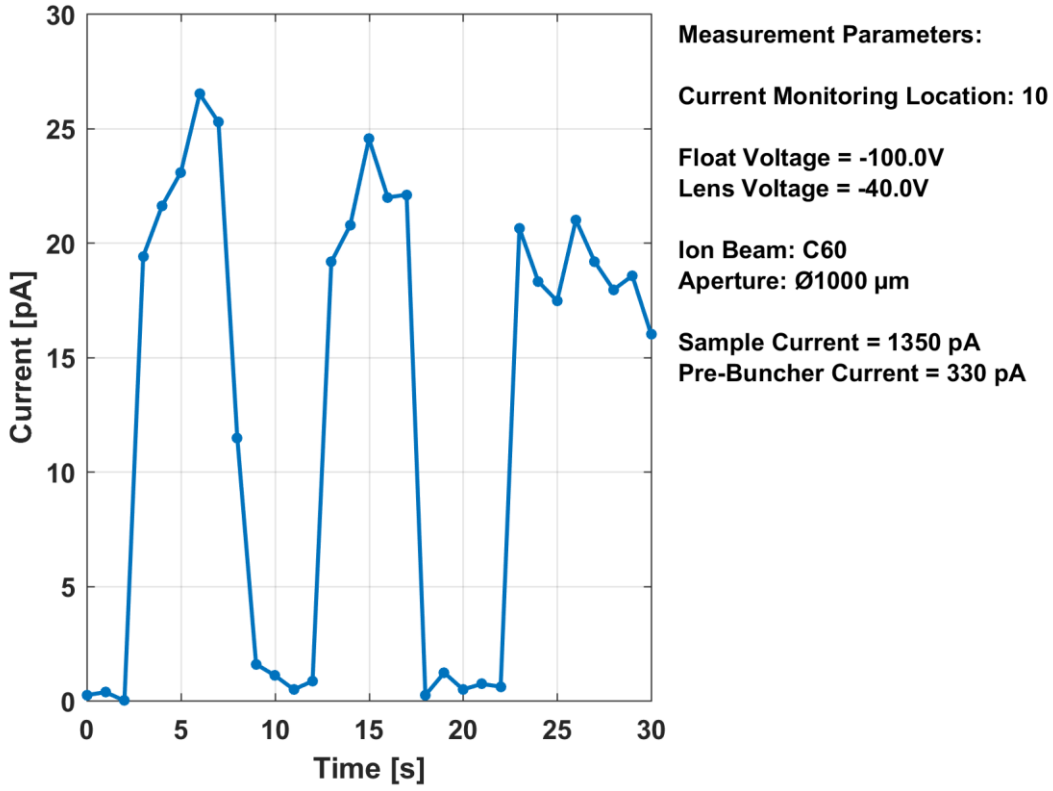

Figure 6.6 - Current measured against time for point 10 of the ion transfer assembly, with other measurement parameters shown in the annotations. Times of minimal measured ion current correspond to the primary ion beam having been blanked.

Figure 6.7 shows the current measured at V_{inj} of the ion transfer assembly, which is the final measurement point before ions enter the orbital ion trap through the Ø1mm injection aperture slot. An ion transmission of approximately 32pA can be seen between blanking and un-blanking of the primary ion beam. This represents a transmission of around 50% of ions from the entrance to the ion transfer assembly to the injection aperture just prior to the orbital ion trap.

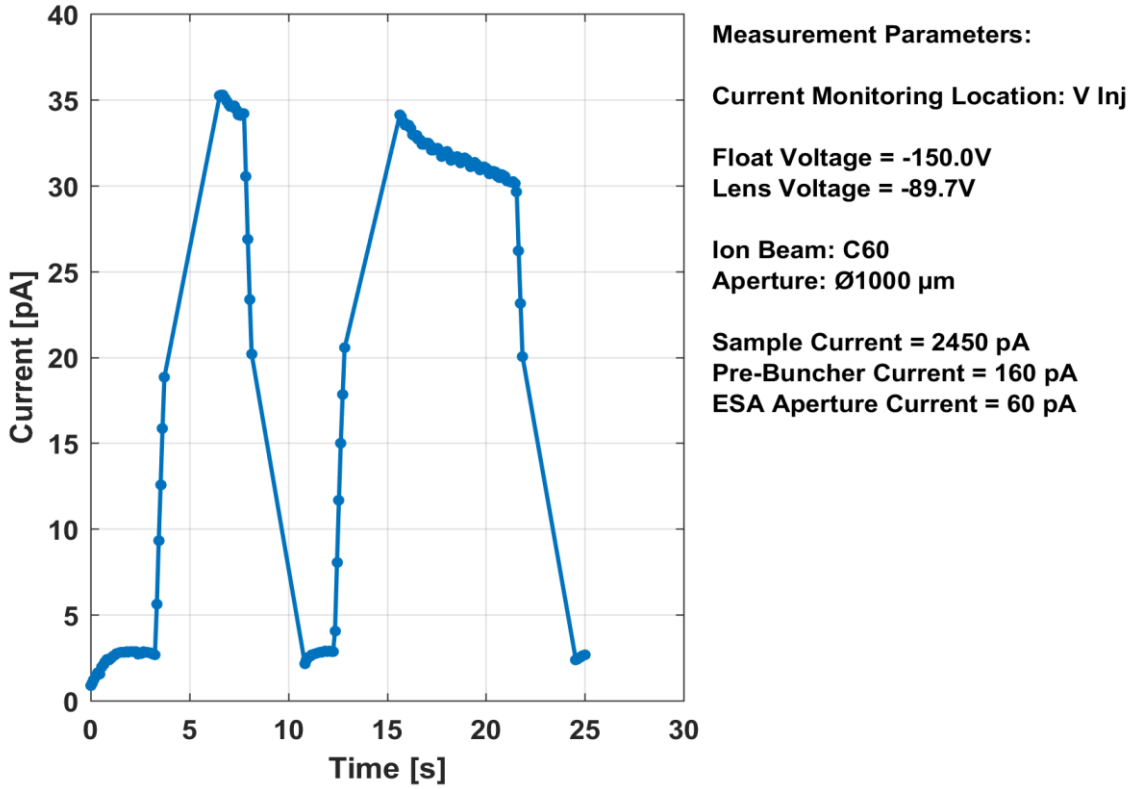

Figure 6.7 - Current measured against time at V_{inj} of the ion transfer assembly, with other measurement parameters shown in the annotations. Times of minimal measured ion current correspond to the primary ion beam having been blanked.

Figure 6.8 shows the current measured on the internal electrode of the orbital ion trap, with a current difference of nearly 0.8pA seen between the primary ion beam being blanked and un-blanked. This represents a transmission of <1% for ions entering the ion transfer assembly, which would mean a large amount of generated secondary ions are not able to be used to analysed if acquiring spectra from the orbital ion trap with this level of transmission. The reason for this comparatively poor transmission compared to that observed for V_{inj} is likely to be a combination of; space charge repulsion effects causing the beam to diverge strongly when focussed at the entrance

to the orbital ion trap, as well as potentially some misalignment between the orbital ion trap injection slot and the preceding ion optics elements.

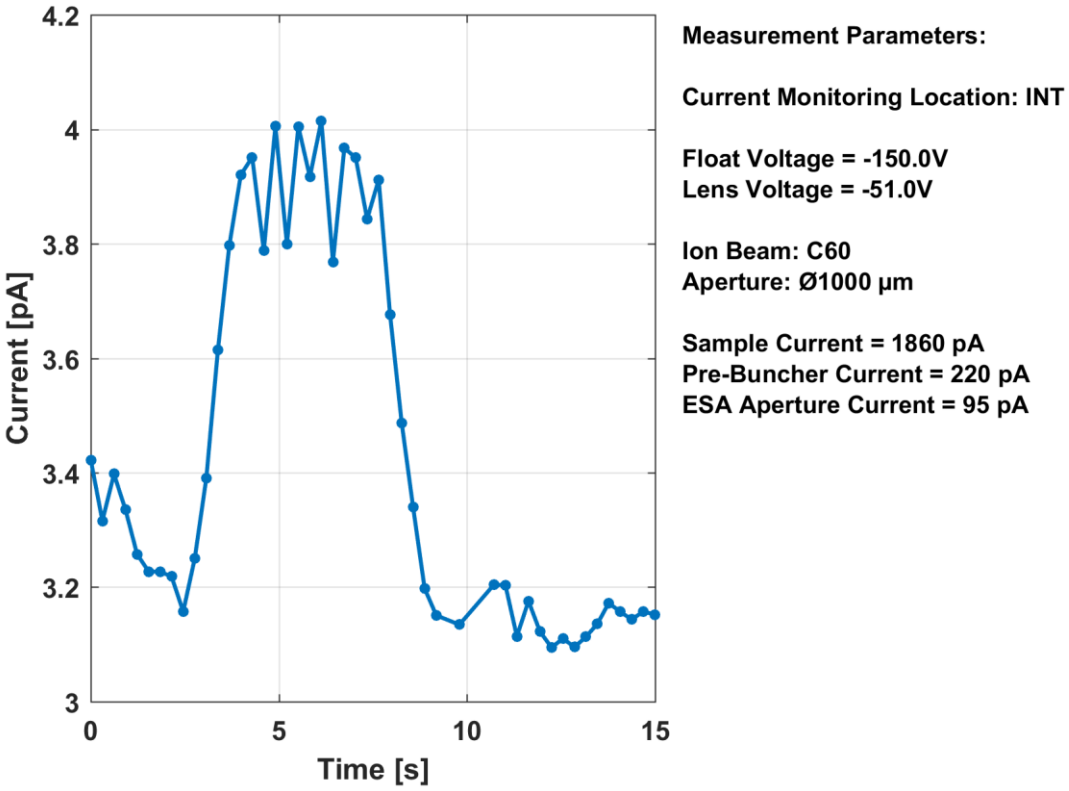

Figure 6.8 - Current measured against time at V_{INT} of the orbital ion trap, with other measurement parameters shown in the annotations. Times of minimal measured ion current correspond to the primary ion beam having been blanked.

6.5.3 Ion Transmission: Lower Primary Ion Current

Experiments were also trialled using a lower primary ion beam current, to determine the effect on transmission. It was thought that there would be some advantage due to reduced space charge repulsion effects in the secondary ion beam, however measurement noise could prevent the detection of successful transmission.

Figure 6.9 shows the current measured at V_{Float}, just prior to the orbital ion trap chamber, as in Figure 6.1. This dataset was gathered for a much lower primary ion beam current than the other data shown so far, with a sample current of 7pA measured at the Faraday cup corresponding to a value that may be typically used for mass spectral imaging on the J105 SIMS. Measurement noise is obviously a significant issue when detecting currents of this magnitude, as can be seen in the noisy current

recording. However, a difference in current of between 0.2pA and 0.4pA can be seen which is attributable to the ion beam, this represents a transmission of between 20% and 40% of the beam as measured at the entrance to the ion transfer assembly, at the ESA aperture.

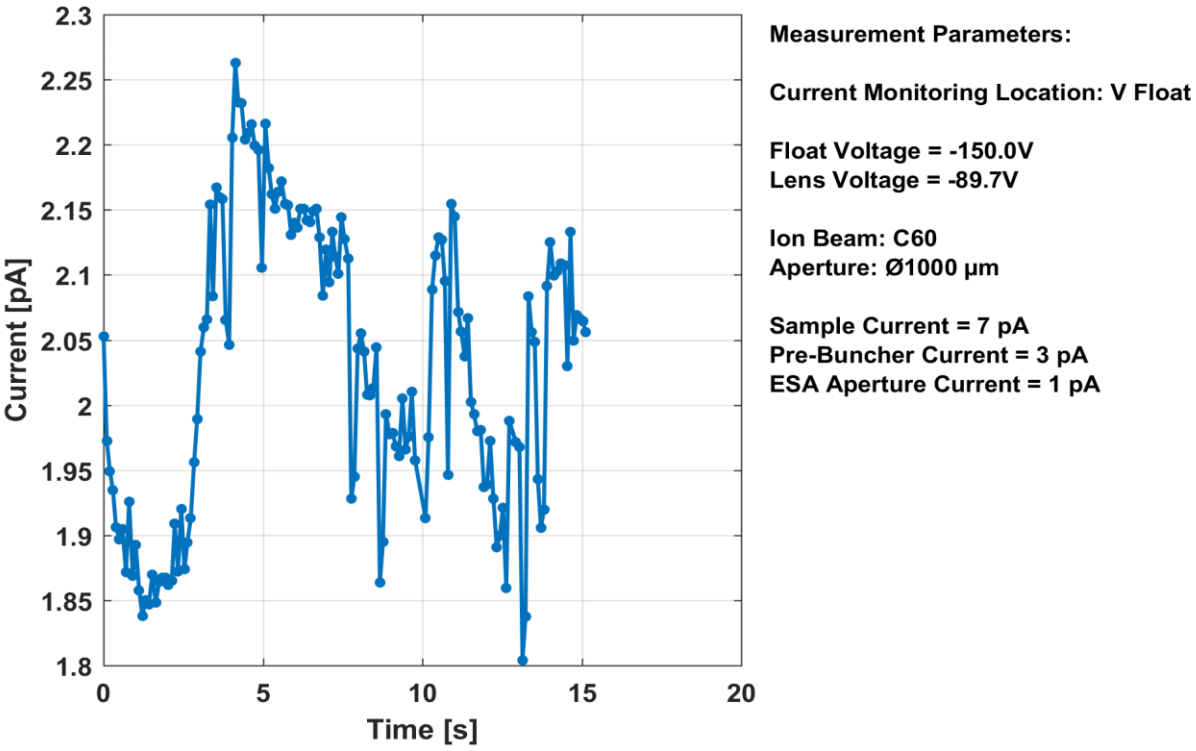

Figure 6.9 - Current measured against time at V_{float} of the ion transfer assembly, with other measurement parameters shown in the annotations. Times of minimal measured ion current correspond to the primary ion beam having been blanked.

Figure 6.10 shows the measured current at V_{inj}, one step closer to the orbital ion trap than V_{float}. Once more, a low primary beam current was used, measured as 10pA on this occasion, with 1pA detected at the entrance to the ion transfer assembly. A 10% transmission is higher than the typical transmission shown between the sample and the ion transfer assembly, as shown in Figure 6.4. Figure 6.10 clearly shows a current difference of up to 0.5pA which can be attributed to the ion beam, which would represent up to 50% transmission of ions from the entrance to the ion transfer

assembly to V_{inj}. This is approximately equal to the transmission observed between these two points for a much larger primary ion current, shown in Figure 6.7.

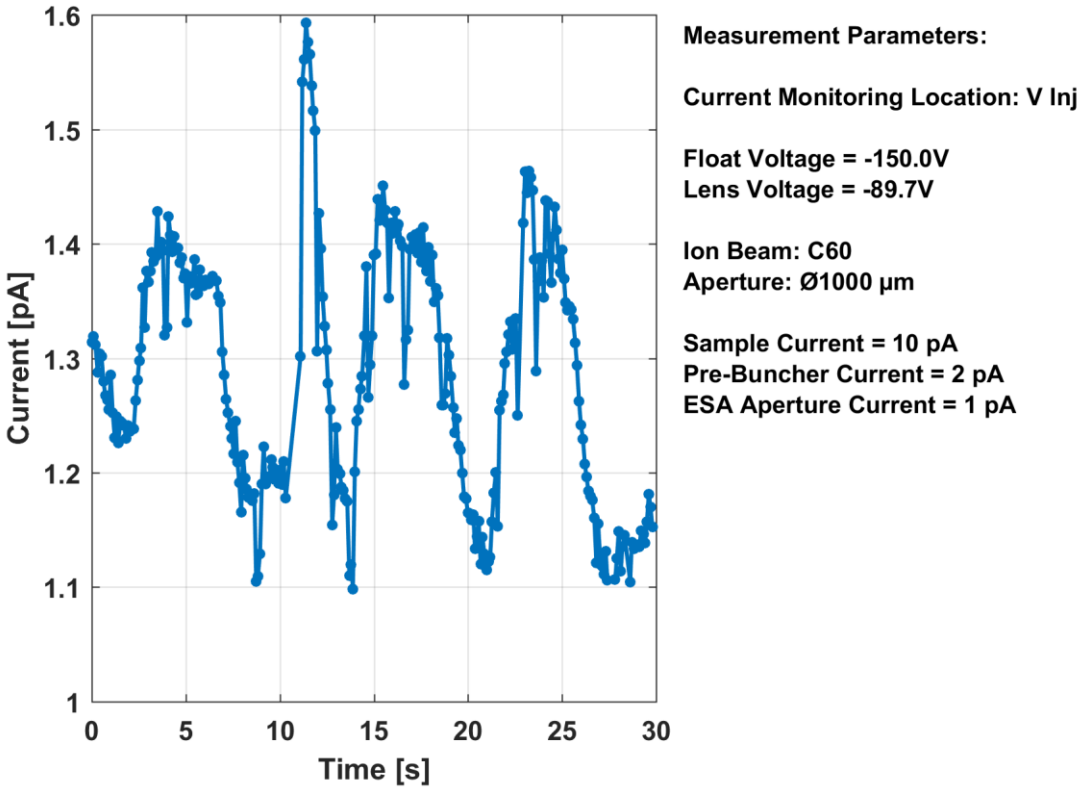

Figure 6.10 - Current measured against time at V_{inj} of the ion transfer assembly, with other measurement parameters shown in the annotations. Times of minimal measured ion current correspond to the primary ion beam having been blanked.

Figure 6.11 shows the results of attempts to detect secondary ion current on the internal electrode of the orbital ion trap when using a low primary ion beam current, of 25pA. A longer averaging period was chosen on the Keithley electrometer to reduce measurement noise, hence why fewer data points were acquired over a 30s period. A measured current difference of up to 0.8pA can be attributed to the ion beam, although this diminished significantly between the first and second blanking of the primary ion beam, reducing to less than 0.4pA. This represents an ion transmission of between 40% and 80% of that measured at the entrance to the ion transfer assembly, which is far superior to that measured for larger primary ion currents. Repeatable transmission of this magnitude of ion current would be sufficient to acquire spectra with the orbital ion trap.

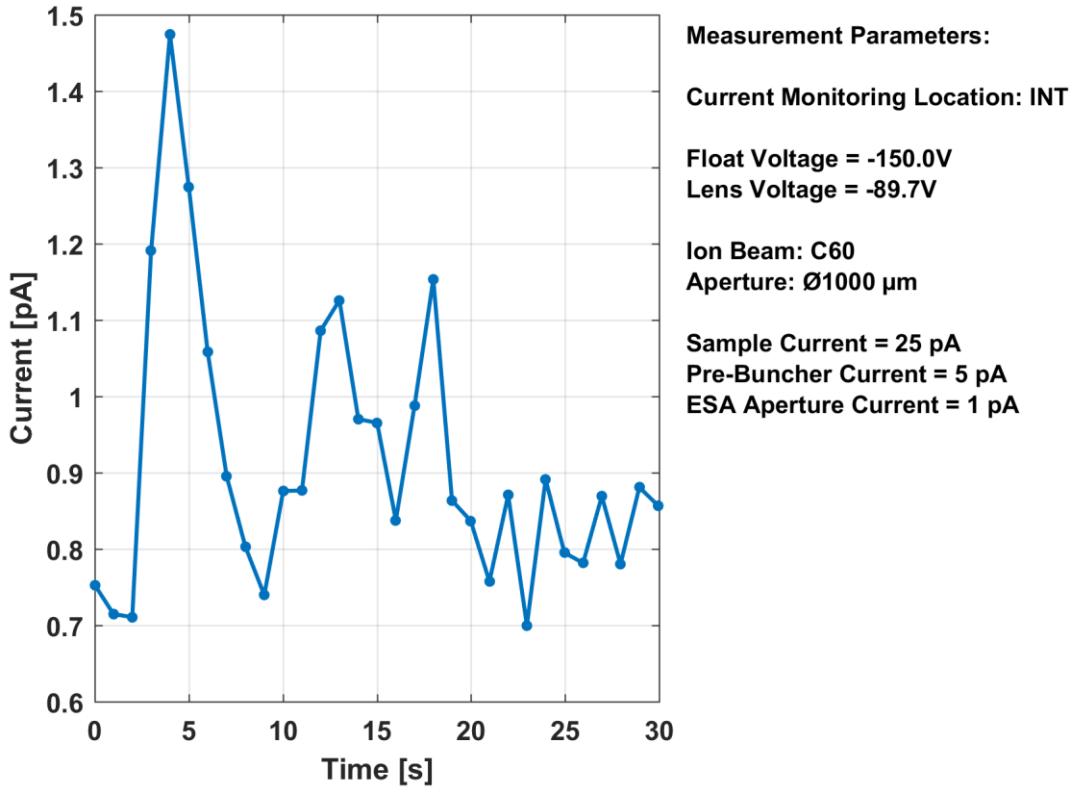

Figure 6.11 - Current measured against time at V_{INT} of the orbital ion trap, with other measurement parameters shown in the annotations. Times of minimal measured ion current correspond to the primary ion beam having been blanked. In this case, a longer averaging period of 1s was chosen for the Keithley electrometer.

6.6 Detection of Ion Trapping

Experiments to detect ion motion whilst trapped were undertaken, with software written in LabVIEW to control the timing of the internal electrode voltage, as discussed in Chapter 4. The internal electrode voltage was set to ramp up via an electronic trigger, with a waveform to blank the ion beam triggered at a 2μs delay after this, to prevent ions from entering the trap after the initial ion packet had begun its oscillations. A 20ms delay was then programmed to allow the voltage to settle before transient recordings were initiated. Transients of length 1000ms were recorded at a sampling frequency of 100MHz, for ions with kinetic energy 100 ± 1eV, and an associated internal electrode voltage of 175V. The transients recorded did not exhibit harmonic motion above the noise level of the detection electronics, after fast Fourier transform in MATLAB, so none are presented here.

6.7 Improving Ion Transmission

One path which was pursued to improve ion transmission into the orbital ion trap was to include a deflection element near to the entrance of the ion trap, which would compensate for any slight misalignment between the axis of the ion optics transfer assembly and the injection apertures. The two options considered were either a magnetic deflector, which could potentially be located outside of vacuum for ease of maintenance, or a pair of orthogonal electrostatic deflectors, located in vacuum. A magnetic element was discounted as it could potentially interfere with ion motion whilst trapped, unless further magnetic shielding were to be added. As such, the electrostatic XY deflector plates detailed in the Design and Manufacture chapter were designed and installed, with the aim of compensating for slight misalignments, whilst also fine tuning the angle of ion injection into the orbital ion trap to maximise transmission.

The addition of further pumping capacity was also considered to improve the base vacuum possible in the orbital ion trap chamber, and in the transfer assembly itself, with the aim of improving ion transmission and permitting longer duration ion trapping by reducing collisions with residual gas molecules. A Saes Group Nextorr pump was tested, mounted on the transfer assembly as shown in Figure 6.12. The pump is a combined non-evaporable getter and ion pump, with a pumping speed of 100l/s for H_2, (Saes Getter, 2016). It was found however that the continued use of the pump was impractical as the base pressure in the ion transfer assembly could not be maintained

below 10^{-7} mbar during experiments, as the quadrupole gas from the J105 increased pressure above this level, which prohibits operation of the Saes getter pump.

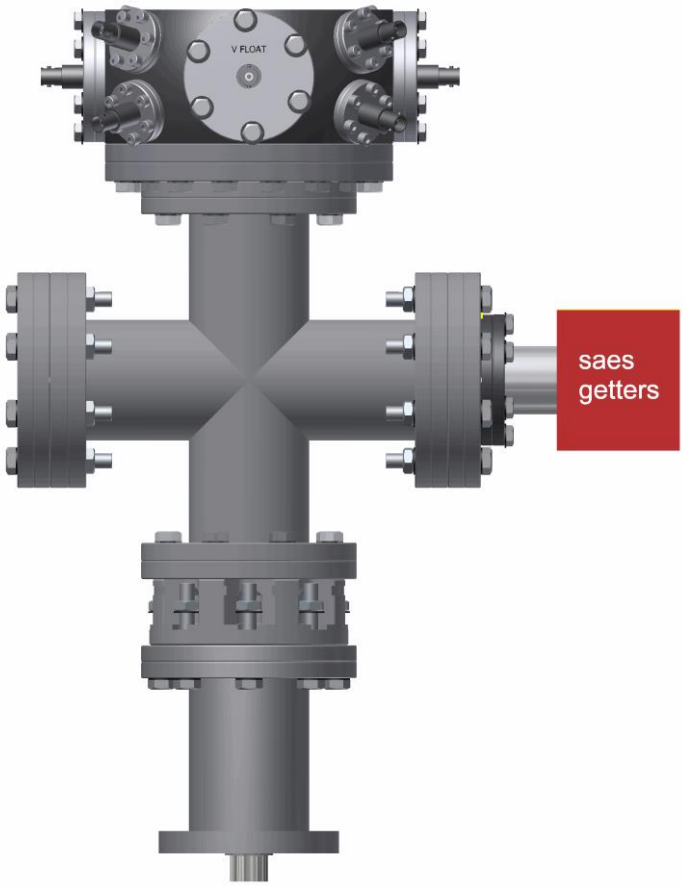

Figure 6.12 - Mounting location of Saes Nextorr ion pump

Improved vacuum was able to be achieved in the ion transfer assembly through the addition of a bypass connection, going from the orbital ion trap main chamber, to the 4-way DN63CF cross, in place of the Saes getter pump in Figure 6.12. This served to provide a larger diameter pumping flow channel between the transfer assembly and the orbital ion trap chamber than the Ø5mm ion beam aperture in the main beam line, resulting in lower observed pressures in the transfer assembly, and improved ion transmission.

Chapter 7. Conclusions and Further Work

7.1 Conclusions

The combination of high mass resolving power, $m/\Delta m > 10{,}000$, with high spatial resolution imaging is a widely sought analytical solution in the field of SIMS. This is particularly the case with the advent of modern high energy cluster primary ion sources, which are able to desorb large molecules intact from the sample surface, which require high mass resolution to determine their exact composition.

Firstly, an orbital ion trap has been simulated, designed, and manufactured in-house at Newcastle University, (Hood and Cumpson, 2016). An assembly to mount such a device on the Ionoptika J105 SIMS has been designed and constructed, without compromising the performance of the time-of-flight reflectron mass analyser of the J105. Software has been developed to aid in the precision manufacturing of complex profiles, via the implementation of Jakubczyk's algorithm to decompose smooth analytical functions into a series of piecewise continuous bi-arcs with any arbitrary tolerance, (Jakubczyk, 2012). Manufacturing following from this has been demonstrated for the quadro-logarithmic profiles of the internal and external electrodes of the orbital ion trap. Designs have been advanced for orbital ion traps which would be capable of even higher mass resolving power, in the form of the manufactured high-field orbital ion trap, and the proposed ultra-high-field geometry orbital ion trap.

Alternative ion trap geometries have been investigated, with a function not found in the literature proposed to form the logarithmic portion of a general harmonic ion trap comprising a combination of quadrupolar and logarithmic potential fields.

Simulations have been developed to model a wide range of operating conditions for the orbital ion trap, including thorough investigation of the predicted mass resolving power of the device for ions of different masses and energies trapped for varying lengths of time. The effect of misalignment on the performance of the orbital ion trap has also been simulated, and used to instruct manufacturing tolerances. A regime of parametric excitation of trapped ions has been developed and simulated, with the possibility of mass-selectively exciting only the masses of interest for high mass resolution analysis. Stability bound for this method have been investigated, to identify the excitation parameters which can be chosen to rapidly excite a narrow mass range.

Finally, ions have been successfully transmitted into the orbital ion trap, with transmission demonstrated even for the low primary ion currents which are required for high spatial resolution imaging SIMS. Electrical noise problems have prevented the final detection of ion oscillations. Software has been written to control spectral acquisition, and to convert recorded time-domain transient acquisitions into high resolution mass spectra.

7.2 Further Work

This section proposes some avenues which could be explored to extend this research in the field of increasing mass resolution in secondary ion mass spectrometry. This thesis has focussed on the simulation, design and manufacture of an orbital ion trap coupled to an existing secondary ion mass spectrometer, it is hoped that in the future, further new instrumentation could be developed using the manufacturing and simulation methods described.

7.2.1 Buncher-Orbi System

In this research, the orbital ion trap mass analyser which has been designed and manufactured has been coupled to the Ionoptika J105 SIMS without any preliminary ion trapping or beam conditioning. This could be improved upon to optimise the transmission of ions into the orbital ion trap, and to improve the dynamic mass range of ions which can be simultaneously trapped. One possible avenue would be to insert an ion buncher into the ion transfer assembly, on top of the electrostatic assembly (ESA) on the J105. This would allow ions to be injected into the orbital ion trap in a temporally and spatially narrow packet, reducing the time between ion injection and detection in the operation of the orbital ion trap. This would increase the repetition rate of mass analysis with the orbital ion trap. There is already a buncher present on the J105, which is located before the time-of-flight refelectron, the required time-focus for orbital ion trapping would be less stringent than for time-of-flight analysis, meaning a shorter and less expensive buncher could be used.

7.2.2 Alternative Ion Traps

In Chapter 4, a MATLAB program was described which generates a bi-arc representation of the ideal profile of the electrodes of the orbital ion trap, which can be used for CNC manufacture of the electrodes. This program could be utilised with minimal modification to generate similar bi-arc profiles for alternative ion trap

geometries, such as the Cassinian trap discussed in the Chapter 2 and Chapter 3 of this thesis. The program could also be used in the manufacturing of electrode geometry for a harmonic ion trap with a potential field incorporating the new function for the logarithmic potential proposed towards the end of Chapter 3.

7.2.3 Multiple-Reflection Time-of-Flight Mass Spectrometry

As covered in the Literature Review, there have been significant recent advances in the mass resolving power of multiple reflection time-of-flight analysers, with mass resolution exceeding 1,000,000 reported (Verenchikov *et al.*, 2017). It would be interesting to consider the implications of coupling such an analyser to the J105, where the extant buncher would provide an excellent initial time focus of ions prior to analysis. At the time of writing, there are not thought to be any instruments which combine a multiple reflection time-of-flight analyser with SIMS, this is likely due to issues of sensitivity, which could be overcome if transmission were improved through better vacuum. This would however be a less compact system than an orbital ion trap mass analyser, but could provide access to higher mass resolution than single reflectron analysers, without the need for sub-micron machining accuracy required to manufacture an orbital ion trap

Appendix A. Multiple Scales Perturbation Analysis

Multiple scales perturbation analysis of the resonant excitation of ions trapped in an orbital ion trap, following the method laid out in (Gallacher *et al.*, 2006).

The equation of motion being analysed is:

$$\ddot{z} + 2\varepsilon\eta\omega_n\dot{z} + {\omega_n}^2\left[1 + \varepsilon\left(\sum_{r=1}^{\infty} V_r e^{ir\omega t} + \sum_{r=1}^{\infty} V_r^* e^{-ir\omega t}\right)\right]z = 0 \quad \text{(A1)}$$

The solution is of the form:

$$z(\bar{t}, \hat{t}) = z^{(0)}(\bar{t}, \hat{t}) + \varepsilon z^{(1)}(\bar{t}, \hat{t}) + O(\varepsilon^2) \quad \text{(A2)}$$

where, $z^{(0)}(\bar{t}, \hat{t})$ or simply $z^{(0)}$,is solution for $\varepsilon = 0$, and $z^{(1)}(\bar{t}, \hat{t})$ or simply $z^{(1)}$,is solution for $\varepsilon = 1$.

Differential operators can be defined as:

$$\begin{aligned} D &= \frac{d}{dt} = \widehat{D} + \varepsilon\overline{D} \\ \widehat{D} &= \frac{d}{d\hat{t}} \\ \overline{D} &= \frac{d}{d\bar{t}} \end{aligned} \quad \text{(A3)}$$

For $\varepsilon = 0$, the expansion of (A1) becomes:

$$\widehat{D}^2\left[z^{(0)}\right] + {\omega_n}^2 z^{(0)} = 0 \quad \text{(A4)}$$

For $\varepsilon = 1$, the expansion of (A1) becomes:

$$\begin{aligned} &\widehat{D}^2\left[z^{(1)}\right] + 2\widehat{D}\overline{D}\left[z^{(0)}\right] + 2\eta\omega_n\widehat{D}\left[z^{(0)}\right] + \\ &{\omega_n}^2\left[\sum_{r=1}^{\infty} V_r e^{ir\omega t} + \sum_{r=1}^{\infty} V_r^* e^{-ir\omega t}\right]z^{(0)} + {\omega_n}^2 z^{(1)} = 0 \end{aligned} \quad \text{(A5)}$$

Equation (A4) has a general solution of the form:

$$z^{(0)} = A_0(\bar{t})e^{i\omega_n\bar{\hat{t}}} + B_0(\bar{t})e^{-i\omega n\hat{t}} \tag{A6}$$

Equation (A5) can be arranged to give:

$$\begin{aligned}\widehat{D}^2\left[z^{(1)}\right] + {\omega_n}^2 z^{(1)} = -2\widehat{D}\overline{D}\left[z^{(0)}\right] - 2\eta\omega_n\widehat{D}\left[z^{(0)}\right] - \\ {\omega_n}^2\left[\sum_{r=1}^{\infty} V_r e^{ir\omega t} + \sum_{r=1}^{\infty} V_r^* e^{-ir\omega t}\right] z^{(0)}\end{aligned} \tag{A7}$$

where:

$$\begin{aligned}\widehat{D}\overline{D}\left[z^{(0)}\right] &= i\omega_n\frac{d}{d\bar{t}}\left(A_0(\bar{t})\right)e^{i\omega_n\bar{\hat{t}}} - i\omega_n\frac{d}{d\bar{t}}\left(B_0(\bar{t})\right)e^{-i\omega n\hat{t}} \\ \widehat{D}\left[z^{(0)}\right] &= i\omega_n\left(A_0(\bar{t})\right)e^{i\omega_n\bar{\hat{t}}} - i\omega_n\left(B_0(\bar{t})\right)e^{-i\omega n\hat{t}}\end{aligned} \tag{A8}$$

Equation (A7) becomes:

$$\begin{aligned}\widehat{D}^2\left[z^{(1)}\right] + {\omega_n}^2 z^{(1)} \\ &= -2i\omega_n\frac{d}{d\bar{t}}\left(A_0(\bar{t})\right)e^{i\omega_n\bar{\hat{t}}} \\ &- i\omega_n\frac{d}{d\bar{t}}\left(B_0(\bar{t})\right)e^{-i\omega n\hat{t}} \\ &- 2\eta\omega_n[i\omega_n\left(A_0(\bar{t})\right)e^{i\omega_n\bar{\hat{t}}} \\ &- i\omega_n\left(B_0(\bar{t})\right)e^{-i\omega n\hat{t}}] \\ &- {\omega_n}^2\left[\sum_{r=1}^{\infty} V_r e^{ir\omega t}\right. \\ &\left.+ \sum_{r=1}^{\infty} V_r^* e^{-ir\omega t}\right]\left(A_0(\bar{t})e^{i\omega_n\bar{\hat{t}}} + B_0(\bar{t})e^{-i\omega n\hat{t}}\right)\end{aligned} \tag{A9}$$

Resonance causing terms are then of the form: $e^{\pm i\omega n\hat{t}}$. Letting $r\omega = r\omega_n + \varepsilon\lambda$. Gathering resonant terms gives:

$$\begin{aligned}-2i\omega_n\frac{d}{dt}A_0(\bar{t}) - 2i\eta\omega_n^2 A_0(\bar{t}) - \omega_n^2 B_0(\bar{t})V_2 e^{i\lambda\bar{t}} = 0 \\ +2i\omega_n\frac{d}{dt}B_0(\bar{t}) + 2i\eta\omega_n^2 B_0(\bar{t}) + \omega_n^2 A_0(\bar{t})V_2^* e^{i\lambda\bar{t}} = 0\end{aligned} \tag{A10}$$

where V_2 is the ratio of the excitation voltage at twice resonance relative to the DC electrode voltage.

Attempting a solution of $A_0(\bar{t}) = A^{(0)}e^{\left(\sigma+\frac{i\lambda}{2}\right)\bar{t}}$ and $B_0(\bar{t}) = B^{(0)}e^{\left(\sigma-\frac{i\lambda}{2}\right)\bar{t}}$ where σ is the relative phase between DC and excitation voltages, gives:

$$\begin{aligned}\left[-2i\omega_n\left(\sigma+\frac{i\lambda}{2}\right)-2i\eta\omega_n^2\right]A^{(0)}-\omega_n^2V_2B^{(0)}=0\\ \left[2i\omega_n\left(\sigma-\frac{i\lambda}{2}\right)+2i\eta\omega_n^2\right]B^{(0)}-\omega_n^2V_2^*A^{(0)}=0\end{aligned} \quad \text{(A11)}$$

Simplifying (A11) gives:

$$\begin{bmatrix}(\sigma+\eta\omega_n)+\frac{i\lambda}{2} & -\frac{1}{2}i\omega_nV_2\\ \frac{1}{2}i\omega_nV_2^* & (\sigma+\eta\omega_n)-\frac{i\lambda}{2}\end{bmatrix}\begin{bmatrix}A^{(0)}\\ B^{(0)}\end{bmatrix}=\mathbf{0} \quad \text{(A12)}$$

The determinant of the left-hand matrix must be equal to zero, therefore:

$$\left[(\sigma+\eta\omega_n)+\frac{i\lambda}{2}\right]\left[(\sigma+\eta\omega_n)-\frac{i\lambda}{2}\right]-\left[-\frac{1}{2}i\omega_nV_2\cdot\frac{1}{2}i\omega_nV_2^*\right]=0 \quad \text{(A13)}$$

This simplifies to:

$$\sigma^2+2\eta\omega_n\sigma+(\eta\omega_n)^2+\frac{1}{4}\lambda^2-\frac{1}{4}\omega_n^2|V_2|^2=0 \quad \text{(A14)}$$

The real component of σ must equal zero for the system to be stable, as such, stability will be found for:

$$(\eta\omega_n)^2+\frac{1}{4}\lambda^2-\frac{1}{4}\omega_n^2|V_2|^2=0 \quad \text{(A15)}$$

This simplifies to:

$$\lambda^2+(2\eta\omega_n)^2-\omega_n^2|V_2|^2=0 \quad \text{(A16)}$$

Thus a stability boundary would be defined as a solution to this quadratic equation:

$$\lambda=\pm i\sqrt{(2\eta\omega_n)^2-\omega_n^2|V_2|^2} \quad \text{(A17)}$$

As λ must be real, this definition of the stability boundary can be written as:

$$\lambda = \pm\omega_n\sqrt{|V_2|^2 - (2\eta)^2} \tag{A18}$$

In the main body of the thesis, notation of $\Lambda = \lambda$, $\nu = |\mathrm{V}_2|$ and $\zeta = \eta$ is preferred.

References

Ady, M. and Kersevan, R. (2014) ‘MolFlow+ 2.4 User Guide’, (June).

Allectra (2014) ‘Allectra 2014 Catalogue’. Berlin.

Alnajeebi, A. M., Vickerman, J. C. and Lockyer, N. P. (2018) ‘The influence of polyatomic primary ion chemistry on matrix effects in secondary ion mass spectrometry analysis’, *Rapid Communications in Mass Spectrometry*. doi: 10.1002/rcm.8265.

Amster, I. J., Loo, J. A., Furlong, J. J. P. and Mclafferty, F. W. (1987) ‘Cesium Ion Desorption Ionization with Fourier Transform Mass Spectrometry’, *Analytical Chemistry*, 59(20), pp. 313–317.

Angerer, T. B., Magnusson, Y., Landberg, G. and Fletcher, J. S. (2016) ‘Lipid heterogeneity resulting from fatty acid processing in the human breast cancer microenvironment identified by GCIB-ToFSIMS imaging’, *Analytical Chemistry*, 88(23), pp. 11946–11954. doi: 10.1021/acs.analchem.6b03884.

Appelhans, A. D. and Dahl, D. A. (2005) ‘SIMION ion optics simulations at atmospheric pressure’, *International Journal of Mass Spectrometry*, 244(1), pp. 1–14. doi: 10.1016/j.ijms.2005.03.010.

Appelhans, A. D. and Delmore, J. E. (1989) ‘Comparison of Polyatomic and Atomic Primary Beams for Secondary Ion Mass Spectrometry of Organics’, *Analytical Chemistry*, 61(10), pp. 1087–1093. doi: 10.1021/ac00185a009.

Aston, F. W. (1919) ‘A positive ray spectrograph’, *The London, Edinburgh, and Dublin Philosophical Magazine and Journal of Science*, 38(228), pp. 707–714. doi: 10.1080/14786441208636004.

Aston, F. W. (1920) ‘Isotopes and Atomic Weights’, *Nature*, 105, pp. 617–619.

Barsky, B. A. and DeRose, T. D. (1990) ‘Geometric Continuity of Parametric Curves: Constructions of Geometrically Continuous Splines’, *IEEE Computer Graphics and Applications*, 10(1), pp. 60–68. doi: 10.1109/38.45811.

Benguerba, M. *et al.* (1991) ‘Impact of slow gold clusters on various solids: nonlinear effects in secondary ion emission’, *Nuclear Inst. and Methods in Physics Research, B*, 62(1), pp. 8–22. doi: 10.1016/0168-583X(91)95922-Z.

Benninghoven, A. (1970) ‘The analysis of monomolecular layers of solids by secondary ion emission’, *Zeitschrift für Physik*, 230(5), pp. 403–417.

Beu, S. C., Blakney, G. T., Quinn, J. P., Hendrickson, C. L. and Marshall, A. G. (2004) ‘Broadband phase correction of FT-ICR mass spectra via simultaneous excitation and detection’, *Analytical Chemistry*, 76(19), pp. 5756–5761. doi: 10.1021/ac049733i.

Böcker, S., Letzel, M. C., Lipták, Z. and Pervukhin, A. (2009) ‘SIRIUS: Decomposing isotope patterns for metabolite identification’, *Bioinformatics*, 25(2), pp. 218–224. doi: 10.1093/bioinformatics/btn603.

Boldin, I. A. and Nikolaev, E. N. (2009) ‘Theory of peak coalescence in Fourier transform ion cyclotron resonance mass spectrometry’, *Rapid Communications in Mass Spectrometry*, 23, pp. 3213–3219. doi: 10.1002/rcm.

Boldin, I. A. and Nikolaev, E. N. (2011) ‘Fourier transform ion cyclotron resonance cell with dynamic harmonization of the electric field in the whole volume by shaping of the excitation and detection electrode assembly’, *Rapid Communications in Mass Spectrometry*, 25(1), pp. 122–126. doi: 10.1002/rcm.4838.

Breuer, L., Popczun, N. J., Wucher, A. and Winograd, N. (2017) ‘Reducing the Matrix Effect in Molecular Secondary Ion Mass Spectrometry by Laser Post-Ionization’, *Journal of Physical Chemistry C*, 121(36), pp. 19705–19715. doi: 10.1021/acs.jpcc.7b02596.

Briggs, D. and Hearn, M. J. (1988) ‘Sub-micron molecular imaging. A viability study by time-of-flight SIMS’, *Surface and Interface Analysis*, 13(4), pp. 181–185. doi: 10.1002/sia.740130403.

Bristow, A. W. T. and Webb, K. S. (2003) ‘Intercomparison study on accurate mass measurement of small molecules in mass spectrometry’, *Journal of the American Society for Mass Spectrometry*, 14(10), pp. 1086–1098. doi: 10.1016/S1044-0305(03)00403-3.

Carl Zeiss Microscopy GmbH (2012) *ORION NanoFab Product Information*.

Carvalho, T. C. *et al.* (2016) ‘Qualitative analysis of designer drugs by paper spray ionisation mass spectrometry (PSI-MS)’, *Analytical Methods*, 8(3), pp. 614–620. doi: 10.1039/c5ay01265a.

Castro, M. E. and Russel, D. H. (1984) ‘Cesium Ion Desorption Ionization with Fourier Transform Mass Spectrometry’, *Analytical Chemistry*, 56(3), pp. 578–581.

Champneys, A. (2011) ‘Dynamics of Parametric Excitation’, in Meyers, R. A. (ed.) *Mathematics of Complexity and Dynamical Systems*. New York: Springer, pp. 183–204. doi: 10.1007/978-3-642-27737-5_144-3.

Chen, H., Hou, A., Corilo, Y. E., Lin, Q., Lu, J., Mendelssohn, I. A., Zhang, R., Rodgers, R. P. and McKenna, A. M. (2016) ‘4 years after the deepwater horizon spill: Molecular transformation of Macondo well oil in Louisiana salt marsh sediments revealed by FT-ICR mass spectrometry’, *Environmental Science and Technology*, 50(17), pp. 9061–9069. doi: 10.1021/acs.est.6b01156.

Chen, Y. H., Gonin, M., Fuhrer, K., Dodonov, A., Su, C. S. and Wollnik, H. (1999) ‘Orthogonal electron impact source for a time-of-flight mass spectrometer with high mass resolving power’, *International Journal of Mass Spectrometry*, 185, pp. 221–226. doi: 10.1016/S1387-3806(98)14152-0.

Cheng, J. and Winograd, N. (2005) ‘Depth profiling of peptide films with TOF-SIMS and a C60 probe’, *Analytical Chemistry*, 77(11), pp. 3651–3659. doi: 10.1021/ac048131w.

Cho, E., Witt, M., Hur, M., Jung, M. J. and Kim, S. (2017) ‘Application of FT-ICR MS Equipped with Quadrupole Detection for Analysis of Crude Oil’, *Analytical Chemistry*, 89(22), pp. 12101–12107. doi: 10.1021/acs.analchem.7b02644.

Cho, Y., Ahmed, A., Islam, A. and Kim, S. (2014) ‘Developments in FT-ICR MS Instrumentation, Ionization Techniques, and Data Interpretation Methods for Petroleomics’, *Mass Spectrometry Reviews*, 34, pp. 248–263. doi: 10.1002/mas.

Cody, R. B., Hein, R. E., Goodman, S. D. and Marshall, A. G. (1987) ‘Stored Waveform Inverse Fourier Transform Excitation for Obtaining Increased Parent Ion Selectivity in Collisionally Activated Dissociation: Preliminary Results’, *Rapid Communications in Mass Spectrometry*, 1(6), pp. 99–102.

Comisarow, M. B. and Marshall, A. G. (1974) ‘Fourier-Transform Ion Cyclotron Resonance Spectroscopy’, *Chemical Physics Letters*, 25(2), pp. 141–160. doi: 10.1039/9781847556653-00141.

Comisarow, M. B. and Marshall, A. G. (1976) ‘Theory of Fourier transform ion cyclotron resonance mass spectroscopy. I. Fundamental equations and low-pressure line shape’, *The Journal of Chemical Physics*, 64(1), pp. 110–119. doi: 10.1063/1.431959.

Culpepper, M. L. (2004) ‘Design of quasi-kinematic couplings’, *Precision Engineering*, 28(3), pp. 338–357. doi: 10.1016/j.precisioneng.2002.12.001.

Czerwiński, B., Samson, R., Garrison, B. J., Winograd, N. and Postawa, Z. (2006) ‘Desorption of organic overlayers by Ga and C60 bombardment’, *Vacuum*, 81(2), pp. 167–173. doi: 10.1016/j.vacuum.2006.03.012.

Dahl, D. A. (2000) ‘SIMION for the personal computer in reflection’, *International Journal of Mass Spectrometry*, 200, pp. 3–25. doi: 10.1016/S1387-3806(00)00305-5.

Dahl, D. A., Appelhans, A. D. and Ward, M. B. (1999) ‘A modular ion beam deflector’, *International Journal of Mass Spectrometry*, 189(1), pp. 47–51. doi: 10.1016/S1387-3806(99)00051-2.

Dahl, D. and Appelhans, T. (2000) ‘Advanced SIMION Ion Optics’, *The Idaho National Engineering and Environment Laboratory*.

Davies, N., Weibel, D. E., Blenkinsopp, P., Lockyer, N., Hill, R. and Vickerman, J. C. (2003) ‘Development and experimental application of a gold liquid metal ion source’, *Applied Surface Science*, 203–204, pp. 223–227. doi: 10.1016/S0169-4332(02)00631-1.

Dawson, J. H. J. and Guilhaus, M. (1989) ‘Orthogonal-acceleration Time-of-flight Mass Spectrometer’, *Rapid Communications in Mass Spectrometry*, 3(5), pp. 155–159.

Dejay Distribution (2015) *Synthetic Sapphire (Ruby) Balls*. Available at: http://www.dejaydistribution.co.uk/balls8.html (Accessed: 1 August 2016).

Deline, V. R., Katz, W., Evans, C. A. and Williams, P. (1978) ‘Mechanism of the SIMS matrix effect’, *Applied Physics Letters*, 33(9), pp. 832–835. doi: 10.1063/1.90546.

Dennis, E. A., Gundlach-Graham, A. W., Ray, S. J., Enke, C. G. and Hieftje, G. M. (2016) ‘Distance-of-Flight Mass Spectrometry: What, Why, and How?’, *Journal of the American Society for Mass Spectrometry*, 27(11), pp. 1772–1786. doi: 10.1007/s13361-016-1458-1.

Dickel, T. *et al.* (2015) ‘A high-performance multiple-reflection time-of-flight mass spectrometer and isobar separator for the research with exotic nuclei’, *Nuclear Instruments and Methods in Physics Research, Section A: Accelerators, Spectrometers, Detectors and Associated Equipment*. Elsevier, 777, pp. 172–188. doi: 10.1016/j.nima.2014.12.094.

Dickel, T. *et al.* (2019) ‘Recent upgrades of the multiple-reflection time-of-flight mass spectrometer at TITAN , TRIUMF’, *Hyperfine Interactions*, (240), p. 62.

Exelis Applied Kilovolts (2013) *Applied Kilovolts Power Supply MS005MAAxxx - Datasheet*. Available at: http://www.exelis-ps.com/docs/datasheets/MS005.pdf (Accessed: 9 November 2016).

Fearn, S. (2015) *An introduction to time-of-flight secondary ion mass spectrometry (ToF-SIMS) and its application to materials science*, *An Introduction to Time-of-Flight Secondary Ion Mass Spectrometry (ToF-SIMS) and its Application to Materials Science*. doi: 10.1088/978-1-6817-4088-1.

Fisher, G. L., Belu, A. M., Mahoney, C. M., Wormuth, K., Lt, M. P. and City, C. (2009) ‘Three-Dimensional TOF-SIMS Imaging of a Pharmaceutical in a Coronary Stent Coating as a Function of Elution Time’, *Analytical Chemistry*, 81(24), pp. 9930–9940.

Fisher, G. L., Hammond, J. S., Larson, P. E., Bryan, S. R. and Heeren, R. M. A. (2016) ‘Parallel imaging MS/MS TOF-SIMS instrument’, *Journal of Vacuum Sciene & Technology B*, 34(3), p. 03H126. doi: 10.1116/1.4943568.

Fletcher, J. S., Rabbani, S., Barber, A. M., Lockyer, N. P. and Vickerman, J. C. (2013) ‘Comparison of C60 and GCIB primary ion beams for the analysis of cancer cells and tumour sections’, *Surface and Interface Analysis*, 45(1), pp. 273–276. doi: 10.1002/sia.4874.

Fletcher, J. S., Rabbani, S., Henderson, A., Blenkinsopp, P., Thompson, S. P., Lockyer, N. P. and Vickerman, J. C. (2008) ‘A New Dynamic in Mass Spectral Imaging of Single Biological Cells’, *Analytical Chemistry*, 80(23), pp. 9058–9064. doi: 10.1021/ac8015278.

Gallacher, B. J., Burdess, J. S. and Harish, K. M. (2006) ‘A control scheme for a MEMS electrostatic resonant gyroscope excited using combined parametric excitation and

harmonic forcing', *Journal of Micromechanics and Microengineering*, 16(2), pp. 320–331. doi: 10.1088/0960-1317/16/2/017.

GaN Systems (2015) 'GS66508T-EVBHB 650V GaN E-HEMT Half Bridge Evaluation Board', pp. 1–21.

Gao, Yan *et al.* (2015) 'Targeted Data-Independent Acquisition and Mining Strategy for Trace Drug Metabolite Identification Using Liquid Chromatography Coupled with Tandem Mass Spectrometry', *Analytical Chemistry*, 87(15), pp. 7535–7539. doi: 10.1021/acs.analchem.5b01205.

Giglio, E. (2015) *Boundary Conditions in SIMION*. Caen.

Gillen, G. and Roberson, S. (1998) 'Preliminary evaluation of an SF5+ polyatomic primary ion beam for analysis of organic thin films by secondary ion mass spectrometry', *Rapid Communications in Mass Spectrometry*, 12(19), pp. 1303–1312. doi: 10.1002/(SICI)1097-0231(19981015)12:19<1303::AID-RCM330>3.0.CO;2-7.

Gilmore, I. S. and Vickerman, J. C. (2009) *Surface Analysis – The Principal Techniques 2nd Edition*, *Wiley*. doi: 10.1002/9780470721582.

Gorshkov, M. V. *et al.* (1998) 'Electrospray ionization-fourier transform ion cyclotron resonance mass spectrometry at 11.5 Tesla: Instrument design and initial results', *Journal of the American Society for Mass Spectrometry*, 9(7), pp. 692–700. doi: 10.1016/S1044-0305(98)00037-3.

Gorshkov, M. V., Good, D. M., Lyutvinskiy, Y., Yang, H. and Zubarev, R. A. (2010) 'Calibration function for the orbitrap FTMS accounting for the space charge effect', *Journal of the American Society for Mass Spectrometry*. Elsevier Inc., 21(11), pp. 1846–1851. doi: 10.1016/j.jasms.2010.06.021.

Grinfeld, D., Monastyrskiy, M. and Makarov, A. (2015) 'Control of Aberration and Space-Charge Effects in the Orbitrap Mass Analyzer', *Microscopy and Microanalysis*, 21(S4), pp. 176–181. doi: 10.1017/S1431927615013331.

Gross, J. H. (2011) *Mass spectrometry*. doi: 10.1016/S0168-9525(99)01879-X.

Hardman, M. and Makarov, A. (2003) 'Interfacing the orbitrap mass analyzer to an electrospray ion source', *Analytical Chemistry*, 75(7), pp. 1699–1705. doi:

10.1021/ac0258047.

Harish, K. M., Gallacher, B. J., Burdess, J. S. and Neasham, J. A. (2008) ‘Simple parametric resonance in an electrostatically actuated microelectromechanical gyroscope: theory and experiment’, *Journal of Mechanical Engineering Science*, 222(1), pp. 43–52. doi: 10.1243/09544062JMES742.

Hendrickson, C. L., Drader, J. J., Laude, D. A., Guan, S. and Marshall, A. G. (1996) ‘Fourier transform ion cyclotron resonance mass spectrometry in a 20 T resistive magnet’, *Rapid Communications in Mass Spectrometry*, 10(14), pp. 1829–1832. doi: 10.1002/(SICI)1097-0231(199611)10:14<1829::AID-RCM697>3.0.CO;2-U.

Hendrickson, C. L., Quinn, J. P., Kaiser, N. K., Smith, D. F., Blakney, G. T., Chen, T., Marshall, A. G., Weisbrod, C. R. and Beu, S. C. (2015) ‘21 Tesla Fourier Transform Ion Cyclotron Resonance Mass Spectrometer: A National Resource for Ultrahigh Resolution Mass Analysis’, *Journal of the American Society for Mass Spectrometry*, 26(9), pp. 1626–1632. doi: 10.1007/s13361-015-1182-2.

Herzog, R. F. K. and Viehböck, F. P. (1949) ‘Ion Source for Mass Spectrography’, *Physical Review*, 76(6), pp. 855–856. doi: 10.1103/PhysRev.76.855.

Hill, R., Blenkinsopp, P., Thompson, S., Vickerman, J. and Fletcher, J. S. (2011) ‘A new time-of-flight SIMS instrument for 3D imaging and analysis’, *Surface and Interface Analysis*, 43(1–2), pp. 506–509. doi: 10.1002/sia.3562.

Hoffmann, E. de and Stroobant, V. (2007) *Mass Spectrometry: Principles and Applications*. Third, *Mass Spectrometry*. Third. Chichester: Wiley. doi: 10.1007/978-1-4899-5672-9.

Honig, R. E. (1958) ‘Sputtering of surfaces by positive ion beams of low energy’, *Journal of Applied Physics*, 29(3), pp. 549–555. doi: 10.1063/1.1723219.

Hood, J. C. (2019) *Design, Manufacture, and Applications of High Mass Resolution Orbital Trapping for Secondary Ion Mass Spectrometry - James Hood Thesis Code GitHub Repository*. Available at: https://github.com/jhoodncl/JH_Thesis_Code (Accessed: 20 September 2019).

Hood, J. C. and Cumpson, P. J. (2016) ‘Design and Manufacture of a High Resolution Orbital-Trapping Mass-Analyser for Secondary Ion Mass Spectrometry’, *International*

Journal of Modern Engineering Research, 6(10), pp. 76–83.

Hu, Q., Cooks, R. G. and Noll, R. J. (2007) 'Phase-Enhanced Selective Ion Ejection in an Orbitrap Mass Spectrometer', *Journal of the American Society for Mass Spectrometry*, 18(6), pp. 980–983. doi: 10.1016/j.jasms.2007.02.004.

Hu, Q., Makarov, A. A., Graham Cooks, R. and Noll, R. J. (2006) 'Resonant ac dipolar excitation for ion motion control in the Orbitrap mass analyzer', *Journal of Physical Chemistry A*, 110(8), pp. 2682–2689. doi: 10.1021/jp054485v.

Hu, Q., Noll, R. J., Li, H., Makarov, A., Hardman, M. and Graham Cooks, R. (2005) 'The Orbitrap: a new mass spectrometer', *Journal of Mass Spectrometry*, 40(4), pp. 430–443. doi: 10.1002/jms.856.

Hua, X. *et al.* (2016) 'Chemical imaging of molecular changes in a hydrated single cell by dynamic secondary ion mass spectrometry and super-resolution microscopy', *Integr. Biol.*, 8(5), pp. 635–644. doi: 10.1039/C5IB00308C.

Ionoptika (2015) *J105 SIMS*. Available at: http://www.ionoptika.com/tof-sims/products/tofsims/j105-sims (Accessed: 1 April 2016).

IONTOF GmbH (2017) *IONTOF TOF-SIMS V*. Available at: https://www.iontof.com/tof-sims-5-product-version-100mm-200mm-300mm.html (Accessed: 14 November 2017).

Jakubczyk, K. (2012) 'Approximation of Smooth Planar Curves by Circular Arc Splines', pp. 1–13. Available at: http://www.kaj.pr.radom.pl/prace/Biarcs.pdf.

Johnson, E. G. and Nier, A. O. (1953) 'Sector Shaped Electromagnetic of Charged Particles', *Physical Review*, 91(1).

Johnson, J. B. (1927) 'Thermal agitation of electricity in conductors', *Physical Review*, 541(1918).

Jones, E. A., Lockyer, N. P., Kordys, J. and Vickerman, J. C. (2007) 'Suppression and Enhancement of Secondary Ion Formation Due to the Chemical Environment in Static-Secondary Ion Mass Spectrometry', *Journal of the American Society for Mass Spectrometry*, 18(8), pp. 1559–1567. doi: 10.1016/j.jasms.2007.05.014.

Kaiser, N. K., Quinn, J. P., Blakney, G. T., Hendrickson, C. L. and Marshall, A. G. (2011) 'A Novel 9.4 Tesla FTICR Mass Spectrometer with Improved Sensitivity, Mass

Resolution, and Mass Range', *Journal of The American Society for Mass Spectrometry*, 22(8), pp. 1343–1351. doi: 10.1007/s13361-011-0141-9.

Karas, M., Bachmann, D. and Hillenkamp, F. (1985) 'Influence of the wavelength in high-irradiance ultraviolet laser desorption mass spectrometry of organic molecules', *Analytical Chemistry*, 57(14), pp. 2935–2939. doi: 10.1021/ac00291a042.

Kayser, S., Rading, D., Moellers, R., Kollmer, F. and Niehuis, E. (2013) 'Surface spectrometry using large argon clusters', *Surface and Interface Analysis*, 45(1), pp. 131–133. doi: 10.1002/sia.4932.

Keithley (2001) *Low Current Measurements*, *Keithley Application Note Se-ries*.

Keithley (2003) *Keithley 6514 Programmable Electrometer Manual*.

Kharchenko, A., Vladimirov, G., Heeren, R. M. a. and Nikolaev, E. N. (2012) 'Performance of Orbitrap Mass Analyzer at Various Space Charge and Non-Ideal Field Conditions: Simulation Approach', *Journal of The American Society for Mass Spectrometry*, 23(5), pp. 977–987. doi: 10.1007/s13361-011-0325-3.

Kilgour, D. P. A., Nagornov, K. O., Kozhinov, A. N., Zhurov, K. O. and Tsybin, Y. O. (2015) 'Producing absorption mode Fourier transform ion cyclotron resonance mass spectra with non-quadratic phase correction functions', *Rapid Communications in Mass Spectrometry*, 29(11), pp. 1087–1093. doi: 10.1002/rcm.7200.

Kim, S., Rodgers, R. P. and Marshall, A. G. (2006) 'Truly "exact" mass: Elemental composition can be determined uniquely from molecular mass measurement at ~0.1 mDa accuracy for molecules up to ~500 Da', *International Journal of Mass Spectrometry*, 251(2-3 SPEC. ISS.), pp. 260–265. doi: 10.1016/j.ijms.2006.02.001.

Kingdon, K. H. (1923) 'A method for the neutralization of electron space charge by positive ionization at very low gas pressures', *Physical Review*, 21(4), pp. 408–418. doi: 10.1103/PhysRev.21.408.

Knight, R. D. (1981) 'Storage of ions from laser-produced plasmas', *Applied Physics Letters*, 38(4), pp. 221–223. doi: 10.1063/1.92315.

Knight, R. D. (1983) 'The general form of the quadrupole ion trap potential', *International Journal of Mass Spectrometry and Ion Physics*, 51(1), pp. 127–131. doi:

10.1016/0020-7381(83)85033-5.

Köster, C. (2009) ‘The concept of electrostatic non-orbital harmonic ion trapping’, *International Journal of Mass Spectrometry*, 287(1–3), pp. 114–118. doi: 10.1016/j.ijms.2009.01.014.

Köster, C. (2015) ‘Twin trap or hyphenation of a 3d Paul- and a Cassinian ion trap’, *Journal of the American Society for Mass Spectrometry*, 26(3), pp. 390–396. doi: 10.1007/s13361-014-1050-5.

Kotter, F. and Benninghoven, A. (1998) ‘Secondary ion emission from polymer surfaces under Ar q , Xe q q ion bombardment’, *Applied Surface Science*, pp. 47–57.

Krohn, V. E. and Ringo, G. R. (1975) ‘Ion source of high brightness using liquid metal’, *Applied Physics Letters*, 27(9), pp. 479–481. doi: 10.1063/1.88540.

Kucher, A., Jackson, L. M., Lerach, J. O., Bloom, A. N., Popczun, N. J., Wucher, A. and Winograd, N. (2014) ‘Near infrared (NIR) strong field ionization and imaging of C60 sputtered molecules: Overcoming matrix effects and improving sensitivity’, *Analytical Chemistry*, 86(17), pp. 8613–8620. doi: 10.1021/ac501586d.

Kurt J Lesker (2005) ‘Installation Instructions Standard Gate Valves’.

Lange, O., Damoc, E., Wieghaus, A. and Makarov, A. (2014a) ‘Enhanced Fourier transform for Orbitrap mass spectrometry’, *International Journal of Mass Spectrometry*. Elsevier B.V., 377(369), pp. 16–22. doi: 10.1016/j.ijms.2014.07.040.

Lange, O., Damoc, E., Wieghaus, A. and Makarov, A. (2014b) ‘Reprint of “Enhanced Fourier transform for Orbitrap mass spectrometry”’, *International Journal of Mass Spectrometry*. Elsevier B.V., 377(369), pp. 16–22. doi: 10.1016/j.ijms.2014.07.040.

Letzter, S. and Webster, N. (1970) ‘Noise in amplifiers’, *IEEE Spectrum*, (August), pp. 67–75.

LIGO (2014) ‘LIGO Vacuum Compatible Materials List’, *Laser Interferometer Gravitational Wave Observatory*. Pasadena, CA: LIGO, pp. 1–24.

Maharrey, S., Bastasz, R., Behrens, R., Highley, A., Hoffer, S., Kruppa, G. and Whaley, J. (2004) ‘High mass resolution SIMS’, *Applied Surface Science*, 231–232, pp. 972–975. doi: 10.1016/j.apsusc.2004.03.197.

Mahoney, C. M. (2013) *Cluster secondary ion mass spectrometry*. Edited by C. M. Mahoney. New Jersey: Wiley. doi: 10.1007/978-3-319-01360-2_4.

Mahoney, C. M., Fahey, A. J. and Belu, A. M. (2008) 'Three-dimensional compositional analysis of drug eluting stent coatings using cluster secondary ion mass spectrometry', *Analytical Chemistry*, 80(3), pp. 624–632. doi: 10.1021/ac701644j.

Mahoney, C. M., Fahey, A. J., Gillen, G., Xu, C. and Batteas, J. D. (2006) 'Temperature-controlled depth profiling in polymeric materials using cluster secondary ion mass spectrometry (SIMS)', *Applied Surface Science*, 252(19), pp. 6502–6505. doi: 10.1016/j.apsusc.2006.02.078.

Makarov, A. (2000) 'Electrostatic axially harmonic orbital trapping: A high-performance technique of mass analysis', *Analytical Chemistry*, 72(6), pp. 1156–1162. doi: 10.1021/ac991131p.

Makarov, A., Denisov, E., Kholomeev, A., Balschun, W., Lange, O., Strupat, K. and Horning, S. (2006) 'Performance Evaluation of a Hybrid Linear Ion Trap / Orbitrap Mass Spectrometer', *Analytical Chemistry*, 78(7), pp. 2113–2120.

Makarov, A., Denisov, E. and Lange, O. (2009) 'Performance evaluation of a high-field orbitrap mass analyzer', *Journal of the American Society for Mass Spectrometry*, 20(8), pp. 1391–1396. doi: 10.1016/j.jasms.2009.01.005.

Makarov, A., Denisov, E., Lange, O. and Horning, S. (2006) 'Dynamic Range of Mass Accuracy in LTQ Orbitrap Hybrid Mass Spectrometer', *Journal of the American Society for Mass Spectrometry*, 17(7), pp. 977–982. doi: 10.1016/j.jasms.2006.03.006.

Mamyrin, B. A., Karataev, V. I., Shmikk, D. V. and Zagulin, V. A. (1973) 'The mass-reflectron, a new nonmagnetic time-of-flight mass spectrometer with high resolution', *Sov. Phys. - JETP*, 37(1), pp. 45–48.

March, R. E. (1997) 'An Introduction to Quadrupole Ion Trap Mass Spectrometry', *Journal of mass spectrometry : JMS*, 32(February), pp. 351–369. doi: 10.1002/(SICI)1096-9888(199704)32:4<351::AID-JMS512>3.0.CO;2-Y.

Marshall, A. G., Blakney, G. T., Chen, T., Kaiser, N. K., McKenna, A. M., Rodgers, R. P., Ruddy, B. M. and Xian, F. (2013) 'Mass Resolution and Mass Accuracy: How Much Is Enough?', *Mass Spectrometry*, 2(Special_Issue), pp. S0009–S0009. doi:

10.5702/massspectrometry.s0009.

Marshall, A. G. and Hendrickson, C. L. (2008) ‘High-Resolution Mass Spectrometers’, *Annual Review of Analytical Chemistry*, 1(1), pp. 579–599. doi: 10.1146/annurev.anchem.1.031207.112945.

Marshall, A. G., Hendrickson, C. L. and Jackson, G. S. (1998) ‘Fourier transform ion cyclotron resonance mass spectrometry: a primer.’, *Mass spectrometry reviews*, 17, pp. 1–35. doi: 10.1002/(SICI)1098-2787(1998)17:1<1::AID-MAS1>3.0.CO;2-K.

Mathur, R., Knepper, R. W. and O’Connor, P. B. (2007) ‘A Low-Noise, Wideband Preamplifier for a Fourier-Transform Ion Cyclotron Resonance Mass Spectrometer’, *Journal of the American Society for Mass Spectrometry*, 18(12), pp. 223–2241. doi: doi:10.1016/j.jasms.2007.09.013.

Mattauch, J. and Herzog, R. (1934) ‘Über einen neuen Massenspektrographen’, *Zeitschrift für Physik*, 89(447), pp. 786–795.

McKenna, A. M., Donald, L. J., Fitzsimmons, J. E., Juyal, P., Spicer, V., Standing, K. G., Marshall, A. G. and Rodgers, R. P. (2013) ‘Heavy petroleum composition. 3. Asphaltene aggregation’, *Energy and Fuels*, 27(3), pp. 1246–1256. doi: 10.1021/ef3018578.

Mclafferty, F. W. (1981) ‘Tandem Mass Spectrometry’, *Science*, 214(October), pp. 280–287. doi: 10.1126/science.7280693.

McLafferty, F. W. (2011) ‘A Century of Progress in Molecular Mass Spectrometry’, *Annual Review of Analytical Chemistry*, 4(1), pp. 1–22. doi: 10.1146/annurev-anchem-061010-114018.

McPhail, D. S. (2006) ‘Applications of Secondary Ion Mass Spectrometry (SIMS) in materials science’, *Journal of Materials Science*, 41(3), pp. 873–903. doi: 10.1007/s10853-006-6568-x.

Michalski, A. *et al.* (2012) ‘Ultra High Resolution Linear Ion Trap Orbitrap Mass Spectrometer (Orbitrap Elite) Facilitates Top Down LC MS/MS and Versatile Peptide Fragmentation Modes’, *Molecular & Cellular Proteomics*, 11(3). doi: 10.1074/mcp.O111.013698.

N. Nikolaev, E., N. Vladimirov, G., Jertz, R. and Baykut, G. (2013) ‘From Supercomputer Modeling to Highest Mass Resolution in FT-ICR’, *Mass Spectrometry*, 2(Special_Issue), pp. S0010–S0010. doi: 10.5702/massspectrometry.s0010.

National Instruments (2003) ‘NI PXI-5122 Digitizer Specifications’.

National Instruments (2004) ‘NI PXI-5412 Arbitrary Waveform Generator AWG Specifications’.

National Instruments (2013) ‘NI IVI with LabVIEW or LabWindows / CVI’, pp. 4–8.

Nier, A. O. (1939) ‘The isotopic constitution of uranium and the half-lives of the uranium isotopes. I’, *Physical Review*, 55(2), pp. 150–153. doi: 10.1103/PhysRev.55.150.

Nier, A. O. (1991) ‘The development of a high resolution mass spectrometer: A reminiscence’, *Journal of the American Society for Mass Spectrometry*, 2(6), pp. 447–452. doi: 10.1016/1044-0305(91)80029-7.

Nier, A. O. (2009) ‘Some reminiscences of mass spectrometry and the Manhattan Project’, *Journal of Chemical Education*, 66(5), p. 385. doi: 10.1021/ed066p385.

Nikolaev, E. N., Boldin, I. A., Jertz, R. and Baykut, G. (2011) ‘Initial experimental characterization of a new ultra-high resolution FTICR cell with dynamic harmonization’, *Journal of the American Society for Mass Spectrometry*, 22(7), pp. 1125–1133. doi: 10.1007/s13361-011-0125-9.

Nikolaev, E. N., Kostyukevich, Y. I. and Vladimirov, G. N. (2014) ‘Fourier transform ion cyclotron resonance (FT ICR) mass spectrometry: Theory and simulations’, *Mass Spectrometry Reviews*, 35(2), pp. 219–258. doi: 10.1002/mas.21422.

Nyquist, H. (1928) ‘Thermal agitation of electric charge in conductors’, *Physical Review*, 32(1918), pp. 110–113. Available at: https://journals.aps.org/pr/pdf/10.1103/PhysRev.32.110.

O’Hanlon, J. F. (2003) *A User’s Guide to Vacuum Technology*. 3rd edn, *Wiley-Interscience*. 3rd edn. Hoboken, NJ. doi: 10.1109/MCD.2005.1438817.

Oviano, M. and Bou, G. (2019) ‘Matrix-Assisted Laser Desorption Ionization – Time of Flight Mass Spectrometry for the Rapid Detection of Antimicrobial Resistance Mechanisms and Beyond’, *Clinical Microbiology Reviews*, 32(1), pp. 1–29.

Palacio Lozano, D. C. *et al.* (2019) ‘Pushing the analytical limits: new insights into complex mixtures using mass spectra segments of constant ultrahigh resolving power’, *Chemical Science*, 10(29), pp. 6966–6978. doi: 10.1039/c9sc02903f.

Pan, Y., Ridge, D. P. and Rockwood, A. L. (1988) ‘Harmonic signal enhancement in ion cyclotron resonance mass spectrometry using multiple electrode detection’, *International Journal of Mass Spectrometry and Ion Processes*, 84(3), pp. 293–304. doi: 10.1016/0168-1176(88)80106-X.

Pasa-Tolic, L., Smith, D. F., Leach, F. E., Robinson, E. W. and Heeren, R. M. (2013) ‘C60 Secondary Ion FT-ICR Mass Spectrometry: High Mass Resolving Power and High Mass Accuracy SIMS’, *Microscopy and Microanalysis*, 19(S2), pp. 660–661. doi: 10.1017/S1431927613005291.

Paša-Tolić, L., Huang, Y., Guan, S., Kim, H. S. and Marshall, A. G. (1995) ‘Ultrahigh-resolution matrix-assisted laser desorption/ionization Fourier transform ion cyclotron resonance mass spectra of peptides’, *Journal of Mass Spectrometry*, 30(6), pp. 825–833. doi: 10.1002/jms.1190300607.

Passarelli, M. K. *et al.* (2017) ‘The 3D OrbiSIMS - Label-free metabolic imaging with subcellular lateral resolution and high mass-resolving power’, *Nature Methods*, 14(12), pp. 1175–1183. doi: 10.1038/nmeth.4504.

Paul, W. (1989) ‘Electromagnetic Traps for Charged’, in Ekspong, G. (ed.) *Nobel Lectures in Physics 1981-1990*. Singapore: World Scientific Publishing.

Paul, W. and Steinwedel, H. (1953) ‘Ein neues Massenspektrometer ohne Magnetfeld’, *Zeitschrift für Naturforschung A*, 8(7), pp. 448–450.

Pauly, H. (2000) *Atom, Molecule, and Cluster Beams II*. Berlin: Springer.

Perry, R. H., Cooks, R. G. and Noll, R. J. (2008) ‘Orbitrap mass spectrometry: Instrumentation, ion motion and applications’, *Mass spectrometry reviews*, 26(2), pp. 223–257. doi: 10.1002/mas.

Perry, R. H., Hu, Q., Salazar, G. a., Cooks, R. G. and Noll, R. J. (2009) ‘Rephasing ion packets in the orbitrap mass analyzer to improve resolution and peak shape’, *Journal of the American Society for Mass Spectrometry*. American Society for Mass Spectrometry, 20(8), pp. 1397–1404. doi: 10.1016/j.jasms.2009.02.011.

Piechaczek, A., Shchepunov, V., Carter, H. K., Batchelder, J. C., Zganjar, E. F., Liddick, S. N., Wollnik, H., Hu, Y. and Griffith, B. O. (2008) 'Development of a high resolution isobar separator for study of exotic decays', *Nuclear Instruments and Methods in Physics Research, Section B: Beam Interactions with Materials and Atoms*. Elsevier B.V., 266(19–20), pp. 4510–4514. doi: 10.1016/j.nimb.2008.05.149.

Pirkl, A., Moellers, R., Arlinghaus, H., Kollmer, F., Niehuis, E., Horning, S., Passarelli, M., Havelund, R., Rakowska, P., Race, A. and Gilmore, I. S. (2016) 'A Novel Hybrid Dual Analyzer SIMS Instrument for Improved Surface and 3D- Analysis', 22(Suppl 3), pp. 340–341. doi: 10.1017/S1431927616002555.

Pirkl, A., Moellers, R., Arlinghaus, H., Kollmer, F., Niehuis, E., Horning, S., Passarelli, M., Havelund, R., Rakowska, P., Race, A., Gilmore, I. S., *et al.* (2016) 'A Novel Hybrid Dual Analyzer SIMS Instrument for Improved Surface and 3D-Analysis', *Microscopy and Microanalysis*, 22(Suppl 3), pp. 340–341. doi: 10.1017/S1431927616002555.

Pittman, J. L. and O'Connor, P. B. (2005) 'A minimum thickness gate valve with integrated ion optics for mass spectrometry', *Journal of the American Society for Mass Spectrometry*, 16(4), pp. 441–445. doi: 10.1016/j.jasms.2004.12.010.

Plaß, W. R., Dickel, T. and Scheidenberger, C. (2013) 'Multiple-reflection time-of-flight mass spectrometry', *International Journal of Mass Spectrometry*. Elsevier B.V., 349–350(1), pp. 134–144. doi: 10.1016/j.ijms.2013.06.005.

Popczun, N. J., Breuer, L., Wucher, A. and Winograd, N. (2017) 'On the SIMS Ionization Probability of Organic Molecules', *Journal of the American Society for Mass Spectrometry*. Journal of The American Society for Mass Spectrometry, 28(6), pp. 1182–1191. doi: 10.1007/s13361-017-1624-0.

Qi, Y., Thompson, C. J., Van Orden, S. L. and O'Connor, P. B. (2011) 'Phase correction of fourier transform ion cyclotron resonance mass spectra using matlab', *Journal of the American Society for Mass Spectrometry*, 22(1), pp. 138–147. doi: 10.1007/s13361-010-0006-7.

Rabbani, S., Barber, A. M., Fletcher, J. S., Lockyer, N. P. and Vickerman, J. C. (2011) 'TOF-SIMS with argon gas cluster ion beams: A comparison with C 60+', *Analytical Chemistry*, 83(10), pp. 3793–3800. doi: 10.1021/ac200288v.

Radionaova, A., Filippov, I. and Derrick, P. J. (2016) ‘In pursuit of resolution in time-of-flight mass spectrometry: A historical perspective’, *Mass Spectrometry Reviews*, 35, pp. 738–757. doi: 10.1002/mas.21470.

Rose, R. J., Damoc, E., Denisov, E., Makarov, A. and Heck, A. J. R. (2012) ‘High-sensitivity Orbitrap mass analysis of intact macromolecular assemblies.’, *Nature methods*, 9(11), pp. 1084–6. doi: 10.1038/nmeth.2208.

Saes Getter (2016) ‘Saes Getter NEXTorr D 100-5 Ion Pump Manual’.

SARC Manchester (2016) *Ionoptika J105 Animation*. Available at: http://www.sarc.manchester.ac.uk/wordpress/wp-content/uploads/2013/10/J105-operation.gif (Accessed: 5 February 2019).

Sauer, T. (2006) *Numerical analysis*. Second. London: Pearson Education. doi: 10.1016/0378-4754(90)90072-q.

Schaub, T. M., Hendrickson, C. L., Horning, S., Quinn, J. P., Senko, M. W. and Marshall, A. G. (2008) ‘High-performance mass spectrometry: Fourier transform ion cyclotron resonance at 14.5 Tesla’, *Analytical Chemistry*, 80(11), pp. 3985–3990. doi: 10.1021/ac800386h.

Scheltema, R. A., Hauschild, J.-P., Lange, O., Hornburg, D., Denisov, E., Kuehn, A., Makarov, A., Mann, M. and Damoc, E. (2014) ‘The Q Exactive HF, a Benchtop Mass Spectrometer with a Pre-filter, High Performance Quadrupole and an Ultra-High Field Orbitrap Analyzer.’, *Molecular & cellular proteomics : MCP*, pp. 3698–3708. doi: 10.1074/mcp.M114.043489.

Schottky, W. (1926) ‘Small-shot effect and flicker effect’, *Physical Review*, 28(1), pp. 74–103. doi: 10.1103/PhysRev.28.74.

Schwartz, J. C., Senko, M. W. and Syka, J. E. P. (2002) ‘A Two-Dimensional Quadrupole Ion Trap Mass Spectrometer’, *Journal of the American Society for Mass Spectrometry*, 13, pp. 659–669. doi: 10.1016/S1044-0305(02)00384-7.

Schweikhard, L., Lindinger, M. and Kluge, H. J. (1990) ‘Quadrupole-detection FT-ICR mass spectrometry’, *International Journal of Mass Spectrometry and Ion Processes*, 98, pp. 25–33.

Scigelova, M., Hornshaw, M., Giannakopulos, a. and Makarov, A. (2011) ‘Fourier Transform Mass Spectrometry’, *Molecular & Cellular Proteomics*, 10(7), p. M111.009431-M111.009431. doi: 10.1074/mcp.M111.009431.

Selliez, L. *et al.* (2019) ‘Identification of organic molecules with a laboratory prototype based on the Laser Ablation-CosmOrbitrap’, *Planetary and Space Science*. Elsevier Ltd. doi: 10.1016/j.pss.2019.03.003.

Senko, M. W., Hendrickson, C. L., Paša-Tolić, L., Marto, J. A., White, F. M., Guant, S. and Marshall, A. G. (1996) ‘Electrospray ionization Fourier transform ion cyclotron resonance at 9.4 T’, *Rapid Communications in Mass Spectrometry*, 10(14), pp. 1824–1828. doi: 10.1002/(SICI)1097-0231(199611)10:14<1824::AID-RCM695>3.0.CO;2-E.

Shannon, T. W. and McLafferty, F. W. (1966) ‘Identification of Gaseous Organic Ions by the Use of “Metastable Peaks”’, *Journal of the American Chemical Society*, 88(21), pp. 5021–5022. doi: 10.1021/ja00973a045.

Shaw, J. B., Lin, T. Y., Leach, F. E., Tolmachev, A. V., Tolić, N., Robinson, E. W., Koppenaal, D. W. and Paša-Tolić, L. (2016) ‘21 Tesla Fourier Transform Ion Cyclotron Resonance Mass Spectrometer Greatly Expands Mass Spectrometry Toolbox’, *Journal of the American Society for Mass Spectrometry*, 27(12), pp. 1929–1936. doi: 10.1007/s13361-016-1507-9.

Shen, K., Wucher, A. and Winograd, N. (2015) ‘Molecular Depth Profiling with Cluster Ion Beams’, *The Journal of Physical Chemistry*, 119(C), pp. 15316–15324. doi: 10.1002/9781118589335.ch5.

Sheraz née Rabbani, S., Barber, A., Fletcher, J. S., Lockyer, N. P. N. and Vickerman, J. C. (2013) ‘Enhancing secondary ion yields in ToF-SIMS using water cluster primary beams’, *Analytical chemistry*, 85, pp. 5654–5658. doi: 10.1021/ac4013732.

Sheraz née Rabbani, S., Barber, A., Razo, I. B., Fletcher, J. S., Lockyer, N. P. and Vickerman, J. C. (2014) ‘Prospect of increasing secondary ion yields in ToF-SIMS using water cluster primary ion beams’, *Surface and Interface Analysis*, 46(S1), pp. 51–53. doi: 10.1002/sia.5606.

Sheraz née Rabbani, S., Razo, I. B., Kohn, T., Lockyer, N. P. and Vickerman, J. C. (2015) ‘Enhancing ion yields in time-of-flight-secondary ion mass spectrometry: A

comparative study of argon and water cluster primary beams', *Analytical Chemistry*, 87(4), pp. 2367–2374. doi: 10.1021/ac504191m.

Sheraz née Rabbani, S., Tian, H., Vickerman, J. C., Blenkinsopp, P., Winograd, N. and Cumpson, P. (2019) 'Enhanced ion yields using high energy water cluster beams for secondary ion mass spectrometry analysis and imaging', *Analytical Chemistry*, p. Just Accepted Manuscript. doi: 10.1021/acs.analchem.9b01390.

Shi, S. D. H., Drader, J. J., Hendrickson, C. L. and Marshall, A. G. (1999) 'Fourier transform ion cyclotron resonance mass spectrometry in a high homogeneity 25 tesla resistive magnet', *Journal of the American Society for Mass Spectrometry*, 10(3), pp. 265–268. doi: 10.1016/S1044-0305(98)00152-4.

SIS (2015) *SIMION® Ion and Electron Optics Simulator*. Available at: http://simion.com/ (Accessed: 19 November 2015).

Smentkowski, V. S. (2014) *Surface Analysis and Techniques in Biology*. Edited by V. S. Smentkowski. doi: 10.1007/978-3-319-01360-2.

Smith, D. F., Kiss, A., Leach, F. E., Robinson, E. W., Paša-Tolić, L. and Heeren, R. M. A. (2013) 'High mass accuracy and high mass resolving power FT-ICR secondary ion mass spectrometry for biological tissue imaging', *Analytical and Bioanalytical Chemistry*, 405(18), pp. 6069–6076. doi: 10.1007/s00216-013-7048-1.

Smith, D. F., Podgorski, D. C., Rodgers, R. P., Blakney, G. T. and Hendrickson, C. L. (2018) '21 Tesla FT-ICR Mass Spectrometer for Ultrahigh-Resolution Analysis of Complex Organic Mixtures', *Analytical Chemistry*, 90(3), pp. 2041–2047. doi: 10.1021/acs.analchem.7b04159.

Smith, D. F., Robinson, E. W., Tolmachev, A. V, Heeren, R. M. A. and Pasa-Tolic, L. (2011) 'C60 Secondary Ion Fourier Transform Ion Cyclotron Resonance Mass Spectrometry', *Analytical Chemistry*, 83(24), pp. 9552–9556. doi: 10.1021/ac2023348.

Smith, D. F., Robinson, E. W., Tolmachev, A. V, Heeren, R. M. A., Pasa-Tolic, L., Pa, L. and Pasa-Tolic, L. (2011) 'C60 Secondary Ion Fourier Transform Ion Cyclotron Resonance Mass Spectrometry', *Analytical Chemistry*, 83(24), pp. 9552–9556. doi: 10.1021/ac2023348.

Sonalikar, H. S. and Mohanty, A. K. (2017) 'Numerical study of segmented-electrode

planar Orbitraps', *International Journal of Mass Spectrometry*. Elsevier B.V., 417, pp. 58–68. doi: 10.1016/j.ijms.2017.03.004.

Sonalikar, H. S., Ovhal, A. A. and Mohanty, A. K. (2015) 'Numerical analysis of segmented-electrode Orbitraps', *International Journal of Mass Spectrometry*. Elsevier B.V., 395, pp. 36–48. doi: 10.1016/j.ijms.2015.12.001.

Stahl Electronics (2013) '2-Channel Amplifier & Cryogenic Biasing Module - A3-5b, A3-7b, A7 / RTA50'.

Stahl Electronics (2015) *NexGen3 Dual Channel Cryogenic Super Low Noise Amplifier*. Mettenheim, DE.

Stephan, T. (2001) 'ToF-SIMS in Cosmochemistry', *Planetary and Space Science*, 49(9), pp. 859–906. doi: 10.1016/S0032-0633(01)00037-X.

Stephens, W. E. (1946) 'A Pulsed Mass Spectrometer with Time Dispersion', *Proceedings of the American Physical Society1*, 69(11–12). Available at: https://journals.aps.org/pr/pdf/10.1103/PhysRev.69.674.2.

Stojilovic, N. (2012) 'Why can't we see hydrogen in X-ray photoelectron spectroscopy?', *Journal of Chemical Education*, 89(10), pp. 1331–1332. doi: 10.1021/ed300057j.

Strupat, K., Kovtoun, V., Bui, H., Viner, R., Stafford, G. and Horning, S. (2009) 'MALDI Produced Ions Inspected with a Linear Ion Trap-Orbitrap Hybrid Mass Analyzer', *Journal of the American Society for Mass Spectrometry*. Elsevier Inc., 20(8), pp. 1451–1463. doi: 10.1016/j.jasms.2009.04.013.

Thomson, J. J. (1897) 'Cathode Rays', *Philosophical Magazine*, 44, p. 293.

Thomson, J. J. (1913) 'Rays of Positive Electricity', *Proceedings of the Royal Society, A. Mathematical and Physical Sciences*, LXXXIX.

Tian, H., Maciazek, D., Postawa, Z., Garrison, B. J. and Winograd, N. (2016) 'CO2 Cluster Ion Beam, an Alternative Projectile for Secondary Ion Mass Spectrometry', *Journal of the American Society for Mass Spectrometry*, 27(9), pp. 1476–1482. doi: 10.1007/s13361-016-1423-z.

Tian, H., Maciążek, D., Postawa, Z., Garrison, B. J. and Winograd, N. (2019) 'C-O

Bond Dissociation and Induced Chemical Ionization Using High Energy (CO 2) n+ Gas Cluster Ion Beam', *Journal of the American Society for Mass Spectrometry*, 30(3), pp. 476–481. doi: 10.1007/s13361-018-2102-z.

Tian, H., Six, D. A., Krucker, T., Leeds, J. A. and Winograd, N. (2017) 'Subcellular Chemical Imaging of Antibiotics in Single Bacteria Using C 60 -Secondary Ion Mass Spectrometry', *Analytical Chemistry*, 89(9), pp. 5050–5057. doi: 10.1021/acs.analchem.7b00466.

Tian, H., Wucher, A. and Winograd, N. (2016) 'Reduce the matrix effect in biological tissue imaging using dynamic reactive ionization and gas cluster ion beams', *Biointerphases*, 11(2), p. 02A320. doi: 10.1116/1.4941366.

Todd, P. J., Gregory Schaaff, T., Chaurand, P. and Caprioli, R. M. (2001) 'Organic ion imaging of biological tissue with secondary ion mass spectrometry and matrix-assisted laser desorption/ionization', *Journal of Mass Spectrometry*, 36(4), pp. 355–369. doi: 10.1002/jms.153.

Touboul, D., Kollmer, F., Niehuis, E., Brunelle, A. and Laprévote, O. (2005) 'Improvement of biological time-of-flight-secondary ion mass spectrometry imaging with a bismuth cluster ion source', *Journal of the American Society for Mass Spectrometry*, 16(10), pp. 1608–1618. doi: 10.1016/j.jasms.2005.06.005.

Trek (2015) 'Trek Model 623B 0 to ±2kV Power Amplifier'.

Ubieto-Díaz, M., Rodríguez, D., Lukic, S., Nagy, S., Stahl, S. and Blaum, K. (2009) 'A broad-band FT-ICR Penning trap system for KATRIN', *International Journal of Mass Spectrometry*, 288(1–3), pp. 1–5. doi: 10.1016/j.ijms.2009.07.003.

Verenchikov, A., Kirillov, S., Khasin, Y., Makarov, V., Yavor, M. and Artaev, V. (2017) 'Multiplexing in Multi-Reflecting TOF MS', *Journal of Applied Solution Chemistry and Modeling*, 6(1), pp. 1–22. doi: 10.6000/1929-5030.2017.06.01.1.

Vetere, A. and Schrader, W. (2017) 'Mass Spectrometric Coverage of Complex Mixtures: Exploring the Carbon Space of Crude Oil', *ChemistrySelect*, 2(3), pp. 849–853. doi: 10.1002/slct.201601083.

Vickerman, J. C. and Briggs, D. (2001) *ToF-SIMS Surface Analysis by Mass Spectrometry*. 1st edn. Manchester: IM Publications and SurfaceSpectra Limited.

Vickerman, J. C. and Winograd, N. (2015) ‘SIMS-A precursor and partner to contemporary mass spectrometry’, *International Journal of Mass Spectrometry*. Elsevier B.V., 377(1), pp. 568–579. doi: 10.1016/j.ijms.2014.06.021.

Vladimirov, G., Hendrickson, C. L., Blakney, G. T., Marshall, A. G., Heeren, R. M. A. and Nikolaev, E. N. (2012) ‘Fourier transform ion cyclotron resonance mass resolution and dynamic range limits calculated by computer modeling of ion cloud motion’, *Journal of the American Society for Mass Spectrometry*, 23(2), pp. 375–384. doi: 10.1007/s13361-011-0268-8.

Walker, A. V. and Winograd, N. (2003) ‘Prospects for imaging with TOF-SIMS using gold liquid metal ion sources’, *Applied Surface Science*, 203–204, pp. 198–200. doi: 10.1016/S0169-4332(02)00624-4.

Waugh, A. R., Bayly, A. R., Walls, M., Vohralik, P. and Fathers, D. (1986) ‘Recent Developments in the Application of Liquid Metal Ion Sources To Sims’, *Le Journal de Physique Colloques*, 47(C2), pp. C2-133-C2-136. doi: 10.1051/jphyscol:1986219.

Weibel, D., Wong, S., Lockyer, N., Blenkinsopp, P., Hill, R. and Vickerman, J. C. (2003) ‘A C60 primary ion beam system for time of flight secondary ion mass spectrometry: Its development and secondary ion yield characteristics’, *Analytical Chemistry*, 75(7), pp. 1754–1764. doi: 10.1021/ac026338o.

Wells, D. D., Moon, H. K. and Gardella, J. A. (2009) ‘Time of Flight Secondary Ion Mass Spectrometric Determination of Molecular Weight Distributions of Low Polydispersity Poly(Dimethyl Siloxane) with Polyatomic Primary Ions’, *Journal of the American Society for Mass Spectrometry*. American Society for Mass Spectrometry, 20(8), pp. 1562–1566. doi: 10.1016/j.jasms.2009.04.015.

Wiley, W. C. and McLaren, I. H. (1955) ‘Time-of-flight mass spectrometer with improved resolution’, *Review of Scientific Instruments*, 26(12), pp. 1150–1157. doi: 10.1063/1.1715212.

Wirtz, T., Dowsett, D., Audinot, J.-N. and Eswara, S. (2016) ‘SIMS on the Helium Ion Microscope: a Powerful Tool for High-Resolution High-Sensitivity Nano-Analytics’, *Microscopy and Microanalysis*, 22(Suppl 3), pp. 160–161. doi: 10.1017/S1431927616001653.

Wolf, R. N. *et al.* (2012) ‘On-line separation of short-lived nuclei by a multi-reflection time-of-flight device’, *Nuclear Instruments and Methods in Physics Research, Section A: Accelerators, Spectrometers, Detectors and Associated Equipment*, 686, pp. 82–90. doi: 10.1016/j.nima.2012.05.067.

Wong, S. C. C., Hill, R., Blenkinsopp, P., Lockyer, N. P., Weibel, D. E. and Vickerman, J. C. (2003) ‘Development of a C 60+ ion gun for static SIMS and chemical imaging’, *Applied Surface Science*, 203–204, pp. 219–222. doi: 10.1016/S0169-4332(02)00629-3.

Wu, G., Noll, R. J., Plass, W. R., Hu, Q., Perry, R. H. and Cooks, R. G. (2006) ‘Ion trajectory simulations of axial ac dipolar excitation in the Orbitrap’, *International Journal of Mass Spectrometry*, 254(1–2), pp. 53–62. doi: 10.1016/j.ijms.2006.05.007.

Wucher, A. (2013) ‘Laser post-ionisation - Fundamentals’, in Vickerman, J. C. and Briggs, D. (eds) *ToF-SIMS: Material Analysis by Mass Spectrometry*. 2nd Editio. Manchester: IM Publications and SurfaceSpectra Limited, pp. 1–30. doi: 10.1255/tofch8.

Wucher, A., Cheng, J. and Winograd, N. (2007) ‘Protocols for three-dimensional molecular imaging using mass spectrometry’, *Analytical Chemistry*, 79(15), pp. 5529–5539. doi: 10.1021/ac070692a.

Xian, F., Hendrickson, C. L., Blakney, G. T., Beu, S. C. and Marshall, A. G. (2010) ‘Automated broadband phase correction of fourier transform ion cyclotron resonance mass spectra’, *Analytical Chemistry*, 82(21), pp. 8807–8812. doi: 10.1021/ac101091w.

Yamada, I., Matsuo, J., Toyoda, N. and Kirkpatrick, A. (2001) *Materials processing by gas cluster ion beams Isao*, *Materials Science and Engineering Reports*.

Yang, L., Amad, M., Winnik, W. M., Schoen, A. E., Schweingruber, H., Mylchreest, I. and Rudewicz, P. J. (2002) ‘Investigation of an enhanced resolution triple quadrupole mass spectrometer for high-throughput liquid chromatography/tandem mass spectrometry assays’, *Rapid Communications in Mass Spectrometry*, 16(21), pp. 2060–2066. doi: 10.1002/rcm.824.

Yavor, M. I., Plaß, W. R., Dickel, T., Geissel, H. and Scheidenberger, C. (2015) ‘Ion-optical design of a high-performance multiple-reflection time-of-flight mass

spectrometer and isobar separator', *International Journal of Mass Spectrometry*. Elsevier B.V., 381–382(1), pp. 1–9. doi: 10.1016/j.ijms.2015.01.002.

Zubarev, R. and Makarov, A. (2013) 'Orbitrap Mass Spectrometry', *Analytical Chemistry*, pp. 5288–5296. Available at: http://pubs.acs.org/doi/ipdf/10.1021/ac4001223 (Accessed: 12 October 2015).